Optimisation of Locking Plate Fixation Methods for Periprosthetic Fractures

Jonathan Mak

Submitted in accordance with the requirements for the degree of
Doctor of Philosophy

The University of Leeds
School of Mechanical Engineering

September, 2013

The candidate confirms that the work submitted is his own, except where work which has formed part of jointly-authored publications has been included. The contribution of the candidate and the other authors to this work has been explicitly indicated below. The candidate confirms that appropriate credit has been given within the thesis where reference has been made to the work of others.

The work within my thesis which has been published as part of jointly-authored papers are as follows:

1. Moazen M, Mak JH, Etchels LW, Jin Z, Wilcox RK, Jones AC, Tsiridis. The effect of fracture stability on the performance of locking plate fixation in periprosthetic femoral fractures. The Journal of Arthroplasty.

   (i) The following chapters of this thesis will include work from this publication; Experimental Results, and Computational Model Development.

   (ii) The candidate provided the experimental and computational models for the stable fracture data presented in the publication. Mehran Moazen developed the unstable fracture computational models presented in this study, as well as the 2300N stable fracture data. The candidate and Mehran Moazen co-wrote the paper. The other authors were involved as supervisors of the two projects.

2. Moazen M, Mak JH, Jones AC, Jin Z, Wilcox RK, Tsiridis E. Evaluation of a new approach for modelling the screw-bone interface in a locking plate fixation – a corroboration study. Proceedings of the Institution of Mechanical Engineers, Part H: Journal of Engineering in Medicine.

   (i) The following chapters of this thesis will include work from this publication; Experimental Results, and Computational Model Development.

   (ii) This paper used data from two projects. The candidate developed the locking plate computational models with fixed interfaces used in this study only. Mehran Moazen developed the computational models using spring interactions at the screw to bone interface presented in this study, and far cortical locking models. The candidate and Mehran Moazen co-wrote the paper. The other authors were involved as supervisors of the two projects.

Acknowledgements

Throughout my four years as a PhD student at the University of Leeds, I would like to thank all of the staff and students who have helped me through journey.

I would particularly like to thank my primary supervisor, Ruth Wilcox, for all of the help and guidance she has given me throughout my PhD. I am certain her patience and insight at every 9:00AM meeting resulted extraordinary levels of optimism and motivation that would not only last all week, but would spread throughout the office, inspiring the whole group with vigour and energy. I count myself lucky to have had the opportunity to be part of Ruth's research group, and am certain I won't forget the great time I had here.

I would like to thank Alison Jones for all of her help over the years, her ability to make me stop talking gibberish, and identify the fundamental problem like a needle in a hay stack is unmatched. The skill of AI-ifying a problem, to reduce an immensely complex problem being badly explained to its bare essentials and to find a way forward, is one I hope I have learnt and be able apply to future problems.

I would like to thank Mehran Moazen for all of his support and advice through my studies. I would like to thank him for teaching me the black art of working with strain gauges, and for always providing help when I was banging my head against the desk, arguing with Abaqus. His Dutch mug will forever come to mind whenever the topic of model development or a certain comedy film comes to mind.

I would like to thank Eleftherios Tsiridis for his leadership and direction throughout my PhD. His drive and dedication are second to none and I hope to have gained some of his unrelenting work ethic.

I would also like to thank Zhongmin Jin for all of his help and guidance on all things computational.

The happy and friendly IMBE environment has made working here a real pleasure. I would like to thank Lee, Ju, Sami, Seb, Kieran, Fernando, Dan, Beth and Corinne for making every day in the office an event to remember. I would also like to thank the Technical staff at IMBE, Phil, Lee, Irvin, Amisha and Tony for helping me complete my project, and would also like to thank

Graham, Mags and Ted for their continued help and support. I think we went through a hard drive a year.

Finally, I would like to thank my girlfriend Eleanor Knight for her unwavering love and support throughout this voyage into the unknown. Thanks for toughing it out, especially when events involving river horses of very very questionable intellect are involved.

Abstract

Periprosthetic fracture (PPF) of the Femur is a common complication of hip arthroplasty. With increasing rates of total hip replacements, the occurrence of periprosthetic fractures is expected to rise. These fractures are often challenging to treat effectively due the technical challenges presented with the combination of fractured bone and an unstable prosthesis. Failure of locking plate fixation of fractures around the tip of a stable prosthesis (Vancouver type B1) have been reported clinically, suggesting that further investigation into their treatment is needed.

This study developed a computational periprosthetic fracture fixation model, using experimentally tested specimens to validate the model. Clear relationships could be identified between the experimental and computational results for the Intact Femur, total hip replacement (THR) and PPF cases. The model could predict the magnitude of the strain in the plate and hence the likelihood of plate fracture, as well as assessing the relative stiffness of different fixation scenarios. The model was suitable for the identification and prediction of changes in strain and stiffness between a set of comparative cases and was used to comment on their relative biomechanical performances.

The angle of a periprosthetic fracture was shown to have a significant effect on stabilised construct mechanics and specifically, the direction of the fracture has a very large effect on fracture stabilisation. Fractures in the ML direction were less stable than fractures in the LM direction. The 45° Medial to Lateral fracture case was the least stabile and the instrumentation configuration used in this study is clearly not optimal for this fracture case. It is recommended that the orientation of the fracture should be taken into account by surgeons when deciding on B1 PPF management.

Table of Contents

List of Tables

List of Figures

Standard terms and definitions

For the purposes of this study, the following teams and definitions apply,

- Arthroplasty- a procedure involving the surgical reconstruction of a natural joint with a hip replacement
- Bicortical screw- a screw designed to penetrate both the proximal and distal cortices
- Bone plates- a device used to give rotational stability to a bone fracture
- Cancellous bone- inner, light and porous layer of bone
- Cerclage – a technique where wires or cables are wound around a bone or fragments to secure them
- Cemented- where bone cement is used to provide fixation between the bone and prosthesis
- Cementless- where fixation between the prosthesis and bone is provided by bone growth, without the use of cement
- Conical screw- a screw shape where the profile tapers towards the tip of the screw
- Core diameter- the diameter of the solid central bar of a screw
- Cortical bone- outer layer of dense compact bone
- Cylindrical screw- a screw shape where the profile remains consistent for the entire length
- Femoral component- part of a hip replacement which is inserted into a Femur
- Femurs- the common term for femora, the plural of a singular Femur
- Instrumentation- components used to stabilise a fracture, e.g. locking plates, screws and locking inserts
- Locking plate- a bone plate designed to bind with supporting screws
- Major diameter- maximum diameter of a screw
- Osteon- a functional unit of cortical bone consisting of concentric rings of bone cells, osteocytes, around a central canal containing blood, nerves and lymphatic vessels
- Pullout strength- maximum load prior to free displacement of implanted bone screw
- Pullout test- experimental test to determine pullout strength
- Revision- a procedure to remove and replace an existing prosthesis
- Screw length- the length from the bottom of the screw head to its tip
- Screw Pitch- the distance between screw threads

- Stiffness- how much a body will resist deformation when subjected to a load
- Thread width- the size of the screw threads
- Unicortical screw- a screw designed to penetrate only the proximal cortex
- Woven bone- temporary unorganised bone with poor mechanical properties

Chapter 1 : Introduction

1.1 Overview

Periprosthetic fracture of the Femur is a complication associated with hip arthroplasty. It has been reported to have an occurrence rate between 0.1-2.3% after primary arthroplasty, and 2.8-7.8% after revision arthroplasty[1-3]. With an ageing population and the rate of total hip arthroplasty increasing to over 71,000 in the United Kingdom in 2011, the occurrence of periprosthetic fractures is expected to rise accordingly[4, 5]. These fractures are often challenging to treat as the mechanical scenario is influenced by the presence of the metal prosthesis within the bone[1, 2], in addition to the combinations of bone fracture geometries. Failure of locking plates following fractures around the tip of a stable prosthesis (Vancouver type B1) have been reported clinically, suggesting that further investigation into their treatment is needed [2].

1.2 Project Aims Objectives and Deliverables

1.2.1 Aim

The overall aim of this project is to improve the management of periprosthetic fractures. By investigating fixation combinations for commonly encountered periprosthetic fractures, this study aims to expand the knowledge base from which clinicians can inform their treatment decisions, reduce the risk of implant failure, reduce patient recovery time, and increase patient quality of life.

The scope of this project is to evaluate fixation methods for periprosthetic fractures of the Femur (PPF), where the prosthesis stem is well fixed and does not require revision. This project will focus on fracture stabilisation using trauma plates secured using screws. Comparisons conducted using finite element models will be comprehensively validated against on-site experimental studies. A range of fracture configurations will be tested and the performance of the fixation method evaluated in each case.

1.2.2 Objectives

The objectives of this study include both experimental and computational goals:

- Preparation of clinically representative experimental test specimens. Fractures stabilised with instrumentation and techniques typical to those used in surgery.
- Design and manufacture of an experimental loading rig. Allowing reliable and repeatable specimen loading, simulating anatomic forces.
- Development of computational model. Achieve balance between detail level and computational requirements.
- Validation of the computational model against experimental results. Establish parameters of validation, identify areas where computational model results are valid and define limits.
- Characterisation and evaluation of the performance of investigated fixation method.
- Investigation of construct properties on fixation method performance from computational model. Determine sensitivity of model to relevant variables.
- Development of computational model to investigate different clinical scenarios. Characterise trends and identify treatment recommendations.

1.2.3 Deliverables

The completion of this study resulted in the following deliverables:

- An operational test bed for experimental loading and evaluation of periprosthetic fracture fixation methods.
- A comprehensively validated computational model of a periprosthetic fracture case, with existing hip prosthesis and trauma plate fixation.
- Characterisation of fixation construct performance and construct behaviour for the validated fracture case.
- Characterisation of fracture configuration on fixation behaviour.

1.3 Chapter Layout

The thesis chapters are presented as follows:

Chapter 1: Introduction presents the overall aims and objectives of the study, a basic introduction to periprosthetic fractures, and a review of the literature related to the area of this study. The review focuses on the specimens currently used to simulate the *in vivo* problem and the methods used to replicate the natural loading environment.

Chapter 2: Experimental Methods describes the experimental methods used in the study including the preparation and instrumentation of the Sawbone specimens, the introduction of the cemented primary prosthesis, fracture creation and construct stabilisation, and the mechanical testing regime.

Chapter 3: Experimental Results presents the experimental results for the specimens at the basic intact Femur stage, introducing a cemented primary hip replacement to the intact Femur, and finally investigating a periprosthetic fracture fixation case.

Chapter 4: Computational Model Development describes the computational methods used in this study to create and develop the representative model of the intact Femur, total hip replacement, and stabilised periprosthetic fracture fixation development stages. The evaluation of different methods, model geometries, and input variables completed throughout the model development is also detailed.

Chapter 5: Comparisons Experimental vs. Computational presents the model validation undertaken by comparing the computational models against the corresponding experimental test data at each development stage.

Chapter 6: Computational Studies describes the initial model development stages away from the validated baseline computational model case. The changes resulting from compromises made when selecting the loading set up and instrumentation configuration used to support and stabilise the periprosthetic fracture specimens, were investigated and quantified, resulting in a developed model.

Chapter 7: Periprosthetic Fracture Configuration Studies describes the results of applying the developed computational model to investigate the effect of various fracture configurations on construct performance. The investigated variables included the angle of the fracture and the distance of the fracture from the tip of the prosthesis stem.

1.4 Background

This section outlines a basic outline of the biology of bone and the different healing modes targeted by the current construct fracture fixation techniques. This section includes an introduction to total hip replacements, and also the causes, classification and treatment methods for periprosthetic fractures.

1.4.1 Bone anatomy

Long bones including the Femur comprise of two main layers, a dense outer layer of cortical bone and a spongy interior layer of cancellous bone. The Femur is split into three regions, the proximal and distal epiphyses, and the diaphysis. The epiphyses consist of cancellous bone with an exterior layer of cortical bone, whereas the diaphysis mainly consists of cortical bone around a central medullary cavity, as shown in Figure1.
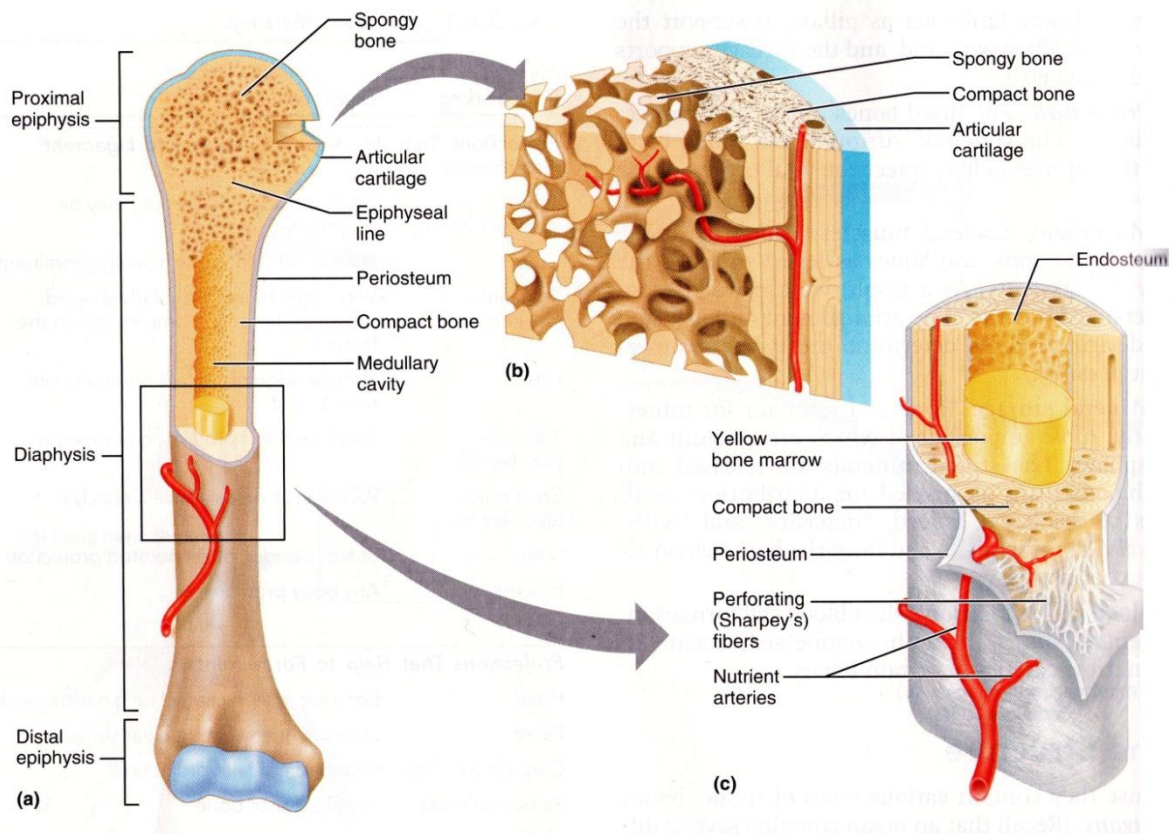
Figure 1 Anatomy of the Femur[6]

The hip joint is a classic example of a ball and socket joint. This is formed between the head of the Femur and the acetabulum of the pelvis. Between the surfaces of these two bones lies a region of fibrocartilage named the acetabular labrum which increases the depth of the socket, allowing for a wide range of motion, with freedom in all axes without compromising the stability of the joint. The joint is reinforced by three main ligaments, the anterior iliofemoral ligament, the inferior pubofemoral ligament and the posterior ischiofemoral ligament, as shown in Figure 2. During the action of standing up, these ligaments will act to tighten the femoral head into the acetabulum, restricting motion and stabilising the joint [7].
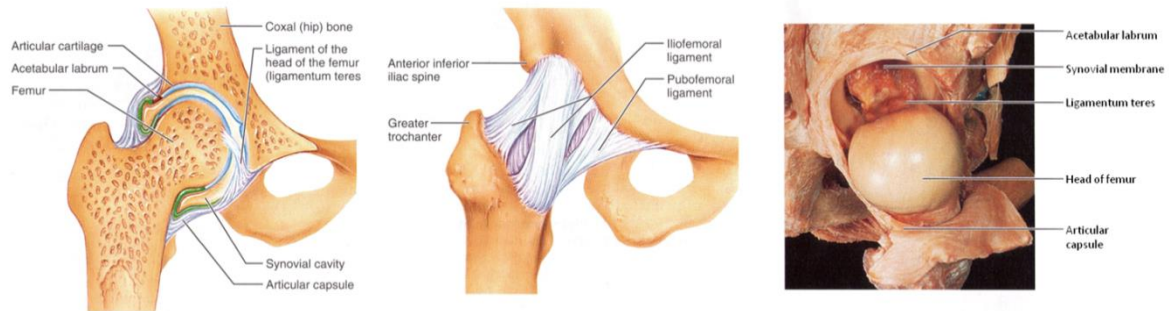
Figure 2 Anatomy of the hip joint[7]

1.4.2 Total hip replacements

The aim of a total hip replacement is to restore functionality of the joint for the patient, increase their quality of life and reduce pain [8]. The number of total hip replacements has increased dramatically over recent years due to the aging population and advances in the design of total hip replacements, allowing younger patients to benefit from arthroplasty. From 2004/05 the number of total hip replacements in the U.K. has risen from 55,000 to 72,000 in 2011[4, 5]. The average age of candidate for total hip replacement has decreased by approximately two years since 2004 to 66.7 years old, and roughly 60% female patients. While the number of patients graded "fit and healthy" at the time of surgery has significantly decreased to 18% from 37% in 2004, this could be due to it now being considered that a compromise in quality of life constitutes a valid reason for hip replacement[8]. The most common indication for hip arthroplasty is osteoarthritis which accounts for 93% of all replacements, although there are other significant reasons such as osteonecrosis, femoral neck fracture and chronic trauma[4].

Total hip replacements have allowed previously incapacitated patients to regain functionality with good long term success rates[9-11]. Patients are usually able to perform physical activities that they were unable to achieve before surgery. Perhaps due to the current success rates, patients now have much higher expectations of total hip replacements than in previous years, and as a result, hip replacement designs have had to adapt and improve to meet this expectation. The prosthesis must now be able to withstand large forces encountered in patients with high activity profiles, such as those engaging in vigorous exercise. Development has been aimed at reducing failure rates, increasing the useful life expectancy of the hips and accommodating the increased expectations from patients with high activity profiles.

1.4.3 Cemented and cementless hip replacement

In order in ensure good functionality of a hip prosthesis, it is important that the stem it is securely anchored to the Femur. Both cemented and cementless hip revisions are capable of providing this stability[12].

1.4.3.1 Cementless Hip Replacement

A cementless hip prosthesis can be implanted into the Femur without the use of cement. They are designed to provide sufficient initial fixation to stabilise the joint, which will subsequently be supplemented by ossification into and around the implant. The lateral surface of a cementless prosthesis will usually be roughened or coated with hydroxyapatite to encourage and support surrounding bone growth until it is firmly secured to the bone.

1.4.3.2 Cemented Hip Replacement

Cemented Hip Replacement is when the prosthesis is fixed in place with polymethyl methacrylate (PMMA) bone cement. Interlock between the cement and bone is vital for successful fixation. This can be aided by pressurisation of the cement which will enable it to infiltrate deep into the bone interstices, increasing tensile and shear strength at the interface.
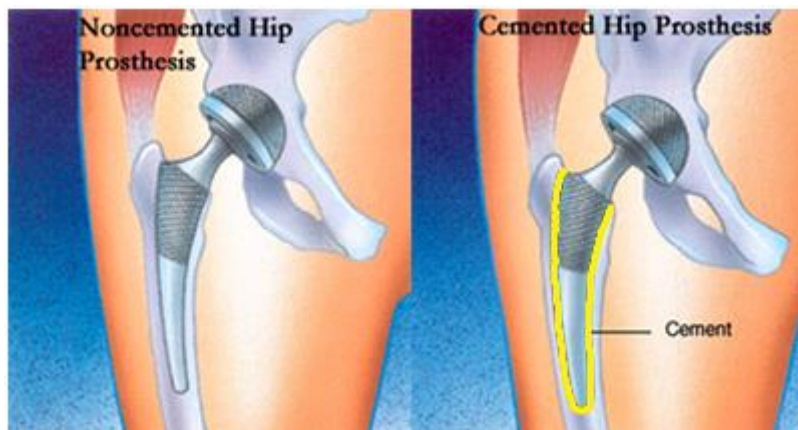
Figure 3 Diagram of Noncemented and Cemented hip arthroplasty[13]

1.4.4 Periprosthetic Fractures

Periprosthetic fracture of the Femur is a complication associated with hip arthroplasty. It has been reported to have an occurrence rate between 0.1-2.3% after primary arthroplasty, and 2.8-7.8% after revision arthroplasty[1-3]. With an ageing population and the rate of total hip arthroplasty increasing to over 72,000 in 2011, the occurrence of periprosthetic fractures is expected to rise accordingly[4, 5]. These fractures can be difficult to treat effectively due the technical challenges presented with combinations of fractured bone and an unstable prosthesis. Reported complication rates have been as high 24%[14]. Periprosthetic fractures can occur intra-operatively, where they result as an error during insertion of the replacement stem, or post-operatively where fractures can result from patient trauma.

A rise in inter-operative periprosthetic fracture incidence rates coincided with the introduction of non-cemented hip prostheses[2, 15]. Where possible, there is an interference fit between the outer surface of the prosthesis and the rasped, internal surface of the bone. Fractures usually occur during insertion when the prosthesis is

too large for the prepared insertion site. Factors such as undersized rasps, tools used to shape the insertion site for hip replacements, and the presence of collars on prostheses to prevent over-insertion into the Femur, have been previously been responsible for initiating cracks. Cemented hip replacements are less likely to cause inter-operative fractures as there is a gap of at least 2mm allocated between the prosthesis and bone for the cement mantle to be formed. If conditions preclude further rasping of the bone and the fit between the prosthesis and the bone is tighter than recommended, the cement mantle can be compromised rather than risking a fracture.

Post-operative fractures can usually be attributed to a recent trauma suffered by a patient. Most of these will be categorised as minor traumas, where the patient suffered a fall which from standing or sitting height. These traumas are most likely to occur within a patient's home. Due to the low energy nature of these traumas, the resultant fractures are commonly simple transverse fractures. A much lower percentage are categorised as high energy traumas and are generally found to result in comminuted fractures, where the bone breaks into multiple fragments. Alternatively, a significant stress riser will frequently be identified as the cause of fracture, such as a bone defect resulting from prosthesis loosening, a screw hole from a previous procedure or from a revision technique with a non-uniform stress transfer pattern.

1.4.4.1 Risk factors

There are a range of factors which can increase the risk of suffering a periprosthetic fracture. They can be categorised into two groups; Patient related factors include osteoporosis[16], rheumatoid arthritis, age[17, 18] and gender[19]. Surgery related factors include reduced bone stock from previous procedures[20], high insertion stress when inserting cementless prostheses and the prevalence of stress risers from old screw holes, ends of plates or stem malposition[21].

1.4.4.2 Classification

There has been a range of classification systems developed to help correctly characterise periprosthetic fractures and in some cases suggest the treatment method. These classification systems have been reviewed by Fink et al.[1] and are summarised in Table 1.

Table 1 Periprosthetic classification systems, describing the categories for each system[1]

Author	Type	Type	Type	Type	Type	Type
Duncan (1995) (Vancouver)	A (L, G) Trochanteric	B (1, 2, 3) around stem	C below tip			
Beals (1996) Tower (1999)	I Intertrochanteric	II Around stem	III (A–C) Around tip	IV Supracondylar		
Roffman (1989)	Stable	Unstable				
Mont (1994)	1 Intertrochanteric	2 Around stem	3 Around tip	4 Below tip	5 Comminuted	6 Supracondylar
Cooke (1988)	1 Comminuted	2 Around stem	3 Oblique below tip	4 Transversal below tip		
Johansson (1981)	I Proximal to tip	II Around tip	III Below tip			
Jensen (1988)	1 Proximal to tip	2 Around tip	3 Below tip			
Bethea (1982)	A Below tip	B Around stem	C Comminuted			
Whittaker (1974)	1 Intertrochanteric	2 Around stem	3 Below stem			

The system which has gained the most acceptance is the Vancouver classification system[22]. It uses the fracture location, the condition of prosthesis fixation and patient bone quality to characterise a fracture. Periprosthetic fractures are divided into three major categories, Type A, B and C. Type A fractures occur in the region of the trochanter, at the superior end of the Femur. A_l fractures refer to those concerning the lesser trochanter and A_g fractures to those concerning the greater trochanter.

The most commonly encountered periprosthetic fracture is the type B. A recent study by the Swedish hip registry revealed that 80% of periprosthetic fractures were type B[17]. These fractures are located in the shaft region around the implanted stem, but do not extend to the distal diaphysis[21]. Type C fractures occur distally, below the tip of the prosthesis, (although the boundary where type B fractures end and type C fractures begin is not explicitly defined).Type B fractures are further categorised into:

B1. Where the femoral stem is stable and there is good surrounding bone stock.
B2. Where the femoral stem is loose and the surrounding bone stock is still good.
B3. Where the femoral stem is loose plus there is deficient bone stock[23].

Due to the location of Type C fractures, which occur significantly distant from the prosthesis, they can be considered as independent of the prosthesis and can be treated using standard fracture reduction and stabilisation techniques.

A study conducted by Leonidou et al, could not identify a trend between fracture classification and fracture angle[24]. The angle of the fracture was found to be independent of the position of the fracture and the surrounding bone quality.

1.4.5 Healing modes

There are two methods of bone repair, direct and indirect, also known as primary and secondary bone healing.

1.4.5.1 Primary bone healing

Primary bone healing occurs when there is no motion at the fracture site and does not involve formation of a fracture callus. A "cutting cone" is formed across the fracture site. This involves bone making cells called osteoblasts, laying down cancellous bone behind bone eating cells, osteoclasts, forming secondary osteons. This is a very slow process and fractures healing in this way can take months to years to fully repair[6]. Direct bone healing can further be divided into two subsets; contact healing where the fracture ends are in direct contact and healing begins immediately, or gap healing where the gap is no more than 500 micrometres and is initially filled with woven bone with is subsequently remodelled into cancellous bone[25, 26].

1.4.5.2 Secondary bone healing

Gaps between bones of over 500 micrometres are healed by secondary bone healing[25, 26]. This occurs in fractures that are not rigidly fixed. Initially, a mass of clotted blood, called a haematoma, is formed around the fracture site. This is replaced by a fibrocartilaginous callus where new blood vessels are formed between the fracture ends and cancellous bone begins to be deposited. Within a week this callus converts to a bony callus of cancellous bone. The final stage of the process is bone remodelling which starts during bony callus formation and continues for several months. Excess material on the exterior of the daiphysis and in the medullary cavity is removed and cortical bone is laid down to reconstruct the shaft walls. Due to local mechanical loading during callus formation, this bone resembles the original, unbroken bone, as shown in Figure 4[6].
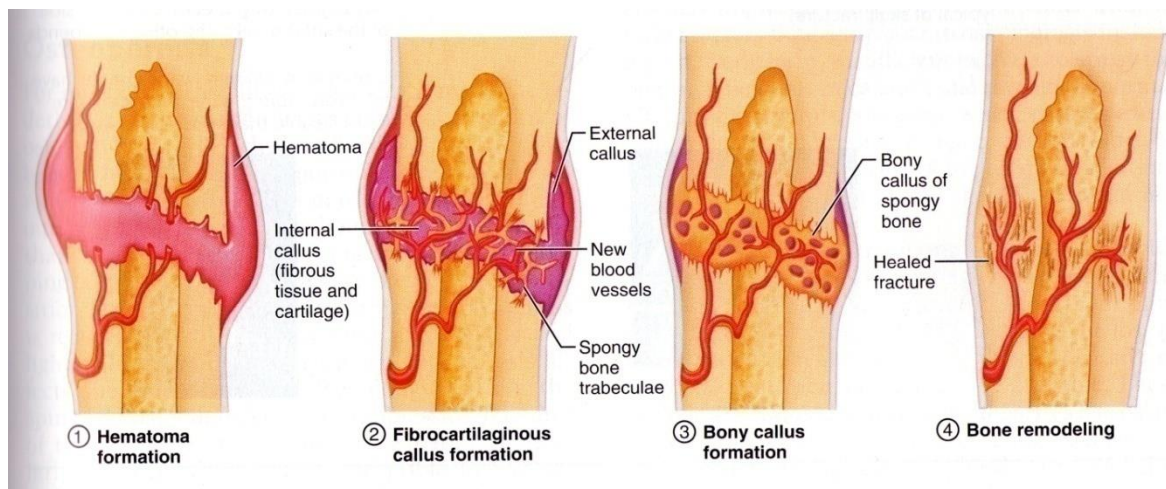
Figure 4 Illustration of Bone healing[6]

Secondary bone healing can be advantageous as the fracture will become more stable, which could promote faster healing than with primary bone healing. This is particularly relevant when considering the average age and bone quality of periprosthetic fracture patients, who are likely to have a reduced number of active osteoblasts[27].

1.4.6 Current treatment and complications

Optimum fracture fixation will promote early union of the fracture, maintain the existing bone stock and restore correct bone geometry. These may result in early mobilisation of the patient as well as restore functionality and improve their quality of life. For both intra-operative and post-operative fractures, prevention is more desirable than treatment. However, there are times where the option of avoiding potential stress risers in the bone from the prosthesis stem are not possible, and it is sometimes hard to evaluate the exact condition of the bone.

When periprosthetic fractures occur, clinicians have a range of methods available to treat them, using combinations of plates, allograft struts and revision stems. Figure 5A shows a periprosthetic fracture and examples of the typical location of plate fixation methods. The use of proximal unicortical screws and distal bicortical screws is shown in Figure 5B and proximal cables and distal bicortical screws shown in Figure 5C.
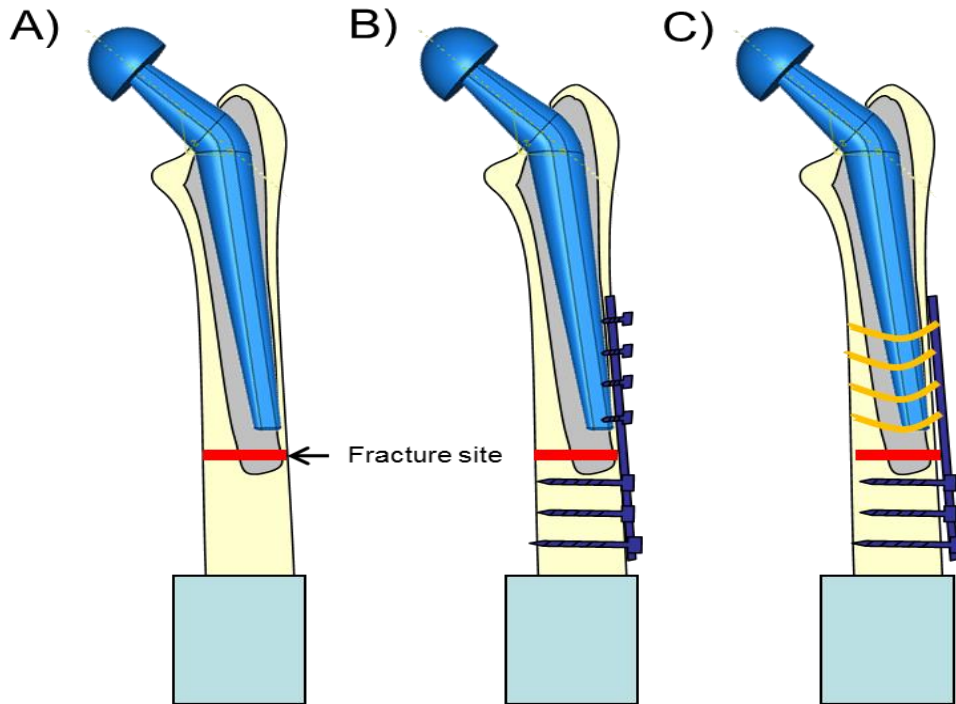
Figure 5 Fixation Methods A) An implanted hip prosthesis and potential fracture site B) A stabilized periprosthetic fracture using a plate with proximal unicortical screws and distal bicortical screws C) A stabilized periprosthetic fracture using a plate with proximal cables and distal bicortical screws

Once a periprosthetic fracture is classified using the Vancouver system, this can be used to help decide which treatment method to use to ensure successful healing. Treatment algorithms have been proposed by Masri et al. [3] and Parvizi et al.[28] to aid this process.

VANCOUVER TYPE

A

A-$_L$: lesser trochanter, symptomatic treatment only even if displaced. Intervene only if substantial segment medial cortex attached.
A-$_G$: greater trochanter, symptomatic treatment with crutches and limit abduction. Intervene only if displaced to avoid pain, weakness, limp, or instability.

B

C

Ignore implant, fix fracture, if necessary address implant after fracture healed

FIXATION OF STEM

WELL FIXED STEM
B$_1$
ORIF with cerclage and struts and plat

LOOSE STEM
B$_2$

GOOD BONE STOCK?

yes

no

B$_2$
Revision with long stem – Cemented or cementless

B$_3$
Revision and augmentation of bone stock with allograft in physiologically young or tumor prosthesis in elderly patients

Figure 6 Masri Treatment Algorithm[3]

Masri et al.[3] reports that type A$_g$ and A$_l$ fractures usually do not require internal fixation, that fracture should be stabilised with protected weight bearing and limited loading of the fracture. A$_g$ fractures larger than 2mm could lead to instability causing the patient pain, and may lead to treatment with internal fixation. A$_l$ fractures are usually minor, and intervention should only occur if there is significant displacement of the fracture which could lead to further complications for the patient. For type C fractures it may be necessary for only fracture fixation to be conducted initially, with implant revision to take place in a later operation.

For B1 fractures open reduction and internal fixation using cerclage cables, screws, plates and allograft struts is suggested. In the case of B2 fractures, long stem revision should be used to bypass fracture , with the addition of an allograft strut if the construct needs additional rotational stability. Type B3 fractures may be the most difficult to treat due to the poor bone quality around the loose prosthesis. For young patients, both Masri et al. [3] and Parvizi et al.[28] recommend the use of long stem revision with the addition of allograft struts and bone stock augmentation, while femoral replacement is recommended for elderly patients.
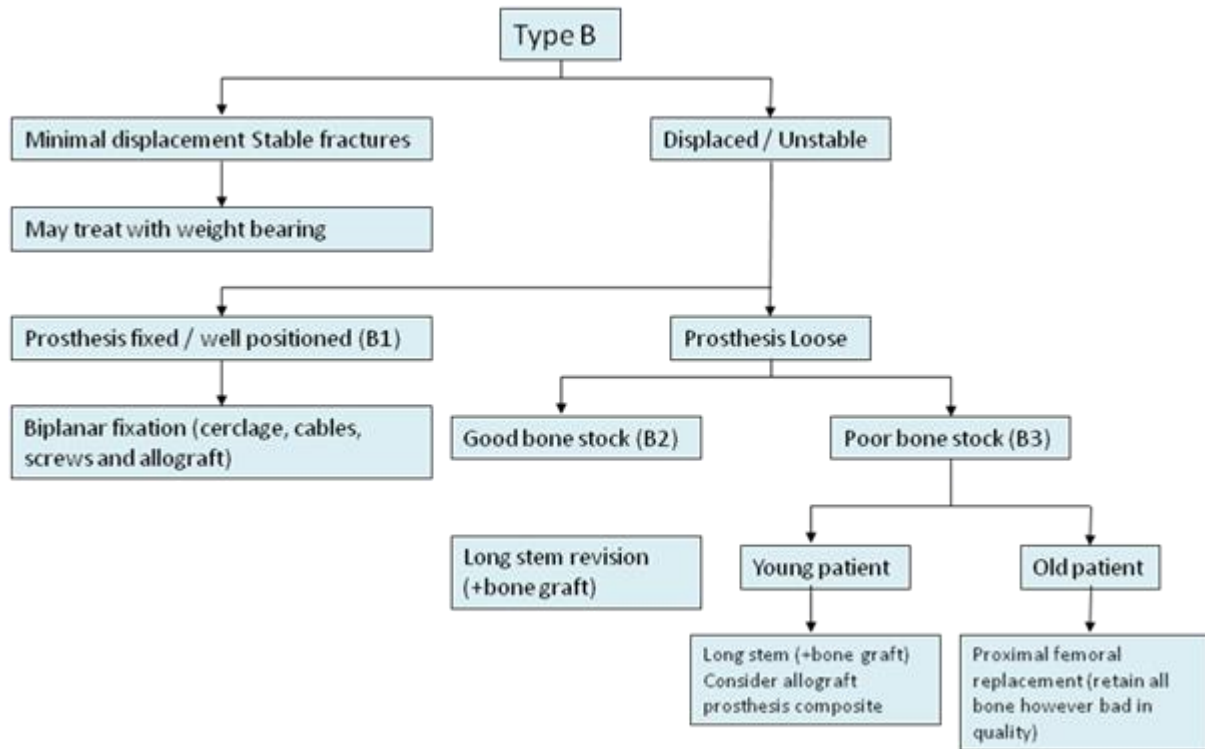
Figure 7 Parvizi Treatment Algorithm[28]

Springer et al.[29] reported that the most common problems associated with periprosthetic fracture fixation include aseptic loosening of the femoral component, fracture non-union, and deep infection. The most encountered of these was implant loosening with an occurrence in 21 cases in a study of 118 patients. In addition, Tsiridis et al.[30] reported an additional complication of fixation plate failure (Figure 8). A revision surgery rate due to plate failure of 25% was reported, with all of the failures occurring within the first 6 months after the initial fracture fixation[30].
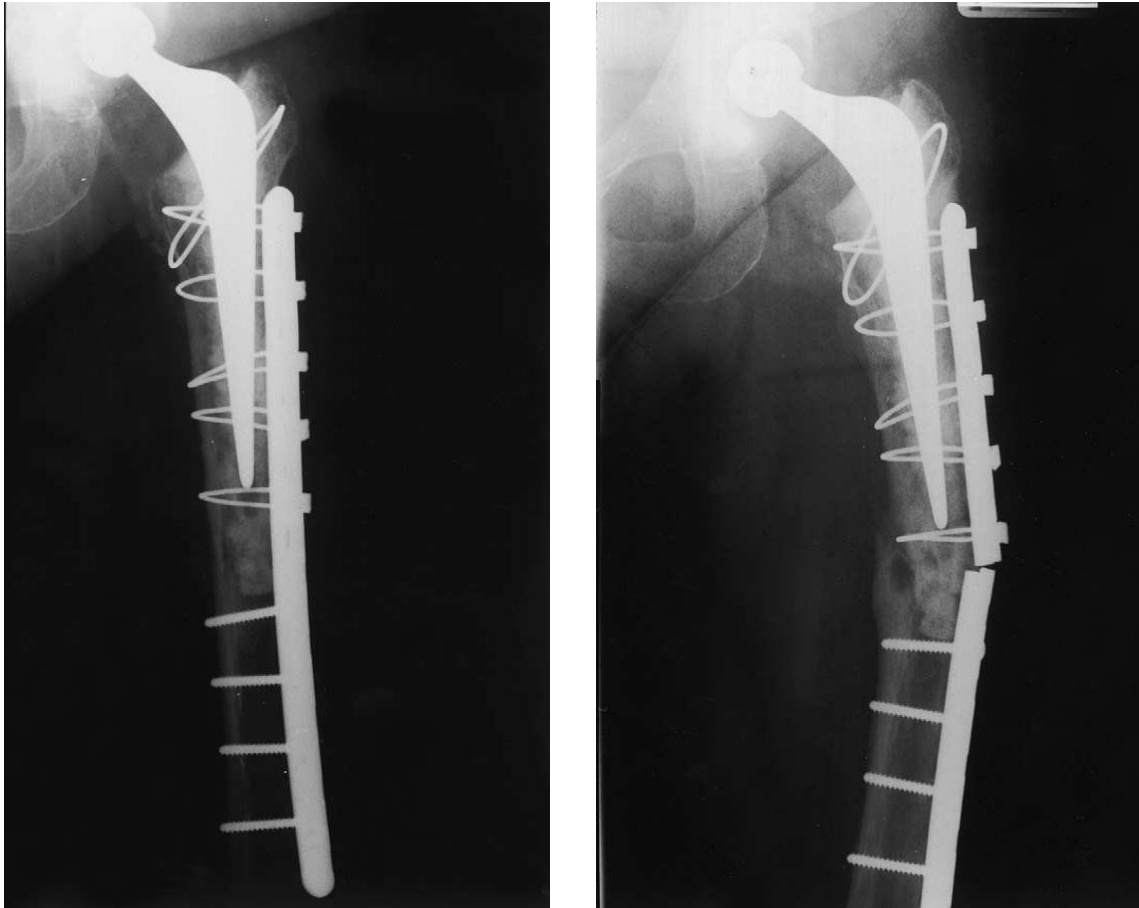
Figure 8 Fixation plate failure. A shows the stabilised fracture immediately after the initial fracture fixation while B shows the same patient after 4 months following a domestic fall, with a fractured plate[30]

Even with the use of classification systems, it has been reported that differentiation between classification groups can be difficult, such as between type B1 and B2 fractures[17]. Due to the unpredictable nature of fractures and variations in individual patients' bone quality, it can be difficult to choose and employ the correct fixation technique. Incorrect fixation can lead to fracture instability and can lead to failure [30, 31].

1.4.7 Fixation plates

The plates used to stabilise a fracture can be manufactured for a range of materials including stainless steel, titanium, and carbon fibre[32].

1.4.7.1 Compression plates

Conventional compression plates provide a mechanism for anatomical reduction and provide stable, rigid internal fixation for a fracture. They are an established fixation

method and have been shown to perform well when stabilising periprosthetic fractures[33]. This method requires a plate with smooth holes to be pre-contoured such that it matches the anatomy of the target bone and a series of non-locking screws. These screws are used to attach the plate to the bone, which will act to compress the two bones together, therefore reducing the fracture. By placing the ends of the fracture site in direct contact and by ensuring a very rigid construct, compression plates aim to promote primary bone healing at the fracture site. The rigidity of a compression plated fracture is dependent on the friction between the plate and the bone, which is dictated by the pressure exerted on the plate by the screws.

A clinical disadvantage of this system is that it can be invasive, requiring wide exposure of the fracture in order to facilitate reduction and plate fixation. This can increase both the chances of delayed union and non-union of the fracture, and the risk of infection. In order for good plate to bone contact, it may be necessary for the bone surface to be aggressively prepared. There is also the risk of further compromising the periosteal blood supply due to disturbing the fracture haematoma. Compression plates have the best success with good quality bone stock and precise anatomical reduction which is not always available when dealing with periprosthetic fractures[34].

1.4.7.2 Locking plates

Locking internal fixators consist of plates with threaded holes and screws with threaded heads, Figure 9A. When tightened into the plate, the screws will "lock" onto the threaded holes, perpendicular to the plate. This locking action will reduce the amount of compression the screws apply to the plate onto the bone and as a result, the plate may not be touching the bone. This is not important as the compression of the plate to the bone is not necessary to achieve stability. These plates can be pre-contoured to the average anatomical profile of the bone and do not need to be adapted to fit an individual patient's anatomy. This reduces failure due to mismatches between a plate and patients' bone contours. Also, as the plate is not required to be touching the bone, the contact region on the bone does not need to be prepared, which can help preserve the periosteal blood supply around the fracture[35].

Locking plates provide flexible yet stable fracture fixation (elastic), promoting secondary healing at the fracture site[36, 37]. The stability of a locking plate system is directly proportional to the stiffness of the whole construct. As the screws are locked onto the plate, they benefit from increased angular and axial stability as well as reducing the possibility for micro-motion between the screw and plate, which reduces the risk of loosening. A construct using locking plates transfers loads from the bone to the fixation through the screw-plate interface.

In practice, the use of locking fixators has been implemented with the use of locking compression plating (LCP), where the screw holes on the plate can accommodate both, locking or non-locking screws[38, 39], Figure 9B. Non-locking screws can be used to reduce the gap between the plate and bone and to apply axial compression to aid fracture reduction, while locking screws can be used to provide angular stability to the construct. By allowing the use of both types of screws at all locations along the plate, this flexibility has allowed surgeons to use a range of combinations of locking and conventional screws to stabilise a fracture[40]. Locking plates will not fail if the screw threads in the bone are stripped, the whole screw and plate construct would have to completely come away from the bone in order for support to no longer be provided.
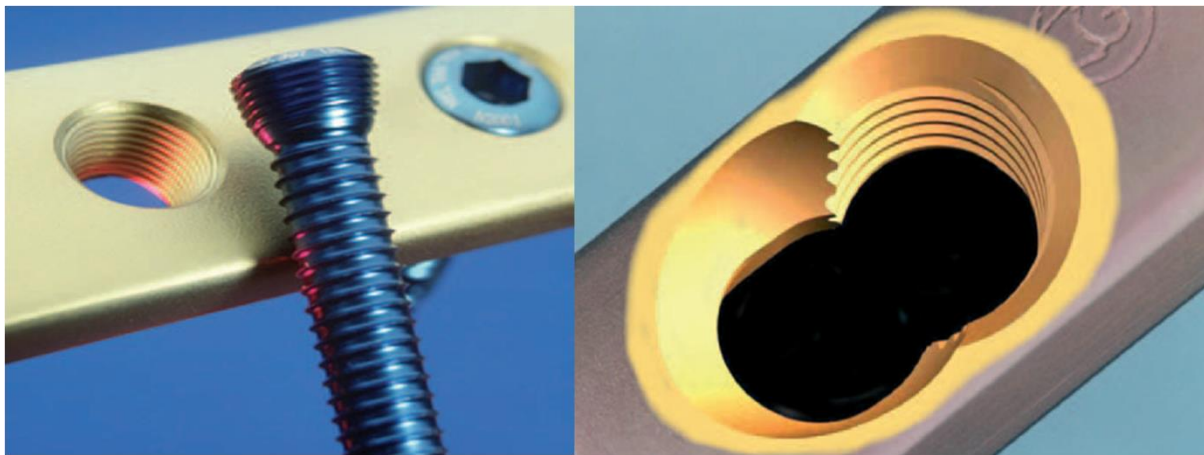
Figure 9 Locking plate fixation[26], A illustrates the threaded head of a locking screw, B illustrates a sample screw hole on an LCP plate

For Vancouver type B1 fractures, the use of multiple plates or a combination of a plate and an allograft strut is recommended for the majority of cases[20, 41]. If the bone quality around the prosthesis is poor, the preference is for a locking plate to be used to stabilise the fracture[42]. The plate would bisect the fracture with unicortical screws used around the prosthesis stem and bicortical screws securing the plate to the distal Femur.

1.4.7.3 Alternative fixation methods

A number of fixation methods deviating from the standard compression and locking plates have been investigated in the literature.

The Mennen plate is a fracture fixation device, using a central plate, supporting a numerous series of fastening arms[43]. These arms clamp around the femur, providing a large surface area in contact with the bone. Originally developed to provide support to non-weight bearing bone fractures, the concept was further developed for use in weight bearing bones, such as the Femur[44]. The treatment of

unstable periprosthetic femoral fractures resulted in high failure rates of up to 75%[44-46], and is not currently recommended in the treatment of these fractures.

The use of cerclage cable only solutions are aimed at removing the need to insert a screw into the medullary canal. Using cerclage cables as a single tool for fracture fixation was abandoned, because it was mechanically too weak to fulfill the requirement of functional aftercare[47, 48]. The Odgen construct, a plate system with cerclage only fixation on the level of the prosthesis stem has exhibited clinical results with a failure rate of up to 30%[49].

1.4.8 Bone screws

One of the most commonly encountered methods for securing trauma plates in long bones is the bone screw. Internal fixation techniques for treatment of periprosthetic fractures can include cables or bone screws to assist in the securing of the plate to the bone[50]. Previous biomechanical studies have shown that the use of bone screws in combination with plate and cerclage cables provide a security of fixation, and have been shown to perform better than in examples where plates and cerclage were used alone [1]. While relatively simple in design, there are a wide range of characteristics that can be varied to alter the performance of a screw.

Primarily bone screws are subjected to both axial forces, along the long axis of the screw, and bending moments. The axial forces can cause shear stresses in the region of bone surrounding the screw, specifically in the area between screw threads. These forces are responsible for the pull out failure of bone screws[51]. The bending moments can result in compressive stresses being applied to the immediate surrounding bone and can cause bone to be crushed between the threads of the screws[52].

1.4.8.1 Locking and Non-locking screws

Conventional screws used in fracture fixation are used to compress a plate onto the bone, creating friction. As the screw is tightened, the infiltration of the screw through the bone combined with the resistance of the screw head creates an axial traction force which produces the bone-to-plate compression. In osteoporotic bone, compression plating failure can occur when the force needed to sufficiently secure the plate onto the bone is higher than the force required to cause the bone around the screw to fail and strip its thread. In compression plating, this would cause a reduction in the friction between the plate and bone, reducing the rigidity of the construct, which could lead to component loosening and subsequent failure.

The head of a locking screw is designed to bind with a corresponding hole on a locking plate. This action is facilitated by threading the surfaces of the screw and hole and also by profiling the screw head into a steep conical shape. As the locking screws are not compressing the plate to the bone, the plate does not inherently load the screw, reducing the forces exerted through the screw, reducing the potential for screw stripping to occur. These lower forces allow more flexibility, which is fully exploited in the current generation of locking screw designs, which have a larger core diameter and smaller thread width than non-locking screws, Figure 10. The smaller thread width allows the screws to bind better with the thinner cortices found in osteoporotic bone while the increase in core diameter will increase their resistance to bending.
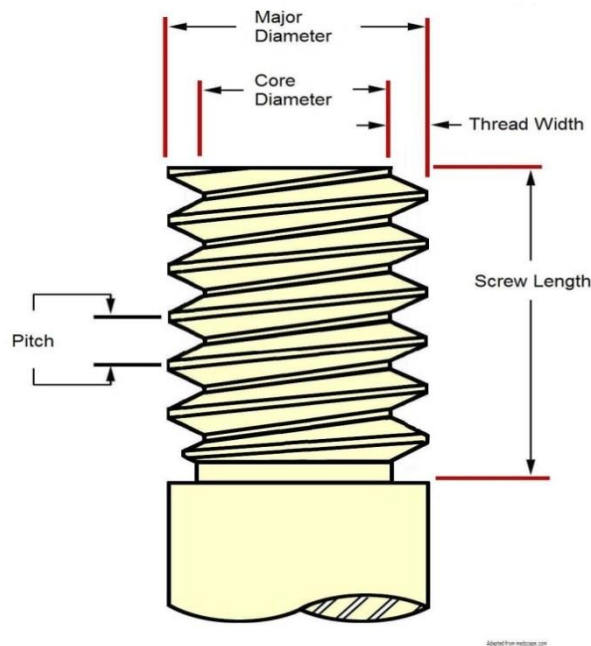
Figure 10 Major Screw properties including Pitch, Major diameter, Core diameter, Thread width and Screw length

1.4.9 Comparative metrics

The metrics defined below are the most commonly encountered measurements used to quantify the performance characteristics of bone screws.

1.4.9.1 Pullout strength

Pull out strength remains the preferred metric to evaluate bone screw performance. While many studies have proposed other possible metrics, pullout strength remains the most popular due to its simplicity and repeatability. Pull out strength, otherwise known as pull out force or push out force, is defined as the maximum load prior to free displacement of the screw. It has been found to be directly proportional to the insertion torque of a the screw, and has been found to have a linear relationship with the shear strength of material medium. It has also been shown to be strongly

correlated with the surface area of the screw threads. There are several landmark papers in this field, Ansell and Scales[53], Yerby et al.[54] and Stromsoe et al.[55], which have established a bench-mark pull out force to be between 3- 7.5kN in human cadaveric long bones using unicortical screws[56].

1.4.9.2 Stress

Stresses can be calculated from both mechanical testing and finite element analysis. Stress distribution across a screw can be used to identify potential failure points and it is important that a screw does not exceed its yield stress when under maximum clinical load as this could lead to failure when implanted. Von Mises stress criterion is commonly used in the literature, chosen as it is suitable in the analysis of plastic deformation in ductile materials, which includes metals such as medical grade stainless steel. It is calculated from the principal stresses acting at a discrete point and is used to determine if the material will yield by comparison with the yield stress. When analysing the stress occurring in a particular screw design, an underestimation could potentially lead to failure of the design in practice. An overestimation of stress may result in a less optimal screw design, but it should not fail under design loads .

1.4.9.3 Bending

A screws resistance to bending has been suggested to reduce the susceptibility to loosening[51]. Bending moments acting on a stiffer screw will result in lower compressive stresses in the bone and a lower occurrence of bone crushing. These are also used in screw and plate studies and aim to test angular stability. Insertion angles of greater than 0° but less than 5° have been shown to increase resistance to bending without a significant reduction in pull out strength in comparison with an insertion angle of 0° [52].

1.4.9.4 Torque

High torque values during screw insertion is a major clinical problem which will lead to stripping of either the pre-tapped self-tapped thread in the bone. Nunamaker et al[57]. showed this could lead to compromised screw strength as the screw is not fully supported within the bone. During screw insertion, maximum torque values and axial compression occur at the same time. In order to minimise torque, even tightening of the screws throughout insertion is important in order to evenly distribute the load.

1.4.9.5 Types of failure

There have been three main failure modes observed in the literature, and are shown in Figure 12;

1. Firstly cylindrical tearing failure, where the bone fails in-between the threads of the screw, resulting in a "cored" effect. The screw will detach from the bone block with bone trapped between its screw threads. The

term "envelope stress" has been used by Chaudhary et al.[58] to define the weakest point in the bone region before cylindrical failure occurs.

2. The second failure mode is diagonal cracking failure where cracks propagate from the screw insertion point. Diagonal cracking is more likely to occur as the density of the bone increases.

3. The final failure mode is vertical cracking. This is not a clinical failure mode and is attributed to the experimental set up of the pull out test.

Adapted from Chaudhary et al. {6}
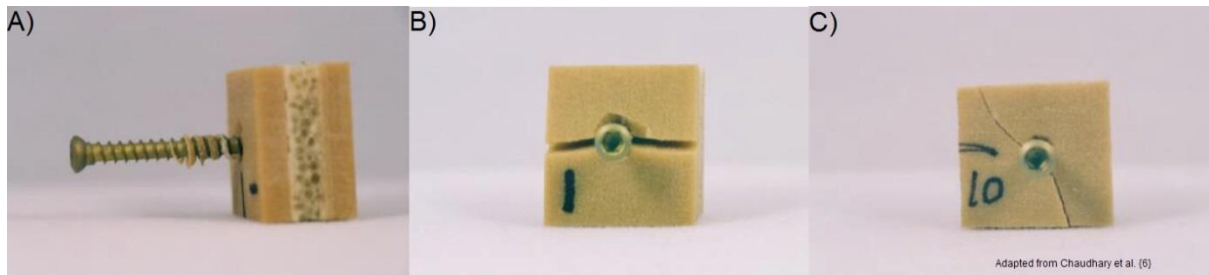
Figure 11 Screw failure modes, A shows cylindrical tearing failure, B shows diagonal cracking failure while C shows vertical cracking[58]

1.4.10 Experimental testing

Experimental tests were carried out on screws embedded in a material and loaded using a compression testing machine. The specimens were placed in the centre of the machine with the screw positioned directly vertically. The specimens were typically secured using a vice, with the addition of clamps on the specimen surface for smaller samples. A range of loading rates were used ranging between 5 and 10mm/min[58-60]. The maximum loading force was recorded when the screw was fully disengaged from the bone.

1.4.11 Analytical formula

An analytical formula is used to accurately predict the pullout force of a screw based upon its design properties. The landmark paper in this field was derived by Chapman et al.[61] and uses a combination of the shear strength of the bone, thread depth and pitch, and major diameter to predict screw performance, Figure 10[61]. Using the formula, a designer can calculate the optimum thread diameter for a screw given its pitch. The screw shape factor formula does not consider pre-drilling pilot holes and therefore also pre-tapping of the hole. It does not account for conical screw thread patterns and additionally, assumes cylindrical tearing failure.

An alternative method called the integral method has also been proposed [62]. This formula differs from Chapman's formula[61] in that it does account for pilot hole size, pre-tapping and conical shaped screws, but it has only been validated using data from spine pedicle screws. However, the authors hypothesise that it may be applicable for other bone screws, but this has not yet been investigated.

1.4.12 Computational modelling

Computational modelling represents an attractive alternative to experimental methods for evaluation of bone screw design. Modelling provides a quantitative analysis method which is easy to interpret, and can be more accurate and precise than existing testing methods. While stress values at discrete points could be gathered though the placement of strain gauges at predetermined points on the investigated screw and bone region, modelling allows the observation of the complete mechanical response of the system. It is simple to vary the loading positions of any applied forces on the model, and thus a wide range of forces can easily be modelled. This is an advantage over traditional evaluation methods where constraints such as cost and availability of test materials may restrict the number of load cases tested and so limit the range of the investigation.

There are two distinct modelling approaches which have been taken to investigate bone screw performance: one simple and one more complex. Examples of both modelling approaches are shown in Figure 12.

1.4.12.1 Simple approach

This style is normally encountered when an investigation involves both mechanical and mathematical model investigation. As a result, such models will include experimental features such as clamps and guides in order to accurately replicate the experimental set up. While these models have the advantage of experimental validation, the inclusion of the experimental features can have a large effect on the results. This can be seen in the study by Chaudhary et al.[58] where the inclusion of clamps supporting the bone block changed the failure type of the system.

1.4.12.2 Complex approach

These are ideal load cases, usually without experimental validation. This approach can reduce experimental influences and typically employ simplification to reduce the complexity of the models. Studies such as Hsu et al.[63] and Zhang et al.[64, 65] have exploited the increased efficiency of these models to incorporate complex contact conditions between the screw and bone, better simulating the behaviour between the two components.
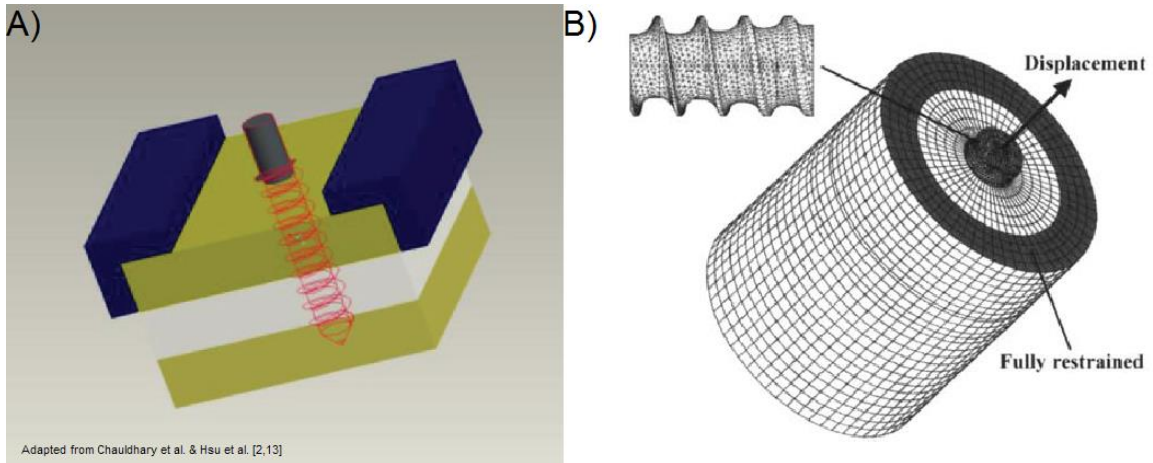
Figure 12 Examples of the two modelling approaches, A-from an simple approach study which includes experimental clamps and B- from a complex approach study.

Complex models are more likely to provide accurate results when investigating the significance of individual screw properties. The use of complex contact conditions to better replicate the screw and bone interaction are more likely to allow the accurate evaluation of screw performance. As their geometry is defined to match that of the laboratory tests, comprehensive validation of experimental style models will likely be less complicated than for theoretical style models.

1.4.12.3 Model design

Due to the complex nature of the screw geometry, many studies constructed their bone and screw models separately in CAD software before importing them in the finite element software[58, 63, 64]. Where possible, the geometries of the screws were generated from the manufacturers specifications[58], but if not readily available, the dimensions were measured from sample screws[63, 66]. The corresponding hole in the bone block was defined to match the profile of the screw[64-66]. This was done to facilitate model assembly and to simplify the surface contacts[58, 67]. For the three-dimensional models, tetrahedral or brick solid elements were commonly used to mesh the models. In order to maximise the computational efficiency of the models, simple models could initially be run to identify areas of interest. Mesh refinement was then employed to increase the mesh density in the predicted areas of high stress while lowering mesh density in low or consistent stresses. As a result, mesh density was usually higher in the threads of the screw and the immediate surrounding region of bone. Materials used in the models were assigned their respective material properties.

1.4.12.4 Simplifications

In order to reduce the complexity of the screw models, geometric simplifications were applied. Simplifications have included reducing the volume of the bone specimen from its original geometry to a regular cuboid[58]. This included two layers of cortical bone with a layer of cancellous bone in between. This resulted in a reduction in overall model size as well as simplifying the definition of boundary conditions. A two dimensional model have also been developed, using symmetry to simplify their model, reducing its size by half[67]. Zhang et al.[65] also used symmetry to help simplify their model. However, as the load case was simple and there were no experimental features to include, only a quarter of the screw and bone block was chosen to be modelled.

1.4.12.5 Contact

The least complicated method of representing the contact assumed perfect bonding between the screw and bone block. Perfectly bonding was also assumed between the different cortical and cancellous bone layers in the bone block[58]. A similar approach, where a bilinear cohesive zone model controlled bonded contact pairs, defined between the elements at the screw-bone boundary, has also been taken[19]. This was used to provide a more accurate representation of the failure behaviour inside the bone using a function for shear stress and relative movement between the surfaces. To simulate a more complex interaction, definition of surface to surface, rigid to flexible contact elements at the bone-screw interface have be used[11]. The contact area on the screw thread was defined as the master surface with the surface of the threaded hole defined as the slave surface. Whilst the accurate representation of the bone and screw boundary can be accomplished with the introduction of these methods, they are more computationally intensive and complicated than the simple models. It may be difficult to introduce these methods to complex models representing multiple screw fixation encountered with periprosthetic fracture fixation techniques.

1.4.12.6 Material properties

Cortical and cancellous bone properties were typically defined as linear elastic isotropic materials with elastic modulus of 16.7 GPa and 23 GPa respectively[58]. Hsu et al.[63] made significant modifications to their model to aid accurate simulation of conical screws. The bone compaction effects resultant from the deployment of conical screws were simulated by adjusting the elastic modulus in relation to the change in density of the bone surrounding the conical screw core. The magnitude of this adjustment was made based upon the resultant volume reduction in the bone.

1.4.12.7   Boundary conditions

In order for a mathematical model to accurately replicate an experimental test, it is important to mimic the experimental conditions as closely as possible. In the theoretical style models, the outer surfaces of the bone block were constrained in all directions. Usually, the screw was restricted in two axes such that it could only be displaced along its length[52]. In the experimental style set ups where clamps were used to restrict the bone block, the clamps were assumed to be perfectly bonded with the bone and were constrained in all directions[58]. Simulating loading on the models was done simply by applying a load on the screw head perpendicularly away from the bone block. Alternatively, if testing until failure, a displacement was applied to the screw head to calculate the force necessary for failure.

1.5 Strain and strain gauges

1.5.1 Introduction

Strain can be measured to determine the amount of deformation of a specimen, with respect to an applied force. Strain is dimensionless and can be either positive or negative, under tensile or compressive loading respectively. When placed under load, this produces a proportional stress within the specimen. This results in a corresponding stress which will deform the specimen. The ratio of the change in length of the specimen (ΔL) divided by the original length of the specimen (L) is defined as strain (ε)[68] Figure 13.
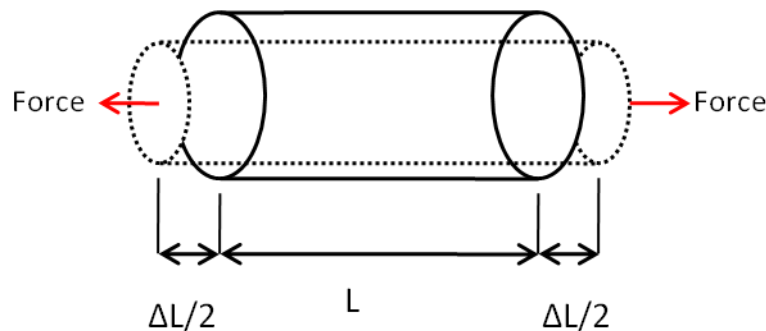
Figure 13 Illustration of Strain definition

The most common method for measuring strain is using strain gauges. Strain gauges are manufactured from ferritic materials, whose electrical resistance will change as a material is deformed. They usually consist of a grid of fine wire or foil placed on an insulating base, Figure 14. The grid pattern will aim to maximise the amount of wire or foil in the direction parallel to the investigated strain while minimising the amount in the perpendicular direction. This increases the accuracy of the gauges by reducing the effect of shear strain on the gauge readings. Strain gauges are attached to the surface of the tested specimen, where any deformation in the material will produce a proportional deformation in the strain gauge. As

deformation of a test material occurs due to an applied force, the electrical resistance of the strain gauge will vary, and this variation be used to calculate strain.
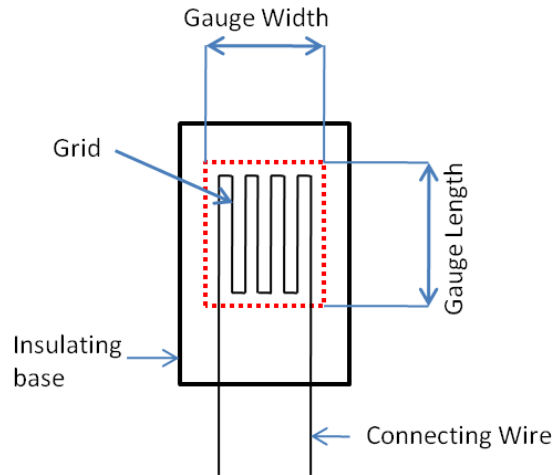
Figure 14 Schematic showing strain gauge features

1.5.2 Wheatstone bridge

Experimentally measured strains are usually in the microstrain range. A lone strain gauge is unable to respond accurately within this range. In order to obtain accurate readings strain gauges can be used in a Wheatstone bridge configuration ,Figure 15, with voltage excitation. This will involve a combination of four active gauges (full bridge), two active gauges and two resistors (half bridge), or one active gauge and three resistors (quarter bridge).
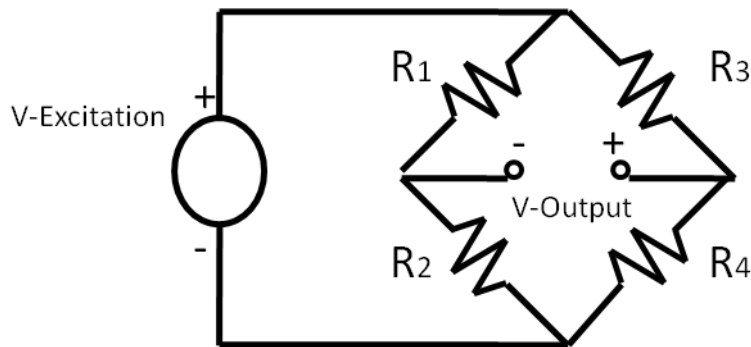
Figure 15 Schematic of a Wheatstone bridge configuration Abbreviations: R$_{(x)}$ = Resistor

The output voltage of the bridge is;

$$V0 = \left[\frac{R1}{R1 + R2} - \frac{R3}{R3 + R}\right] * Vex$$

When each of the resistors have the same value, the bridge is said to be balanced and the output voltage will be zero. If the resistance changes in one of the resistors, the bridge become unbalanced and the output voltage will deviate from

zero. By replacing a resistor with an active strain gauge, variations in the strain gauge resistance will cause a proportional change in the output voltage[69].

1.5.3 Null Offset

Due to individual resistor and wire variation, and instillation factors such as soldering, it is unlikely that the initial, unstrained output voltage will be exactly zero volts. In order to compensate for this potential error, a null offset calibration can be performed. By taking a preliminary strain reading, the initial offset error can be recorded. The excitation voltage applied to the bridge will then be varied until the initial voltage reading is zero.

1.5.4 Gauge factor

The gauge factor describes the ratio between the change in length and the resultant electrical resistive variation of a strain gauge. This determines how sensitive a gauge is to strain changes on the test specimen. It is important that the gauge factor is sensitive enough at the predicted strain variation range during an experimental test[70].

1.5.5 Excitation voltage and self-heating

The larger the excitation energy applied to a bridge, the higher the resultant output energy will be. Higher excitation voltage can be advantageous as the effect of noise will be minimised. However, higher excitation energy may cause an increased self-heating effect across the strain gauge and a greater voltage loss through the wires. The use of recommended excitation levels for individual gauges will optimise the signal to noise ratio without the introduction of significant thermal effects.

While the output voltage should only be affected by a variation in test specimen strain, in practice the strain gauges themselves can be affected by changes in temperature. Strain gauge manufacturers compensate for local temperature variations and the heating effect of electrical currents by matching the strain gauge material to a specific test specimen material. As a result, it is important to use the correct strain gauges for a specific test material. In the experimental periprosthetic fracture fixation experiments, different strain gauges will have to be used for the plate and the bone in order to ensure accurate results.

The temperature effect can be further minimised by the use of two strain gauges, one active and one "dummy" gauge, Figure 16. The dummy gauge is placed on an unloaded section of the same material. In this position, the dummy gauge will not record strain in the active gauge direction, but both gauges will be affected equally by any temperature variation. If temperature variation were to occur, the

resistance ratio between the gauges would be unaffected, thereby reducing the thermal effect.
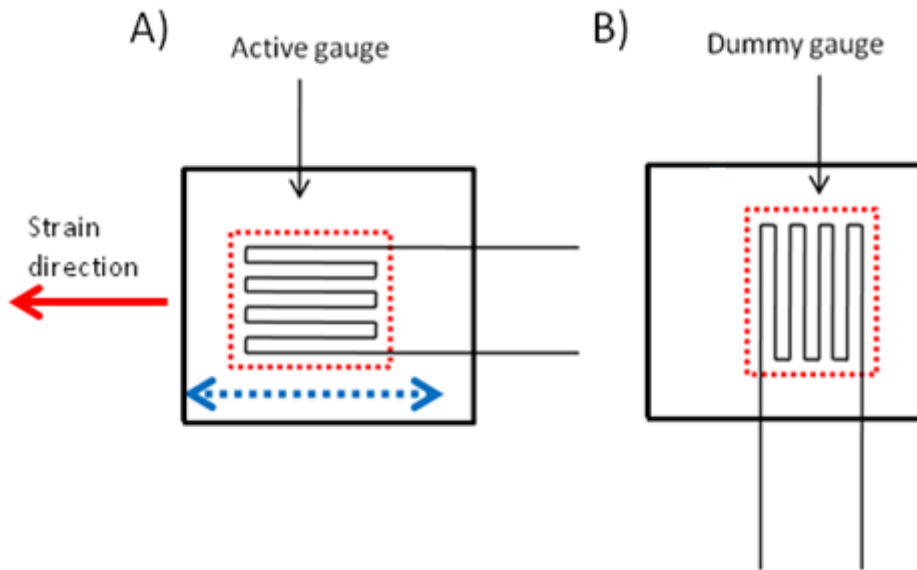
Figure 16 The direction of the active gauge with respect to strain direction (A) with the corresponding dummy gauge (B)

1.5.6   Remote Sensing

A potential source of strain gauge error occurs in the wires connecting the strain gauges with the data acquisition device. Increasing the length and reducing the diameter of the connecting wires can result in a significant resistance increase. This can introduce errors into the readings by causing a voltage drop across the wires. The remote sensing, Figure 17, introduces a separate pair of connecting wires for reading the voltage change across the strain gauges in addition to the excitation wires. Without the excitation voltage passing through the sensing wires, the voltage drop across them is greatly reduced, reducing reading errors[71].
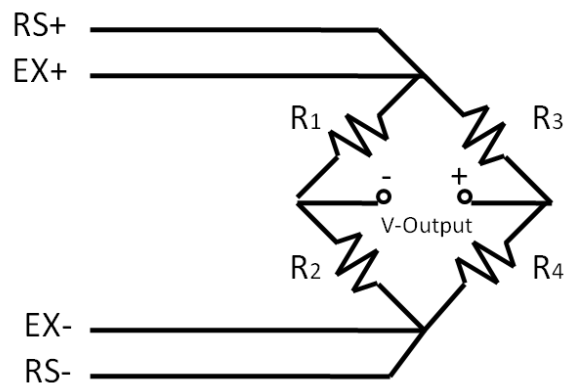
Figure 17 Remote sensing wiring

1.5.7 Shunt calibration

Another method for reducing the error incurred with the connection wires is shunt calibration. As null offset corrects for the initial error across the bridge, shunt calibration corrects for the initial resistive error across the connecting wires, Figure 18. This calibration is performed by replacing one of the resistors across the bridge with a larger resistor of known value, replicating a strain reading across a strain gauge. By comparing the resultant voltage change with the predicted change, this can be used to determine the voltage drop across the wires and the system can be calibrated accordingly[71].
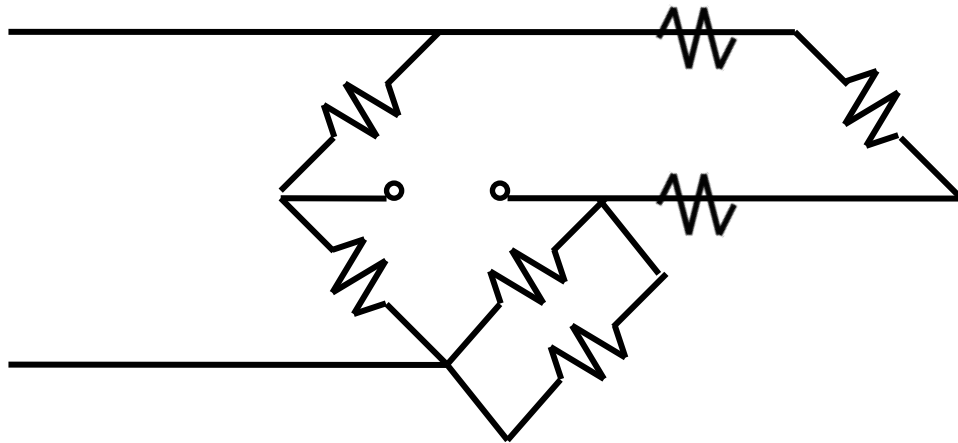
Figure 18 Shunt calibration wiring

1.6 Literature review

1.6.1 Review of biomechanical periprosthetic femoral fracture tests

Mechanical representations of the fixation techniques used to treat periprosthetic fractures have been created in laboratory tests. This approach allows for quantitative investigation into the biomechanical properties of the different treatment techniques. While it may not be possible to provide exact replication of the *in vivo* conditions, due to the lack of soft tissue representation and bone remodelling, laboratory testing can be used to evaluate and characterise the different fixation methods, determine how well they may perform under loading and predicting potential failure modes. The aim of this review is to evaluate the experimental methods used in previous studies and to establish if a biomechanically optimal fixation method can be demonstrated from existing literature.

1.6.2 Experimental Testing

The combinations of periprosthetic fracture fixation techniques evaluated in previous studies are shown in Table 2[33, 72-78]. Twelve different techniques have been investigated, each using a different combination of proximal and distal fixation devices and implant types. Within each technique, each author has their own preference for the number of fixation devices used. This means that even within fixation types, the number of variables is so great that it is hard to compare exact like-for-like loading cases. This could be due to there being no current standardised testing methods for evaluating periprosthetic fracture fixation techniques. The loading method, specimen and stem type, and the fracture type used in each study is also shown. These also vary greatly between studies, with only two studies having directly comparable set-ups. These also vary greatly throughout the studies making inter-study comparison near impossible.

The above mentioned, directly comparable loading cases between studies in current literature are with an Ogden fixation method between Dennis et al.[72] and Fulkerson et al.[73], where a compression plate is used with 3 cerclage wires for proximal fixation and 3 bicortical screws for distal fixation. There is a large disagreement between the results from the two studies for this loading case.

In biomechanical studies investigating periprosthetic fractures, stiffness will represent how the investigated fixation technique will perform during loading. During loading, the resultant amount that the construct deforms will be recorded. When the load is plotted against this displacement, the gradient of the curve in the linear region of the plot can be used to calculate stiffness.

Authors	Specimen no. and type	Prosthesis	Fracture	Loading	Femur position
Panjabi et al. (1985)	8 Cadaveric	Cemented ATS Howmedica, NJ Cemented STH Zimmer, IN	Drill hole and reaming defect 90 mm below lesser trochanter	Isometric Axial compression to 417-500 N depending on the neck length and to keep the bending moment 35 N-m in all samples	5° of adduction
Stevens et al. (1995)	27 Synthetic	No prosthesis	Transverse 200 mm distal to the greater trochanter	Physiological Displacement applied monotonically up to 25 mm in 50 sec then 20 displacement cycles between 25 and 15 mm at 1 Hz and finally monotonic displacement increased from 25 to 40 mm in 60 sec	29° of adduction 60° posteriorly relative to the frontal plan with the relative angle of 20°between the loading arm and femur in the anterio-posterior view
Schmotzer et al. (1996)	7 (4 left,3 right) Cadaveric	Cementless, Porous-coated Anatomic [PCA], ESeries, Stryker, NJ	Transverse at the tip of the stem	Physiological Via a rigid load arm in 10 N steps up to failure	15° flexion 7° adduction
Han (2000)	11 Cadaveric	Cementless, Straight tapered, collarless Natural, Sulzer Orthopedics, TX	Induced via a stem one size larger than the templated stem[a]	Isometric Compression to 890 N followed by 1780 N and 2670 N each for 15 sec	Not clear
Dennis et al. (2000)	30 (6 for each test) Synthetic	Cemented, Charnley, DePuy, IN	Oblique 45° to shaft axis distal to the tip of the stem	Isometric Axial compression to 500 N Lateral bending to 250 N Torsion to 200 N	25° of valgus
Dennis et al. (2001)	6 matched pairs Cadaveric	Cemented, Charnley, DePuy, IN	Oblique 45° to shaft axis	Isometric Axial compression to 500 N Lateral bending to 250 N Torsion to 200 N	25° of valgus
Kuptniratsaikul et al. (2001)	5 matched pairs Cadaveric	Cemented, Charnley, DePuy, IN	Spiral	Isometric is not clear	Not clear
Haddad et al. (2003)	16 Cadaveric	No prosthesis	Transverse 100 mm distal to the base of lesser trochanter	Physiological Cyclic cranial-caudal 1.53 BW approx 0-1000 N for 100 cycles at 1 Hz simultaneously loaded under anterior-posterior 0.15 BW approx -100 to80 N at 1.5 Hz	12° of adduction
Peters et al. (2003)	5 Cadaveric	Cemented, Premier Stem, Sulzer Orthopedics Inc, TX	Transverse 15 mm below the tip of the stem	Isometric Axial compression to 2250 N	Two set up tested 1) 21° of varus 2)30° of flexion
Wilson et al. (2005)	6 Cadaveric	Cemented, Charnley-Muller, Stryker, NJ	Transverse at the tip of the stem	Physiological Cyclic cranial-caudal 1.53 BW approx 0-1000 N and anterior-posterior 0.15 BW approx -100 to 80 N	12° of adduction
Barker et al. (2006)	14 Synthetic	Cemented Exeter, Stryker, NJ	Cortical perforation at the tip of the standard stem	Physiological Initial loading cycled between 10 and 500 N, then every 100 cycles the peak load increased in steps of 500 N up to 2500 N	12°medially and 8°posteriorly relative to the frontal plan

Table 2 Existing study comparison

1.6.3 Specimen Type

The two types of femoral specimens used in the literature are cadaveric bone and synthetic Sawbones[78]. While using cadaveric bone has the advantage of directly representing the anatomy and material properties of an *in vivo* Femur, using samples for laboratory testing can be challenging as they present a biological hazard, they can be difficult to prepare and store, can be affected by temperature and display significant variance between samples. Using synthetic Sawbones represents a practical alternative to cadaveric bone. They are have much lower variance between samples and do not require additional ethical approval for their use and storage, which is inexpensive compared to their natural alternative.

The difference in mechanical performance is shown between the results from Dennis et al.[72], in the allograft struts with both proximal and distal cerclage fixation loading case. A construct stiffness of 3000N/mm using Sawbone specimens was initially recorded, while their subsequent study measured a stiffness of 442N/mm using cadaveric Femurs[33, 72]. This indicates a significant performance difference between the two specimen types, and that the use of cadaveric Femurs will result in a lower bending stiffness compared to Sawbone specimens.

1.6.4 Loading device

There have been two published approaches for transmitting load from a tensile/compression testing machine to the head of a femoral specimen. Dennis et al.[72], Fulkerson et al.[73] and Wilson et al.[79] all used a flat plate to apply the loads onto the test specimens[73, 79]. Using a flat plate allows free movement of the femoral head during loading. This loading method is simple to manufacture and use, and does not lead to problems with alignment of the Femur during loading. Also, a new loading head would not be required to test any intact Femurs necessary for baseline tests. The use of a conforming cup machined into a solid block to replicate the anatomic acetabular cup was favoured by Zdero et al.[77], Schmotzer et al.[75] and Talbot et al. [76] There was no fixation used between the head of the hip prosthesis and the cup and consequently, the prosthesis was allowed to rotate freely.

Loading specimens with a cup component is likely to result in more repeatable results, as it better replicates the anatomical loading case, makes the testing rig more stable under loading. This may allow for a more controlled testing case when conducting tests to failure. Using a cup may require the placement of the specimens within a compression testing machine to be more accurate than with a loading plate as the head of the Femur must accurately line up with the cup.

1.6.5 Fracture type
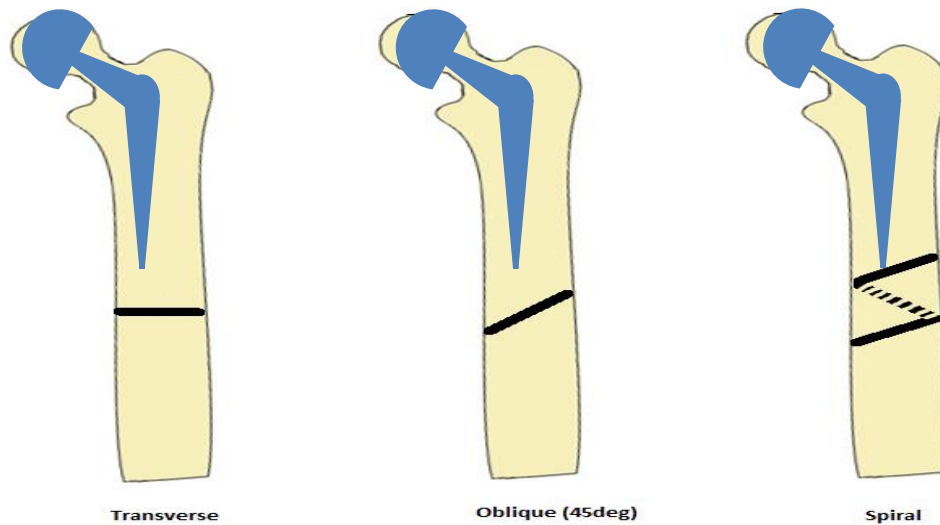
Figure 19 Common fracture types: Transverse, Oblique(45°) and Spiral

The most common fracture used to represent a periprosthetic fracture in previous studies was a 45 degree oblique mid-shaft fracture, in an infero-medial to supero-lateral direction, Figure 19. Dennis et al.[72] and Fulkerson et al.[73] osteotomised their Femurs with the middle of the oblique fracture at a level equal to the distal end of the hip prosthesis while Zdero et al.[77] moved this level 2.5cm distally, to the end of the prosthesis. A reason for this could have been to ensure the cement mantle remained intact. Alternatively, Schmotzer et al.[75], Talbot et al.[76] and Wilson et al.[79] created a transverse fracture, level with the distal end of the prosthesis. Kuptniratsaikul et al.[74] recreated a spiral fracture by creating an indentation level with the distal end of the cement mantle and applied a torque to create and propagate the fracture. Transverse and oblique would likely be the simplest fractures to replicate for experimental tests. Spiral fracture creation would be the most complicated fracture to create and it is likely that fractures created with this method would have a poor repeatability.

All of the studies have only investigated their stabilised periprosthetic fracture specimens for a single fracture type. No study has conducted loading tests on specimens with different fractures. Groups who have conducted multiple studies have kept the configuration of the periprosthetic fracture consistent between the individual studies[33, 72].

1.6.6 Fracture Gap

Many of the studies did not specify whether a gap was left between the fracture surfaces. In the case of Fukerson et al.[73], no bone apposition

occurred until the specimens were under loading, while Talbot et al.[76] left a gap of 12mm between the bone ends. The study conducted by Zdero et al.[77] included the most comprehensive study, explicitly comparing the performance of fixation methods with and without the presence of a bone gap[77]. Specimens were first prepared and tested with the fracture surfaces in direct contact, and subsequently, a 5mm gap between the osteotomised bone surfaces was introduced and the specimens retested. The results showed a 41% reduction in axial stiffness when the gap was present.

This would suggest that the presence of a fracture gap has a significant influence on fixation biomechanics and needs to be a controlled variable during any further studies. The presence of a fracture gap could be difficult to represent in a computational model. In the initial stages of loading, the fracture surfaces would not be in contact. However, should enough construct displacement occur, the contact between the surfaces needs to be accurately represented in order to acquire valid results. If the contact surfaces were placed in contact before the specimen was loaded, without the presence of a fracture gap, contact assumptions could be made, such as defining tied contacts between the two surfaces. This would simplify the model and reduce the computational requirements necessary to run the model.

1.6.7 Loading modes
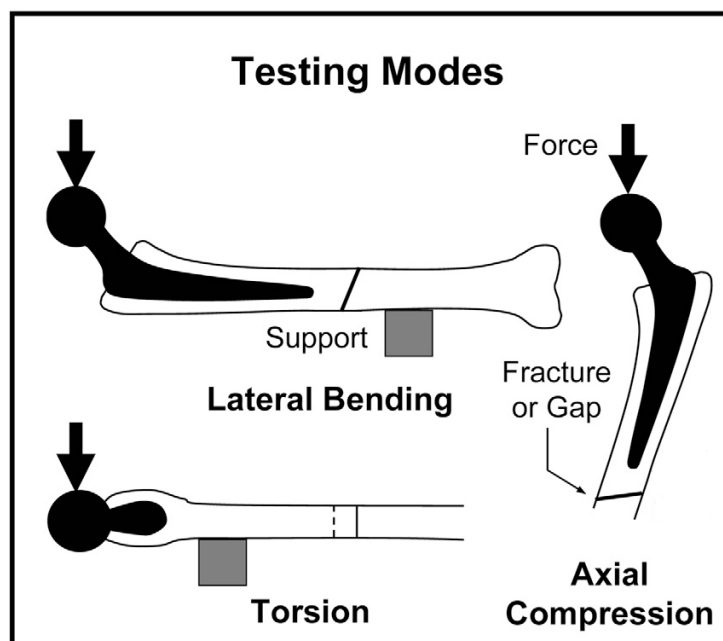
Figure 20 Illustration of testing modes[77]

Three different loading positions were investigated in the literature, replicating extreme physiological loading conditions, when loading through

the Femur would be at its highest. These positions included axial, lateral and torsional loading and are shown in Figure 20. Axial loading tests aimed to replicate loading conditions experienced during standing in a single-leg stance or during the heel strike phase of walking. Axial tests were used to evaluate the fixation methods in compression along the long axis of the Femur. When loaded in the lateral position, the test evaluates the bending strength of the investigates fixation technique. The torsional loading position evaluates the construct's ability to withstand rotation around the long axis of the Femur. This aims to replicate the loading condition when a patient rises from a seated to standing position. The axial compression tests may be the most significant for evaluating fixation techniques, with the largest forces exerted on a Femur transmitted in this loading mode.

The majority of the mechanical testing carried out in previous studies, loaded their specimens within their elastic limits. Non-destructive testing allows multiple loading tests to be performed on the same sample, as no permanent damage will be caused during testing. Statistical methods can then be used to reduce the influence of errors in the results and to determine significance. Destructive testing involves loading a specimen to failure. Destructive testing analyses a specimen to its mechanical limits, allowing evaluation of specimen's material behaviour under the entire loading range. Where possible, destructive testing is preferable as complete material behaviour is experimentally determined. Failure loading can also be used to identify specimen failure pattern.

Cyclic loading was used to evaluate the effect of fatigue on the specimens. Cyclic loading for all three loading positions were carried out for a range of fixation methods. A force of 500N was applied at a rate of 3 cycles a second, 3Hz, to a maximum of 10,000 cycles[72, 73]. To investigate the effect further, Talbot et al.[76] tested their samples to 100,000 cycles with a higher maximum load, 1200N compared to 500N for Dennis et al.[72] and 400N for Fulkerson et al. [73] Cyclic loading at higher loads for longer cycles are likely to result in larger performance differences between investigated fixation techniques.

1.6.8 Specimen movement

Both Dennis et al.[33] and Fulkerson et al.[73] attempted to quantify the movement of the superior femoral shaft during loading. Two digital displacement gauges were used, one parallel and the other perpendicular to the load axis, with a resolution of 0.001mm and an accuracy of 0.003mm. The heads of the gauges were smooth spheres and were spring loaded to ensure that they remained in contact with the surface of the Femur.

1.6.9 Fracture movement

There are two reported methods for evaluating fracture movement in the literature. A motion analysis system based on ultrasound, with a resolution of 0.1mm and an accuracy of 0.2mm, was used by Schmotzer et al.[75]. The emitted ultrasound pulse is reflected at boundaries where there are significant changes in density, for example, at the fracture site when the pulse travels between bone and air. The time taken for the pulse to return can be used to calculate the distance of these boundaries from a fixed point. They discovered in calibration experiments that their readings were affected by dynamic loading, so in order to obtain reliable results, they only recorded measurements when a constant load was being applied to their specimens. Displacements ranging between 0.2mm and 5.5mm were recorded during the study. An alternative method was used by Wilson et al.[79], using a 3-dimensional camera to track movement at the fracture site. This used an infrared light source combined with reflective markers, placed above and below the fracture, to measure movement to an accuracy of 0.15mm. This system enabled them to measure both 'translation', the movement between the markers and thus the inter-fragmentary motion, and 'rotation', the movement around the long axis of the Femur specimen. Fracture site movement varied between 0.1mm and 4.2mm during the study.

While both methods were successful at measuring fracture movement, the camera method could be used without physical contact with the specimens. The ultrasound method requires the careful positioning of the sensor at the fracture site, during every measurement point, whereas the camera could be used from a fixed position to continuously track the fracture movement during loading.

1.6.10   Results

The results for all the previous studies investigating the mechanical behaviour of periprosthetic fracture fixation techniques were categorised by loading case[Appendix A]. The collated results of the previous studies are inconclusive, with each author recommending a different fixation technique. Compression plate performance was found to be maximised when unicortical screws and cables were used in combination with allograft struts for plate fixation by Zdero et al.[77]. Locking plates were found to perform better than compression plates by Fulkerson et al.[73]. This was supported by Talbot et al.[76] who found that locking plates in combination with allograft struts performed better that compression plates with allograft struts, using screws and cables for both proximal and distal fixation to the bone. Construct fixation using screws in combination with cables was found to be superior than with cables alone[76]. The improvement in specimen stiffness

with the addition of an allograft strut is expected as the effective volume of bone resisting loading is increased.

A direct comparison can be drawn for the Ogden loading case from the results of the studies conducted by Dennis et al. [72] and Fulkerson et al.[73] under axial loading, Dennis et al. recorded a construct stiffness of 474N/mm compared to Fulkerson who observed a stiffness of 304N/mm. This amounts to a 36% difference in measured stiffness between the studies. In the lateral bending tests large stiffness differences occurred between constructs with and without a bone gap. A 74% reduction in bending stiffness was observed when a gap was introduced. The presence of a bone gap had the largest effect in lateral bending when compared with the other testing modes. The results of the torsional results clearly showed that the use of unicortical screws in addition to cerclage cables in proximal fixation resulted in stronger constructs than with cerclage cables alone.

The results of the cyclic loading tests for comparable locking and non-locking constructs were compared against the respective non-cyclic loading results. The results showed that locked plating was significantly stiffer in axial and torsional cyclic loading compared to compression plating, and both locking and non-locking constructs stiffness were significantly affected. Conversely, Talbot et al.[76] concluded that cyclic loading did not decrease stiffness in their tested fixation techniques, in all loading modes. While the results of cyclic loading tests have been mostly inconclusive, locking plates have been reported to perform better than other fixation techniques.

1.6.11 Computational Testing

To date, there has been a very limited number of studies to date that have attempted to use computational modelling to investigate periprosthetic fracture fixation.

The most comprehensive study was conducted by Shah et al[80], used both experimental and computational modelling to investigate three different fixation combinations; proximal cables with bicortical screws distal to the fracture site, proximal unicortical screws with bicortical screws distal to the fracture site, and a proximal combination of unicortical screws and cables with bicortical screws distal to the fracture site. Transverse fractures were investigated, and the specimens were stabilised with a 5mm gap between the proximal and distal bone fragments. Screw threads were not modelled as the screw to bone interface was modelled as fully bonded. An "axial" load was used to apply 1000N to the specimens, with the cemented distal end of the specimens constrained in all directions. All surface interactions within the model were defined at fully constrained. They successfully managed to

match computational surface bone strain to experimental bone strain. They concluded that the proximal combination of unicortical screws and cables with bicortical screws distal to the fracture site would have the best performance , as that case displayed the highest computational overall stiffness.

A study conducted by Chen et al[66], conducted a purely computational study to investigate four different fixation combinations. They concentrated on cerclage cable fixation in combination with unicortical screws. A long oblique fracture was defined, 55 mm below the lesser trochanter. The specimens were stabilised with a 1mm gap between the proximal and distal bone fragments. The distal femur was computationally dissected and the resulting femoral cross section was defined as fully fixed. A load of 700N was applied to the model. A traditional Ogden construct was found to have the highest bone stress concentration and largest fracture site movement, when compared to the other investigated fixation combinations. This study was not validated against any experimental data.

A study conducted in 1992 by Milhalko et al[81], evaluated plating of periprosthetic femoral fractures neat the tip of a hip implant. A 2-dimensional FE model was developed with an axial load of 500N applied. A maximum plate stress of 67.6MPa was found.

1.6.12   Summary

From the results of previous experimental studies investigating the mechanical behaviour of periprosthetic fracture fixation methods, no clear bio-mechanically optimum fixation method exists[78]. Due to the current lack of standardised testing methods, the variations between the vast majority of experimental results from previous studies are unable to be compared. A The range of fixation methods investigated during each of the studies also varies greatly. In combination with individual fixation method variation, this prevents the clear identification of an optimum fixation method. Very limited number of relevant computational studies exist in the literature, with no consensus on fracture type, fixation instrumentation or model outputs.

While there is a limited range of fracture configurations tested in the literature, due to the significant instrumentation and specimen differences between the studies, it is currently unrealistic to draw conclusions on the effect of fracture configuration on stabilised construct performance.

1.7 Review of bone screw testing

The aim of this section is to evaluate the findings of previous studies of bone screw performance and to identify the screw properties most likely to affect periprosthetic fracture fixation.

1.7.1 Bicortical vs. Unicortical screws

Computational models developed by Chaudhary et al.[58] demonstrated that screws with the same thread width, and a large core diameter unicortical screw could perform better than a corresponding core diameter bicortical screw in terms of peak stress in the surrounding bone. They found that the unicortical screws resulted in lower peak stresses surrounding the bone, reducing the potential for bone damage to occur. However, experimentally determined bicortical screw pullout strength was significantly higher, over double that for the unicortical screws.

In periprosthetic fracture fixation, there are restrictions imposed on the length of screws used in the region by the implanted stem and surrounding cement mantle. Unicortical screws short enough not to impinge the stem are commonly used in this region. However as bicortical screws are unable to be inserted through the stem, if used, they must be inserted at an angle, reducing the volume of bone in contact with the screw, in turn compromising screw performance.

1.7.2 Screw length

It has been reported by Daum et al.[59] that increasing the length of a screw will improve its performance[59]. Higher pullout strengths were strongly correlated with increasing screw length in the medium. Whereas, Chaudhary et al.[58] found no increases in screw performance once it had entered a minimum for three full pitch rotations into the medium[58]. At this point, the bone screw was considered to be fully deployed and performing to its maximum potential. It was shown that any additional length had no effect on the properties of the screw. Computational models developed from these results showed that the main regions of shear stresses in the medium occurred between the top three threads of the screw. The method used by Chaudhary et al. is likely to be less accurate as they not consider the effect of poor bone stock in their investigation. A homogenous polyurethane block was used to test both screw types without taking into account the heterogeneous nature of bone. The results from the study by Daum et al.

used human cadaveric pelvic bone to test their screws and are more likely to accurately recreate anatomical conditions.

Increasing the length of a screw is related to increasing the thread area in contact with the bone and raising the core volume of this screw. These could lead to lower bone stress surrounding the screw and increased bending strength. However, the length is limited by the patient's bone anatomy. Bicortical screws are designed to reach the distal cortex of the Femur, any further length increase past this cortex will not affect screw performance. The length of unicortical screws used in periprosthetic fracture fixation is limited by the distance between the proximal femoral cortex and the stem of the prosthesis. The longest screw that can be inserted without damaging the prosthesis should be used.

1.7.3 Core Diameter of a screw

Current existing finite element and experimental studies agree on a general rule: an increase in core diameter will result in a lower peak stress in the region surrounding the screw [57, 82, 83]. An increase in core diameter is also strongly correlated with an increase in pullout strength. There are examples of small diameter screws resulting in comparatively low shear stresses, however, in these examples there is a very high stress concentration distributed around the top three threads, which increases the susceptibility to diagonal cracking. Kaab et al.[52]. found that screw core diameter has a significant effect on bending. This is supported by Evans et al.[51] who showed that even a small increase in core diameter can cause a large reduction in bending of a screw, with no effect on its pullout strength properties. Core diameter is also the primary factor in determining the effect of torque on a screw. Some studies have recommended that the largest core diameter should be used where possible as the torque required to break a screw is proportional to the cube of its core diameter[57]. The results presented by studies on the effect of thread width on screw performance can be combined with core diameter results. As the core diameter of a screw increases, the thread width will decrease by the same amount. It has been demonstrated that an increase in thread depth, and thus a decrease in core diameter, will result in lower peak stress in the bone surrounding a screw[82]. Pull out strength was strongly correlated with the moment of inertia of the screw threads.

When used in conjunction with a bone plate, the diameter of the screw intended for use with the plate will determine the size of the holes on the plate. If the holes on the plate are too large, the screw will not be able to sufficiently support the plate, while if the is too small the screw may damage the plate upon insertion.

1.7.4 Conical vs. Cylindrical shaped screws

Tsai et al.[62]. and Hsu et al.[63]. have both found that conical shaped screws have a higher experimental pullout strength than correspondingly sized cylindrical screws. However, the studies also showed that the recorded pullout strengths for the conical screws had a significantly higher standard deviation compared to cylindrical screws. Such variability of results could lead to significant unpredictability in clinical results, although this is yet to be investigated. Cylindrical screws do not alter the surrounding bone during insertion whereas conical screws compact the bone, causing it to become denser. When loaded, the denser medium should provide more support to the screw, reducing the potential for micro-movement and failure. This also leads to conical screws having a higher insertion torque compared to cylindrical screws. Hsu et al. also demonstrated that the screw deformation during insertion was minimal, such that screw properties were not significantly affected[63].

To the author's knowledge, there is not a current design of locking plate which utilises conical screws. This could be due to the inherent complexity of manufacturing a screw with both a cylindrical locking thread near the head of the screw, with a conical profile near the tip of the screw. Conical screw designs would also be incompatible with bicortical screws as the tip of the screw would be protruding from the distal cortex of the bone, and so would not have any medium to compact.

1.7.5 Screw pitch

Evans et al.[51] found that by reducing the pitch of a screw, the pullout strength would increase. It has been shown to have a larger effect on bicortical screws where a reduction in angle of pitch will result in a larger reduction in peak stress compared to unicortical screws. Conversely, it was shown that for unicortical screws, any correlation between screw pitch and screw performance were much less significant. DeCoster et al.[82] found that screw pitch becomes more important for finer thread width screws, where a smaller pitch results in more purchase in the target medium. Screw pitch is a major component in Thread Shape Factor, a screw performance predictor proposed by Chapman et al.[61].

Screw pitch may influence locking plate design as the pitch of the tapped holes on the locking plate will need to match that of the inserted bone screw. If the screw pitch used is too coarse, improper binding could occur between the screw and plate and the rigidity of the construct could be compromised.

1.7.6 Pre-tapping and untapped screws

Currently all screw designs require a preliminary pilot hole to be drilled at the target site on the bone. Following this, the screw can either be designed to cut its own path through the bone surrounding an untapped pilot hole, or pre-tapping could occur where threads are added to the pilot hole, matching those of the screw. When inserted, the screws own thread would follow the pre-tapped threads. Nunamaker et al.[57] found that pre-tapping considerably reduces the insertion torque exerted on the bone during screw insertion which will reduce the risk of cracking. In order to optimise the performance of a screw, a pilot hole diameter should be drilled such that it matches the core diameter of the screw as closely as possible. Finlay et al.[83] showed that screws with pilot holes pre-drilled smaller than the core diameter of the screws produced statistically higher pullout strengths than larger pilot holes. This findings have been challenged by Pfeiffer et al.[84] who demonstrated that pullout strength is not affected by pre-tapping the pilot hole, and also that tapping does not improve the consistency of pullout strengths of screws. A significant difference in the standard deviation of the pullout strengths for a set of pre-tapped pilot holes compared to a set of untapped pilot holes was not found. This has been proven in both fully healthy and poor bone stock.

It has also been reported that an untapped pilot hole would perform better than a tapped one[57]. This concurs with the findings of Chapman et al.[61] where tapping was shown to decrease pullout strength by an average of 8%. This could possibly be due to tapping in poor bone stock, removing the available material that a screw could bind with, effectively reducing the density of the bone further. Therefore, it could be advantageous not to pre-tap holes as this will reduce operating time as well as reducing operational complexity. It may be advantageous to pre-tap healthy bone stock to reduce the incurred insertion torque, but this may not apply in poor bone stock. This is because, unlike good bone stock where the tapping head will cleanly cut groves in the bone, in poor bone stock, the bone could be broken rather than tapped leading to a greatly compromised pilot hole.

1.7.7 Distance between screws

It has been demonstrated that if the distance between screws is greater than a screw diameter, there will not be any overlap of stress patterns[52]. This is significant because when screw diameter is increased, the minimum distance between screws will need to be increased. This influences bone plate design as holes on the plate will need to be placed such that resultant screw stress patterns do not coincide.

1.7.8 Summary

The range of screw properties which could significantly affect the performance of a periprosthetic fracture fixation technique have been identified. The use of bicortical and unicortical screws, and the distance between screws will be determined by the fixation technique. The use of untapped screws is not recommended for use in osteoporotic bone. As osteoporosis is a significant risk factor for periprosthetic fractures, this property will not be investigated. Core screw diameter, thread pitch and screw shape will be investigated to determine their significance on periprosthetic fracture fixation.

1.8 Literature review synopsis

Periprosthetic fracture of the Femur is a common complication of hip arthroplasty. With the increasing rates of total hip replacements, the occurrence of periprosthetic fractures is expected to rise. These fractures can be difficult to treat effectively due the technical challenges presented with combinations of fractured bone and an unstable prosthesis. A range of fixation techniques exist, however, clinical controversy remains to identify the best methods to treat different types of fractures. The results of previous experimental studies investigating the different fixation techniques show no optimum fixation method exists. Both previous experimental and computational studies have not focused on the effect of fracture configuration on periprosthetic fracture fixation performance. Due to the current lack of standardised testing methods, inter-study variations between the experimental tests and fixation methods investigated, have not conclusively identified an optimum fixation method. Screw fixation is an important factor in periprosthetic fracture fixation, with a range of properties affecting fixation performance.

1.8.1 Work Flow

The project can be separated into sections, with each linked as shown on the work flow diagram, Figure 21, each with a clear deliverable resulting from the completion of each section.
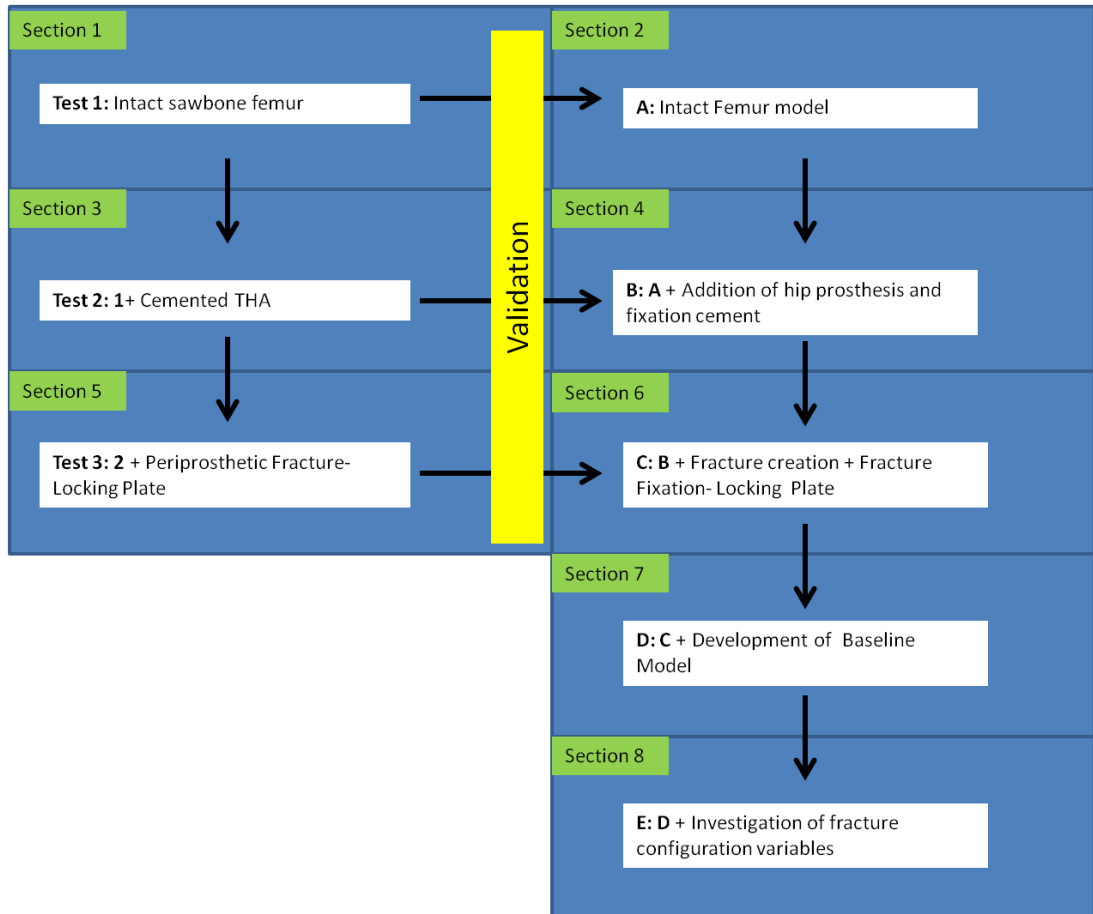
Figure 21: Simplified work flow diagram showing the main development stages and their location within this study

1.8.2 Sections of work flow

Section 1- This included the testing of a set of six intact Sawbone Femurs in the loading rig. The strain gauging protocols were assessed and finalised, as well as the specimen loading procedure in the material testing machine. The deliverable from section 1 was a fully functional experimental testing platform and loading data for the set of intact specimens.

Section 2 – This involved the computational modelling of an intact Femur. The geometry of the model matched the specimens used in the laboratory.

Using the experimental results from section 1, the computational intact Femur model was validated using the specimen bulk stiffness and bone strain. Section 2 resulted in a validated intact Femur model, from which the models in later sections were developed from.

Section 3- This section involved the preparation and insertion of cemented total hip replacements for the set of six Sawbone specimens, from section 1. The specimens were then loaded in the test rig, recording the same metrics as from section 1. Section 3 resulted in loading data for the set THR specimens.

Section 4- This involved developing the computational model of an intact Femur from section 2, by replicating the femoral head dissection and the preparation of the reamed region of bone, followed by the introduction of the prosthesis and cement mantle. Section 4 resulted in a validated THR model.

Section 5- This section involved the creation of periprosthetic fractures in five of the Femurs with hip prostheses from section 3, and their subsequent stabilisation using locking plates and locking bone screws. In addition to the strain gauges locations used in the previous experimental sections, strain data was also collected from the surface of the locking plate. Section 5 resulted in loading data for the set PPF specimens.

Section 6- This included the development of the total hip replacement model from section 4 to include the stabilised fracture fixation using locking plates and locking screws. This model was validated using the experimental data from section 5. Section 6 resulted in a validated baseline PPF model

Section 7- This section used the validated fracture fixation model developed in section 6 as a baseline from which variables resulting from compromises made when selecting the loading set up and instrumentation configuration used to support and stabilise the periprosthetic fracture specimens, were investigated and quantified. Section 7 resulted in a developed PPF model.

Section 8: This section involved using the adapted model developed in section 7 to investigate a range of fracture variables, including the angle of the fracture and the distance of the fracture from the tip of the prosthesis stem. Section 8 resulted a range of fracture configuration models, from which conclusions about the effect of fracture configuration on PPF performance could be gained.

Chapter 2 : **Experimental Methods**

2.1 Introduction

This chapter details the techniques and practices used during the experimental tests conducted in this study. Within the first section of this chapter, the design and functions of the test rig used to support and apply load to the specimens is described. The preparation of the specimens was also detailed.

2.2 Loading Rig

2.2.1 Design

The loading rig was designed to securely support the Sawbone specimens at different stages of instrumentation, and afford the loading flexibility to test the samples over a range of loading conditions. The design comprised of five discrete parts, the loader, angle adjuster, the module, the holder and the base, in addition to three high tensile bolts, as shown in Figure 22. As the test rig was designed to be used in a class 2 tissue laboratory environment, the rig was manufactured from 303 stainless steel. This material was chosen as it was strong and tough enough to withstand the forces encountered in the loading cases while being easy to clean and sterilise, and also had adequate corrosion resistant properties. The femoral specimens were loaded at the head of the hip prosthesis through the loader component. The loader was designed to accommodate a 28 mm diameter prosthesis head. The distal end of the Femur would be secured to the module component of the test rig using PMMA cement and 5 mm diameter grub screws.
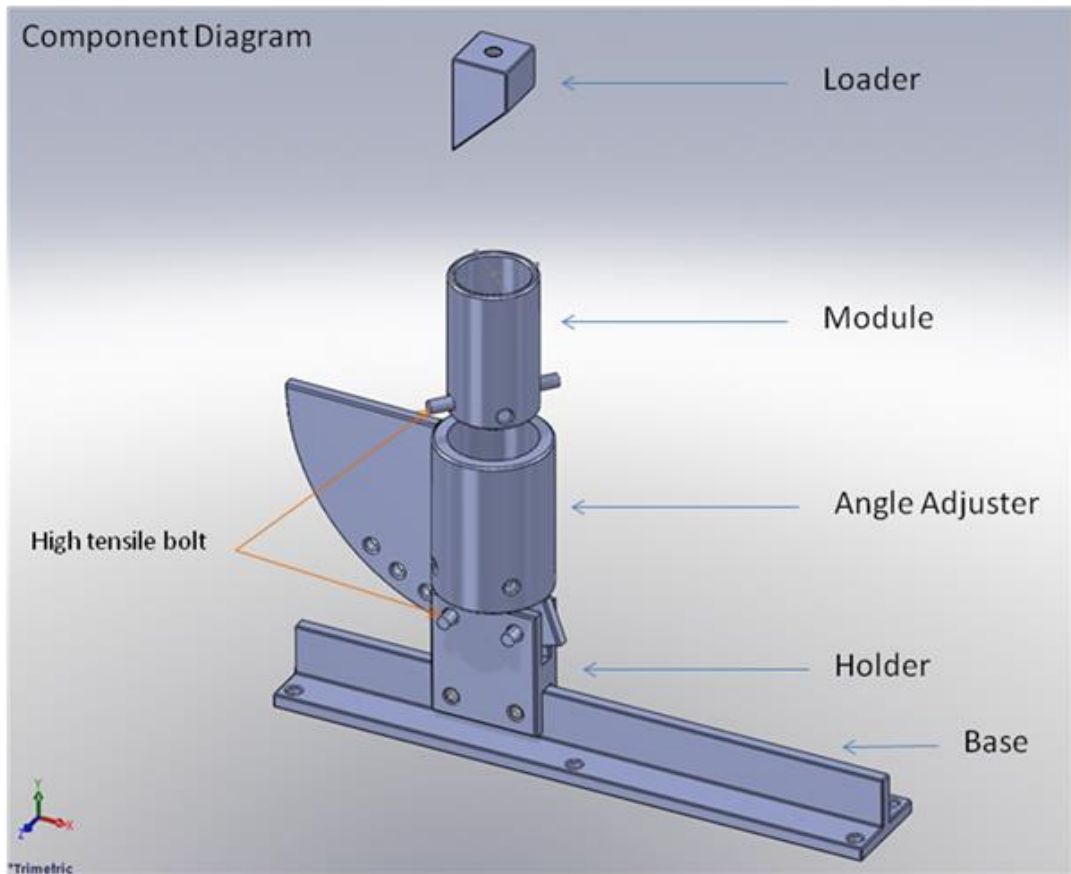
Figure 22 A component diagram of the different parts of the loading rig

2.2.2 Loading angle adjustment

The angle adjuster and holder components, in addition to two high tensile nuts and bolts, could be altered to load the specimen at a range of loading angles. The angle adjuster has holes positioned to allow specimen loading at 0°, 10° and 20°, Figure 23. As specimens were rotated to change the loading angle, the rig was designed to rotate with the centre of rotation situated around the base of the Femur, just proximal to the top of the module. Sufficient space on the angle adjuster was left available between the existing adjustment holes to add 5° loading increments in case they were necessary in future experiments. Anti-fretting grease was applied to the high tensile bolts to ensure they could be removed after loading without difficulty.

As the angle adjuster component was varied, the horizontal position of the femoral head would change. The adjustable holder location on the base component allowed for horizontal rig adjustment while providing solid support during loading. The height of the rig inclusive of the specimen was approximately 630 mm. Moving from the 0° to the 20° loading position, taking into account the height of the loading rig and Sawbone, the rig would need to be moved 215 mm. The base component was designed to allow a maximum horizontal correction of 353 mm while continuing to provide rigid

support for the specimen. The base component was attached to the base plate of the materials testing machine using six high tensile bolts screwed directly through the rig, or alternatively secured using machining blocks to a grooved base plate.
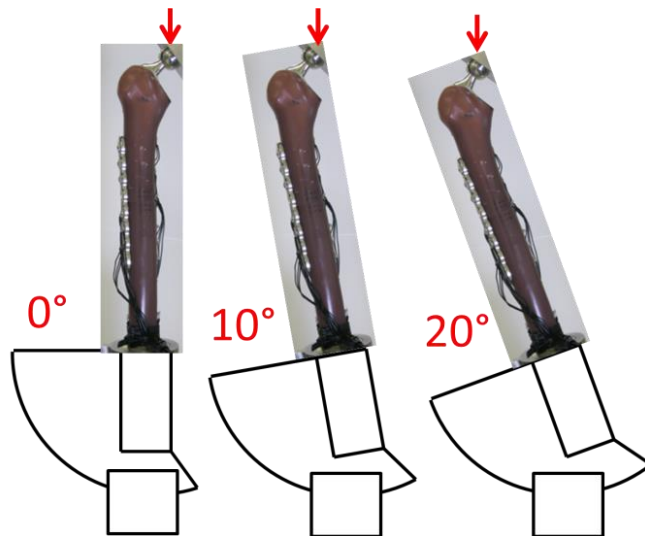
Figure 23 The range of test rig loading angles investigated in this study.

2.2.3 Torsional load

A specimen adjustment was included on the module component that introduce a torsional load on the specimen. This would be used to increase the range of specimen loading angles available in the experiment and would be used to differentiate between fixation method behaviour if necessary. A torsion angle of 8° was chosen as this value reflects the maximum angle observed *in vivo*, and was previously used experimentally by Barker et al.[85]. This angle was changed by altering the position of a high tensile bolt. Two sets of positioning holes were made between the angle adjuster and the module. One set had both holes machined directly in line, creating a 0 degree loading position with no additional torsional loading on the specimen. In the second set, an 8 degree offset between the holes on the module and angle adjuster was introduced. In this configuration, the specimen would be rotated 8 degrees around the long axis of the specimen and additional torsional loading would be introduced.
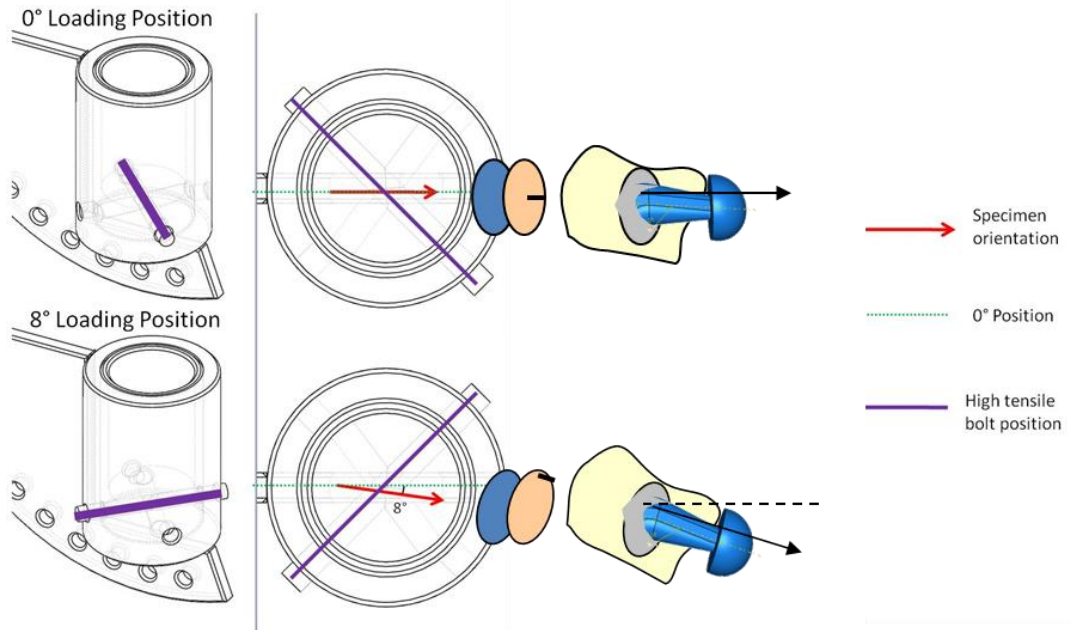
Figure 24 Test rig positioning for the conventional and torsion loading positions

2.3 Specimens

2.3.1 Sawbone surface preparation

The two types of femoral specimens used in the literature are cadaveric bone and synthetic Sawbones. While using cadaveric bone has the advantage of directly representing the anatomy and material properties of an *in vivo* Femur, using samples for laboratory testing can be challenging as they present a biological hazard, they can be difficult to prepare and store, can be affected by temperature, and display significant variance between samples. Using synthetic Sawbones represents a practical alternative to cadaveric bone. They have a lower variance between samples and do not require additional ethical approval for their use and storage, which is inexpensive compared to their natural alternative. Synthetic Sawbones have less variable geometries than cadaveric bone and will have more uniform mechanical properties. Synthetic Sawbones were chosen to be used in this study.

The first step was to prime the surfaces of the synthetic Sawbone Femurs (4th generation, size Large, Sawbones Worldwide, WA, USA). The external surfaces of the Sawbones were initially prepared using both rough followed by smooth sandpaper (Hermes P240 and P120 respectively) to remove the manufacturer's moulding flash and any other excess surface defects. After removing any debris using high pressure air, the Sawbones were then cleaned with a damp cloth and dried. The next step was to prepare the

Sawbones to allow them to be securely mounted into the loading rig. The distal end of the Femur was placed anterior side down into a bespoke cutting jig and fixed in place using a workshop clamp. With the aid of a saw guide, the Femur was then dissected 77 mm from the distal end, perpendicular to the long axis of the Femur, removing the femoral condyles, Figure 25. This would leave a Sawbone length of 340 mm between the level of the Lesser trochanter and the distally dissected end.

Figure 25 Distal dissection of Sawbone Femur specimens within the cutting jig

2.3.2 Mounting Sawbone specimens into modules

Initially, a comprehensive coating of petroleum jelly was applied to the internal surfaces of the module. The module was aligned to the potting jig using the 0° torsion hole. The module was then attached to the base of the potting jig using a 10 mm threaded bolt and secured using a 10 mm nut, Figure 26. The Sawbone was then placed into the empty module with the femoral head facing towards the front of the potting jig. To ensure correct orientation of the Sawbones within module, the manufacturers moulding line marking the mid-point of the lateral surface of the Sawbone was aligned with the corresponding rear marker on the module. If aligned correctly, the manufacturers moulding line on the medial surface of the Sawbone would also be aligned with the front module marker and the screw guide markers positioned higher up on the potting jig. To secure the Sawbone in the correct orientation within the module, two 16 mm long grub screws (5 mm diameter) were inserted into the threaded holes on the anterior side of the module, with two 8 mm long grub screws (5 mm diameter) inserted into the posterior threaded holes. The grub screws were tightened until the Sawbone was secure in the module and all of the heads of the grub screws were flush or lower than the outer surface of the module. If any part of the grub screws

was protruding from the modules, this would prevent correct insertion of the modules into the rest of the loading jig during loading.

Figure 26 The potting jig used to position the specimens within the module

2.3.3 Sawbone fixation within loading module

Laboratory grade PMMA cement (WHW Plastics, Hull, UK) was used as a medium to securely fix the Sawbone Femurs within the modules. In accordance with general laboratory procedure, all work involving the preparation and application of PMMA cement was conducted either in a fume cabinet or on a down-draft table. Using a pair of digital scales, 70g of the acrylic powder was mixed in a beaker with 35g of the liquid methyl-methacrylate in a 2:1 ratio. The mixture was combined with a metal spatula until the powder had completely dissolved into the liquid, ensuring that there were no air pockets in the cement. The mixture was then carefully poured between the module and Sawbone until the cement level had reached the top of the module. The cement was then left to cure for a minimum of 12 hours before any experimental loading.
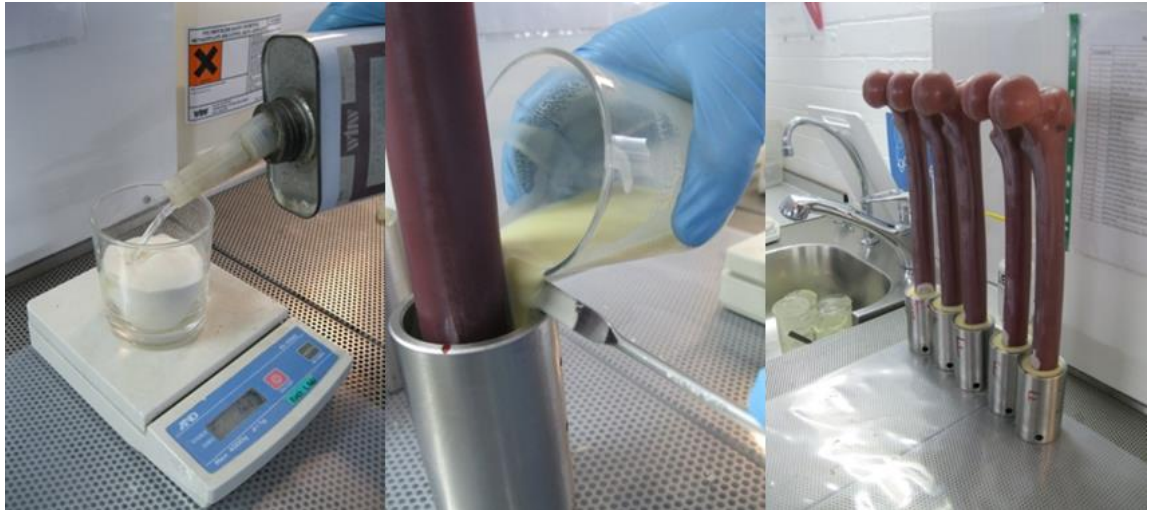
Figure 27 Stages of cement and specimen preparation

2.4 Total hip replacement

The Sawbone was firmly secured in a vice with the proximal end positioned upwards. Custom made vice covers manufactured from rubber were used to firmly secure the Sawbone in place, without damaging the specimen. Using a drill with a 10 mm drill bit, a hole roughly 60 mm in depth was created between the Greater trochanter and start of the femoral neck. Aided by the hole created in the previous step, the femoral head was distally dissected at a 45° angle using a saw.

The cement cavity was prepared by reaming the Sawbone using a series of surgical rasps (Stryker, NJ, USA). The hip replacements used in this study were Exeter primary cemented hip stems (V40, size N°0, offset 37.5, Stryker SA, Switzerland) with a femoral head (28 mm diameter - Stryker, NJ, USA). Once the fit between the stem and the bone was checked, confirming that there would be a sufficient cement mantle around the stem, a cement restrictor was placed down the intramedullary canal, positioned slightly distal the reamed section of the bone. The aim of the restrictor was to prevent excess cement travelling distally down the intramedullary canal without impeding the placement of the prosthesis. The Sawbone was then moved to the downdraft table before stem insertion.

Cement was inserted into the prepared Sawbone, filling the reamed section. Before the prosthesis stem was inserted, a centraliser was placed on the tip of the prosthesis stem, and was used to ensure the correct central positioning of the stem tip within the intramedullary canal. The cement used to support the stem was polymethylmethacrylate (PMMA) cement (Simplex P, Stryker, NJ, USA) prepared to the manufacturer's recommended preparation procedure in accordance with our own laboratory protocols. After

removing any excess cement resulting from the insertion of the stem, the specimen was left to cure for a minimum of 12 hours before testing was conducted.

2.5 Periprosthetic Fracture fixation

A transverse type fracture, a fracture in which the break occurs perpendicular to the long axis of the Femur, was chosen to represent the periprosthetic fracture. The fracture was created 10 mm distal to the tip of the prosthesis stem, using the exposed shoulder of the prosthesis as a reliable measurement reference point. With the distance between the prosthesis shoulder and stem tip of 148 mm, the fracture was created 158 mm from the prosthesis shoulder. This method of calculating the fracture position from a datum point on an exposed section of the prostheses was necessary due to the slight variations in prosthesis positioning during insertion. By using this method, the 10 mm distance between stem tip and fracture could be guaranteed. The fracture was created using a workshop bandsaw, with the distally dissected end of the Femur placed firmly against a saw guide to ensure the accuracy of each fracture. If positioned correctly, the fracture would be created slightly proximal to the position of the cement restrictor.

Prior to fracture fixation, the distal fragment of the Sawbone Femur was secured using a metalworking bench vice, clamped firmly to the module, with its long axis horizontal to the ground. The periprosthetic fracture was stabilised using a combination of a bone plate and screws. The plate used to stabilise the fracture was an eight hole stainless steel bone plate (length: 155 mm; width: 17.5 mm; 82 thickness: 5 mm, Stryker, NJ, USA). Once the fracture had been completely reduced, the plate was positioned with the midpoint of the plate bridging the fracture line.

Initial positioning of the plate onto Sawbone was roughly held in place using two K-wires, each inserted through the plate into the proximal and distal bone fragments. Before proceeding with the insertion of the permanent fixation devices, fracture gap reduction was checked as well as the orientation of the bone fragments with respect to rotation around the long axis of the specimens. The screw hole positions were clearly marked and checked before progressing. To facilitate screw insertion, small pilot holes were drilled into the Sawbone aided by a drill sleeve guide which fixed directly onto the holes of the bone plate(Stryker, NJ, USA). Using this drill guide ensured that each pilot hole in the Sawbone was created perpendicular to the long axis of the Sawbone and also that each pilot hole was in the correct central position with respect to the hole on the plate. As 5 mm diameter locking screws were to be used, the pilot holes were drilled

with a 3 mm diameter drill bit. The positions where unicortical screws were to be inserted were only piloted through one cortex, through to the intramedullary canal, while the bicortical screw positions were piloted through the whole cross-section of the Sawbone. Any debris produced by the creation of the pilot holes was removed using high pressure air. Locking inserts were attached to the three most proximal and three most distal plate holes, leaving the two central holes of the eight hole plate bridging the fracture empty. Self-tapping locking screws, 5 mm in diameter were used at all locations along the plate. The three unicortical screws positioned proximally used 13 mm length self-tapping locking screws while 40 mm bi-cortical screws were inserted distally. Insertion of the locking screws was aided with the use of a torque limiting screwdriver (Stryker SA, Switzerland) to remove the possibility of over tightening the screws. During screw insertion, regular anticlockwise turns were made to back the screws out, clearing any loose material created by the insertion process. The bone screws were inserted in the same order for every specimen in the test group.

After screw insertion was completed, there was a 1 mm gap between the inside surface of the plate and the surface of the bone. Once the fracture was stabilised, the supporting K-wires were removed and fixation checked. X-rays of the completed fixation were taken and used to assess the constructs, the positioning of the prosthesis stem and thickness of cement mantle, also checking that the insertion of the unicortical screws around the proximal bone fragment had not compromised the cement mantle.

2.6 Strain Gauges

This section will detail strain gauges application and methods used to ensure accurate strain readings.

2.6.1 Strain gauge attachment

The use of two Data Acquisition (DAQ) modules allowed strain at eight locations on the specimens to be recorded simultaneously in real time. Prior to attachment to the pre-prepared sandpapered Sawbone, the attachment sites were marked with a guide before being de-greased using rubbing alcohol and cleaned with a cloth until any potential contamination was removed. The rear mounting surface on the strain gauge base was coated with a fine and uniform layer of cyanoacrylate bonding adhesive. Using a thin polyethylene sheet, the gauge was positioned and pressure applied to the gauge base for a minimum of 30 seconds. After the adhesive was cured, the polyethylene sheet was detached and any excess adhesive was removed. The gauge leads were carefully lifted using tweezers and attached to the connecting terminals sited 10mm distal to the strain gauges' position. The strain gauges were then soldered to the terminals and in turn, soldered to the extension lead wires from the Data Acquisition (DAQ) modules.

Enough slack was left between the strain gauges and terminals to prevent damage due to excessive tension during any experimental loading.

Five strain gauges were used to measure the strain on the Sawbone. The gauges were aligned parallel to the long axis of the Sawbone and positioned at predetermined sites, 0, 40, 80 and 200 mm distal to the Lesser Trochanter along the medial length of the Femur. The fifth Sawbone gauge was positioned 200 mm distally on the lateral side. These strain gauge positions are shown in Figure 28. An additional three gauges were positioned on the fixation plate when testing periprosthetic fracture fixation cases. These gauges were positioned in the middle of the plate, around the empty screw holes bridging the fracture.
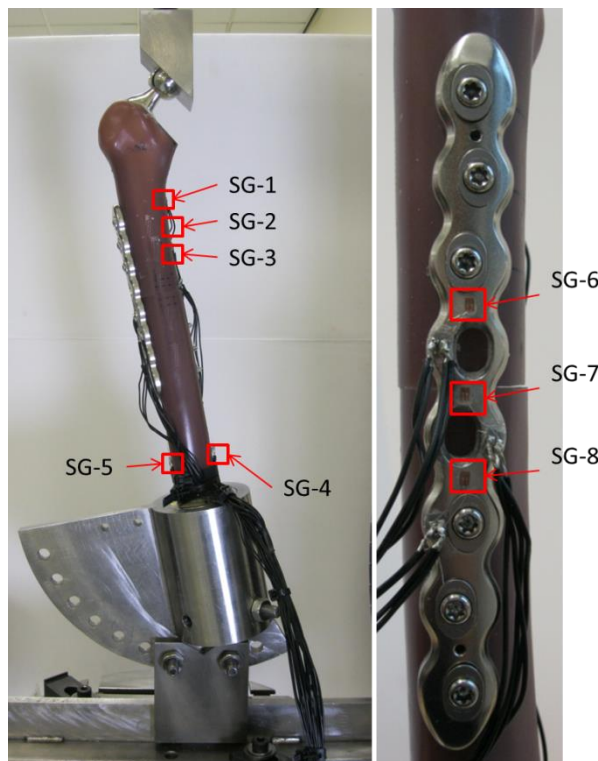
Figure 28 Loading test rig, showing strain gauges positions along Sawbone specimen and fixation plate

2.6.2 Strain data Acquisition

Strain gauges suited for use with low elastic modulus materials such as the Sawbone polymer were used to measure Sawbone strain in this study. These strain gauges (GFLA-3-50, Tokyo Sokki Kenkyujo, Tokyo, Japan) have features designed to ensure accuracy when used on materials with low elastic modulus compared to metals including a specifically designed grid supporting the measurement surface and the use of lower currents. Three strain gauges were positioned around the empty screw holes bridging the fracture. However, with the locking inserts in place on the fixation plate, the available surface area for gauge attachment was small. In order to mount

the gauges in the optimum positions, smaller gauges only 3 mm in length and 2mm in width were used(FLA-03-17, Tokyo Sokki Kenkyujo, Tokyo, Japan). The strain gauges were connected through a Data Acquisition (DAQ) module (9237, National Instruments, USA) to a Compact DAQ chassis (9174, National Instruments, USA) in a half bridge configuration. In addition to the gauges sited on the test Sawbone 4th generation composite Femur and fixation plate, additional "dummy " stain gauges were attached to an additional unloaded Sawbone and plate, using an identical bonding method. Sited on identical materials and in the same surrounding conditions as the loaded strain gauges, they would compensate for any ambient thermal variation. The wires connecting the gauges to the Data Acquisition module were one meter in length. The remote sensing wiring technique was used to reduce the inherent error resulting from delivering an excitation voltage to the strain gauges. This involved using a separate pair of wires to deliver the excitation voltage to the gauges, with an additional pair of wires used to exclusively measure the voltage change across the gauges. Several calibration tests were performed on the strain gauges and connected measurement equipment to ensure the strain readings remained accurate throughout the entire testing period. These calibration tests were performed after the pre loading cycles were completed and subsequently between every loading repeat, while the specimen was in an unloaded state. The gauge factor of the strain gauges used in the calibration tests were obtained from the manufacture's specifications(2.46 and 2.09, GFLA-3-50 and FLA-03-17). Variations in individual resistor and wire resistance in addition to installation factors were compensated by performing a null offset calibration. The resistance of the connecting wires was corrected for by performing a shunt calibration.

Preliminary testing was conducted to check the accuracy of the strain readings and to minimise the effect of noise. Strain data for each of the gauges were simultaneously recorded during loading, using Labview Signal Express (SignalExpress Full, National Instruments, USA) software. The data was then exported from the signal processing software to Microsoft excel. Using both the magnitude of the strains and the time code for each data point cross referenced with the loading profile, the data set for the time period where the specimens were under maximum load was identified and isolated. An average of 40 data points was used to calculate an average strain magnitude at each gauge location, while the standard deviation between the data points was used to evaluate signal noise. When performed for the results of the series of six repeats, the standard deviation between the strain readings was used to assess specimen performance variation over the series of loading repeats. Performed over the strain data for the whole group of loaded specimens, the variation in strain between the complete specimen set was used to evaluate the variance in performance between the specimens in the group.

2.7 Experimental testing

This section will detail the methods used to setup and load the samples tested in this study and the method used to calculate specimen stiffness.

2.7.1 Loading Procedure

Prior to loading, any debris was cleared and anti-fretting grease was applied to the adjustable bolts in the loading rig to prevent the joints from seizing. A materials testing machine (3365, Instron, MA, USA) was used to apply a range of loads to the specimens. Under displacement control, a compressive load was applied at a rate of 2mm/minute to a maximum of 500N. A 10kN load cell was used to measure the applied load. For both bone-instrumentation constructs, a loading cup simulating the acetabular component was used to load the specimens.

The load cell was calibrated to zero after the loading cup was attached to the crosshead but before the specimen was positioned in the machine. The crosshead was lowered manually at its slowest speed, allowing the femoral head to self-centre itself within the loading cup. Once a force reading of greater than 1N was measured, the load cell was recalibrated back to zero. The intact Femurs were loaded with a flat loading head directly to the top of the femoral head. For the these cases, the centre of the femoral head was aligned with the centre of the circular loading plate.

The base of the loading rig was then secured to the testing machine using machining blocks with T-nuts fixed to a solid base plate. A safety screen was attached to protect the user from resultant debris from any potential specimen failure. Both automatic and manual load limits were used to reduce this risk and protect the equipment from any potential damage. In order to reduce any inconsistency and to allow the constructs to become settled, the samples were subjected to 20 pre-loading cycles, before the six measured loading repeats were conducted. Load against displacement data was used to calculate the stiffness of each specimen. The specimens were tested at loading angles of 0°, 10° and 20° of adduction in the frontal plane and were aligned vertically in the sagittal plane.

2.7.2 Calculating overall construct stiffness

The stiffness of the specimens was calculated from the force against displacement data after exporting the raw data from the Bluehill software (BlueHill 2, Instron, MA, USA) used by the material testing machine to Microsoft Excel. Compressive force against displacement would then be

plotted on a graph. All of the loading repeats would have a toe region of the graph where there would be very little increase in force with increasing displacement. This region represents the numerous different parts of the specimen construct and loading rig bedding in. For example, perfect reduction between the two bone fragments is unlikely and any displacement necessary to bring the fracture site to complete closure would be represented in this region. These variables would have varying effects between samples in the test group and could significantly affect the stiffness calculation if the entire set of load displacement data was included. As a result, the specimen stiffness was calculated in the elastic region between the 100N and 500N data points, if the gradient in this region was linear. In some rare cases, the linear elastic region of the load against displacement graph had not been reached before the 100N data point, Figure 29. For these cases, the gradient was calculated between the 400N and 500N data points. The stiffness for each of the six loading repeats was calculated to give an average overall stiffness for each specimen.
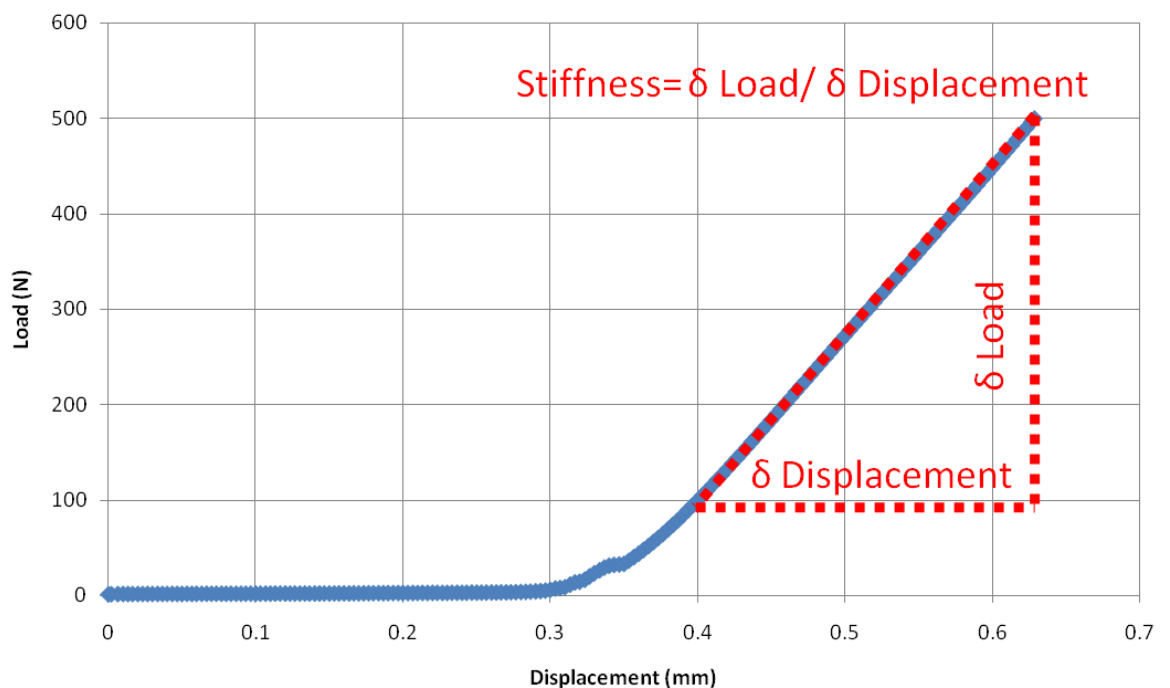
Figure 29 An example overall construct stiffness calculation using load against displacement data for plated specimen 4

.

Chapter 3 **Experimental results**

3.1 Introduction

The results of the experimental work conducted in this study are presented in this section. The results are presented in the order that they were conducted, concluding with a short discussion at the end of every section. The work has been divided into subsections, ordered by the status of the test specimens. The details at each stage of testing is shown in Figure 30, with the features for each stage of specimen preparation detailed in chapter 2. The tests progress from loading the specimens in the basic intact Femur case, introducing a cemented primary hip replacement to the intact Femur (THR), and finally investigating a stabilised periprosthetic fracture fixation case (PPF).

Work Flow- Experimental Testing		New Sawbone from Manufacturer
		Sawbone Surface Preparation
		Sawbone Distal Dissection
		Sawbone mounted into module
		Sawbone fixation into module-PMMA
Section 1		Experimental testing- Intact Femur
		Sawbone Femoral head Dissection
		Cement Cavity Preparation
		Prosthesis Positioning
		Cement Mantle Insertion
Section 3		Experimental testing- THR
		Screw Pilot hole drilling
		Fracture creation
		Construct Stabilisation
Section 5		Experimental testing- PPF

Figure 30 Detailed Experimental Work Flow

3.2 Intact Femur study experimental results

This section presents the experimental results from testing the Sawbone Femurs with the femoral head intact. The only preparation the specimens received at this loading stage was the removal of the femoral condyles and preparation of the distal end of the Femur to support the sample during loading, fixing the samples to the loading rig with cement. For the Intact Femur loading tests, a flat loading plate was fixed to the cross head of the materials testing machine to apply the load directly to the femoral head.

The aim of the work in this section was to characterise the mechanical behaviour of the intact Femurs, focusing on the stiffness of the specimens over a range of loading angles and the strain distribution along the length of the Femur. In addition, various tests investigating the reliability of the loading rig, specimen loading procedure and specimen variability over the test sample group were also undertaken.

3.2.1 Test Rig setup variability

The complete test rig consisted of several parts which could be disassembled between each loading session. The locations where measurements were taken from the specimens were kept consistent across all of the different testing, where possible. To ensure the assembly of the test rig did not affect these results of the study, the potential variability in the results due to the test rig setup was evaluated. The test rig was completely disassembled, reassembled and re fitted to the materials testing machine three times, during three separate laboratory sessions. These readings were measured after a consistent stiffness value had been reached, with the intact Femur positioned at the 0° loading angle.

The results of the three separate setup variability tests are shown in Table 3. The overall stiffness values of the three repeats were very similar. The percentage difference between the highest and lowest overall stiffness was 3.5%.

Table 3 Overall stiffness for set up repeatability tests. The standard deviation for each test was calculated over six loading repeats.

Test	Overall Stiffness (kN/mm)	STDEV
Set up repeat- 1	1.446	0.052
Set up repeat- 2	1.487	0.002
Set up repeat- 3	1.491	0.003

3.2.2 Effect of loading angle on intact Femur stiffness

The results of the axial compression tests over the range of tested loading angles, for a single specimen (S07), are shown in Figure 31. The loading angle was found to have a large effect on intact Femur stiffness. The highest bulk stiffness was measured at the 10 ° loading angle, while the lowest stiffness was measured at the 20 ° loading angle. There was a 56% reduction in stiffness between these two cases. The reloading error, calculated as the standard deviation between six loading repeats was found to be very low.
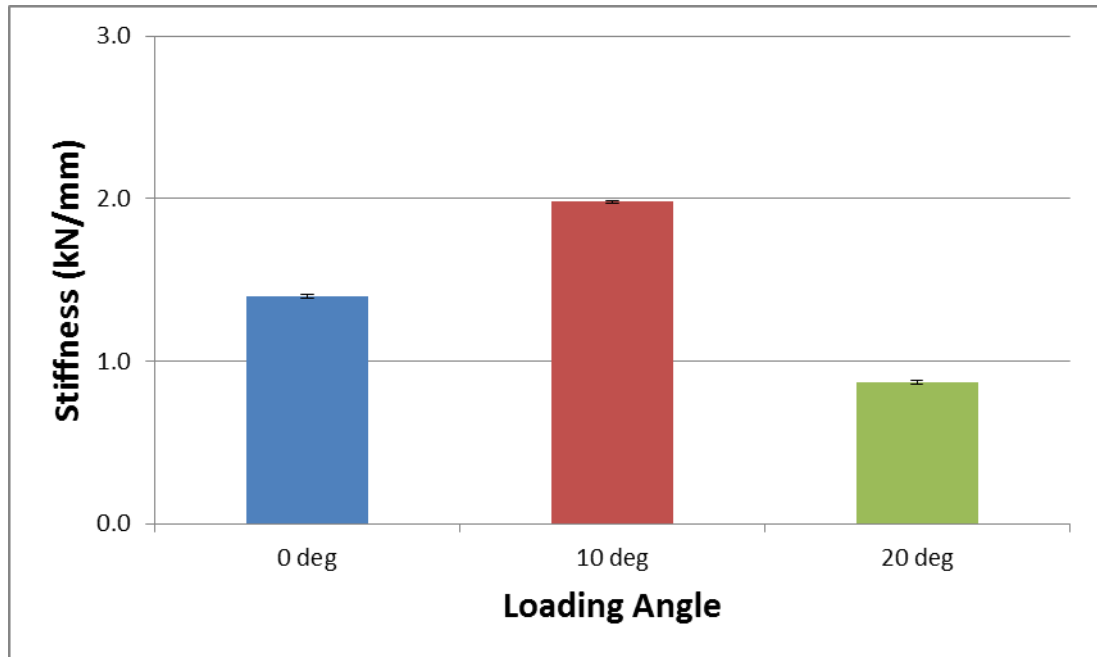
Figure 31 Experimental stiffness of the intact Sawbone Femurs for the 0°, 10° and 20° investigated loading angles. Error bars on the experimental data represent the standard deviation between six re-loading cycles of the same specimen (S07)

3.2.3 Evaluation of test group specimen stiffness variability

The six intact Femurs in the test group which were used throughout this work were loaded at the 0° loading angle. This was used to establish baseline stiffness for each sample and to determine if any specimen had a large difference in stiffness to the rest of the Femurs in the test group.

The overall stiffness for each specimen is shown in Table 4. The average stiffness for the whole test group was 1.373kN/mm with a standard deviation of 0.045. The specimen with the highest overall stiffness was specimen nine with a stiffness of 1.441kN/mm, while the specimen with the lowest stiffness was specimen eight with a stiffness of 1.320kN/mm. The percentage difference between the highest and lowest specimen stiffness was 10%.

Sawbone Identification Number	Overall Stiffness (kN/mm)
S-04	1.387
S-05	1.366
S-06	1.326
S-07	1.399
S-08	1.320
S-09	1.441

Table 4 Intact Femur stiffness for test group of six specimens. The group average stiffness was 1.373kN/mm with a standard deviation of 0.045.

3.2.4 Pre-loading cycles

Preliminary stiffness data from initial rig setup variability tests indicated that the overall specimen stiffness of the intact Femurs would increase slightly over the initial loading repeats. A study was conducted to quantify the stiffness difference between the initial loading cycles and the stabilised stiffness repeats, and to identify the number of pre-loading repeats that would need to be completed before reliable loading data obtained from the specimens could be guaranteed. A single Femur was repeatedly loaded 21 times, on three separate laboratory sessions, with complete test rig assembly and disassembly between sessions. The tests were performed in the order A, followed by B then C.

The stiffness results for the 21 loading cycles are shown in Figure 32. The results show that the initial stiffness of the composite Femur is lower than in subsequent consecutive repeats. The set of loading repeats B had the largest progressive change with an increase of 45% between initial and stabilised stiffness values. For repeats C, the overall specimen stiffness stopped increasing after the third loading repeat. However, for repeats B, a consistent bulk stiffness value was reached after nine repeats. The data showed that once a consistent overall specimen stiffness value was reached, that for the rest of the laboratory session, overall stiffness would remain consistent.
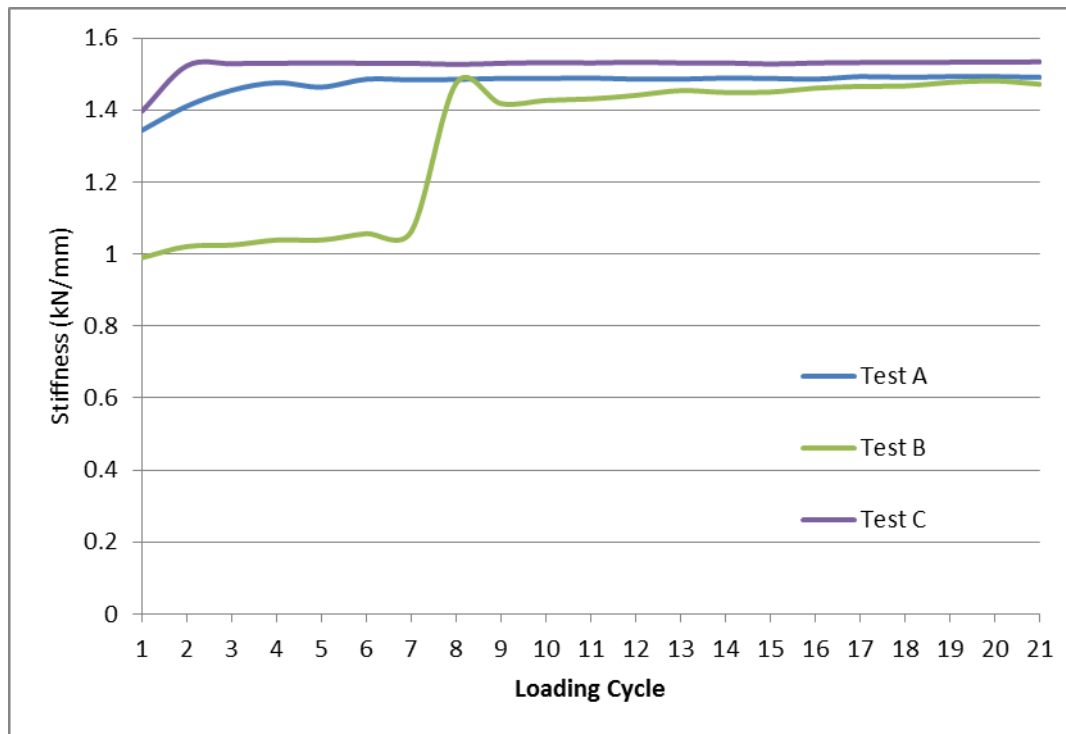
Figure 32 Overall stiffness for the first 21 repeats in three separate laboratory sessions. Identical loading conditions are present in all of the tests, with the composite Femur (S07) oriented at a loading angle of 0 degrees.

3.2.5 Time period between loading repeats

Preliminary strain calibration tests indicated that a small period of time would be required between each loading repeat, to reset and calibrate the strain gauging equipment. As a result, the six loading repeats when strain and stiffness readings would be taken could not be conducted consecutively. To determine if the elapsed time between loading cycles had any effect on overall stiffness, stiffness tests were conducted for loading repeats conducted consecutively, and with five minute gaps between loading repeats. The tests were conducted after 20 pre-loading cycles to ensure the overall stiffness of the specimens had stabilised. The pre-loading cycles were repeated in the same loading regime as the previous test and were kept consistent for all subsequent loading tests .

The results for the consecutive and five minute gap between loading repeats are shown in Table 5. The average stiffness between the consecutive and five minute gap loading repeats were very similar. The difference between the stiffness values of the two methods was within the standard deviation over the six loading repeats of each test.

Table 5 Average stiffness for loading repeats conducted consecutively and with five minute gaps between repeats, for specimen (S07). The standard deviation for each method was calculated over six loading repeats.

Test	Average Stiffness (kN/mm)	STDEV
Consecutive loading repeats	1.423	0.003
5 min gap between repeats	1.425	0.005

3.2.6 Pre-loading Clearance

It was unknown whether allowing contact between the loading plate and the specimen femoral head before loading, would affect the overall stiffness measurements. To investigate this, three different pre-loading clearances were tested; a 1.0 mm gap between the femoral head and the loading plate, a 0.4 mm gap between the femoral head and the loading plate, and a final test where the femoral head and plate started loading already in contact.

The overall stiffness values for the three different pre-loading clearance tests are shown in Figure 33. The overall stiffness values of the different clearance distances were very similar. The highest stiffness was for the pre-loading clearance of 0.4 mm, while the lowest was seen where there was no initial gap. However, the largest percentage difference in stiffness between the tests was less than 2%.
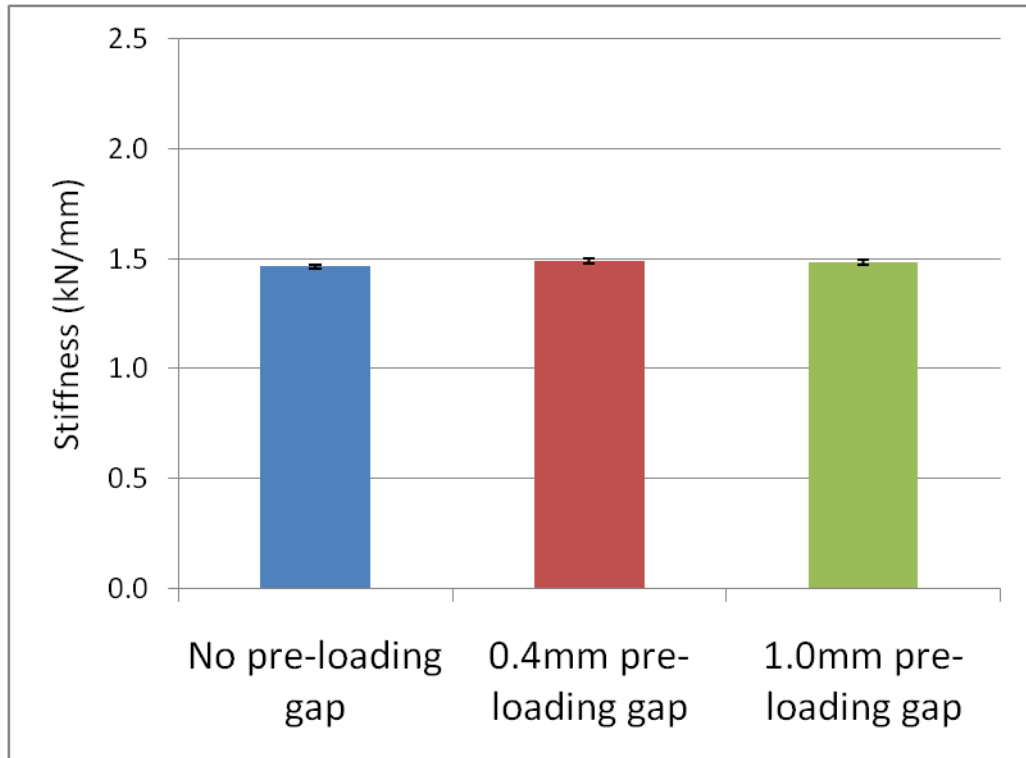
Figure 33 Overall specimen stiffness for the three different investigated pre-loading clearance distances. The error bars show the standard deviation for each method, calculated over the six loading repeats.

3.2.7 Intact Femur strain pattern

A baseline strain distribution along the medial length of the intact Femur was investigated with the specimen tested at the 0° loading angle. The surface strain pattern along the medial length of the intact Femur is shown in Figure 34. The medial strain pattern changed considerably over the length of the Femur, with the highest strains seen in the middle of the Femur, and lower strains recorded at the proximal and distal ends. The highest strain was recorded at gauge 2 while the lowest strain was seen at gauge 1.
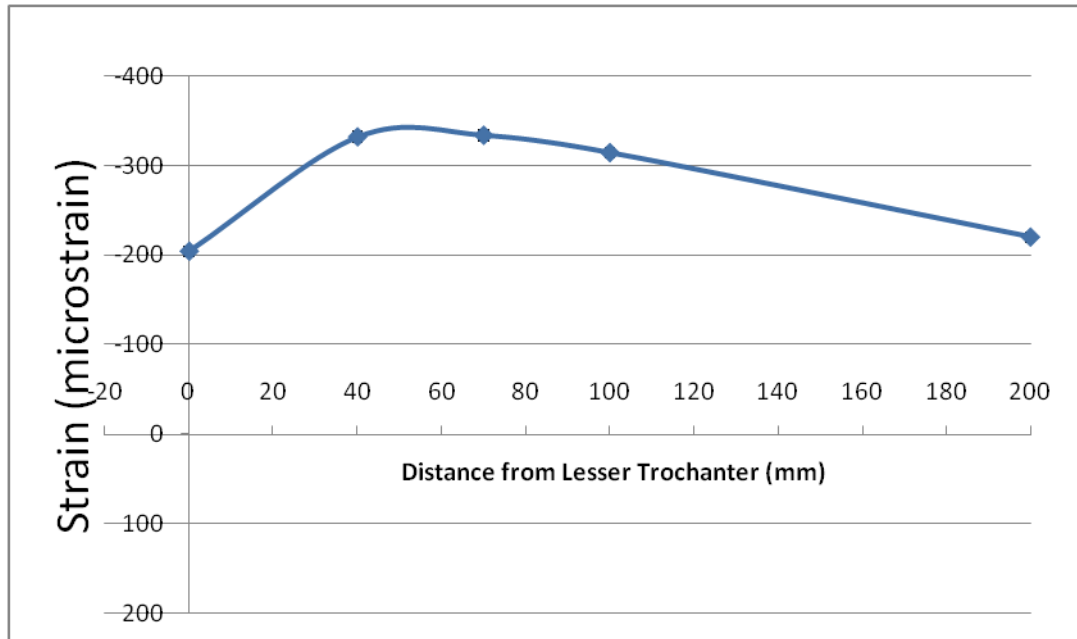
Figure 34 Bone strain along the medial length of the Femur (S07), at the 0 degree loading angle. Error bars represent the standard deviation between 6 re-loading cycles of the same specimen

3.2.8 Discussion

The results of the loading rig setup tests show which of the tested parameters made a difference to specimen behaviour, and would need to be controlled in future tests. The entire test rig could be repeatedly reassembled and refitted to the materials testing machine without affecting overall specimen stiffness.

The standard deviation of overall specimen stiffness for the series of six loading repeats was very low. Expressing the standard deviation as a percentage of the mean stiffness, the spread over the repeats was less than 0.1% of the mean stiffness.

The variations in overall specimen stiffness between the results were within the standard deviation of the measurements. The use of a standard operating procedure(Appendix B), detailing any important loading rig assembly details would be followed at the beginning of any subsequent test session to ensure correct rig setup.

The specimen stiffness was unaffected by the changes in time period in between loading repeats. It is likely that under the applied 500N load, that the Sawbone displays linear elastic behaviour, and therefore the unloading behaviour would not change between time gaps. The specimen stiffness was also unaffected by the pre-loading clearance between the femoral head and the loading fixture. This result was reasonable considering that the materials testing machine was under load control. This does not restrict the

time needed to calibrate the strain gauging equipment between loading repeats, with 5 minutes being ample time to complete these checks.

The loading fixture would be brought into contact with the femoral head as this would aid in accurate specimen and loading rig alignment within the material testing machine. Conducting pre-loading cycles before the measured loading repeats would be necessary before every test. Large increases in stiffness were observed over the first loading repeats in a series of loading cycles. This could be due to the specimens bedding in, temperature changes or micro motion between the different internal materials within the synthetic Femurs.

Although the maximum number of loading repeats before a specimen displayed stabilised specimen stiffness, to guarantee accurate results, 20 pre-loading cycles would be conducted before every test. The maximum stiffness variation between the specimens with the highest and lowest stiffness in the group of tested specimens was 10%. This variation could be caused by material imperfections or slight geometry variations between the Sawbones.

The loading angle that the intact specimens were tested at had a large effect on specimen stiffness. The specimens had the highest stiffness at the angle closest to the anatomically correct loading position. The strain pattern along medial length of Femur was also found to vary greatly. The experimental rig and techniques used to test the specimens worked well and ensured that each sample in the test group was tested correctly for all the loading repeats.

3.3 Comparison to the literature

This section presents the comparison of the experimental results collected in the intact Femur study to relevant experimental studies already published in the literature. Comparing the experimental results of this study to the results of previous studies would allow the evaluation of how our experimental test rig setup and specimen preparation performed in relation to the baselines found in the literature.

3.3.1 Intact Femur stiffness literature comparison

The manufacturers of the synthetic Sawbone specimens used in this study, cited a study by Heiner et al [86], where both natural Femurs and 4th generation Sawbone had been tested, using an experimental setup similar to the test rig used in this study.

The stiffness comparison between the two studies is shown in Table 6. The average specimen stiffness measured in this study, conducted at 10 degrees to the vertical, was within 7% of the bulk stiffness measured at 11° by Heiner et al.[86]. The bulk stiffness of the composite Femur investigated in our study was 20% lower than the stiffness of the natural Femur tested by Heiner.

Table 6 Average stiffness for natural and synthetic intact Femurs between studies.

Test	Study	Loading angle (°)	Avg. Stiffness (kN/mm)	STDEV
Natural Femur	Heiner et al.	11	2.48	-
4th gen Sawbone	Heiner et al.	11	1.86	-
4th gen Sawbone	Leeds	10	1.98	0.01

3.3.2 Intact Femur strain comparison with Literature

A study conducted by Pal. et al. [87] loaded a synthetic Femur in a similar experimental set up to this work and used a 10° loading angle. The specimens in the Pal study were orientated at 10° in both the sagittal and frontal planes. Strain gauge 2 was positioned in an identical position in both studies. In order to match an additional gauge location from the Pal et al study, a strain gauge was positioned on the lateral side of the Femur, 40 mm distal to the lesser trochanter, strain gauge 9. This was possible due to the thee strain gauge channels designated for use on the fixation plate not being used at this stage of specimen testing. Two more additional strain gauges were added at the same level, 40 mm distal to the lesser trochanter, on the ventral and dorsal sides of the Femur. However, both of these gauges would not calibrate correctly during testing and the measured strains did not change during loading. The strain gauges were very fragile and easy to damage, and while great care was taken to ensure their survival, it was subsequently discovered that the dummy gauges for both of the gauge positions were damaged.

The strains for gauge locations 2 and 9 for both studies are shown in Table 7. The experimental strains at gauge location 2 were both compressive between the two studies and were both in tension at gauge 9. While the magnitudes of the strains at gauge 9 were similar, the experimental strain at gauge 2 in the Pal.et.al study[88] was much larger than the strain recorded

in this study. The strains from this study matched better with the computational strains from the Pal.et.al study[88].

Table 7 Experimental strain for gauge locations 2 and 9, for Pal.et.al and this study.

Test	SG-2 (με)	SG -9 (με)
Pal.et.al. Experimental - Rig at 10deg	-606	333
Pal.et.al. Computational - Rig at 10deg	-491	309
Experimental- Rig at 10deg	-268	200

3.3.3 Discussion

The overall stiffness from this study, with the rig at the 10° loading angle was within 7% of the results generated by Heiner et al[86]. This overall stiffness for the Sawbone in this study was lower than the natural bone and for the Sawbone in the Heiner study. This difference could be as a result of variations between the test rig setups used in this study and the study conducted by Heiner et al. The axial loading tests conducted in this study, loaded the Femur at 10° to the vertical, used a flat plate to load the head of the Femur and employed large sized Sawbone Femurs. Heiner et al. [72] positioned their Femur at 11° to the vertical, used medium sized Sawbones and used a mould of the femoral head to apply load to the femoral head. Our study has shown that increasing the loading angle resulted in an increase in overall stiffness of the construct. As a loading angle used in the Heiner et al. study was 11°, we would expect the bulk stiffness values measured in this study conducted at 10° to be slightly lower.

The experimental strain readings measured by this study were significantly lower than the strains at corresponding locations in the comparable study by Pal et al.[87], measured both experimentally and computationally. The medium sized Femur samples used in the Pal study were distally dissected 210 mm from the lesser Trochanter, whereas the large sized femoral samples used in this study were significantly longer having been dissected 260 mm distal to the lesser Trochanter. There were also differences between the orientations at which the Femur specimens were loaded. The specimens in this study were orientated at 10° to the vertical in the sagittal plane only, while the specimens in the comparison study were orientated at 10° in both the sagittal and frontal planes. This could account for the inter-study differences in strain magnitude at both gauge locations.

Taking into account the experimental differences between the different studies, the stiffness results correlated well, and while the strain magnitudes were slightly mismatched, the strain pattern recorded were the same. Confidence in the loading rig and preparation of the Sawbone specimens would be taken forward to the subsequent tests.

3.4 Total Hip Arthroplasty study experimental results

This section presents the experimental results for the Sawbone Femurs after the introduction of a cemented primary hip prosthesis (THR). The specimens were tested over the same range of loading angles as the intact Femurs. Additional tests were also performed where torsional loading was introduced. The specimens were rotated 8° and loaded at the 10°and 20° loading angles.

3.4.1 Effect of loading angle on Total Hip Replacement specimen stiffness

The stiffness of the THR specimens over the range of loading angles is shown in Figure 35. The highest overall stiffness was observed at the anatomically realistic 10°loading case, while the lowest stiffness was at the 20°loading case. The overall stiffness for the 10° loading case was over double that of the 20° loading case.
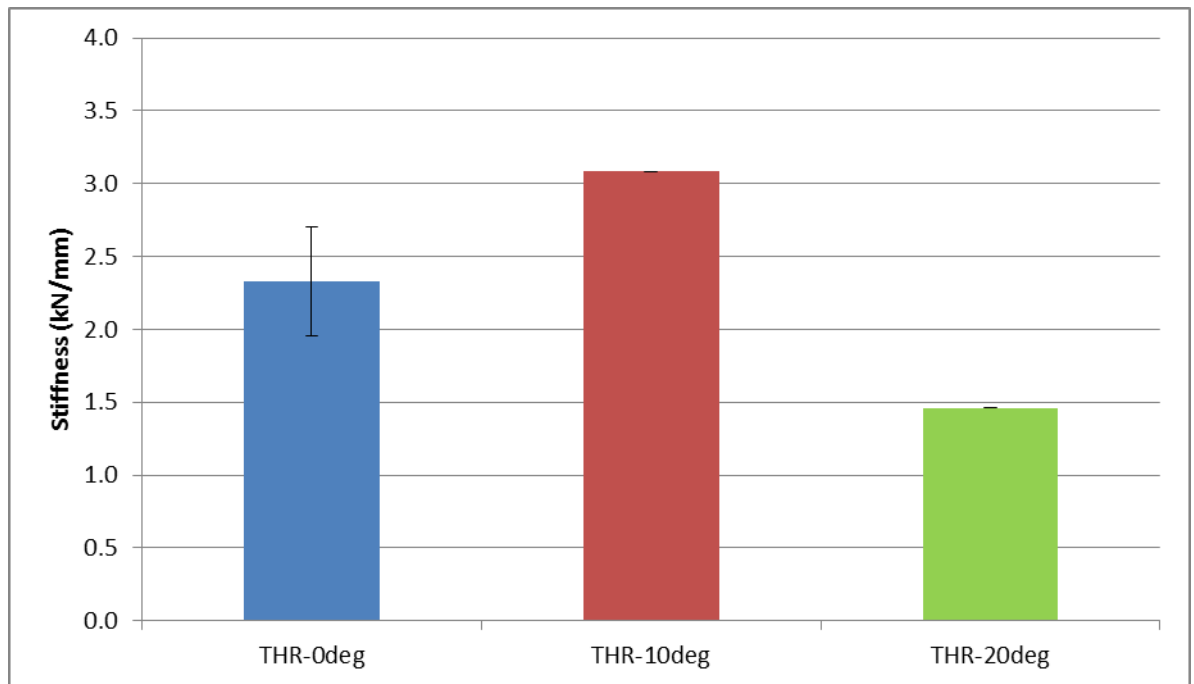
Figure 35 Average overall stiffness for the six THR specimens at loading angles of 0°, 10° and 20°. Error bars represent the standard deviation between 6 re-loading cycles of the same specimen

3.4.2 Total Hip Replacement specimen bone strain

The strain along the medial length of the Femur, for the THR case, over the range of loading angles is shown in Figure 36. The highest strains were observed at the 0° loading case while the lowest were seen at 20° case. The effect of loading angle on medial strain increases as the distance from the lesser trochanter increases. The strain at gauge 1, the most proximal gauge location, does not change markedly over the range of loading angles. However, the most distal gauge changes from being in compression at 0° case, to being in tension in the 20° case, Figure 36. In the 0° loading case, the strain at the most distal gauge in the region of the stem (gauge 3, 80 mm from the lesser trochanter), is higher than the most proximal gauge, while in the 20° loading case, the strain at this gauge is lower.

The strain at the distal end of the Femur, on both the medial and lateral sides, is shown in Figure 37. The distal strain pattern observed in the 0° loading case is opposite to that seen in the 20° case. The medial strain goes from being in compression to tension, with the lateral gauge going from tension to compression. At the 10° loading case, both gauges are in slight compression. As the loading angle is increased, the distal medial strain goes from being in compression to tension while the lateral strain is in tension at 0° and in compression at 20°.
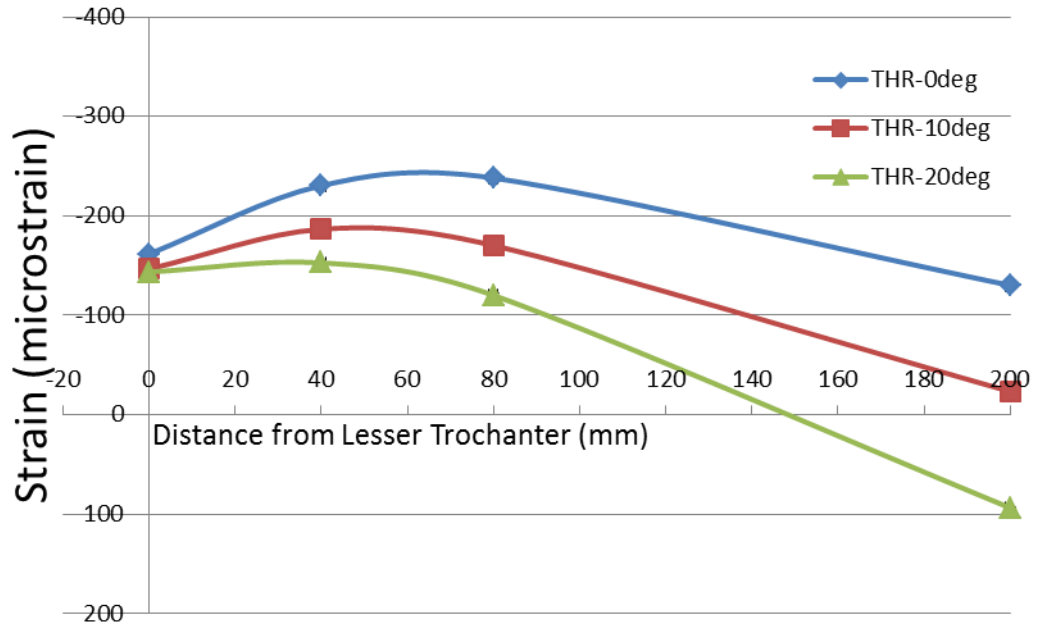
Figure 36 Strain along the length of the Femur on the medial side, for the THR specimens at 0°,10° and 20°.
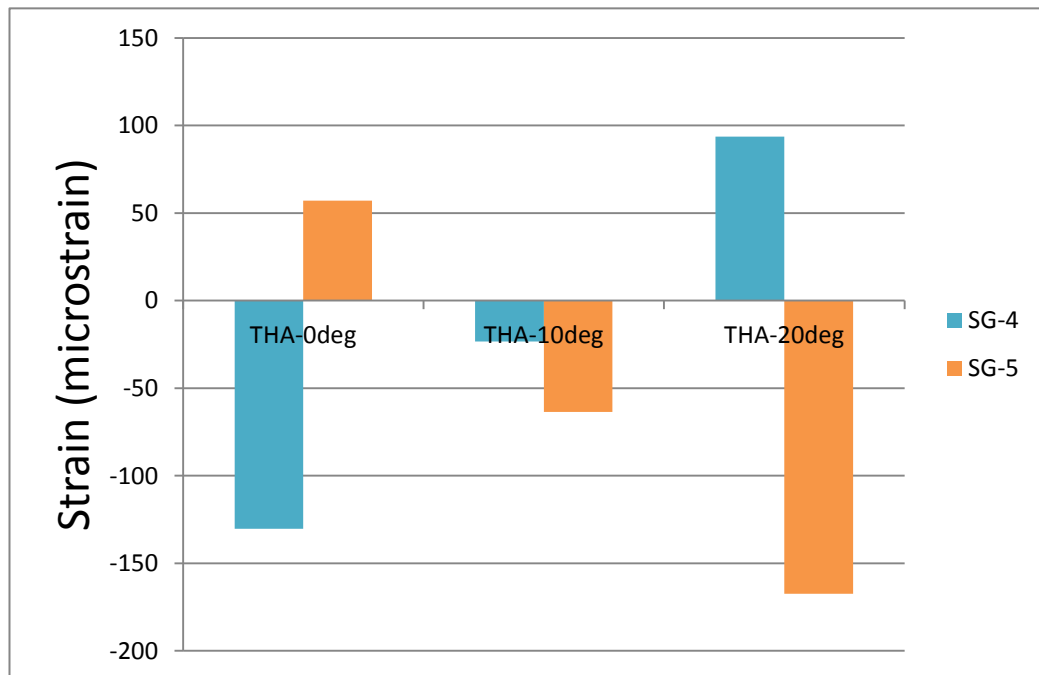
Figure 37 Distal strain at gauge locations 4 (medial) & 5 (lateral), for the THR specimen (S07) at loading angles of 0, 10 and 20 degrees.

3.4.2.1 Discussion

The total hip replacement specimens were tested successfully over the range of investigated loading angles. Large variations in strain and stiffness behaviour were observed for the specimens. The addition of a very rigid fixture sited within a comparatively flexible tube will have changed the stiffness of the construct in the region of the stem, also affecting the load transfer through this region of the bone. With the load applied directly onto the prosthesis femoral head, stress shielding could be occurring in the bone surrounding the proximal part of the prosthesis. In addition, much of the cancellous bone and some of the cortical bone in the proximal region of the Femur was removed during the reaming preparation for cemented stem insertion. The differences in mechanical behaviour were larger for total hip arthroplasty specimens than were observed for the intact Femur specimens.

3.5 Periprosthetic fracture fixation case experimental results

This section presents the experimental results for the specimens after a B type periprosthetic fracture was created in the THR specimens, and stabilised using a combination of a locking fixation plate and bone screws. The Periprosthetic fracture fixation specimens were tested over the same range of loading angles as the previous tests, and were also tested under torsional loading. The aim of introducing a torsional component to the load was to investigate how sensitive the plated Femurs were to the introduction of torsion to the loading conditions. As the fixation plate was present in the plate case specimens, the results of the strain across the bone plate are also presented.

3.5.1 PPF specimens experimental stiffness

The stiffness of the plate specimens over the range of loading angles in the coronal plane, is shown in Figure 38. The highest overall stiffness was observed at the anatomically correct 10° loading case, while the lowest was seen at 20°. The percentage difference between the highest and lowest stiffness cases was 42%. The error bars, representing standard deviation across the five samples in the test group, indicate that there was some variation in overall stiffness across the group of specimens.
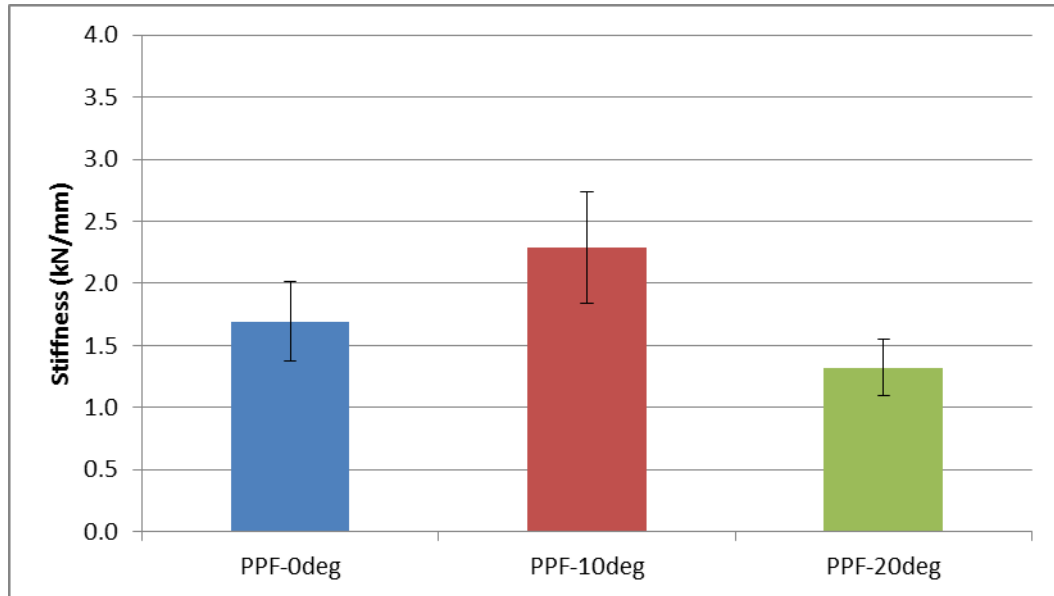
Figure 38 Stiffness of the plate specimens at loading angles of 0°, 10° and 20°. The error bars show the standard deviation over the five samples in the plate specimen group.

3.6 PPF case strain

The strain along the medial length of the Femur, for the plate case at a range of loading angles is shown in Figure 39. The lowest strains were observed at the 20° loading case, while the highest were seen at 0° case. As the investigated loading angles were varied, the larger differences between strains on the same gauge were observed further from the Lesser trochanter. The distal strain on both the medial and lateral sides of the Femur is shown in Figure 40. The largest variation in strain occurred at the most distal gauges, where the strain was in compression at the 0° loading case, but in tension at 20° case. In the 0° loading case, the strain at the gauge positioned directly above the fracture site, was almost three times the magnitude of the strain at the most proximal gauge. In the 20° case, this difference in strain between gauge three and one was much lower. At both the 0° and 10° loading case, both the medial and lateral distal gauges are in compression. The magnitude of the strain is similar for both loading cases. When loaded at 20°, the lateral gauge remains in compression while the medial gauge is in tension. The magnitude of the distal strains at the 20° loading case is also much larger than in the other two loading angles.

The strain along the length of the plate over the range of loading angles is shown in Figure 41. Strains measured from the lateral side of the fixation plate were found to vary greatly across the three strain gauge locations. The highest strain on the plate was recorded at the most proximal gauge position with the lowest strain at the most distally positioned gauge.
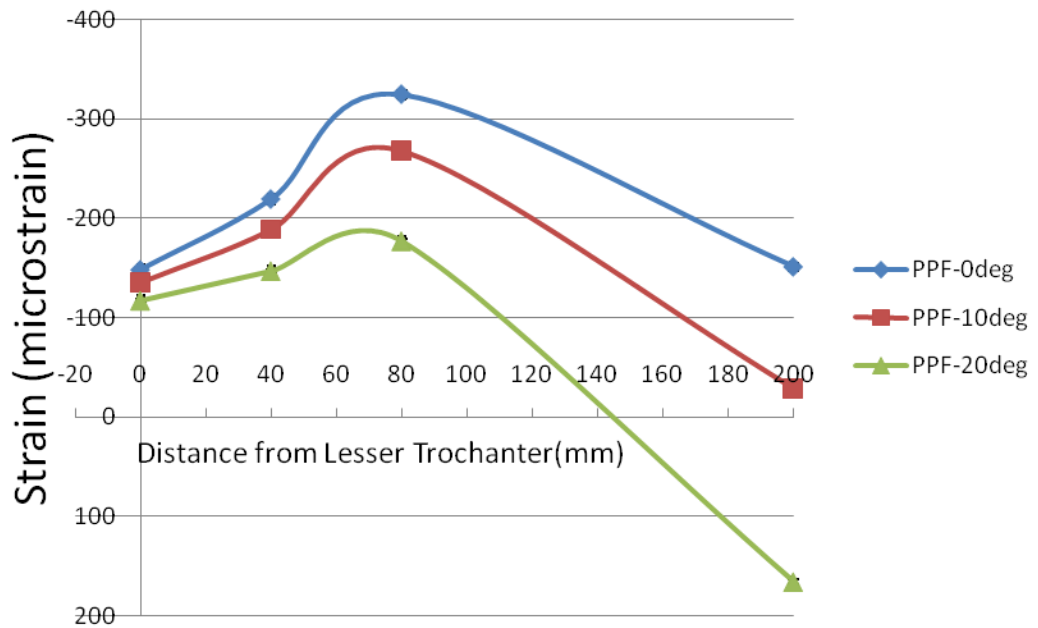
Figure 39 Strain along the medial length of the Sawbone Femur on the medial side, for the plate specimens at 0°, 10° and 20° loading angle.
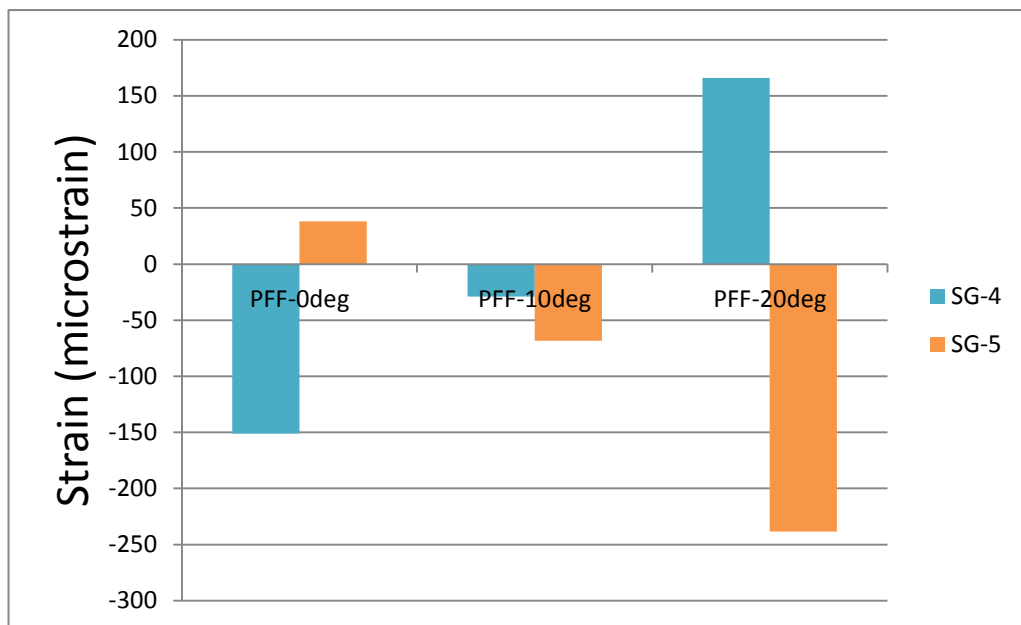
Figure 40 Strain at the distal gauge locations 4 & 5, for the plate specimens at loading angles of 0°, 10° and 20°.
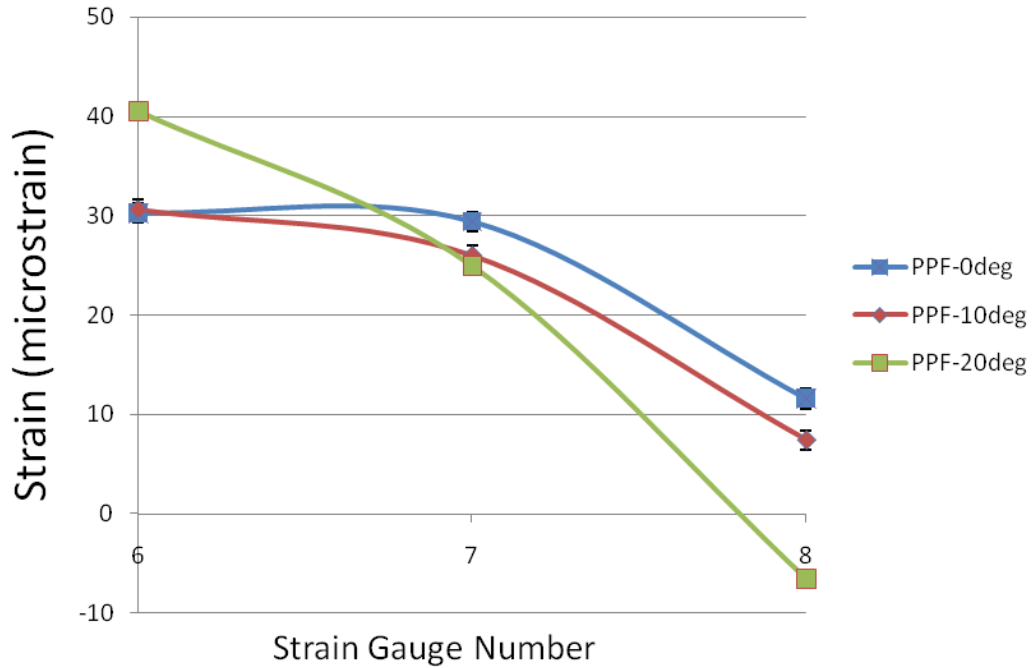
Figure 41 Strain along the lateral length of the plate, for the plate specimens at 0, 10 and 20 degrees loading angle.

3.7 Effect of torsional Loading

3.7.1 Comparison of torsional loading on THR case

The aim of this section of work was to determine how sensitive the THR Femurs were to the introduction of torsion to the loading conditions. The methods used to adapt the loading rig to apply torsion are described in section 2.2.3.

3.7.1.1 Total Hip Replacement specimen stiffness with torsion

The stiffness of the THR specimens with and without torsion, at loading angles of 10° and 20°, are shown in Figure 42. The previous results of the THR samples loaded with no additional torsion were used as a baseline to compare the torsion loading results against. The overall stiffness values with and without torsion were very similar. This was the case for both loading angles. At 10° case, the specimens loaded with torsion had a slightly higher overall stiffness than the specimens without. However, at the 20° loading angle, the torsion case had a slightly lower stiffness than the case without torsion.
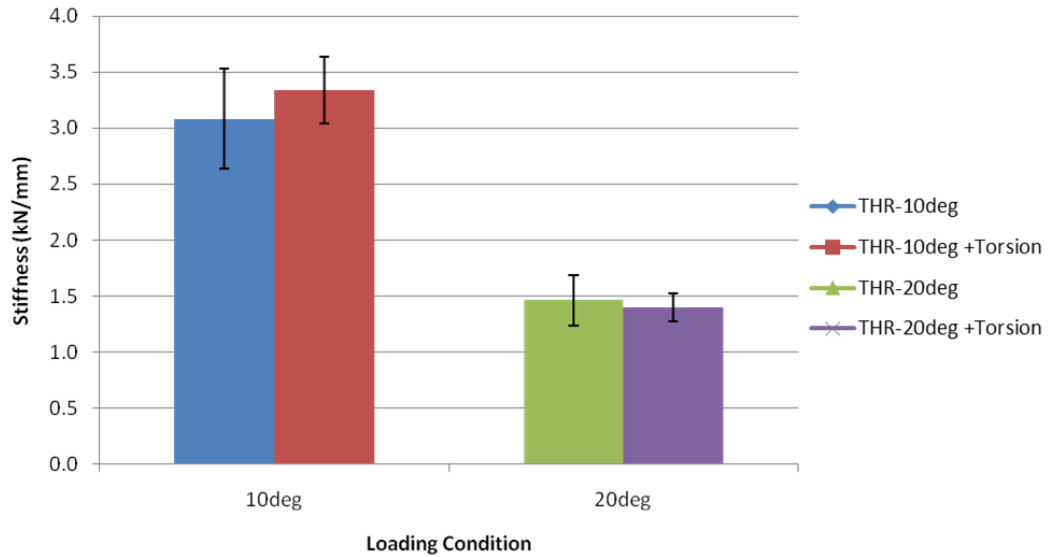
Figure 42 Stiffness of the THR specimens at loading angles of 10° and 20°, with and without torsion. The error bars show the standard deviation for each method, calculated over the six loading repeats.

3.7.1.2 Total Hip Replacement specimen bone strain with torsional loading

The strain along the medial length of the Femur for the THR case with and without torsion, at loading angles of 10° and 20°, are shown in Figure 43. At the 10° loading angle, the proximal strains on the medial side of the Femur in the torsion case are slightly lower than the strains in the case without torsion. For the 20° loading angle, the proximal medial strains with torsion are slightly higher than those in the case without torsion.

The distal strain values on both the medial and lateral sides are shown in Figure 44. These strain patterns were very similar with and without torsion. For both the 10° and 20° loading cases, the magnitude of the strains without torsion was slightly higher than those with torsion.
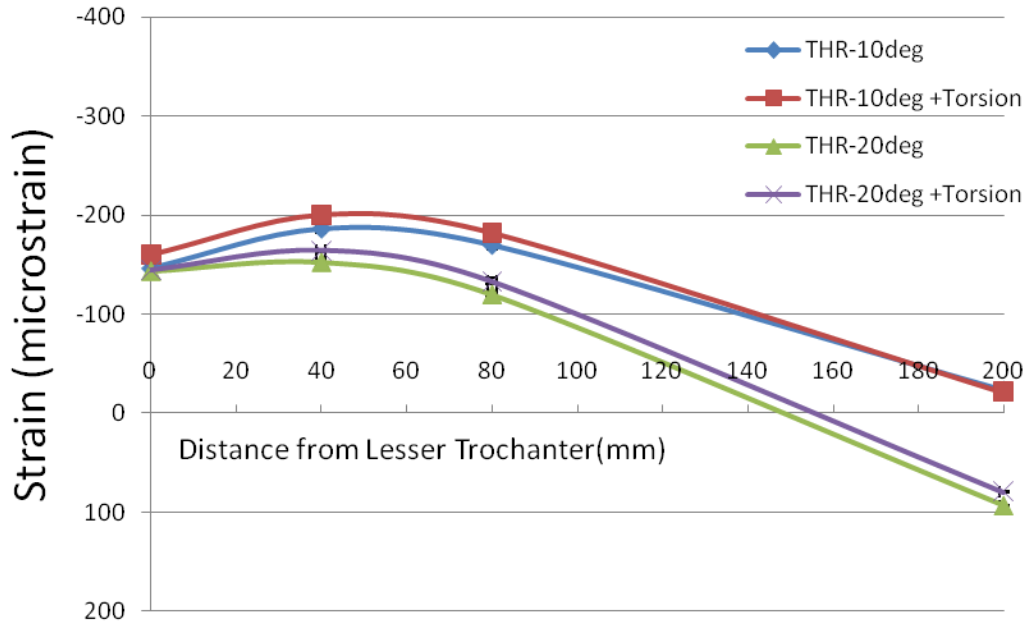
Figure 43 Strain along the length of the Femur on the medial side, for the THR specimens at 10° and 20°, with 0 and 8 degrees of torsion.
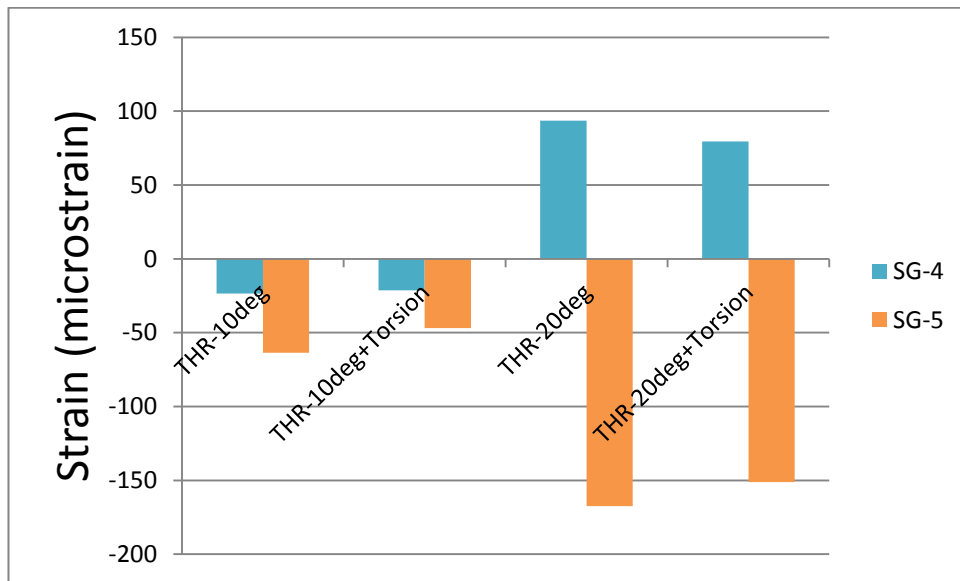
Figure 44 Strain at gauge locations 4 & 5, for the THR cases at 10 °and 20° loading angle, with and without torsion.

3.7.2 Comparison of torsional loading on PPF case

The aim of this section of work was to determine how sensitive the PPF Femurs were to the introduction of torsion to the loading conditions. The methods used to adapt the loading rig to apply torsion are described in section 2.2.3.

3.7.3 Effect of torsion on overall construct stiffness of the PPF samples

The stiffness of the plate specimens, with and without torsion, at loading angles of 10° and 20°, are shown in Figure 45. For the 10° loading angle, the the stiffness of the specimens was higher with the torsional loading than with conventional loading. For the 20° loading angle, the stiffness of the specimens was lower with the torsional loading than with conventional loading. However, the overall stiffness difference with and without torsion was much smaller that the standard deviation of the stiffness of the whole test group of five specimens.
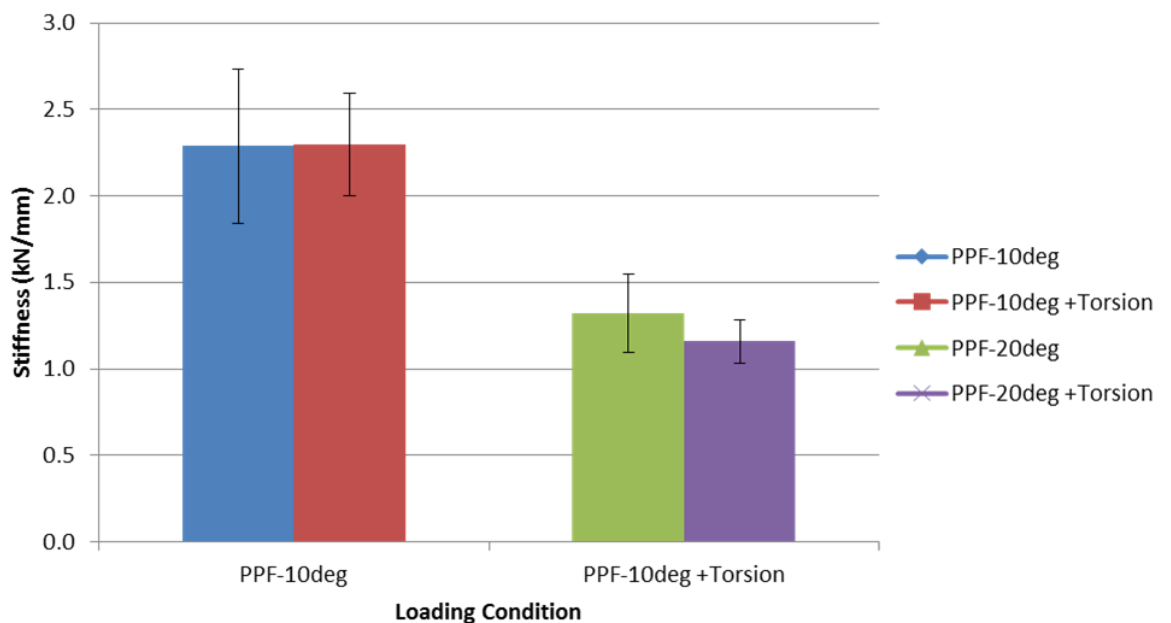
Figure 45 Stiffness of the plate specimens at loading angles of 10° and 20°, with and without torsion. The error bars show the standard deviation of stiffness over the test group of five specimens.

3.7.4 Effect of torsion on strain for PPF samples with torsional loading

At the 10° loading angle, the proximal strains on the medial side of the Femur in the torsion case were very close to the strains in the case without torsion Figure 46. For the 20° loading angle the strains in both torsion cases are very similar, however a significant difference in strain is observed at

gauge 3, located just above the fracture site. At this gauge, a higher strain is measured in the torsion case. The overall stiffness of the plate specimens at 10° loading angle, with and without torsion were very similar. At 20°, there is an increase in overall stiffness in the case without torsion.

For both loading cases, the application of torsional loading did not greatly affect the distal strains patterns, either on the medial or lateral side, for either loading case Figure 47.
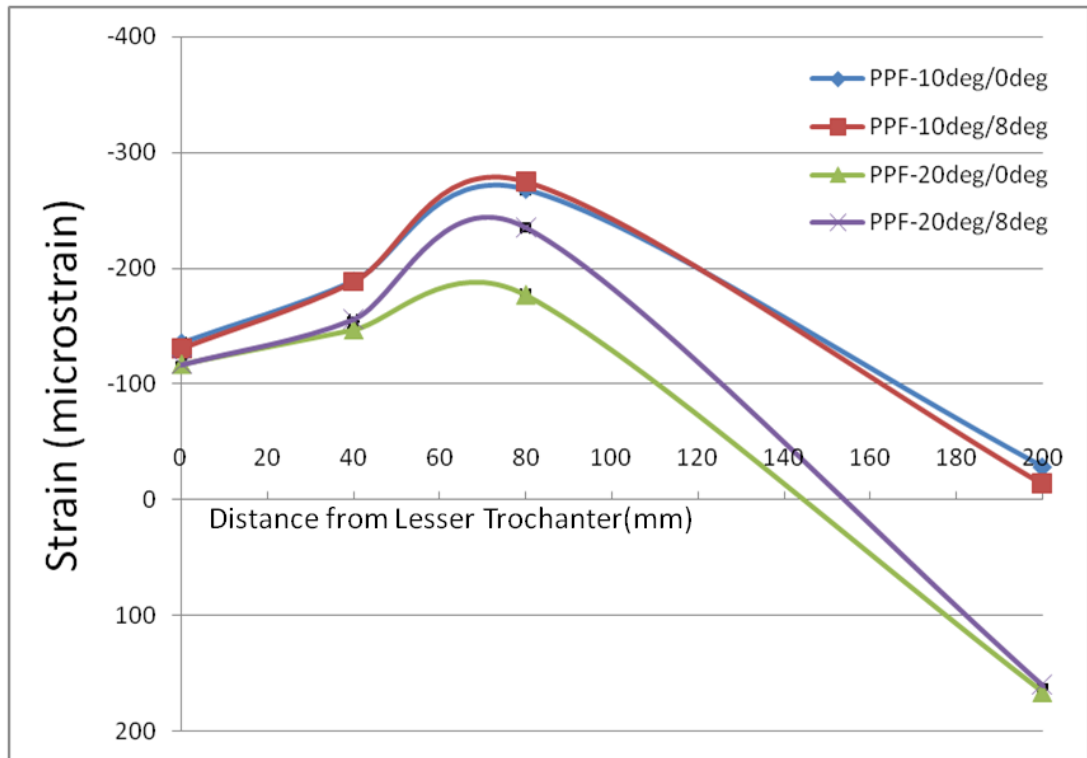
Figure 46 Strain along the length of the Femur on the medial side, for the Plate specimens at 10° and 20°, with 0 and without torsion.
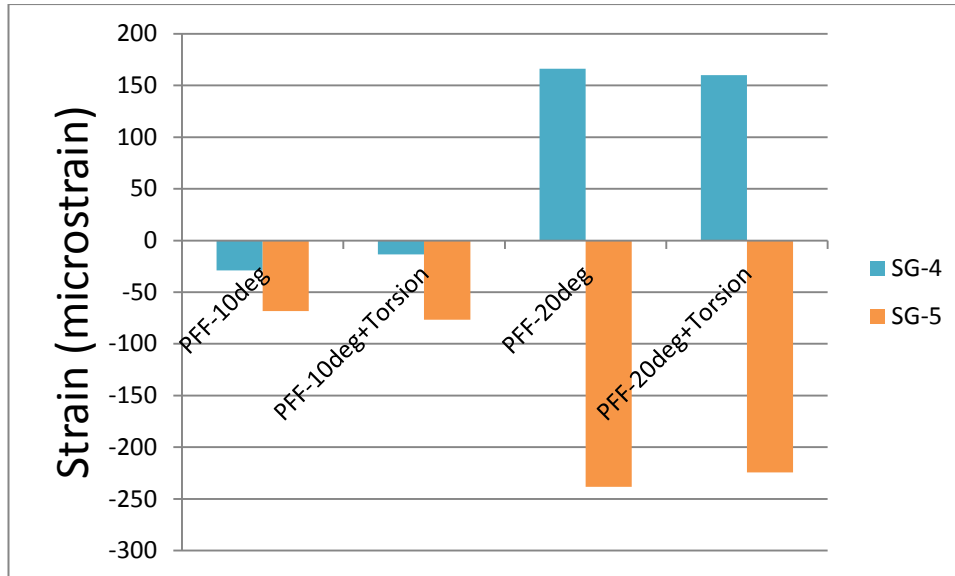
Figure 47 Strain at gauge locations 4 & 5, for the Plate cases at 10° and 20° loading angle, with and without torsion.

3.7.5 Torsion Summary

This section compared the results of loading the specimens both with and without additional torsional loading. The addition of torsional loading did not result in significant changes on either the total hip replacement specimens or the periprosthetic fracture fixation specimen mechanical behaviour, when compared to the baseline conventional loading results.

3.8 The effect of fracture gap size on the PPF specimens.

The aim of this section of the study was to determine and quantify the effect of introducing a fracture gap to the plated specimens. Previous studies in the literature have introduced a fracture gap to represent an unstable fracture. A single sample was adapted by widening the existing, perfectly reduced fracture, to a fracture with a 10 mm gap between bone fragments. An equal amount of bone was removed from each fragment, so that the centre of the fixation plate was bridging the middle of the fracture gap.

3.8.1 Stiffness of Plate specimen with a fracture gap

The overall stiffness of the plated sample with a fracture gap was much lower than the samples without a gap Figure 48. The introduction of a fracture gap reduced the overall stiffness to a quarter of the pre-fracture gap

stiffness. The addition of torsional loading affected the results very little even with the addition of the gap at the fracture site.
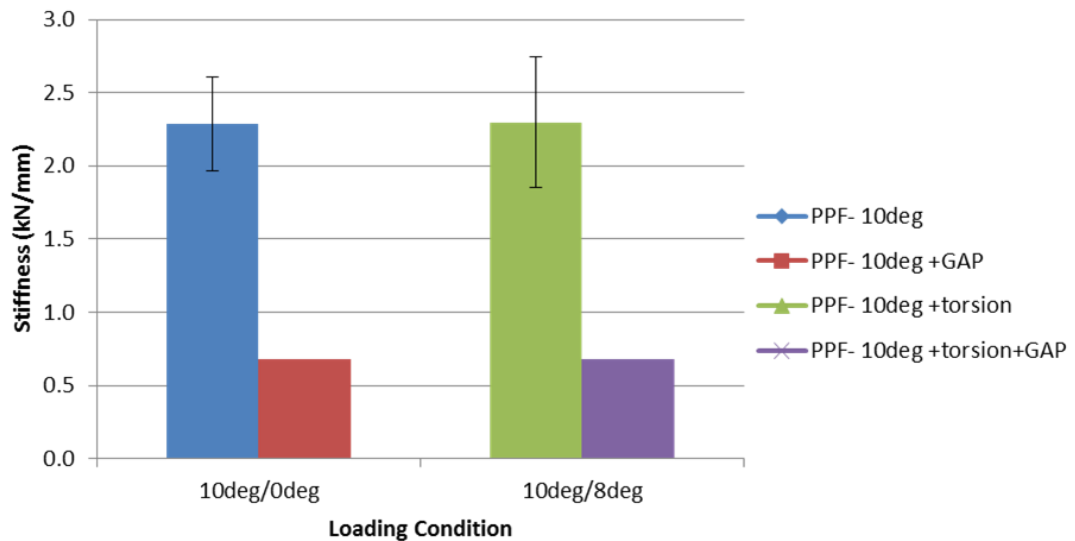
Figure 48 Stiffness of the plate specimens with and without a fracture gap at 10 °loading angle, with and without torsion. The error bars show the standard deviation for each method, calculated over the six loading repeats.

3.8.2 Strain on PPF specimen with a fracture gap

Following the introduction of a fracture gap, the strain pattern observed in the proximal, medial region of the Femur changes markedly, Figure 49. In previous tests on the plate samples, a strain peak was observed at the strain gauge located proximal the fracture gap. The magnitude of the strain at this gauge was usually higher than the strain at the most proximal gauge. In the sample with a fracture gap, the peak strain occurs at the most proximal gauge, while the strain at the gauge above the fracture gap is much lower than the proximal gauge strain.

There were large differences in the lateral and medial, distal strains with and without a fracture gap, Figure 50. The medial gauge was in slight compression without a fracture gap, and in large tension when the gap was introduced. The strain at the lateral gauge greatly increased with the introduction of the fracture gap. With the introduction of the fracture gap, there was a corresponding increase in strains recorded on the plate at all gauge locations. The largest difference was seen at the most proximal gauge on the plate, while the lowest increase was at the distal gauge.

The strain along the length of the plate on the medial side, for the plate specimens with and without a fracture gap, with and without torsion, is

shown in Figure 51. There were large changes in plate strain with the introduction of the fracture gap. While all gauges on the plate remained in tension, the strain magnitudes were much higher, with the largest increase in strain occurring at the most proximal located gauge on the plate, gauge 6.
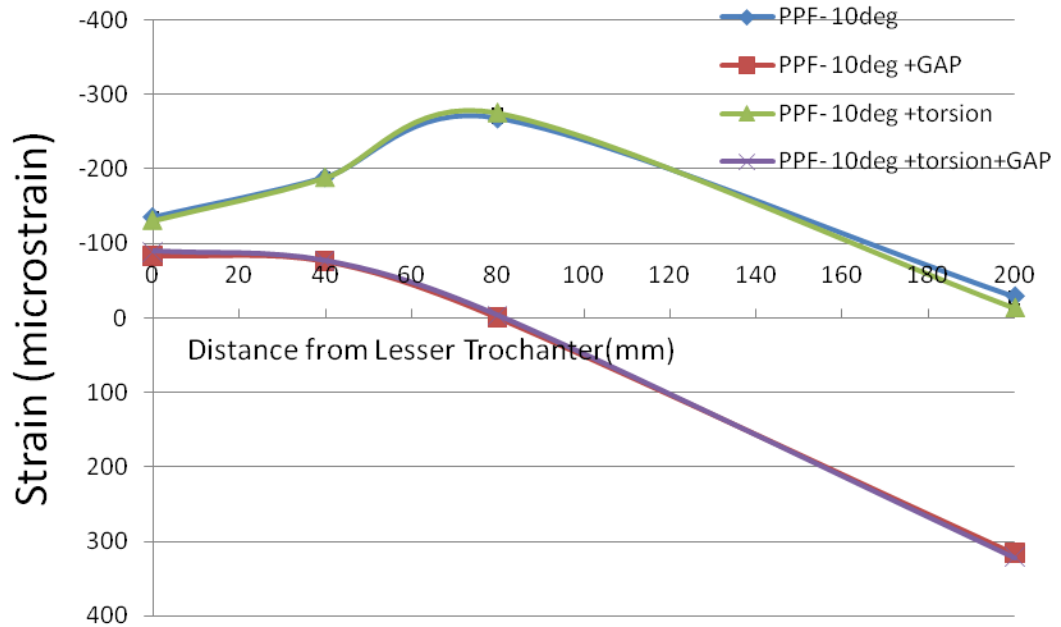
Figure 49 Strain along the length of the Femur on the medial side, for the plate specimens with and without a fracture gap, at the 10° loading angle. The results of torsional and conventional loading are both presented.
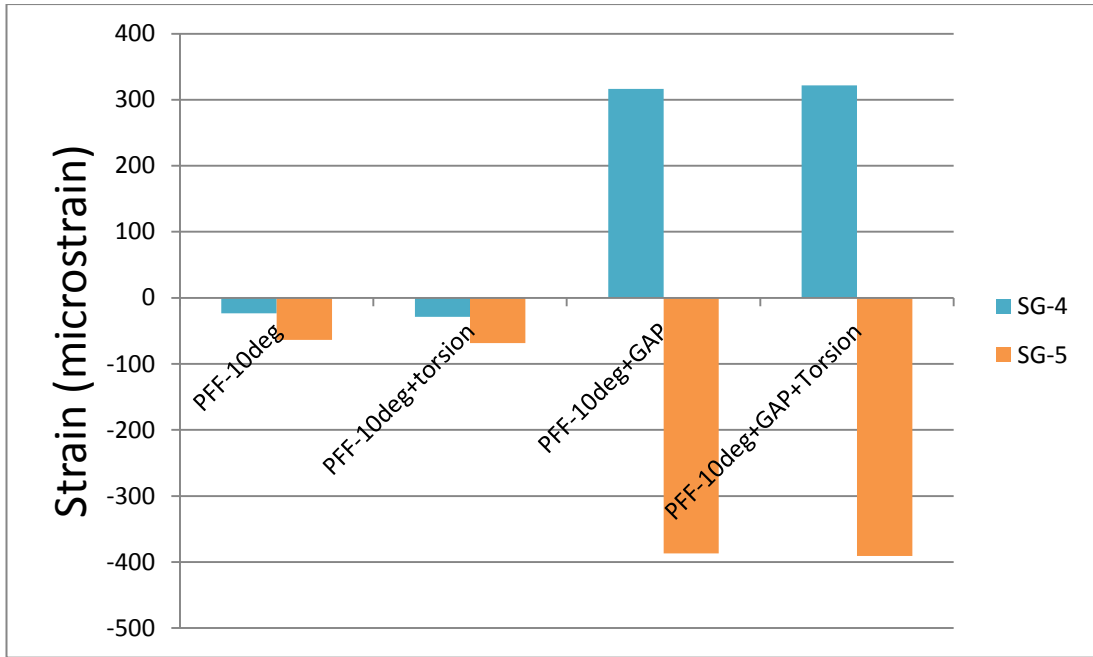
Figure 50 Strain at gauge locations 4 & 5, for the plate cases with and without a fracture gap, at 10° loading angle, with and without torsion.
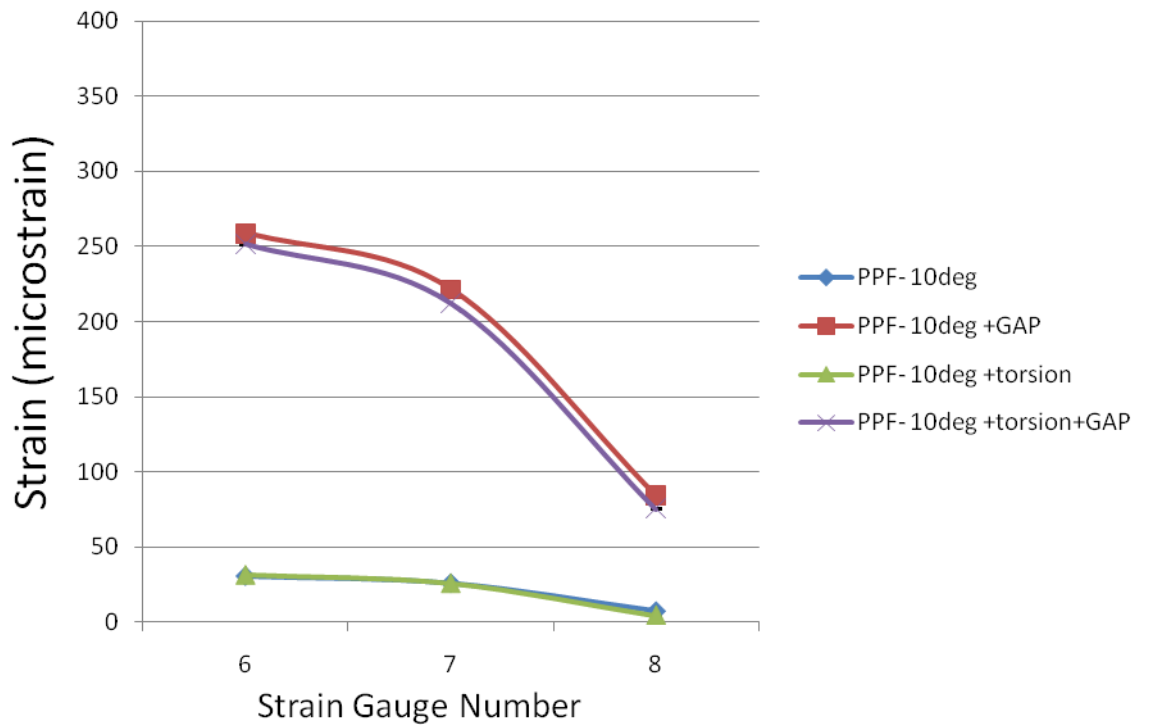
Figure 51 Strain along the length of the plate, for the plate specimens with and without a fracture gap at 10° loading angle, with and without torsion.

3.9 Discussion
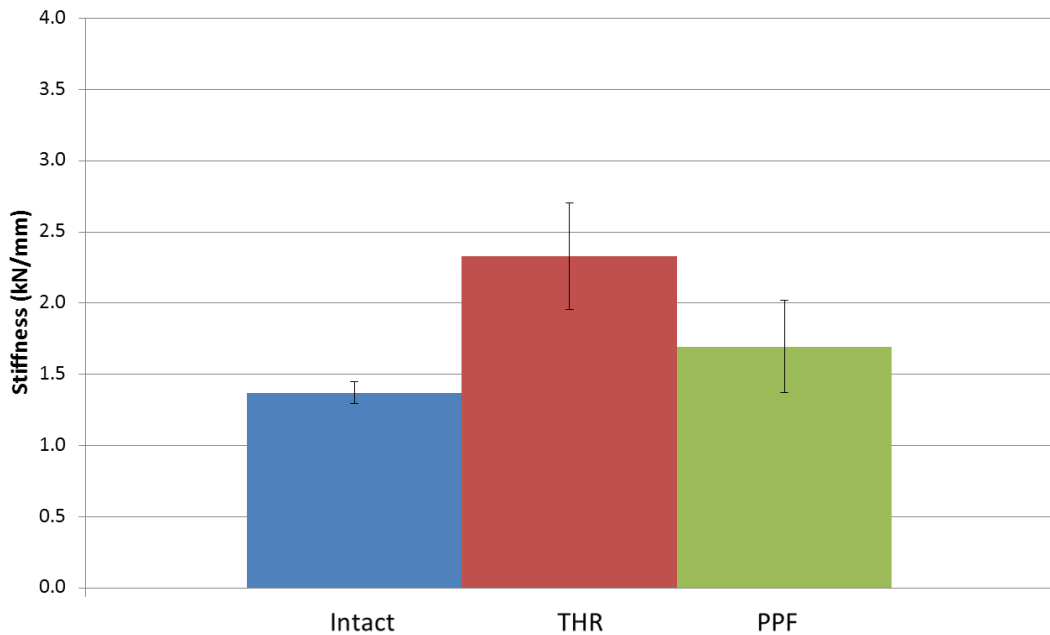
**Figure 52 Overall stiffness of the Intact, THR and PFF cases at the 0°
loading angle. The error bars show the standard deviation for each
method, calculated over the six loading repeats.**

The fixation technique used to stabilise the fractured specimens performed
well and ensured that none of the plated specimens failed during testing.
The range of loading angles was wide enough to cause a large difference in
construct stiffness between the 0°, anatomic 10° and the 20° loading cases.
The stiffness standard deviation across the group of plated specimens was
higher than any of the previous tests. As fracture fixation was the final stage
of specimen testing, with all of the specimen preparation and instrumentation
added to the Femurs, the specimens had the largest inherent susceptibility
to variations over the test group. However, there were also some
experimental issues which could be the cause of the differences.

While every step was taken to ensure perfect fracture reduction, the complex
shape of the Femurs made securing the two bone fragments during plate
fixation very difficult. As a result, the resultant plate stabilised fracture
reduction was not always perfect. As the clinical, plate fixation process was
followed as faithfully as possible, during screw hole preparation, the drill
guides and surgical drill bits were used to create pilot holes in the synthetic
Sawbone. The combination of very tight tolerances, high speed drill and the
large surface area between the drill bit and guide resulted in high
temperatures in the region of the bone surface and medial plate surface.
This caused some of the loose material produced by the drilling to melt and

clog up the pilot holes and also the threads on locking inserts. While the majority was removed, this did impede screw insertion.

The change in the loading rig setup to attempt to introduce additional torsional loading to the samples, in a more anatomically representative method that used in previous studies, section 1.6.7. The torsional loading set up did not result in a measurable difference in either overall construct stiffness or strain for both the THR or PPF case specimens. It is likely that the 8° loading change was not large enough to result in a significant change in behaviour, and that by increasing this angle, differences in behaviour could be identified.

The creation of a large fracture gap between the two bone fragments had a very large effect on construct stiffness. With the load being transmitted solely through the fixation plate, very large strain magnitude were observed on the fixation plate, while the strain pattern measured along the medial length of the bone was changed completely with respect to the perfectly reduced fracture results and also the THR and Intact Femur results.

The standard deviation for the overall construct stiffness loading repeats was much higher for the instrumented specimens than was seen for the same specimens at the intact Femur case. The accuracy of the specimen preparation for stem implantation, manual positioning of the prosthesis and stabilisation instrumentation, was dependent on the quality delivered by the surgeon performing the techniques. This human error factor could contribute to the observed stiffness variability.

3.10 Summary

A group of femoral Sawbone specimens were prepared and loaded in a bespoke loading rig. The specimens were tested in an Intact Femur, THR and stabilised PFF cases. Large differences in behaviour were identified between the investigated cases. The loading angle of the applied load on the tested specimen was found to have a large effect on both overall construct stiffness and strain patterns. The additional torsional load was not found to have an effect on construct behaviour in our experiments.

Chapter 4 **Computational Model development**

4.1 Computational Methods

4.1.1 Introduction

This chapter details the development of the computational methods used to create a computational model of the stabilised periprosthetic fracture construct, tested in the experimental section of this study, section 3.5. This section details the techniques and practices used to create the computational model, describing the assembly of the construct geometry and application of loads and boundary conditions. Both the methodology and results for each stage of model development are presented in this chapter, with the results from preceding stages of model development used to demonstrate the reasoning behind subsequent development steps.

The finite element method is a numerical technique used to find the response of physical systems to defined boundary conditions and simulated applied loads. Advances in finite element software and increased availability of high performance computing as resulted in the method being employed in increasingly complex situations, such as biomechanical simulations. As the knowledge in the literature of parameters such as bone material and bone to cement interaction properties have increased, the level of confidence of the results from these simulations have increases accordingly as they are very dependent on the accuracy of these input parameters. However, it is still necessary to compare any developed computational model to appropriate experimental validation comparisons and parameter sensitivity studies, to properly understand and determine the level of confidence in these models[89].

4.1.2 Software and Computational requirements

The computational models were assembled using computer aided design (CAD) software (Solidworks 2011 SP04, Dassault Systèmes, USA). The model was imported to the finite element software package ABAQUS (6.11-1,Dassault Systèmes Simula Corp., Providence, RI, USA) for solution processing. Finite element analysis was initially performed on a desktop PC, but as the complexity of the models increased, the use of high performance computing was required with all of the models including fracture fixation being run on the university supercomputer. Due to the computational requirements of the models, with over 1.9 million nodes used mesh the construct geometry, 10 computing cores and 80GB of RAM were required to solve the models, with a run time for the PFF models of 37 hours. Data

processing and analysis was performed using a spread sheet package (Microsoft Office Excel 2007 SP01). An example of the script used to submit models to the supercomputer can be found in Appendix C.

4.1.3 Work flow chart

Work Flow- Computational Model Development	Import femur geometry
	Distal Fixation
Section 2	Intact femur- model
	Intact femur Sensitivity studies
	Femoral neck dissection
	Replicate reamed femur region
	Import and position stem
	Create Cement Mantle
Section 4	THR- model
	THR Sensitivity studies
	Periprosthetic Fracture Creation
	Import Stabilisation instrumentation
	Orientation of instrumentation
Section 6	PPF- model
	PPF Sensitivity Studies
	Baseline Model

Figure 53 Work flow for computational model development

4.1.4 Assembly of intact Femur model

This section reports the replication of the geometry of the Sawbone Femur specimens used in the experiments, as well as the reproduction of their pre-testing preparation and fixation within the loading rig.

A 3-D solid model of the 4th generation synthetic Femur was obtained from Biomed Town (BEL repository). The model's geometry matched that of the large sized Femur used in the experiments and was imported into Solidworks in a STEP format. The orientation of the model and location of the origin of the coordinate system, located on the femoral neck, were retained from the original file and are shown in Figure 54.
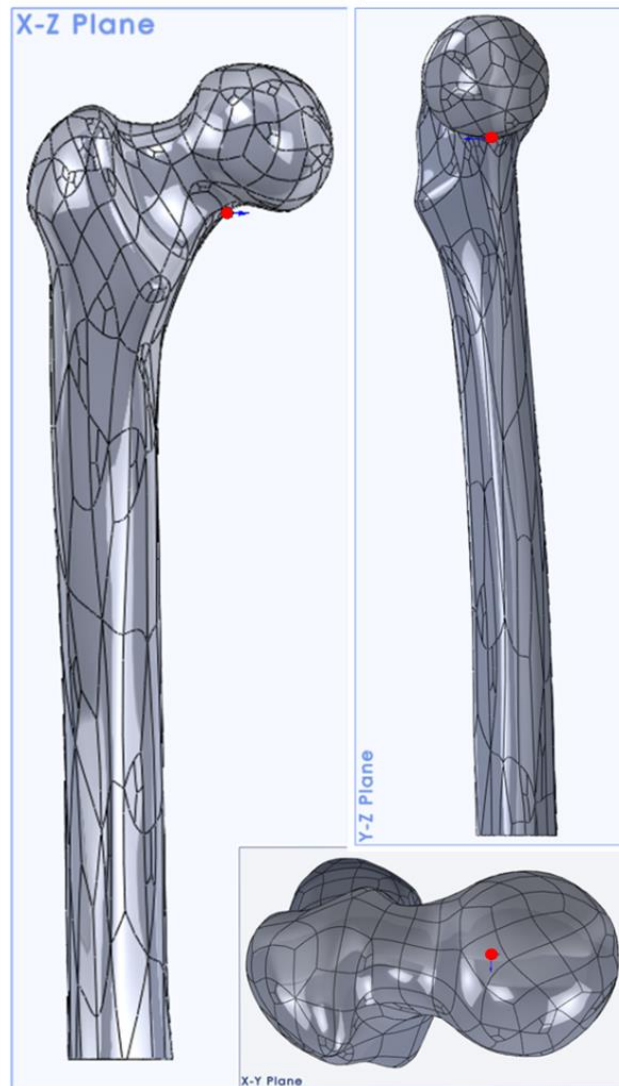
Figure 54 The reference planes used throughout the model development and application, and coordinate origin shown as the red dot

To replicate the experimental preparation of the specimens for distal fixation in the loading modules, the distal end the Femur was transversely dissected at a level 340 mm from the Lesser trochanter, with all of the femoral bone distal to this level being removed from the model. The reference plane used to guide the dissection (X-Y Plane) was perpendicular to the long axis of the Femur.

To replicate the distal fixation of the Femur within the experimental rig, the loading module was added. The CAD model used to manufacture the loading modules was imported into the Sawbone model. Using the surface mate function, the distally dissected Femur surface was selected and brought into contact with the bottom of the loading module cup. Using the long axis of the module and the Y axis of the Femur as a guide, the module

was aligned such that the Femur was sited centrally within the module cup. These positional adjustments were small as the diameter of the Femur at the level of dissection was only slightly lower than the inner diameter of the module cup. Four grub screws (5 mm diameter) were then positioned in their prepared holes on the module, until the heads of the screws were flush with the outer surface of the module.

4.1.5 Cement Fixation

The model of the fixation cement used between the Femur and loading module was made by creating a 50 mm diameter by 80 mm height cylinder, which matched the internal dimensions of the loading module cup. Using the Solidworks mate function, the cylinder was positioned centrally within the loading module, with the exposed cement surface flush with the top of the module. The geometries of the both the Femur and all four grub screws were copied and replicated in their existing positions. Using the cement cylinder as the main body, the combine feature was used to subtract the copied Femur and screw geometries from the cement, shown in Figure 55.
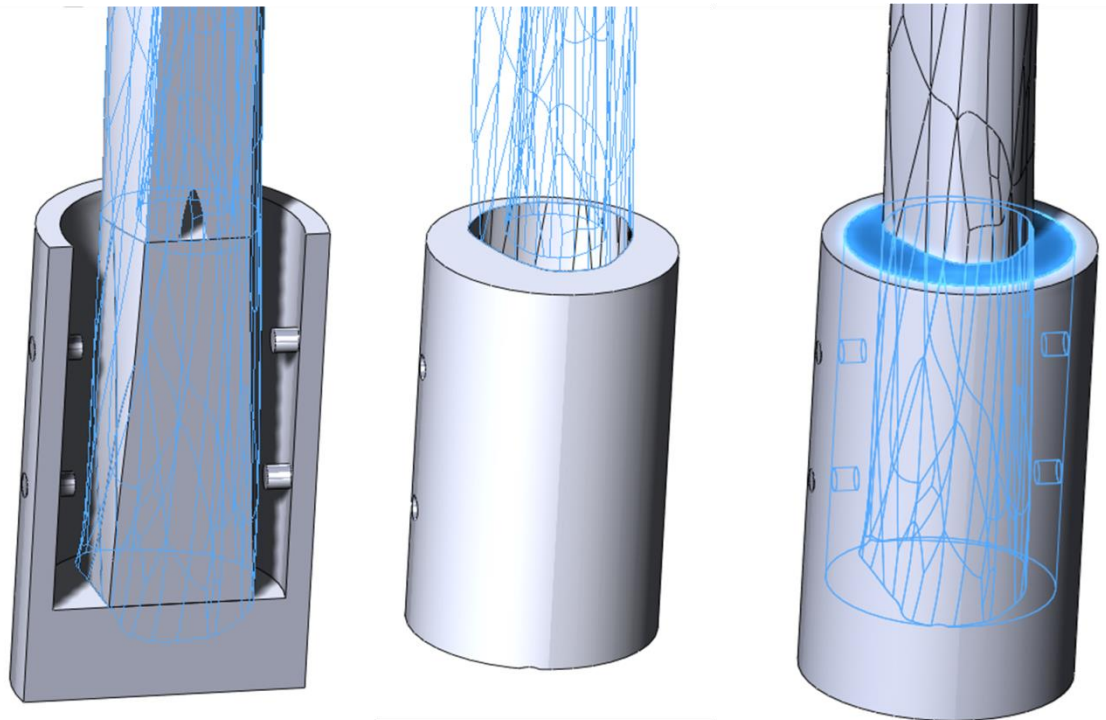
Figure 55 The process of module fixation cement with the distal Femur position within the module, the cement geometry creation, and the final construct.

4.1.6 Introduction of the cemented total hip replacement

To prepare the proximal femoral region for prosthesis insertion, the femoral neck was dissected at a 45° angle to the X-Y plane, and the femoral head and neck were removed, Figure 56. A cemented primary stem prosthesis (Exeter V40, size N°0, offset 37.5, Stryker SA, Switzerland) was added to the model using CAD files provided by Stryker. Using X-ray images of the experimental specimens, taken in both the X-Z and Y-Z planes, the computational stems were then positioned to match the experimental stem placement. In addition, the level of the prosthesis shoulder was used with respect to the level of the greater Trochanter to double check the stem placement. A 28 mm diameter femoral head (Stryker, NJ, USA) was positioned on the neck of the prosthesis stem.

To aid the creation of a representative cement mantle, an additional experimental femoral specimen was used. The proximal region of this specimen was dissected and reamed to the same standard as the other specimens, without stem and cement insertion being performed. CT images of this reamed specimen were then used to define the external geometry of the cement mantle. The geometry of the prosthesis stem was then copied, and defining the cement as the main body, the Solidworks combine feature was used to subtract the copied stem, leaving the geometry of the cement mantle, Figure 56.
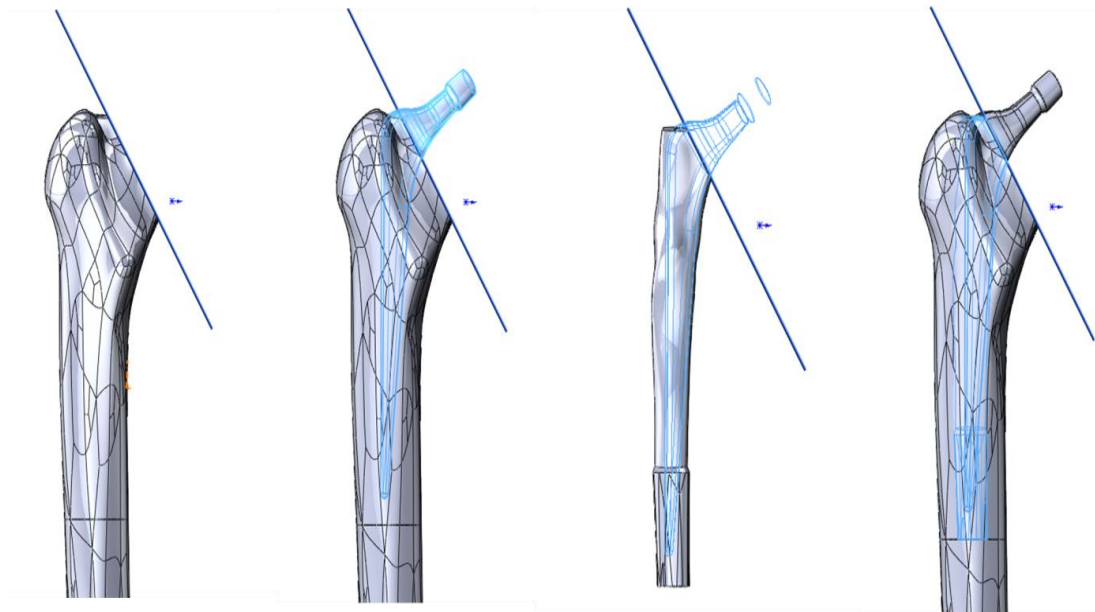
Figure 56 specimen preparation, prosthesis stem positioning, and development of the cement mantle for the computational models.

4.1.7 Periprosthetic Fracture creation and stabilisation

To create the fracture, a plane in the X-Y direction was defined 10mm distal to the tip of the prosthesis stem. Using this plane as a reference, the fracture was then created using the split feature, dividing the cortical bone into two bodies. Matching the experimental specimens, an eight hole locking plate (length: 155 mm; width: 17.5mm; thickness: 5mm, Stryker, NJ, USA) was used to stabilise the fracture with three unicortical screws used in the proximal three screw holes, and three bicortical screws in the three distal screw holes. The plate and screws, from CAD files provided by Stryker, were assembled and initially positioned, with the centre of the plate bridging the fracture. Using the X-rays of the experimental specimens, the positioning of the plate was then adjusted until the experimental plate position was replicated, Figure 57. The plate position was matched with the strain gauged specimen (S07). The position of the locking plate was not perfectly vertical in the Z direction. Care was taken to match the gap between the plate and bone surface at all locations along the length of the plate. To create screw holes in the cortical bone, the geometries of all the screws were copied, and using the combine feature, were subtracted from the cortical bone geometry.
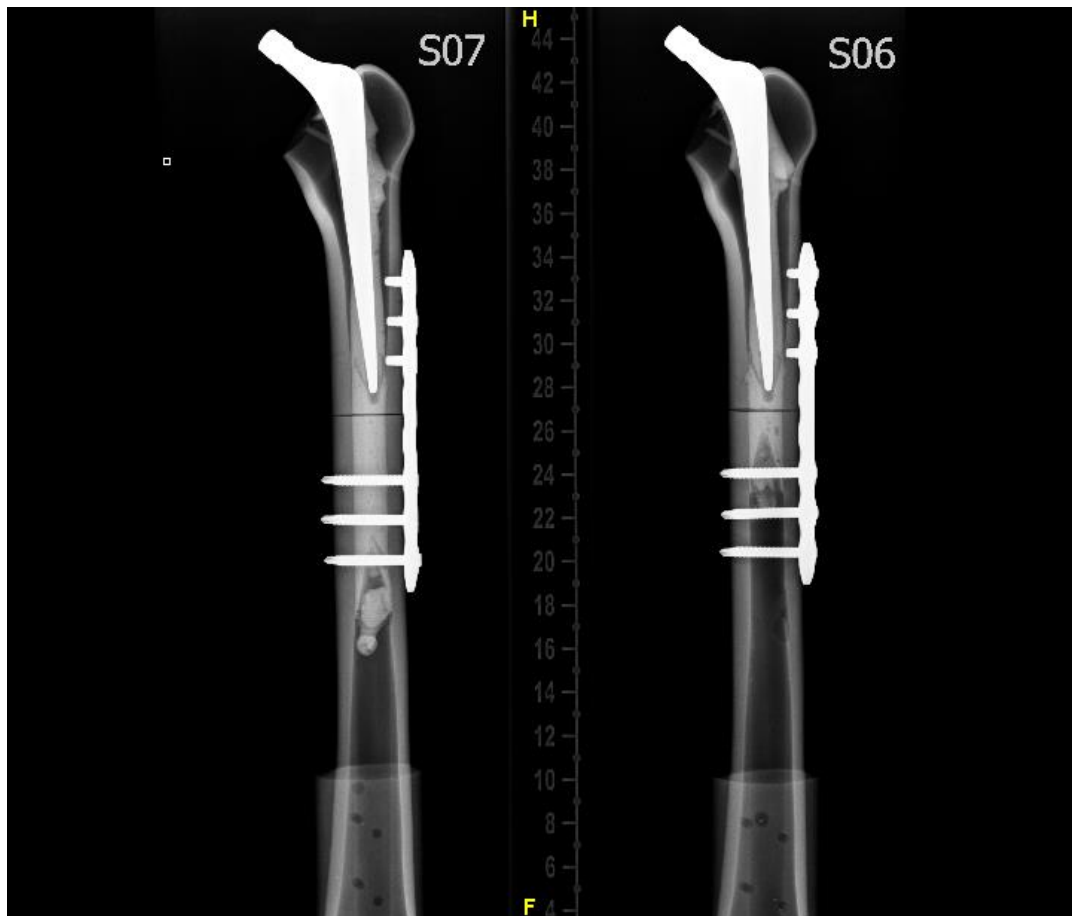
Figure 57 X-rays of both specimens S07 and S06 taken in the Anterior-Posterior plane.

4.1.8 Boundary conditions, mesh and material properties

To replicate the fixation of the loading module within the angle adjuster, encastre boundary conditions were applied to all the external surfaces of the module, except the top surface.

To replicate the experimental loading, a coordinate system was defined with respect to the chosen angle of the load. The load angle was defined in the X-Y plane and if necessary, rotated around the original Y axis of the model. The Y axis of the new system was defined in the direction of the applied load. Using the coordinate system, a datum point was defined on the surface of the femoral head. A 500N point load was applied to the datum point on the prosthesis head, using the defined coordinate system. With the use of the assembly display options, a datum point was created at the centre of the femoral head. Due to the design of the prosthesis, this datum point was located in the stem component. This datum point was then constrained, using the defined coordinate system, to only allow displacement in the direction of the applied load.

Homogenous isotropic material properties were assigned to the cortical shell (E=16.7GPa[90]), cancellous bone (E=0.155GPa[90]), cement mantle (E=2.45GPa, [24, 91]), bone screws and the locking plate (E=200GPa, stainless steel[69, 90]). Over 750,000 quadratic, tetrahedral elements (C3D10M) with over 1.9 million nodes were used to mesh the model. Mesh refinement was performed around the tip of the prosthesis stem, at the strain gauge locations, and a mesh convergence study was also completed, section 4.2.6.

Surfaces in contact within the model were either defined as hard contacts and used a penalty friction formulation for normal and tangential behaviour respectively, or were constrained as tied contacts. The surface interactions and their chosen contact condition are shown in Table 8. For the surfaces in contact, a finite sliding formulation and the surface to surface discretization method were used. Slave adjustment was used to remove overclosure only.

Table 8 The surface interactions and their respective contact condition

Interaction	Contact condition	
	Tangential Behavior	**Normal Behavior**
Stem - Cement Mantle	Penalty Friction Formulation, Coeff 0.3	"Hard" Contact
Plate - Cortical Bone	Penalty Friction Formulation, Coeff 0.3	"Hard" Contact
Cortical Bone - Cortical Bone	Penalty Friction Formulation, Coeff 0.3	"Hard" Contact
Potting Cement - Module	Penalty Friction Formulation, Coeff 0.3	"Hard" Contact
Cortical Bone - Module	Penalty Friction Formulation, Coeff 0.3	"Hard" Contact
Femoral Head – Stem	Tied	
Cement Mantle – Cortical Bone	Tied	
Cement Mantle – Cancellous Bone	Tied	
Cancellous Bone – Cortical Bone	Tied	
Grub Screw – Potting Cement	Tied	
Screw – Loading Module	Tied	
Screw – Cortical Bone	Tied	
Screw – Locking Plate	Tied	
Potting Cement – Cortical Bone	Tied	

4.1.9 Outputs

4.1.9.1 Calculation of Construct Stiffness

To calculate the construct stiffness from the models, the coordinate system used to apply the load was applied to the results. The field output was changed to show displacement in the Y axis direction. The displacement of the node at the constrained datum point at the centre of the femoral head was then probed. The stiffness of the specimens was calculated by dividing the load, 500N, by the probed displacement value.

4.1.9.2 Calculation of strain

Surface strain was calculated at five locations on the bone and three on the locking plate. The bone strain gauge locations were identified with respect to their distance from the Lesser Trochanter.

Due to the varying orientation of the bone surfaces at the different gauge sites, additional coordinate systems were created to ensure that the strain readings were measured in the correct direction with respect to the surface orientation. This was done to ensure replication of the surface strain that the experimental strain gauges would record. The field output was changed to show elastic EE strain in the X axis direction. The bone strain gauges were sited 0, 40, 80 and 200 mm distal to the Lesser trochanter along the medial length of the Femur model. The fifth bone gauge was positioned 200 mm from the Lesser Trochanter on the lateral side. Three gauges were positioned between the empty screw holes bridging the fracture on the locking plate, when testing periprosthetic fracture fixation cases. These gauges were positioned in the middle of the plate width, between screw holes 3 and 4, 4 and 5 , and 5 and 6, i.e. the empty screw holes bridging the fracture. Once the node closest to the gauge location was identified, eight additional nodes were selected distal to the identified node's location, in a diamond pattern, Figure 58, and strain readings recorded for all nine nodes. This was done to measure strain across the entire strain gauge area and not solely at a single point on the strain gauge. An average of the strain across the nine recorded nodes was calculated in order to most accurately replicate the experimental measurement. Where possible, the strain readings were taken from the same nodes between different model versions where the plate or the cortical bone had the same mesh, e.g. where different material properties where investigated.
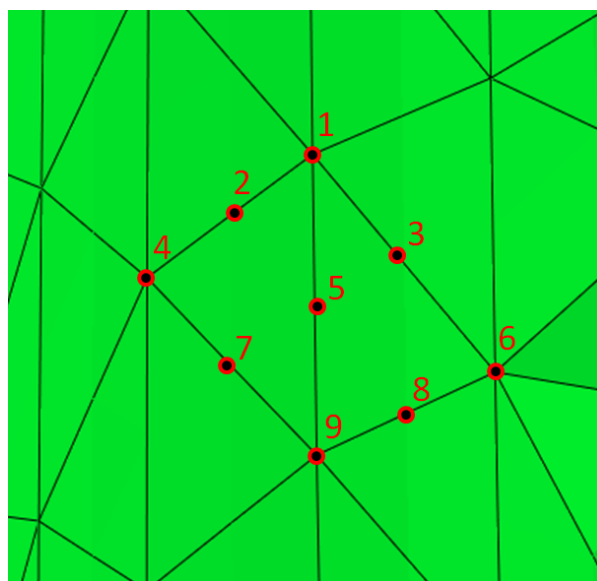
Figure 58 An example of the nine nodes selected when calculating strain at a gauge location

4.2 Model Development and Sensitivity Studies

4.2.1 Introduction

This section details the development stages and sensitivity studies of the computational model. Our approach was to try to include enough of the experimental features into the computational models to replicate the experimental behaviour. As such, the initial development of the computational model was fairly basic, introducing and evaluating extra levels of detail into the model and its input parameters, throughout the complete development. At each development stage, calibration of the model to the experimental results was avoided, meaning that the model inputs were never adjusted until the computational outputs matched the experimentally measured ones. In some cases where was a point of interest or unexpected result, additional measures were used to see what effect had occurred. In order to maintain consistent reporting throughout the study, we have compared the key indicators which can be benchmarked against experimental data.

4.2.2 Intact Femur

At the first stage of model development, the model was tested as the intact Femur geometry. Due to the size of the natural femoral head and the potential difficulty in replicating the acetabular cup in the experimental tests, load was applied to the femoral head using a flat loading plate. As the intention was to load the prosthesis heads through a loading cup at the total hip replacement development stage, constraining head displacement in the X and Y axis but allowing all rotations, two different methods for loading the intact Femurs were applied to the models. These included a point load positioned on the most proximal point on the intact Femur, applied in the direction of the load, in this case at the 0° loading angle, and secondly a rigid flat plate constrained to only displace in the Z axis. A hard contact was defined between the loading plate and natural femoral head, and the load was applied to the superior rigid plate surface. The experimental results used to compare against the intact Femur computational model results were presented in Section 3.2.

4.2.2.1 Intact Femur Stiffness

The results of the computational intact Femur models, for both loading methods, are shown in Table 9. The intact Femur stiffness from the point load model was closer to the experimentally measured stiffness value than the rigid plate models. There was a 5% difference in stiffness between our experimental results and the point load computational model, and a 52% stiffness difference between the experimental results and the rigid plate

computational model. There was a 55% difference in stiffness between the two computational methods of applying the load.

Table 9 Overall stiffness for the intact Femur model, for both loading methods, at the 0 degree loading angle.

Test Description	Overall Stiffness (kN/mm)	STDEV
Computational- Point Load at 0deg	1.30	-
Computational- Rigid plate at 0deg	2.89	-
Experimental- 0deg	1.37	0.77

4.2.3 Intact Femur Strain

The strain distribution pattern, from the proximal to distal gauge positions along the medial side of the Femur, is shown in Figure 59. There is a clear difference in strain pattern between the point load and the rigid plate models. In the point load model, the strain at gauge 1 is significantly lower than at the other gauges. The average strain across gauges 2 to 5 is 470με, with the highest strain occurring at gauge 4. The strain pattern across the rigid plate model has low strain values of 204με and 219με at gauges 1 and gauge 5 respectively. There is a slight strain decrease across gauges 2 to 4 with a peak strain at gauge 2 of 332με.

The strain pattern from the rigid plate model closely resembles the experimental strain patterns. They show a gradual decrease in strain from gauge position 2 to 5 with the lowest strain occurring at gauge 1.
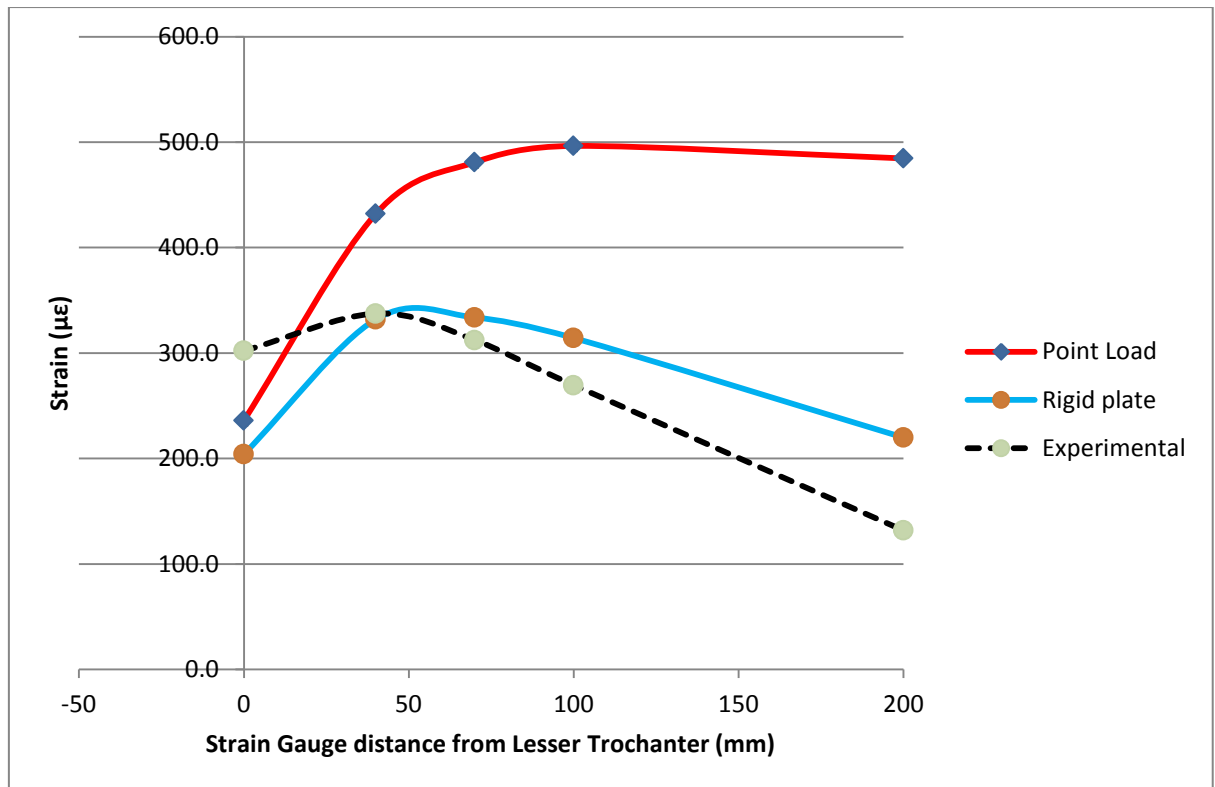
Figure 59 Medial bone strain for both the point load and rigid plate numerical models and experimental strain data, at the 0degree loading angle.

4.2.3.1 Summary

This section presented the results of the intact Femur model, loaded using both a point load and rigid plate. The two methods clearly loaded the intact Femur very differently, as shown by the overall stiffness and medial bone strain patterns. The applying the load through a single point resulted in an overall stiffness similar to the experimentally measured stiffness, however, the strain distribution pattern along the medial length of the Femur was very different from the experimental results. While the model loaded using a rigid plate overestimated the overall stiffness of the intact Femur, the medial strain pattern matched the experimental results.

As the strain pattern using the point load method was very different from the experimental results, this indicates that the good overall stiffness match to the experimental results is likely to be a coincidence. The strain pattern match, in addition to the similarity in medial strain magnitudes for the rigid plate model, suggests that this loading method is replicating the loading pattern of the experimental tests.

The overestimation of the intact Femur stiffness might be due to the boundary conditions used to constrain the model. In the experimental tests,

the Sawbone Femur extends 80 mm distal to the computational dissection level, where it is supported by potting cement and sited within a supporting rig constructed of multiple, adjustable components. The potential micro movement between all of the experimental components is compared against encastre boundary conditions applied to the dissected femoral end. As there is an increase in stiffness as the loading conditions are varied, is it possible that the contact surface between the head and the plate is also contributing to this effect. The overestimation of specimen stiffness will be considered throughout the subsequent model development stages, and alterative distal fixation methods will be investigated.

4.2.4 Total hip replacement

4.2.4.1 Introduction

This section will present the adaptation of the basic intact Femur model with the introduction of a cemented total hip prosthesis. The experimental results used to compare against the total hip replacement model results were presented in Section 3.4.

This section includes general, good practice computational modelling tests to ensure the outputs from the model are robust, such as mesh refinement. In addition, specific tests to determine the effect of variables were also conducted, such as the method for applying the proximal load on the femoral head.

4.2.5 Element type

This section presents the results of investigating different orders of magnitude for the finite element basis functions within the basic THR model. All of the investigated element types were tested on the same THR model case geometry. Due to problems with mesh quality while using hexagonal elements to mesh the geometry of the investigated construct, only tetrahedral elements were investigated. Three different element types were investigated; linear four noded (C3D4), quadratic 10 noded (C3D10) and modified quadratic 10 noded (C3D10M).

Linear tetrahedral elements, C3D4, are not normally recommended to be used exclusively as an extremely fine mesh may be required to produce an accurate solution. The general quadratic tetrahedral elements, C3D10, are recommended for small displacements problems, but may not perform well with contact present in the simulation. The modified quadratic tetrahedral elements, C3D10M, are suitable for problems which include large displacements and contact problems using the hard contact relationship, however, the analysis will be more computationally intensive than with the use of the other element types.

The supercomputer used to run the solution processing in this study allowed a maximum run time of 48 hours. Using the maximum processing power available, the 48 hour runtime limit was the only limiting factor. As long as simulations were within this time limit, differences between individual runtime for the different elements types would not affect the choice of element to be used in further development.

4.2.5.1 Element type stiffness

The overall stiffness for the range of investigated element types for the basic THR case is shown in Figure 60. The C3D10 elements resulted in the highest overall stiffness, while the C3D10M had the lowest overall stiffness. The overall stiffness using the C3D10M elements was closest to the experimentally recorded THR stiffness.
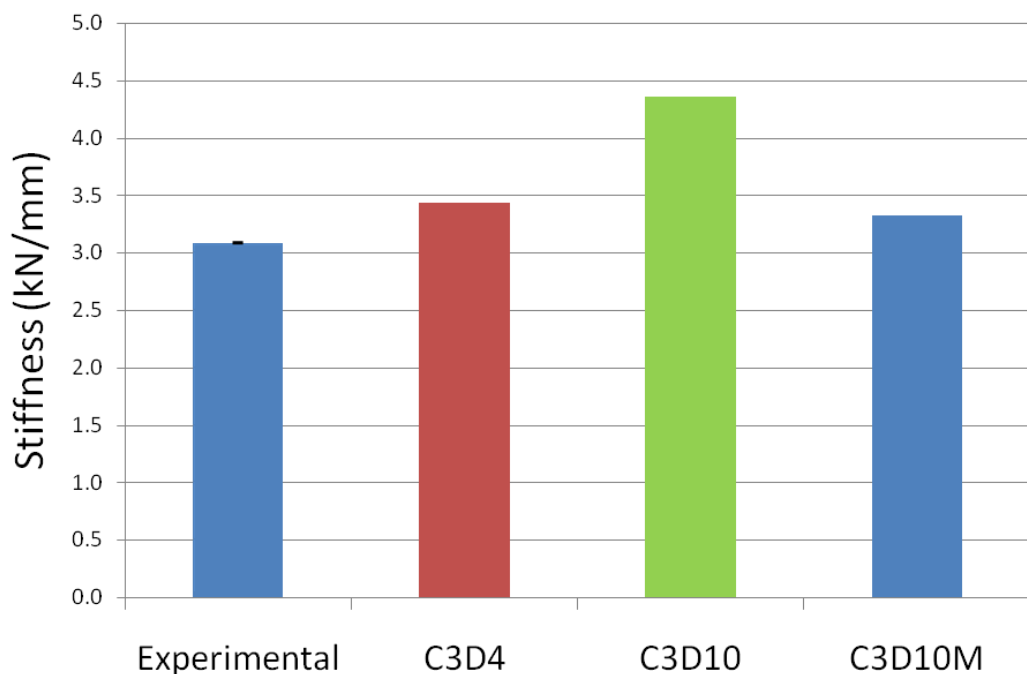
Figure 60 Overall stiffness for the range of investigated element types for the basic THR case. Error bars on the experimental data represent the standard deviation between 6 re-loading cycles of the same specimen.

4.2.5.2 Bone Strain comparison

The strain along the medial length of the Femur for the range of investigated element types, for the basic THR case, is shown in Figure 61. The medial bone strain magnitudes were highest for the C3D10 elements and lowest for the C3D4 elements. The medial strain magnitudes for all of the investigated elements types were much lower than the experimentally measured medial

strains. The strain values for the C3D10 elements were closest to the experimental strains. Changing element type did not affect the strain distribution pattern along the medial length of the Femur. The difference in strain between the different element types was small.
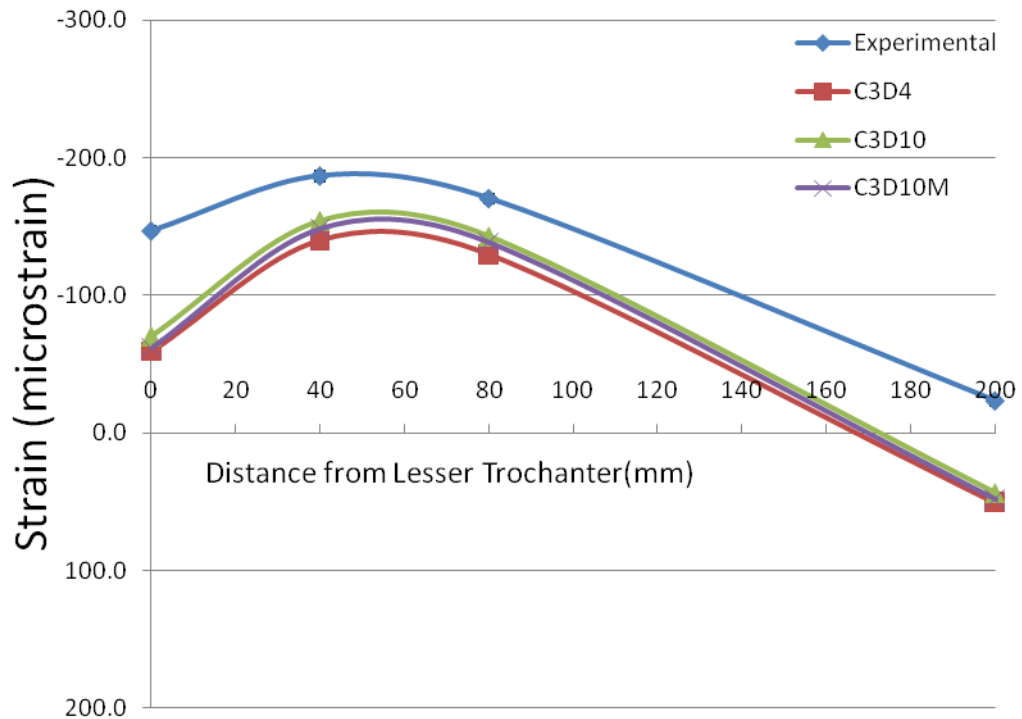
Figure 61 The strain along the medial length of the Femur for the range of investigated element types.

The strain at the distal end of the Femur, on both the medial and lateral sides for the range of investigated element types, is shown in Figure 62. Element type only had a small influence on distal bone strain. While both of the experimental distal strains were in compression, the distal strains for all of the element cases were in tension on the medial side, and in compression on the lateral side. There were only subtle differences in distal strain magnitude between the different element types.
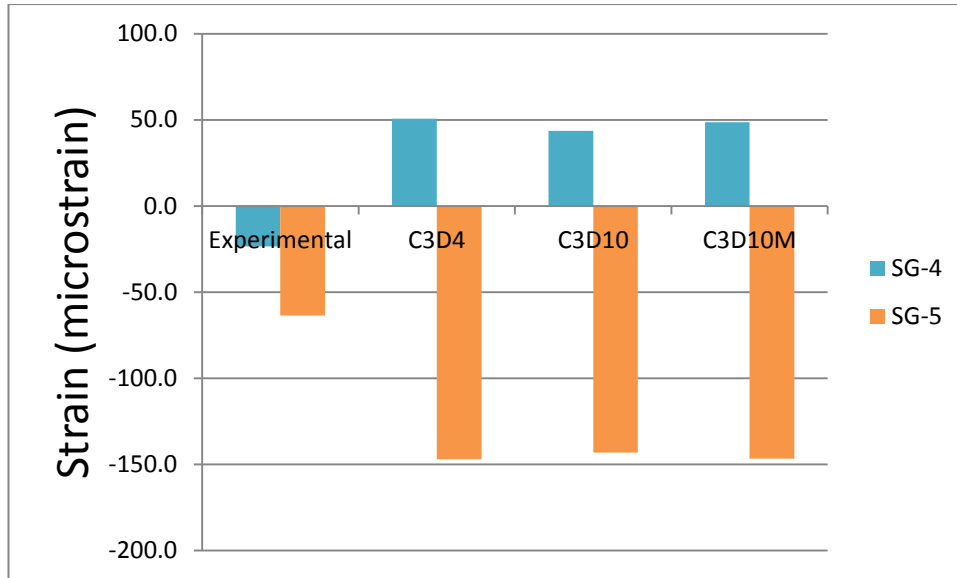
Figure 62 the strain on both the medial and lateral distal Femur for the range of investigated element types.

Table 10 Total run time of the model, using Arc1 Supercomputer

Model	Run time (Hours)
C3D4	19.5
C3D10	22
C3D10M	25

4.2.5.3 Summary

This section presented the results of a range of element types on overall total hip replacement model behaviour. Varying the type of element used to mesh the construct geometry did not have a large effect on strain distribution pattern or strain magnitude, however, element type had a large effect on overall construct stiffness. The most likely reason for the changes seen in the results is that the variation in element types are changing the behaviour of the contact surfaces in the model. As the modified elements are recommended for problems involving contact, such changes are expected. Alternatively, the effect could be influencing the higher strain area within the lower modulus cement mantle surrounding the prosthesis tip, with the effect not reflected in the metrics chosen to be reported.

All of the runtimes of the models was under the 48hour limit, with an average runtime of 25 hours, Table 10. Therefore, time limit was not considered in the evaluation of model element type.

The C3D10M elements were used in all subsequent modelling studies reported in this chapter. With the intention of developing the total hip replacement model to include the periprosthetic fracture, introducing an additional contact surface into the model predicted to have a major effect on construct biomechanics, and with the simulation completion time comfortably within the limit.

4.2.6 Mesh refinement

The aim of this section was to perform mesh sensitivity analysis for the model. The aim was to ensure enough elements were used in the models to ensure the accuracy of the solution results. The number of nodes and elements necessary for a converged solution will be defined as reached when an increase in the number of nodes results in an output metric change of less than 5%. The number of nodes and corresponding number of elements for each investigated case is presented in Table 11.

Table 11 The Number of Nodes used to mesh the THR model for each case, and the respective number of Elements

Case	Number of Nodes (Million)	Number of Elements (Million)
1	0.87	342000
2	1.0	421000
3	1.2	530000
4	1.4	590000
5	1.6	688000

4.2.6.1 Overall construct stiffness

The overall stiffness for the range of investigated mesh densities, for the basic THR case is shown in Figure 63. For the models meshed with 0.87 and 1 million nodes, the results show that the solution has not converged. For the models meshed with more than 1.2 million nodes, an increase in the number of nodes used resulted in differences in overall construct stiffness of less than 5%.
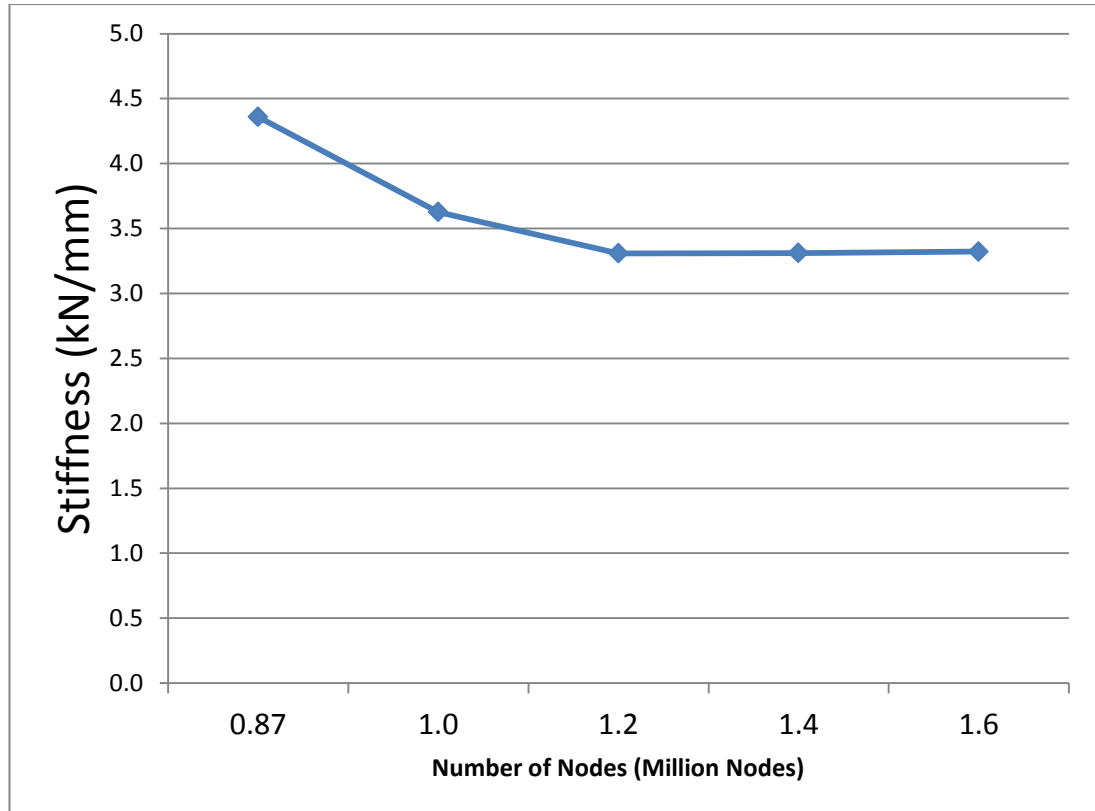
Figure 63 Overall stiffness of the THR model for a range of Mesh densities

4.2.6.2 Bone Strain comparison

The strain at each strain gauge for the range of investigated mesh densities, for the basic THR case, is shown in Figure 64. At gauge locations 2,3,4 and 5, all located at or over 40mm distal from the Lesser Trochanter, there were only minimal variations in bone strain as the number of nodes was increased. However, at strain gauge 1 located at the level of the Lesser Trochanter, there was a large change in strain between the 1.2 and 1.4 million node cases. The difference in strain between the 1.4 and 1.6 million node cases was less than 5%.
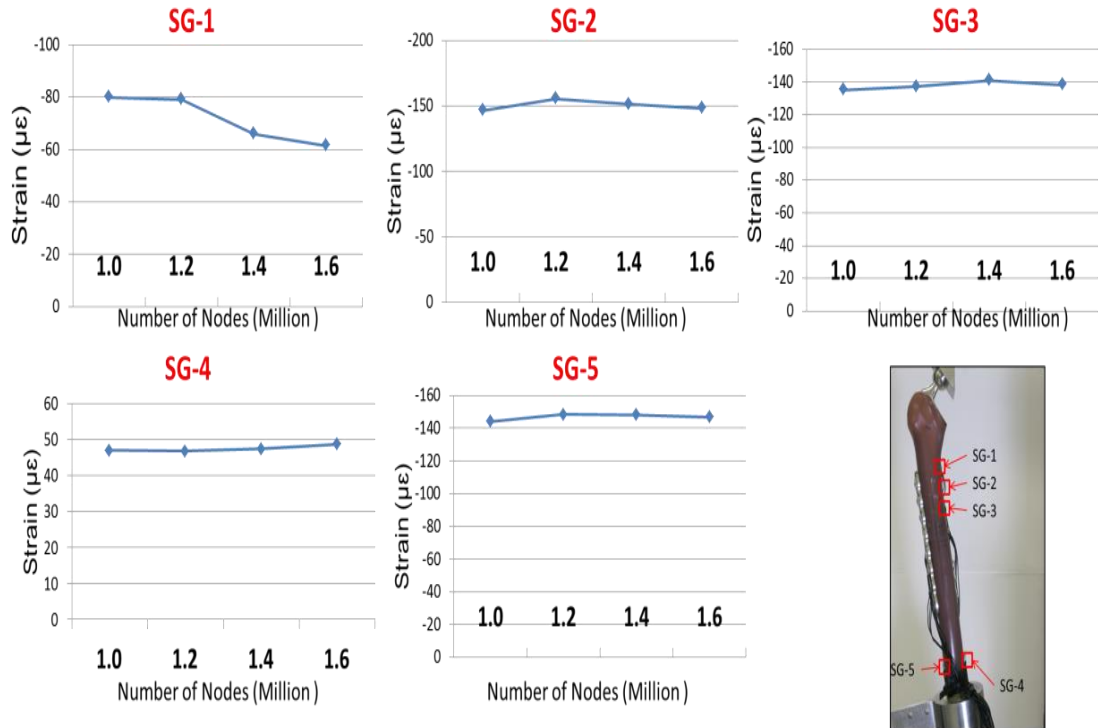
Figure 64 Strain at each strain gauge for the range of investigated mesh densities, for the basic THR case.

4.2.6.3 Summary

A converged solution was reached within the range of mesh refinement cases investigated in this section. The overall construct stiffness metric indicated that a mesh refinement of 1.2 million nodes would be sufficient to produce accurate results. The bone strain metric indicated that a mesh refinement of at least 1.4 million nodes was necessary to ensure an accurate solution. This highlighted the importance of using more than one metric to evaluate mesh refinement.

The strain at gauge 1 was sensitive to the investigated mesh densities in that region, however, at all the other gauge locations, only very small variations in strain magnitude were observed. This could be due to the mesh density affecting the contact surface interaction between the prosthesis and cement mantle, located in this region of the model. A mesh density of at least 1.4 million nodes will be used in the future sections of this study.

4.2.7 Distal Fixation

This section presents the results of the different modelling methods of securing the distal end of the Femur. The level of detail of the experimental testing rig included in the computational models was predicted to affect the construct stiffness overestimation. A range of options describing the level of detail of the experimental distal fixation, influencing the computational boundary conditions, were investigated. All of the investigated distal fixation methods were tested on the same THR model case geometry. The three cases of distal fixation tested are as follows;

Cortex fixed – In this model, the distal Femur was simply dissected at the level above the experimental cement and fixation module, 270 mm from the Lesser Trochanter. Encastre boundary conditions were then applied to the distally dissected surface of the Femur.

Distal cement - In this model, the 80 mm of Femur sited in the fixation module was included. In addition, the supporting cement present between the bone and the fixation module was also included. A tied contact was defined between both the unsupported proximal Femur fragment and the restored 80mm of Femur sited in the fixation module. A tied contact was also defined between the distal 80 mm of Femur and the surrounding potting cement. Encastre boundary conditions were defined on all of the external cement surfaces, excluding the proximal surface.

Distal cement and module - In this model, in addition to the 80 mm of Femur sited in the fixation module and the potting cement, the fixation module was also included in the model. Similar to the distal cement model, tied contacts were defined between the unsupported proximal Femur fragment and the restored 80 mm of Femur, and between the distal 80 mm of Femur and the surrounding potting cement. The interaction between the external cement surfaces and the internal surfaces of the fixation module were defined as a hard contact in the normal direction, and used a penalty friction formulation in the tangential direction. Encastre boundary conditions were defined on all of the external fixation module surfaces.

The aim of this section was to determine whether the method of modelling the distal fixation has an effect on biomechanics, and to determine which method provided the closest match to the experimental results.

4.2.7.1 Distal fixation stiffness

The overall stiffness for the range of investigated distal fixation methods, for the basic THR case is shown in Figure 65. The distal fixation method did not have a large effect on overall construct stiffness. The Cortex fixed case had the highest overall stiffness, while the distal cement with module had the lowest. The overall stiffness for the Distal cement and module method was closest to the experimental results.
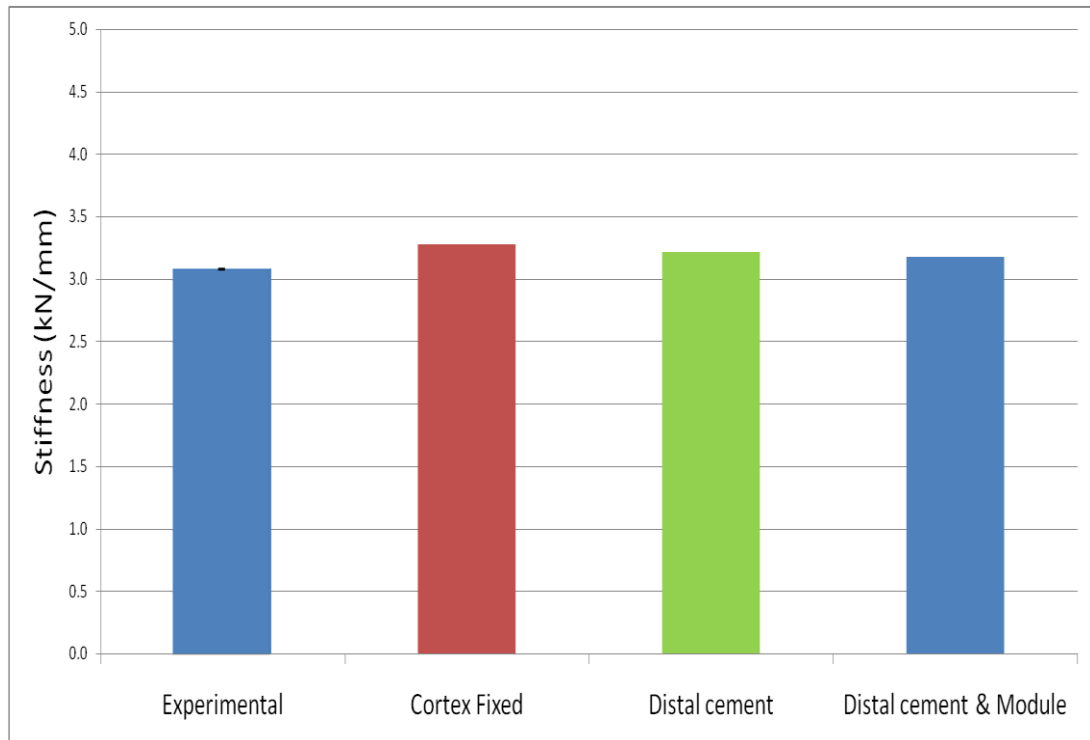
Figure 65 the experimental and computational THR construct stiffness, for the range of investigated distal fixation methods. Error bars on the experimental data represent the standard deviation between 6 re-loading cycles of the same specimen

4.2.7.2 Bone Strain comparison

The strain along the medial length of the Femur for the range of investigated distal fixation methods, for the basic THR case, is shown in Figure 66. There were slight differences in medial strain magnitudes between the different distal fixation methods. The strain distribution pattern remained consistent between the different methods. The Cortex fixed method consistently had the lowest strain magnitudes at all gauge locations, while the distal cement and module method had the largest. The Distal cement and module method strain values were closest to the experimental results.
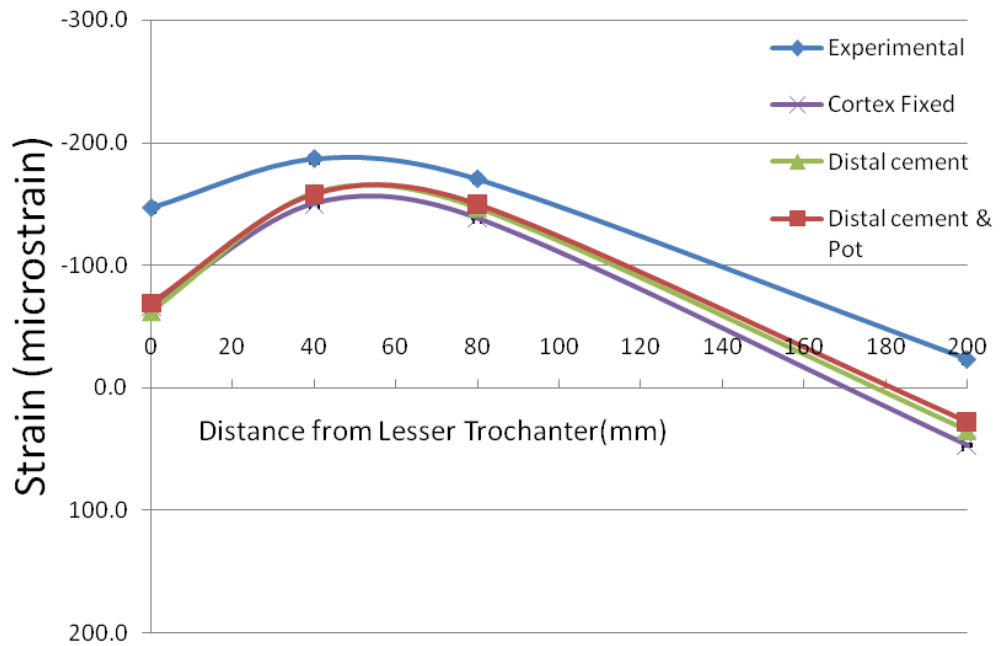
Figure 66 The bone surface strain along the medial length of the Femur, for the range of investigated distal fixation methods.

The strain at the distal end of the Femur, on both the medial and lateral sides for the range of investigated element types, is shown in Figure 67. The distal fixation method had an effect on distal strain. The largest strain magnitudes were seen at the Cortex fixed method, while the smallest were seen at the distal cement and module method. The strain pattern seen in all of the computational methods was different from the experimental strain distribution. While the experimental distal strains were both in compression, the distal strains for all of the computational distal fixation methods were in tension on the medial side, and in compression on the lateral side.
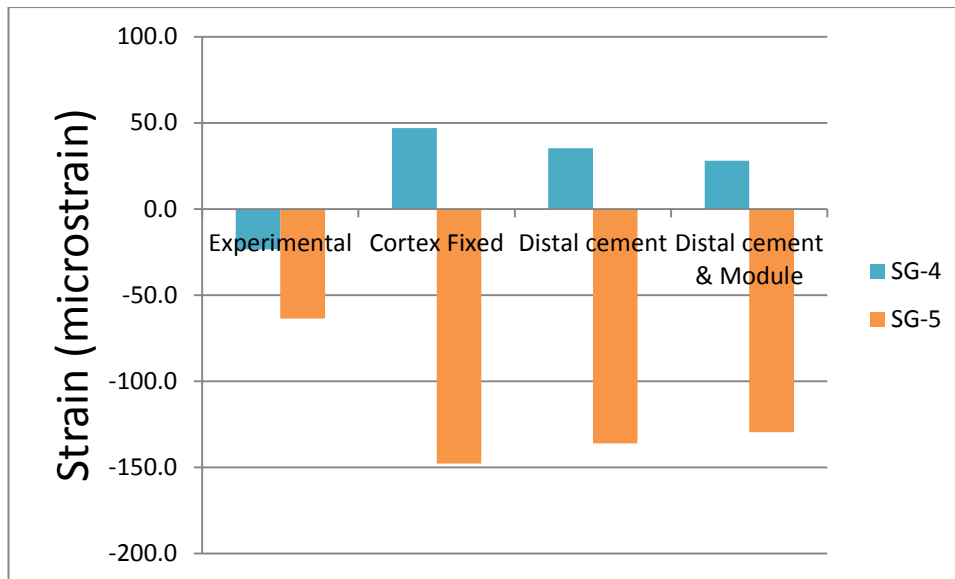
Figure 67 The strain at the distal end of the Femur for the range of investigated distal fixation methods.

4.2.7.3 Summary

The method of representing the distal fixation included in the computational models did have an effect on construct behaviour. There were slight differences seen in overall construct stiffness and on bone strain along the medial length of the Femur. The largest differences were identified at the bone strain located at the distal end of the Femur. This was expected as the changes in behaviour were occurring close to where the variations to geometry and boundary conditions were being applied. As more detail matching the experimental set up was introduced to the models, the level of constraint around the distal region of femoral bone was reduced. In addition, the distance and amount of material between the distal strain gauge locations and the points of fixation were increased. While changes were identified in the distal bone region, the small changes in overall construct stiffness and proximal bone strain indicate that the effect of the changes to distal fixation method are local to the distal bone region, and that overall biomechanics are relatively unaffected.

While there was a reduction in overall construct stiffness with the introduction of more detailed representation of the experimental testing rig, the reduction in stiffness magnitude was small. Further additional parts of the experimental testing rig, such as the angle loader, could be introduced into the computational model, but are unlikely to have a large effect on the stiffness overestimation.

Table 12 Runtime of the distal fixation cases

Model	Run time (Hours)
Cortex Fixed	25
Distal Cement	25
Distal Cement + module	25

While more detail was included for solution processing with this method, the resultant differences to overall model runtime were negligible, Table 12. As the differences between the distal fixation methods were small and the differences in runtime minimal, the method most similar to the experimental method, the distal cement and module method, was chosen to be included in future models.

4.2.8 Contact Surface Interactions

This section presents the results of the varying the properties of the interaction at the surface to surface contacts within the model. The interaction properties were investigated at the three key surface contacts in the model; between the prosthesis stem and cement mantle[92-94], between the cement mantle and cancellous bone, and between the cortical bone and the cement mantle. Three different contact modelling methods were investigated at these key surface interactions and defined as either; hard, soft and tied contact conditions.

Soft contact- Contact relationships defined as "Soft" are specified in terms of overclosure (or clearance) versus contact pressure. A soft contact is pressure-overclosure relationship are more likely to be used to model a soft, thin layer on one or both surfaces. Our models used a contact stiffness of 600 Pa [78].

Hard contact- When surfaces are in contact, any contact pressure can be transmitted between them. The surfaces separate if the contact pressure reduces to zero. Separated surfaces come into contact when the clearance between them reduces to zero [78].Our models used a penalty friction formulation for normal and tangential behaviour respectively,

Tied contact- Ties two surfaces forming a contact pair together for the duration of a simulation. Constrains each of the nodes on the slave surface to have the same value of displacement as the point on the master surface that it contacts[78].

Five different models were created, each with a different combination of contact conditions at each of the key surface interactions. The contact condition and interaction combinations are shown in Table 13.

Table 13 The investigated surface interactions and their respective contact condition for the investigated cases

Interaction	Contact Condition				
	A	**B**	**C**	**D**	**E**
Stem-Cement	600,0.6	Hard,0.6	Tied	600,0.6	Hard,0.6
Cement-Cancellous	600,0.6	Hard,0.6	Tied	Tied	Tied
Cement-Cortical	600,0.6	Hard,0.6	Tied	Tied	Tied

4.2.8.1 Interaction overall construct stiffness

The overall stiffness for the range of investigated interaction properties, is shown in Figure 68. The variations in contact conditions had a large effect on overall construct stiffness.

Changing the contact interaction properties at all three surface interactions resulted in large variations in overall stiffness. Defining all interactions as soft contact resulted in the lowest overall construct stiffness, while defining tied contacts all of the interactions resulted in the highest stiffness, with the results of using hard contacts between the two. The difference between the overall stiffness was large with an increase from 3.18kN/mm to 7.92kN/mm between the soft contact and tied contact cases respectively.

Changing the cement to cortical bone interaction and the cement to cancellous bone interaction from a soft contact to tied contact conditions can be seen by comparing cases A to D. There was an increase in stiffness from 3.18 to 4.19 kN/mm between cases A and D respectively.

Changing both cement to bone interactions from a hard contact to tied contact conditions can be seen by comparing cases B to E. There was an increase in stiffness from 4.46 to 5.57 kN/mm between cases A and D respectively.

The difference between defining a soft or hard contact at the stem-cement interface, with the other two interactions remaining tied, can be seen by comparing cases D and E. There was an increase in stiffness from 4.19 to 5.57 kN/mm between cases D and E respectively.
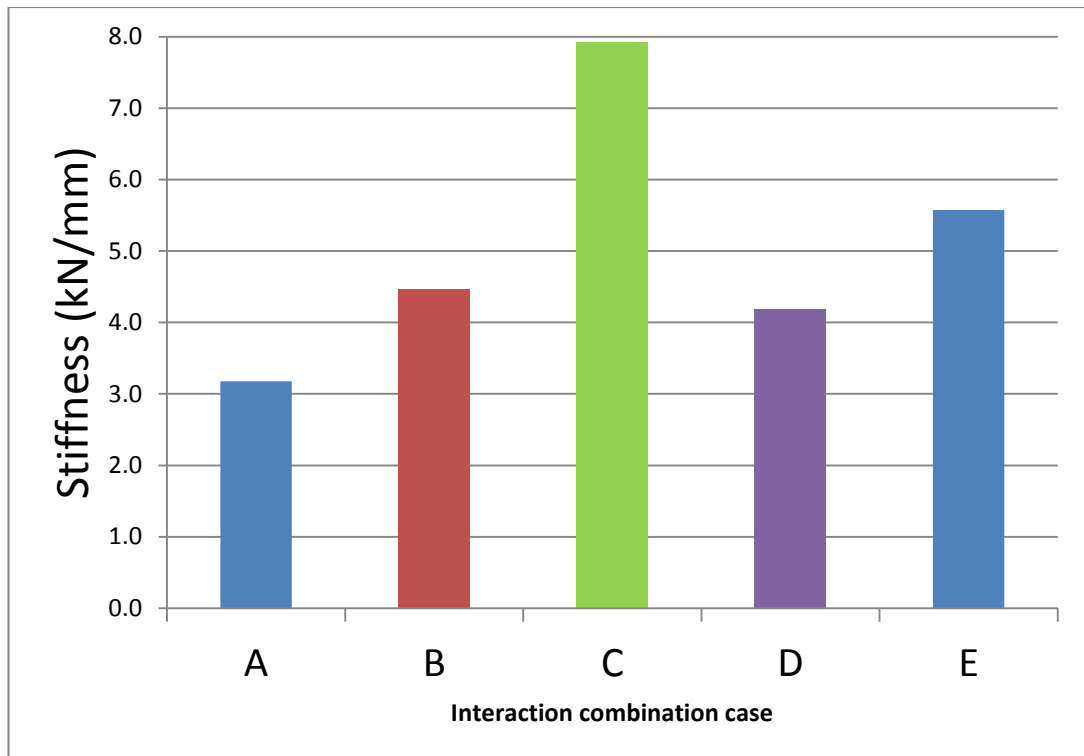
Figure 68 Overall stiffness for the range of investigated interaction properties

4.2.8.2 Interaction bone strain

The strain along the medial length of the Femur for the range of investigated interaction properties, for the basic THR case, is shown in Figure 69. While there was no change in overall strain distribution pattern between the investigated cases, there were variations in medial bone strain magnitudes between the cases. The largest medial strain variations were seen at the post proximal gauge site, gauge 1, located at the level of the lesser trochanter. There was a 30με change in strain magnitude at this gauge location between the hard contact and tied contact condition cases, B and C.
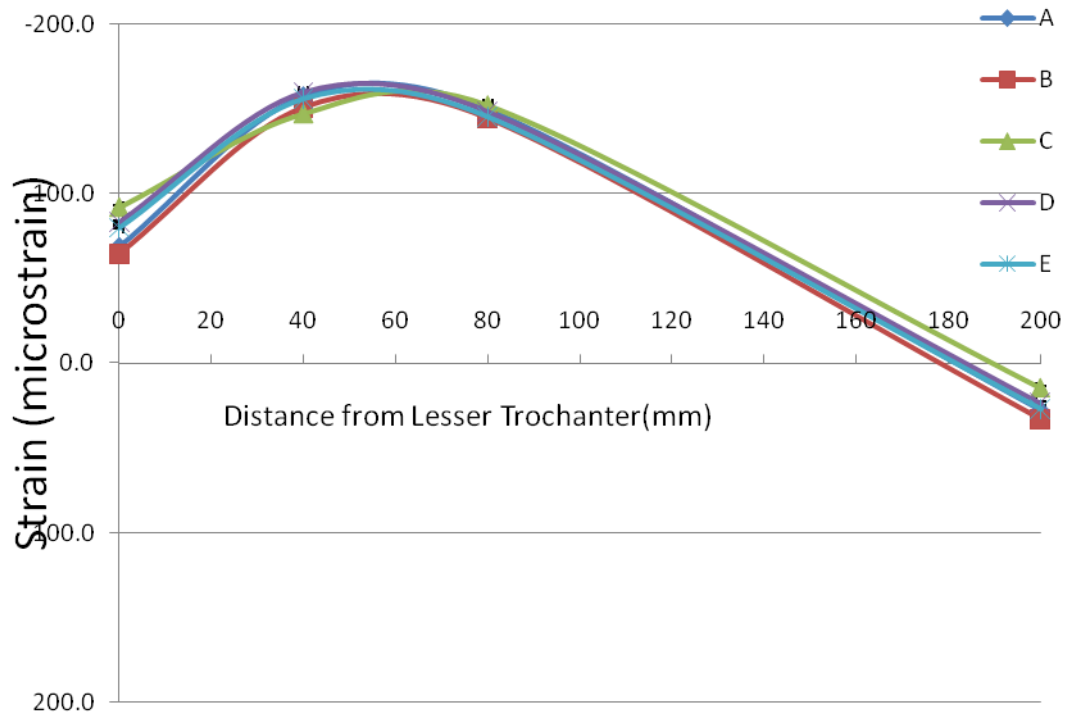
Figure 69 The strain along the medial length of the Femur, for the range of investigated interaction properties.

The strain at the distal end of the Femur, for the range of investigated interaction properties, is shown in Figure 70. The differences in contact conditions did not have an effect on distal strain patterns with the medial strain remaining in slight tension, and the strain on the lateral side remaining in compression for all investigated cases. The variations in strain magnitude remained small between the cases. Case B, with all interactions defined as hard contact surfaces had the largest distal strain magnitudes, while case C, with all interactions defined as tied contacts having the lowest strain magnitudes.
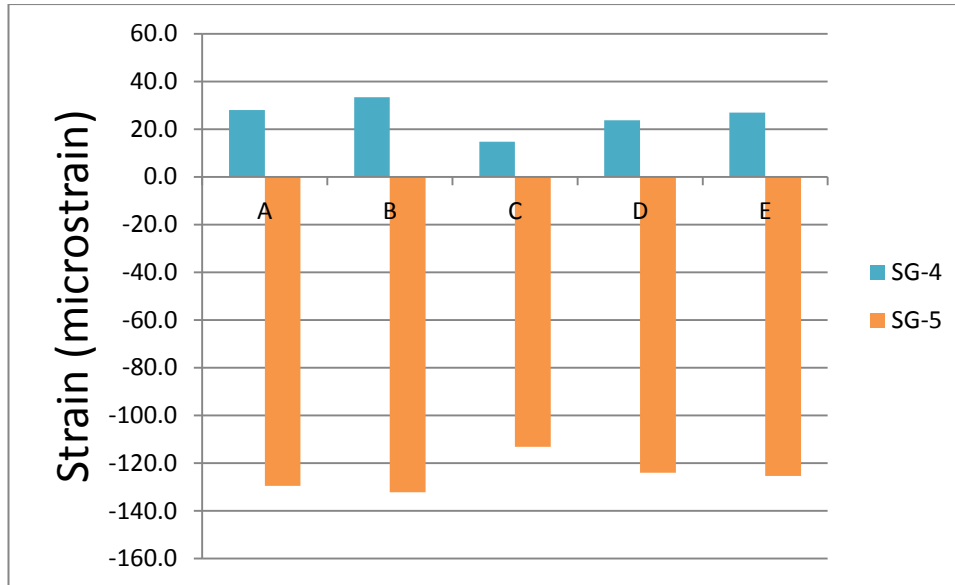
Figure 70 The strain at the distal end of the Femur for the range of investigated interaction properties.

4.2.8.3 Summary

This section investigated the effect of contact conditions over a range of key surface interactions in the model. The method of representing the distal fixation included in the computational models had an effect on overall construct behaviour. Large variations in overall construct stiffness were seen with different contact conditions. Bone strain pattern remained similar between the range of cases with variations in strain magnitude. Variations in construct stiffness did not necessarily correlate with the changes in bone strain.

When choosing which contact conditions would be used in all subsequent models, interaction combinations A and B were discounted as they under constrained the cement to bone interactions properly, while combination C was discounted as it over constrained the prosthesis stem to cement interaction. Between the remaining two tested interaction combinations, E was chosen as in the authors opinion, represented the experimental stem to cement scenario best.

The variations in defined contact properties at the key interactions in the model had an effect on overall construct behaviour. There was a very large effect in overall construct stiffness and bone strain for moving from all contact surfaces defined as soft contacts, to all contact surfaces defined at tied contacts.

The results indicate that Normal behaviour in cement to bone interface does not a large effect. There was a similar scale of change between A and B as

there is between C and D. Therefore, the stem to cement interface is sensitive to the choice of normal behaviour.

The change from B to C is approximately 1.5 times the change from C to E. This indicates that both the cement to stem, and the cement to bone interfaces are affected by the choice of contact surface. However, the interaction change at the stem to cement interface has a larger effect on overall stiffness.

The interaction proven to be the most sensitive to contact condition was the stem to cement interface.

4.2.9 Loading Method

This section presents the results of the varying the method by which the load is applied to the prosthesis head. In the experiments, a steel loading cup attached to the crosshead of the materials testing machine was used to apply load to the constructs. Three different methods of loading the specimens were investigated to determine how the different loading methods affect the behaviour of the models. These methods are detailed below.

Developmental baseline (Figure 71A)– This method attempted to simulate the experimental loading conditions. The loading cup was included in the model, and the region of the cup which was fixed, i.e. where the screw connected the loading cup to the crosshead, was constrained in both the X and Y axis, allowing movement in only the Z axis. The force was applied as a point load to the top of the loading cup.

Fully constrained Loading cup (Figure 71B) – This method also included the loading cup, however, instead of only a small region of the loading cup being constrained, all of the external surfaces of the loading cup were constrained in both the X and Y axis, allowing movement in only the Z axis. The force was applied as a point load to the top of the loading cup.

Constrained point load (Figure 71C) – This method did not include the loading cup, instead a point in the centre of the femoral head of selected and constrained in both the X and Y axis, allowing movement in only the Z axis. The force was then applied to the outer surface of the femoral head, in the appropriate coordinate system.

The aim of this section was to investigate the effect of loading method on construct behaviour and to determine the best method to use in later models. The different loading methods were evaluated over the full range of loading angles.
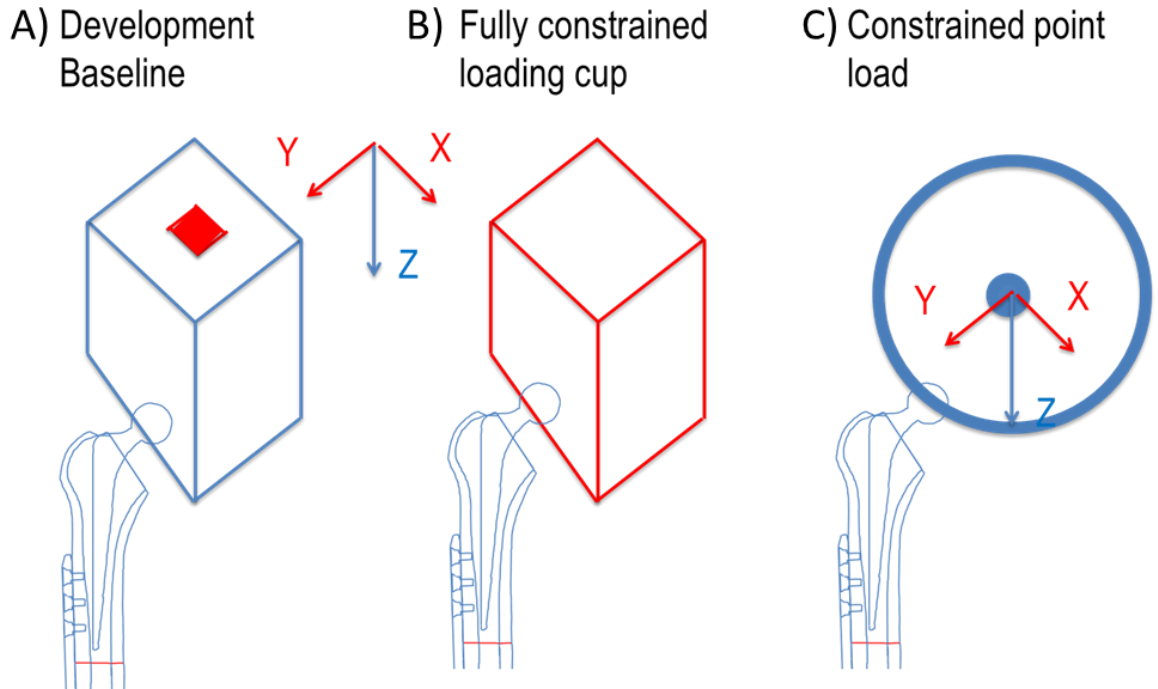
Figure 71 The range of investigated loading methods including the Developmental Baseline, Fully constrained loading cup and the Constrained point load

4.2.9.1 Loading method overall construct stiffness

The overall stiffness for the range of investigated loading methods for the baseline THR case is shown in Figure 72. Changing the loading regime caused large variations in both the overall stiffness magnitudes as well as changing the relationship between angle and stiffness. The use of the loading cup created a significantly different stiffness pattern with respect to loading angle when compared to the experimental results. The differences in stiffness magnitude between loading angles was smaller for the fully constrained method than for the developmental loading cup method. The constrained point load method displayed the same stiffness pattern as the experimental results with respect to loading angle, with the highest stiffness at the 10° loading case and the lowest at the 20° loading case. The computational overall construct stiffness were much higher than the collected experimental results.
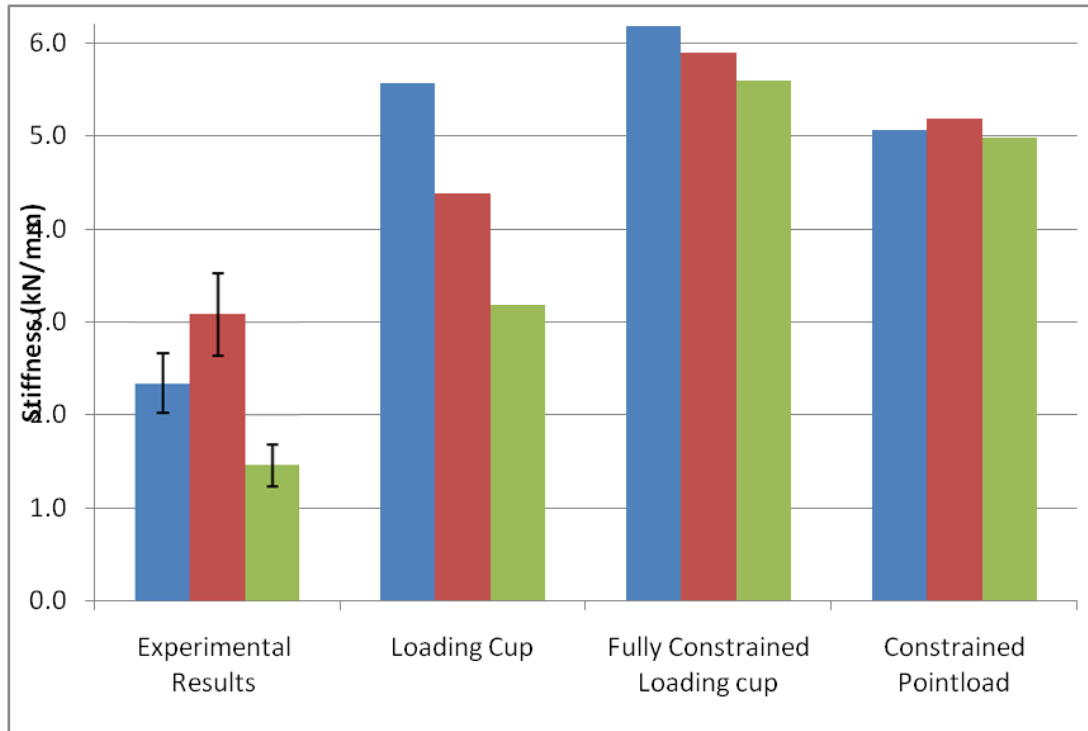
Figure 72 Overall stiffness for the range of investigated loading methods, for the 0° 10° and 20° loading angles. Error bars on the experimental data represent the standard deviation between 6 re-loading cycles of the same specimen

4.2.9.2 Loading method bone strain comparison

The strain along the medial length of the Femur for the range of investigated interaction properties, at the 10° loading angle, is shown in Figure 73. Loading method had an effect on medial bone strain magnitude, with the constrained point load model having the highest strains in the region of the prosthesis. The Fully constrained Loading cup model had the lowest strains in the region of the prosthesis stem, while the Developmental baseline had the highest distal, medial strain.

The strain distribution pattern along the medial length of the Femur was affected by the loading method. The largest strain changes were seen at gauge 2, located 40 mm distal to the Lesser Trochanter.
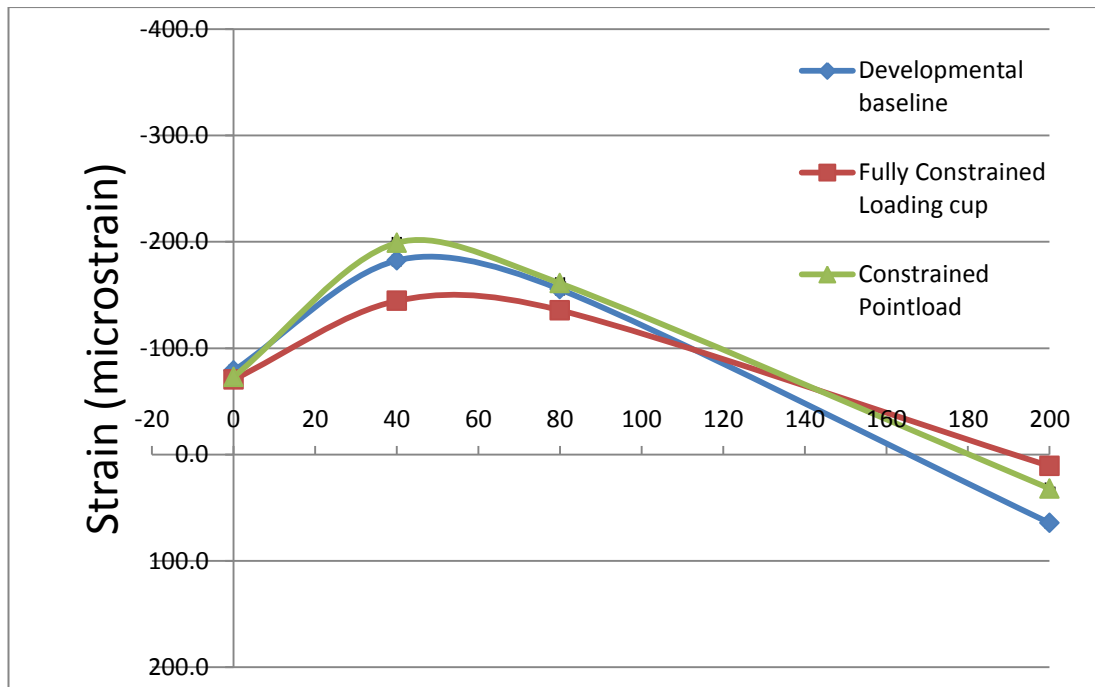
Figure 73 The strain along the medial length of the Femur, for the range of investigated loading method, at the 10 degree loading angle.

The strain at the distal end of the Femur, for the range of investigated loading methods, at the 10° loading angle, is shown in Figure 74. There were slight differences in distal strain pattern as the loading method was varied. The strain pattern was the same for all of the loading methods, with the medial gauge in tension and the lateral gauge in compression. However there were variations in strain magnitude with the largest strains for the loading cup method and the lowest at the fully constrained loading cup method. The same patterns were seen for the other loading angles.
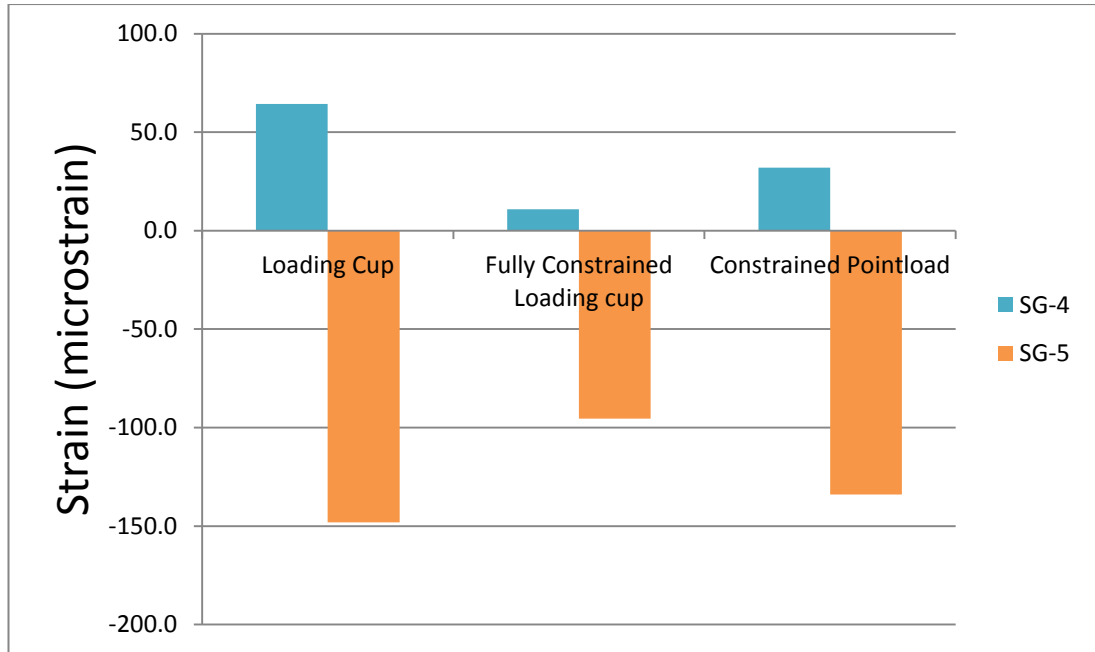
Figure 74 the strain at the distal end of the Femur for the range of investigated loading methods, at the 10 degree loading angle.

4.2.9.3 Summary

Loading method did have an effect on overall construct behaviour. While the strain pattern behaviour between the methods remained similar, the overall construct stiffness behaviour varied greatly. Both of the loading methods including the loading cup did not display behaviour comparable to the experimental results, as the loading angle was changed. This indicates that the loading cup is not applying the load to the construct in a way representative of the experimental methods. This can only be due to the contact between the prosthesis head and the loading cup. It is difficult to accurately represent the friction between these two components. It was also possible that "pinching" between the femoral head and loading cup was occurring in the perfectly aligned computational model, which is not happening in the experiment.

The removal of the loading cup and the use of the simpler prosthesis head constrained point resulted in stiffness pattern behaviour similar to the experimental results. The constrained point method provides a way to replicate the translation constraints imposed by the cup without the complexity of resolving the contact surface accurately. The constrained point load method will be used in future models.

4.3 Stabilised Periprosthetic fracture construct

This section describes the development model from the total hip replacement model, creating a fracture in the region of the prosthesis stem

tip, and stabilising the construct with the introduction of a locking fixation plate and bone screws. The experimental results used to compare against the intact Femur computational model results were presented in Section 3.5

4.3.1 Fracture site coefficient

This section presents the results of the investigated range of fracture site friction coefficients. The effect of this coefficient on the overall construct behaviour of a stabilised periprosthetic fracture is unknown. A study investigating bone on bone friction in human cadaveric Femurs, reported friction coefficients of between 0.394 and 0.407, depending of the type of saw used to create the fracture[95]. The results reported for the reciprocating saw fracture creation method, were most comparable to the band saw used to perform the osteotomy in our study, reported a fracture site coefficient of friction of 0.399. The study also reported results for the reciprocating saw method performed on cadaveric tibias, reporting a much higher coefficient of friction of 0.582. Four friction coefficients were chosen to be investigated at the periprosthetic fracture site, ranging from 0.01, to a maximum of 0.6.

The aim of this section was to determine the effect of the coefficient of friction at the fracture site on overall construct behaviour, and to assess the sensitivity of our computational model to this input parameter .

4.3.1.1 Overall construct stiffness

The overall stiffness, for the range of investigated fracture site friction coefficients, is shown in Figure 75.

There was very little difference in overall construct stiffness between the 0.2, baseline 0.3 and 0.6 friction coefficient cases with only very small variations in overall stiffness. There was a reduction in stiffness from 4.8kN/mm to 4.55kN/mm between the baseline and 0.01 cases.
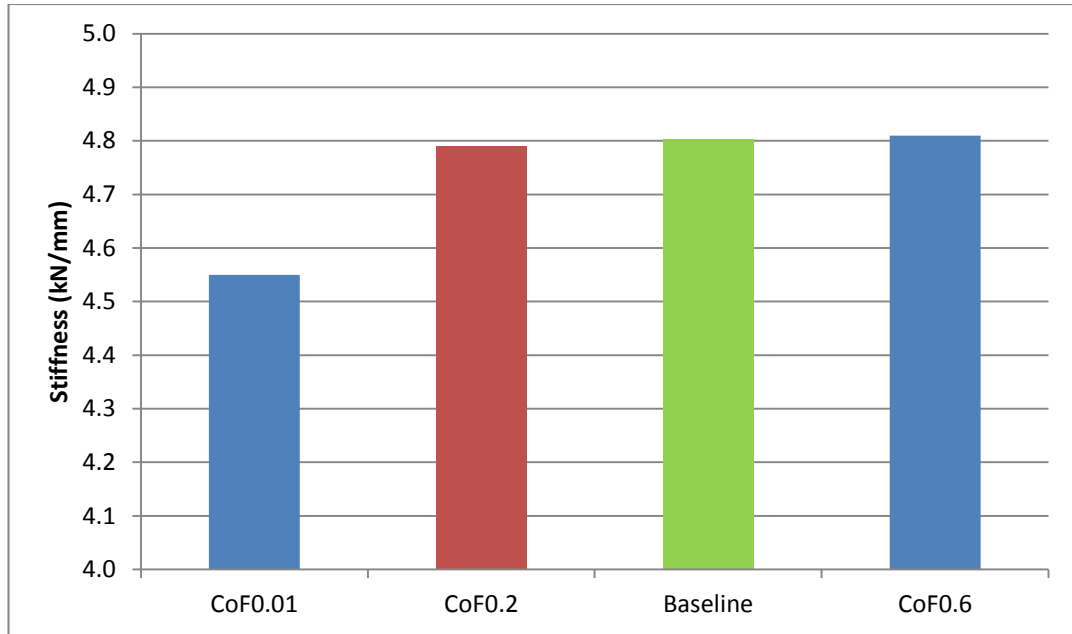
Figure 75 Overall stiffness for the range of investigated fracture site coefficients. N.B. The overall construct stiffness is plotted between 4.0 and 5.0 kN/mm

4.3.1.2 Bone strain

The strain along the medial length of the Femur for the range of investigated fracture site coefficients, is shown in Figure 76. There was no variation in medial strain distribution pattern for the 0.2, baseline 0.3 and 0.6 friction coefficient cases. While the bone strain in the region of the prosthesis stem did not vary between the baseline and 0.01 cases, there was a reduction in bone strain at gauge located just proximal to the fracture site.
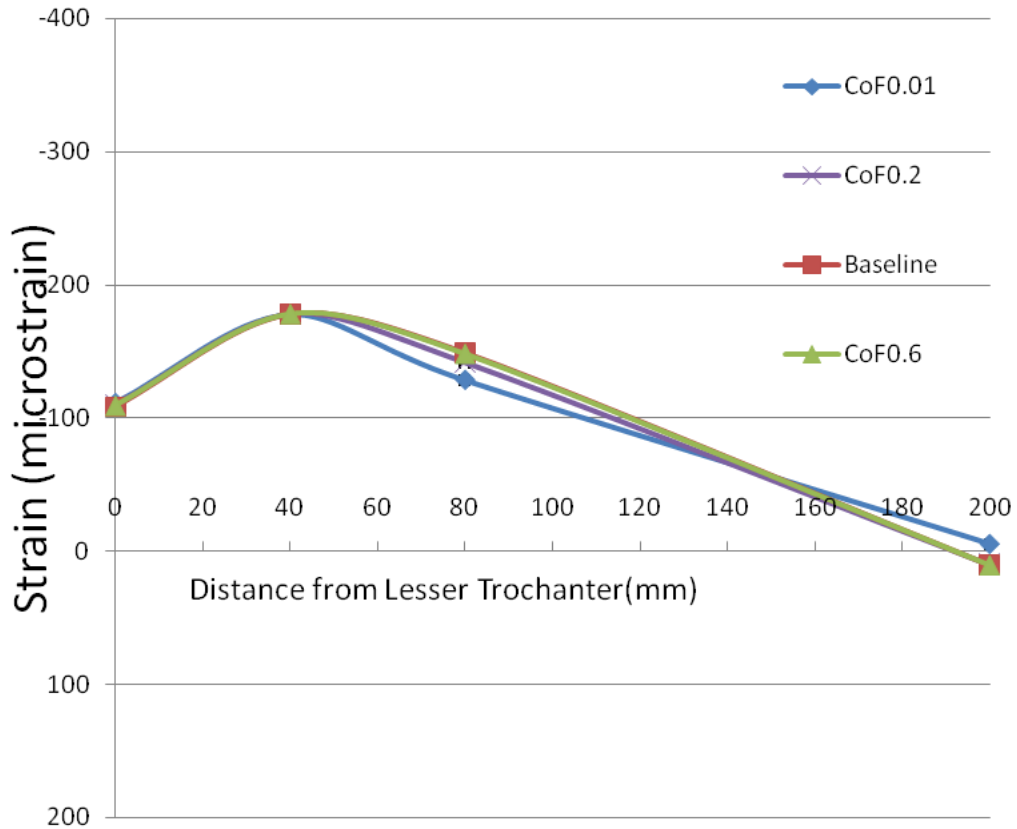
Figure 76 The strain along the medial length of the Femur, for the range of investigated fracture site coefficients.

The strain at the distal end of the Femur, for the range of investigated fracture site coefficients, is shown in Figure 77. There was no variation in distal bone strain, increasing the fracture site friction coefficient from the baseline 0.3 to the 0.6 case. However, there were changes in lateral bone strain magnitude on the lateral side of the Femur, reducing from -108με in the baseline case to -92 με for the 0.01 case. There was also a change in medial bone strain for the 0.01 case, with the distal strain in slight compression.
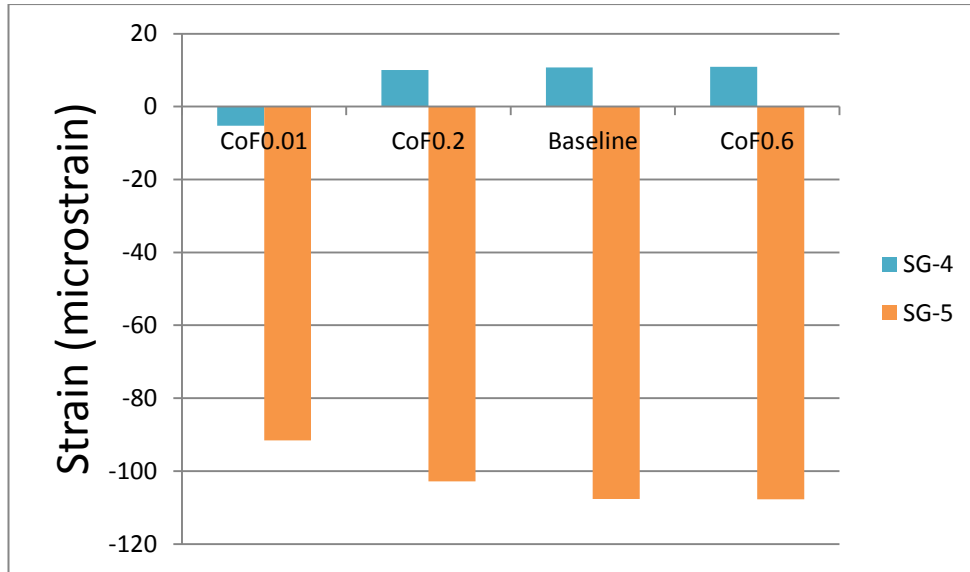
Figure 77 The strain at the distal end of the Femur for the range of investigated fracture site coefficients, at the 10 degree loading angle.

4.3.1.3 Plate strain

The strain on the fixation plate, for the range of investigated fracture site coefficients, is shown in Figure 78. There was no variation in plate strain pattern between the 0.2, baseline 0.3 and 0.6 coefficient cases, with only slight magnitude variation between the cases. There was a very large increase in plate strain for the 0.01 case, with a maximum of 106με at the most proximal gauge location.
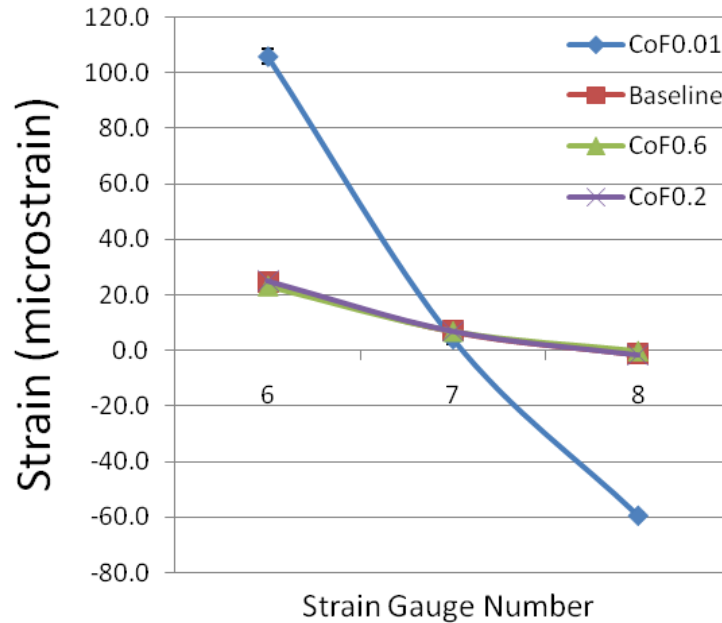
Figure 78 The strain on the fixation plate for the range of investigated fracture site coefficients.

4.3.1.4 Summary

The coefficient of friction at the periprosthetic fracture site was shown to have an effect on the model only at very low values.

Bone on bone friction data between the Sawbone specimens tested experimentally in this study could not be found in the existing literature. The friction coefficients derived from human cadaveric specimens, prepared in a comparable method to that used in this study were within the range of coefficients tested in this section. No differences in stiffness or strain behaviour could be identified between the range of friction coefficient between the 0.2 and 0.6 cases.

The difference in results between models with a fracture site friction coefficient of 0.01 and a model with a frictionless contact properties are expected to be minimal. Reduction in medial strain recorded immediately above fracture site, combined with a large increase in plate strain indicates that there is a change in the load transfer relationship between the bone and fixation construct occurring in this case. Low friction at the fracture site resulted in lower overall stiffness, lower bone strain above the fracture, lower distal strain, and higher plate strain. Variations in all these metrics indicate that there are large changes in the movement at the fracture site.

While the reduction in proximal bone strain and change in distal bone strain is relatively low, there is a large increase in strain on the fixation plate. However, it is unlikely that this type of friction environment would be found at a fracture site *in vivo*.

4.3.2 Cortical bone material properties

This section presents the results of the investigated range of femoral cortical bone material properties. The properties of the cortical bone had homogenous isotropic material properties assigned with a Young's modulus of E=16.7GPa, section 4.1.8. Due to the complex nature of human bone, studies have shown that while this might be the case along the long axis of the Femur, that the Young's modulus in the transverse direction is lower, E=10GPa. Three different cortical bone material properties were investigated, the baseline properties with a Young's modulus of E=16.7GPa, a weaker case with a Young's modulus of E=10GPa, and a transverse anisotropic case with a Young's modulus of E=16.7GPa in the Z axis direction, and a Young's modulus of E=10GPa in X and Y axis directions.

The aim of the section was to determine the effect of cortical bone material properties on overall construct behaviour.

4.3.2.1 The effect of Cortical bone material properties on overall construct stiffness

The overall stiffness for the range of investigated cortical bone material properties, is shown in Figure 79.

As expected, there was a reduction in overall stiffness between the Baseline and low Young's modulus models. However, the construct stiffness between the baseline and the transverse anisotropic case were the same. All three models had an overall stiffness much higher than the experimentally measured value.
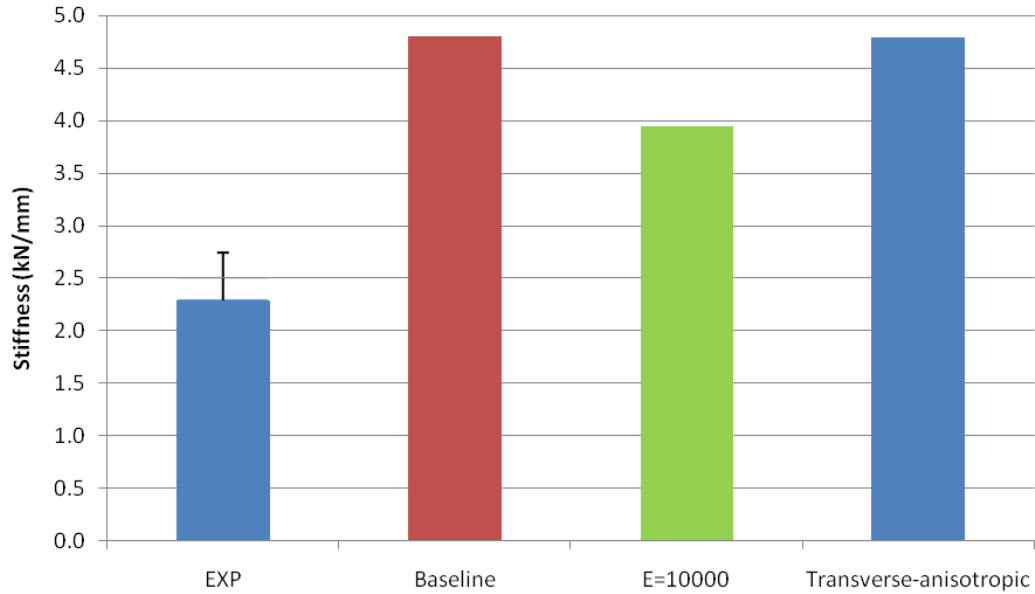
Figure 79 Overall stiffness for the range of cortical material properties. Error bars on the experimental data represent the standard deviation between 6 re-loading cycles of the same specimen

4.3.2.2 The effect of Cortical bone material properties on Bone strain

The strain along the medial length of the Femur, for the range of investigated cortical bone material properties, is shown in Figure 80. There were large changes in medial bone strain magnitude between the baseline and low Young's modulus models. The main changes occurred in the proximal bone region with a doubling of strain values in this region, while maintaining a similar strain distribution pattern. The strain magnitudes and patterns between the baseline and transverse anisotropic models were the same.
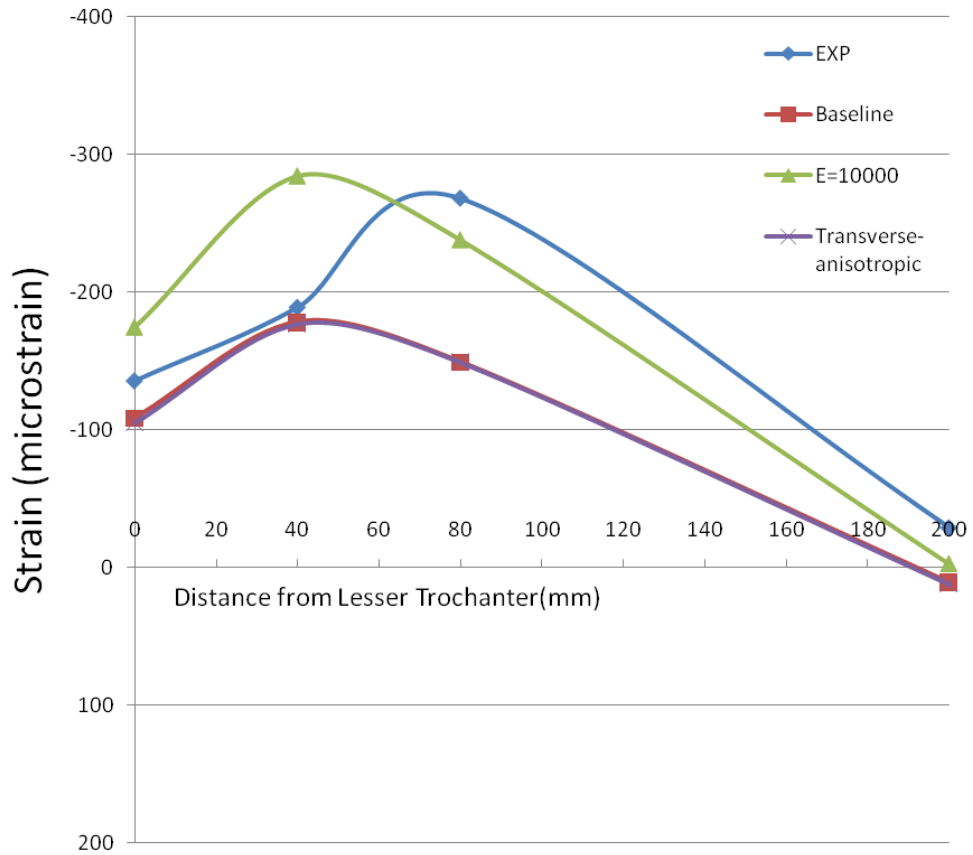
Figure 80 The strain along the medial length of the Femur, for the range of investigated cortical bone material properties.

The strain at the distal end of the Femur, for the range of investigated cortical bone material properties, is shown in Figure 81. While there were slight distal strain magnitude differences between the baseline and transverse ansiotropic cases, the patterns were generally the same. However, there was a change in strain pattern and magnitude between the baseline and the low Young's modulus case. Both gauges were in compression for the low Young's modulus case, matching the experimental pattern, however, the strain magnitudes did not match.
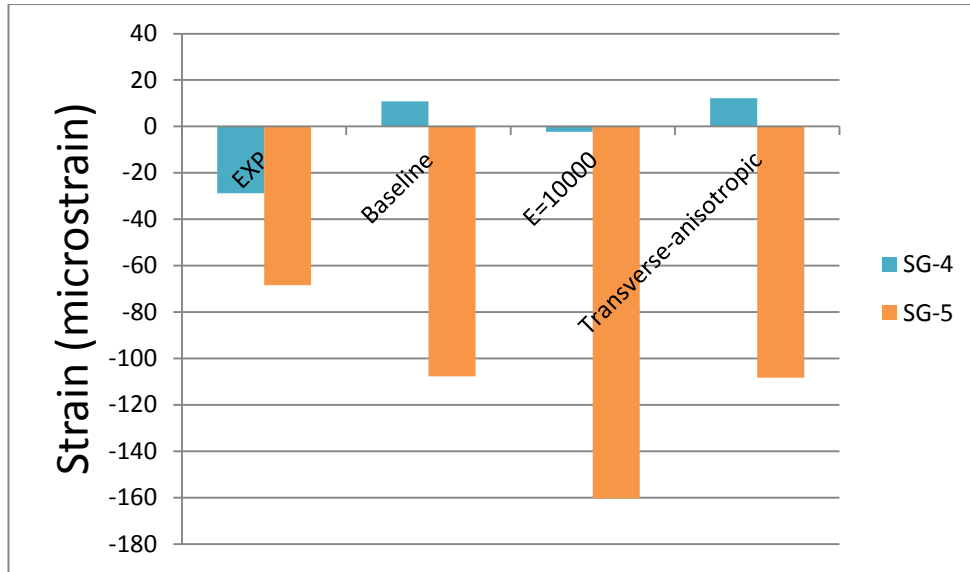
Figure 81 The strain at the distal end of the Femur for the range of investigated cortical bone material properties.

4.3.2.3 The effect of Cortical bone material properties on plate strain

The strain on the fixation plate, for the range of investigated cortical bone material properties, is shown in Figure 82. The plate strain pattern remained the same between the baseline and transverse anisotropic cases. There was an increase in plate strain at all locations for the low Young's modulus case while maintain the same plate strain distribution pattern as the other cases.
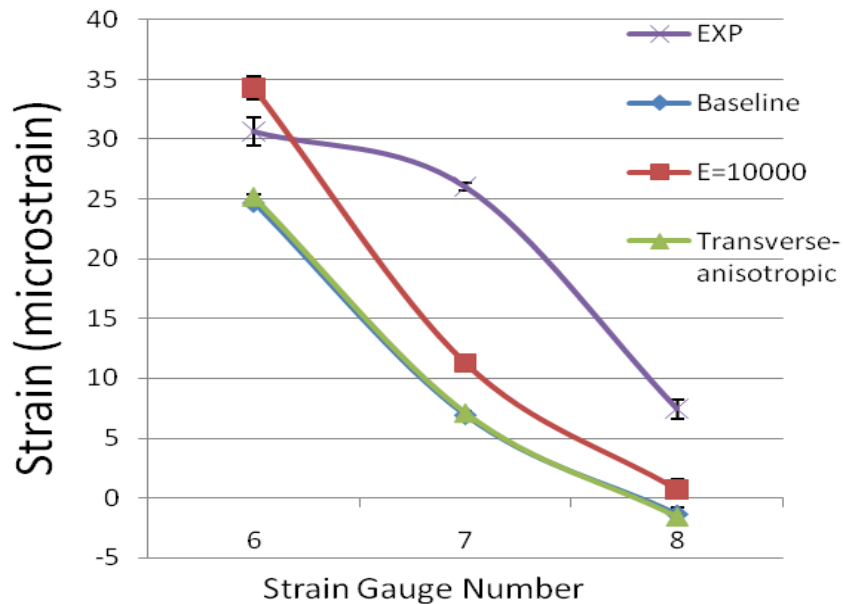
Figure 82 The strain on the fixation plate for the range of investigated cortical bone material properties.

4.3.2.4 Summary

The behaviour of the model was affected by varying the material properties of the cortical bone. The expected changes in behaviour with a reduction in Young's modulus, reduced construct stiffness and increased strains, were seen. This included increased strain on the plate which indicates that at least some of the increased deformation is occurring at the fracture site.

The modelling of the transverse anisotropic properties of natural bone did not have a large effect on overall construct biomechanics. The aim of modelling this case was to quantify the potential effect of the transverse anisotropic properties of natural bone against the homogeneous properties of the Sawbones. Only very slight variations in stiffness and strain were observed. As the 4th generation Sawbones used in the experiments were moulded, they also would not display the transverse anisotropic material behaviour.

When defining material properties in the computational model, the properties are defined in the global axes. While appropriate for the majority of the length of the Femur, this does mean that they are slightly inaccurately applied in the trochanter region of the Femur.

4.3.3 Distal cement

This section presents the results of the investigated the presence of cement in the distal fragment of the Femur. During the experiments, the relatively smooth surface of the medullary canal in the Sawbone specimens, did not allow for secure fixation of the cement restrictor within the Femurs, Figure 83. This lead to the restrictor being forces distally down the medullary canal, with cement present in the region of the bicortical screws. The aim of the cement restrictor is to prevent the cement used to create the mantle around the prosthesis from travelling distally down the medullary canal, in our experiments sited 10 mm distal to the tip of the prosthesis stem. Due to the suboptimal fixation of the cement restrictors and the force of the cement application and expansion during curing, in some specimens, the cement travelled a range of distances down the medullary canal. This section will model the two extreme distal cement scenarios, a best case where the cement restrictor has prevented distal cement flow and is ideally sited 10 mm from the prosthesis tip (No distal cement model, NDC), and a worst case where the restrictor had allowed the cement to flow distally down the medullary canal, to a level below the fixation points of the distal bicortical screws used to stabilise the fracture, Baseline model. The surface interaction between the bicortical screws in contact with the distal cement were modelled as a tied contact.

The aim of the section was to determine the effect of the presence of distal cement in the medullary canal on overall construct behaviour.
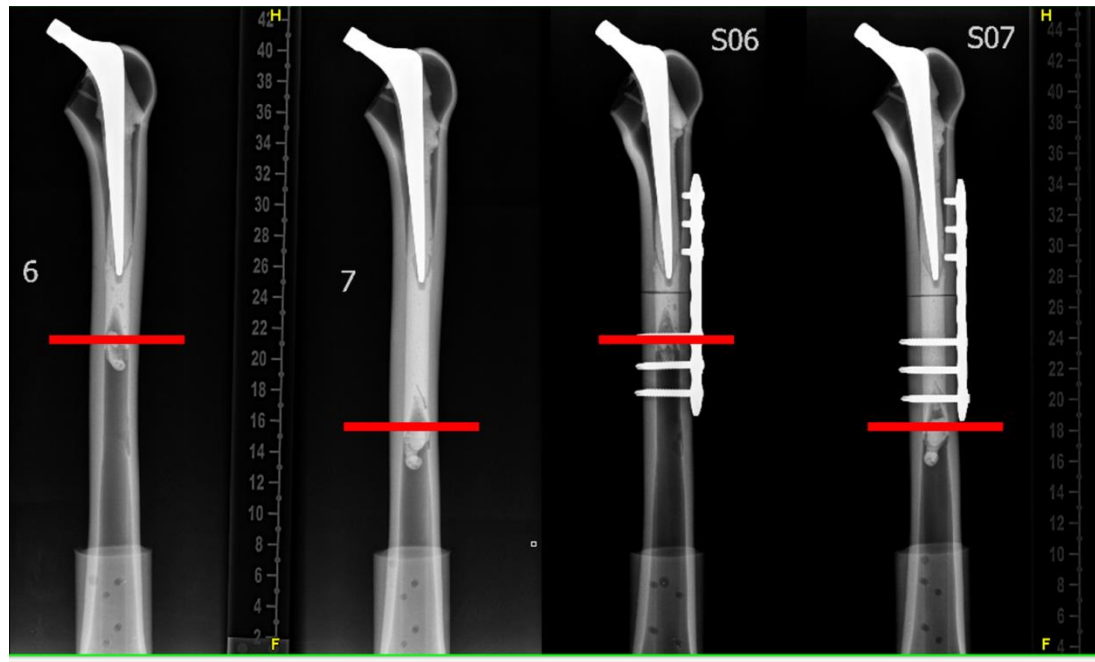
Figure 83 Level of the cement restrictor for the THR and PPF cases for the experimental specimens S06 and S07. The red indicator lines mark the mid-point of the cement restrictors, and illustrate their position in relation to the prosthesis tip and bicortical screws

4.3.3.1 The effect of Distal cement on overall construct stiffness

The overall stiffness, for the two investigated distal cement cases, is shown in Figure 84. The presence of distal cement did not change the overall construct stiffness of the models. There was only a very small reduction in stiffness magnitude as the distal cement was removed. A change of only 0.02kN/mm was seen with the removal of the distal cement.
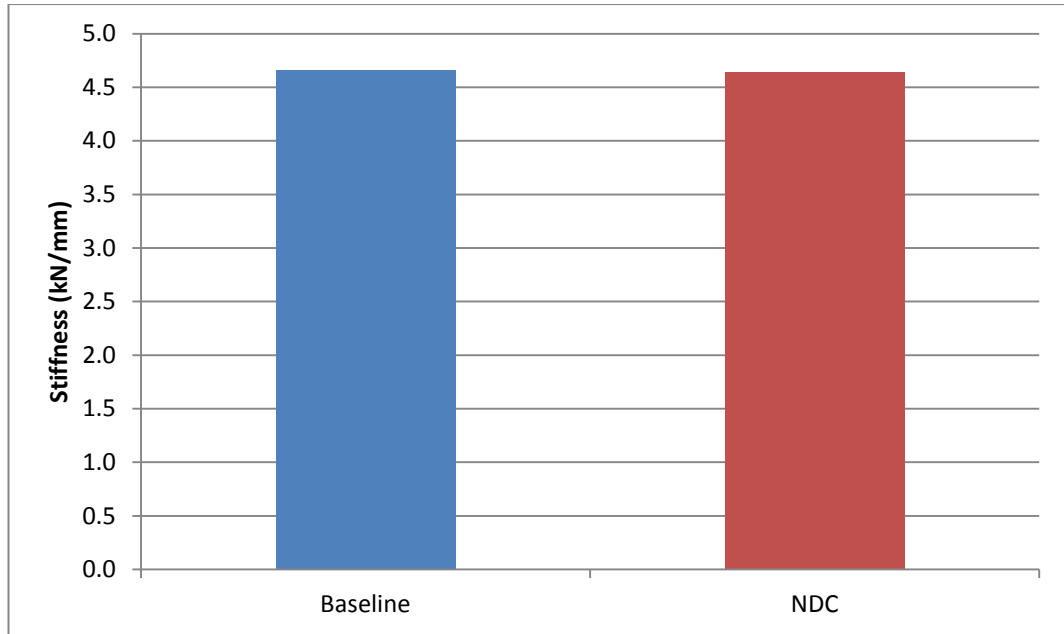
Figure 84 Overall stiffness for the range of investigated distal cement cases.

4.3.3.2 The effect of Distal cement on bone strain

The strain along the medial length of the Femur, for the range of investigated distal cement cases, is shown in Figure 85. There was no change in strain distribution pattern with the removal of the distal cement. There were only very small variations in strain magnitudes between the two cases.
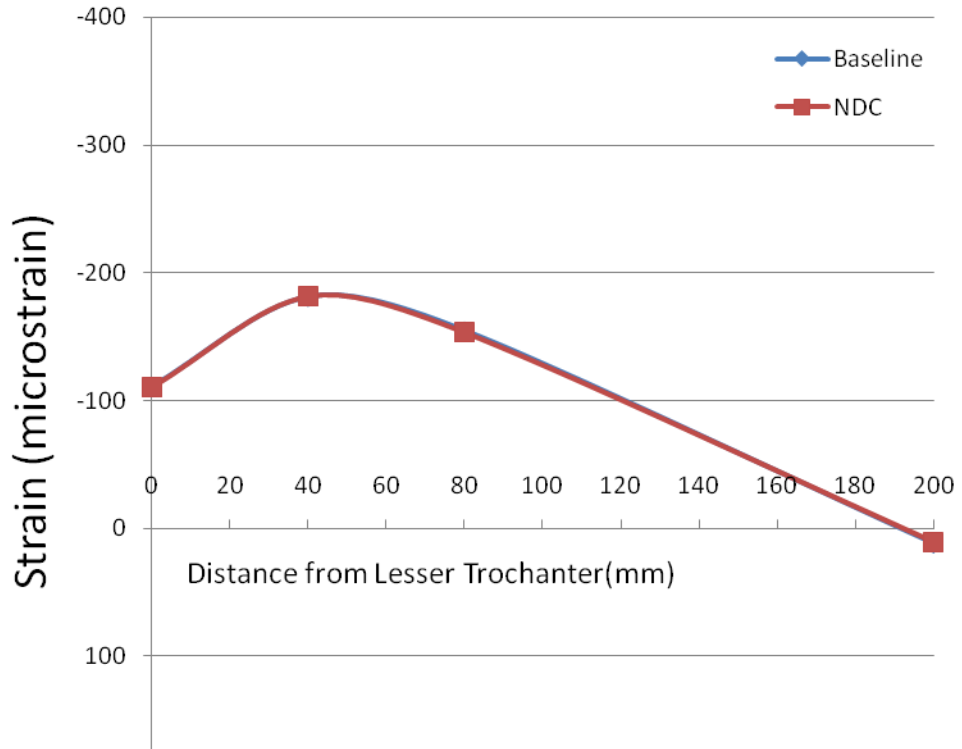
**Figure 85 The strain along the medial length of the Femur, for the range of investigated distal cement cases.**

The strain at the distal end of the Femur, for the range of investigated distal cement cases, is shown in Figure 86. There were only slight changes in distal strain magnitude between the two cases with no change in distal strain pattern.
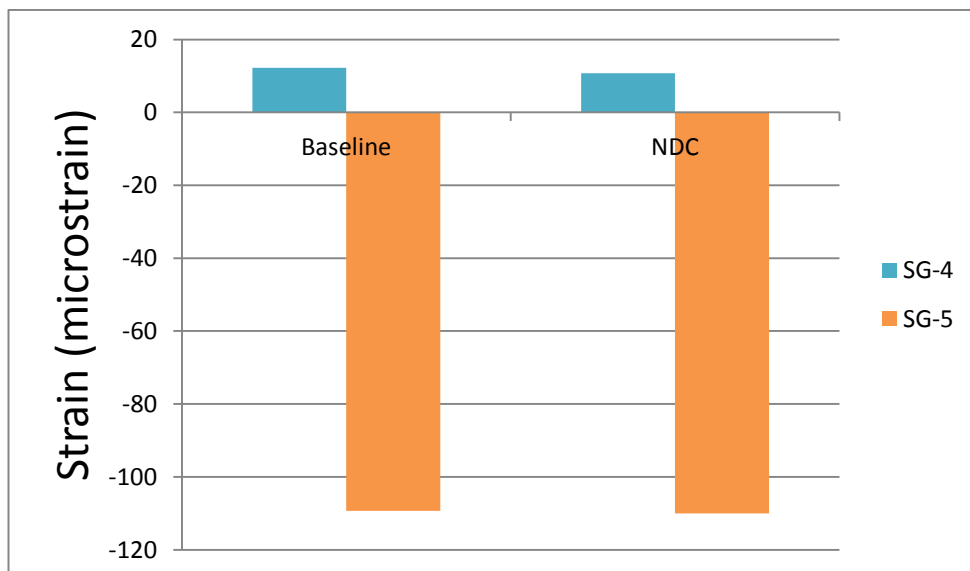
Figure 86 The strain at the distal end of the Femur for the range of investigated distal cement cases.

4.3.3.3 The effect of Distal cement on plate strain

The strain on the fixation plate, for the range of investigated distal cement cases, is shown in Figure 87. The strain pattern remained the same for both cases with only slight variations in strain magnitude.
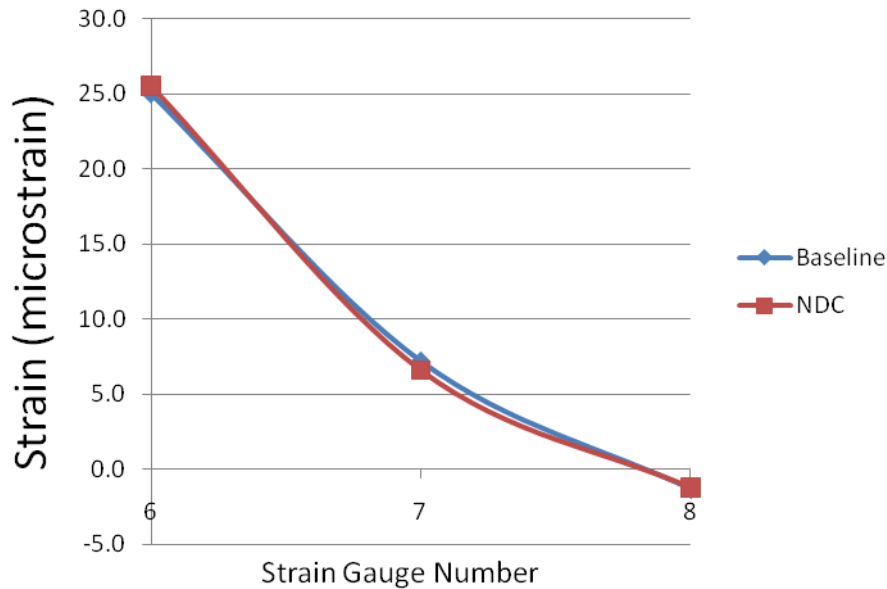
Figure 87 The strain on the fixation plate for the range of investigated distal cement cases.

4.3.3.4 Summary

The presence of cement in the medullary canal did not have an effect on overall behaviour of the constructs, with little to no difference between the investigated best and worst case scenarios. With the difference between an ideal and compromised hip replacement procedure resulting in either an empty a intramedullary canal, or one filled with cement, potentially providing extra stiffness to the distal femoral fragment, and purchase for the distal bicortical screws, a large change in behaviour was anticipated. The relatively low Young's modulus of the cement compared to the metal prosthesis and fixation construct indicates that the construct is dominated by the behaviour of the fixation instrumentation and cortical bone modulus. If the contact between the screws and plate were not modelled as a tied contact, the presence of the cement in the distal fragment may have more influence on construct behaviour.

4.3.4 Overall summary

This chapter described the methods and techniques used to create the computational model, and detailed the sensitivity studies conducted at the intact Femur, total hip replacement and stabilised periprosthetic fracture construct stages of model development.

The range of investigated methods of applying load to the construct was shown to have large effects on construct behaviour. The model was very sensitive to the method of applying load to the model and the contact surface interactions. The model was reasonable sensitive to the element type, the fracture site coefficient of friction, and the cortical bone material properties. The model was not sensitive to the method of distal fixation and the presence of cement in the medullary canal. These sensitivity results are crucial in assessing the significance of the difference between our final clinical cases. A summary of the sensitivity results are shown in Table 14.

Table 14 Summary of the computational model sensitivity to investigated factors presented in the order they were investigated. The model sensitivity to an investigated variable was expressed as a percentage and was calculated using the maximum computational value minus the minimum computational value, dividing the result by the experimental value, for both overall stiffness and strain. (COMPmax – COMPmin)/EXP

Computational Model sensitivity	Overall Stiffness %	Strain %
Intact femur model		
Loading Method	106	55
THR model		
Element Type	33	7
Distal Fixation	3	8
Contact Surface Interactions	153	9
Loading Method	49	22
Periprosthetic Fracture		
Fracture site coefficient	11	64
Cortical bone Material properties	37	42
Distal cement	1	1
Baseline Model		

4.4 Baseline model

From the results of the sensitivity studies completed in the previous sections, the most appropriate values and configurations of the investigated sensitivity variables were selected for use in the baseline model. This baseline model was then developed to investigate the clinically relevant fracture cases. The chosen values and configurations are presented in Table 15.

Table 15 The values of the sensitivity variables chosen to be used in the Baseline computational model

Computational Model sensitivity	Baseline value
Intact femur model	
Loading Method	Rigid Loading Plate
THR model	
Element Type	C3D10M
Distal Fixation	Distal cement & module
Contact Surface Interactions	Stem-Cement- Hard contact
Contact Surface Interactions	Cement-Cancellous- Tied
Contact Surface Interactions	Cement-Cortical- Tied
Loading Method	Constrained Point Load
Periprosthetic Fracture	
Fracture site coefficient	CoF- 0.3
Cortical bone Material properties	E=16.7GPa
Distal cement	No Distal Cement
Baseline Model	

Chapter 5 **Comparisons –Experimental vs. Computational**

5.1 Introduction

As was discussed in Chapter 1, a number of experimental models of periprosthetic femoral fracture (PFF) fixations have been developed [33, 77, 96] to compare various methods of fixation. There have been fewer studies that have investigated the biomechanics of PFF fixation using computational models [97-100]. Previous experimental studies investigating periprosthetic fracture fixation have compared either different fixation methods or fixation configurations. A range of loading methods has been used in previous studies with no consensus standard method used between the studies. Factors including loading method, loading angle and distal fixation techniques vary greatly between studies, making comparisons between the findings of different studies difficult. Due to the inconsistency of specimens used and variability of reported measurements, for example with many studies having chosen to report either strain or stiffness data only, comparison between the results of different studies can be difficult.

Computational models have a huge potential to examine many different fracture and fixation scenarios and identify optimum fixation methods for these types of fractures[101]. However, there is a need to first demonstrate that the modelling method is sufficiently robust for the intended purpose through a process of validation, verification and sensitivity studies.

5.1.1 Aim

This section presents the comparison of the computational models at each development step against their corresponding experimental test. The development stages at which the model was evaluated were:

- **(a)** An intact Femur - where the Femur was transversely dissected at a distance of 340 mm distal to the lesser trochanter. The load was applied to the femoral head using a smooth flat loading plate.
- **(b)** A total hip replacement (THR) - the femoral head of the specimen was removed and the proximal region prepared with a reamer. The specimen was then implanted with a cemented primary stem prosthesis (Exeter cemented hip stem V40, Stryker SA, Switzerland).
- **(c)** Periprosthetic fracture fixation (PPF)- a transverse fracture was created 10 mm distal to the tip of each stem. The fracture then were stabilised with a locking plate, secured using three uni-cortical screws proximally and three bi-cortical screws distal to the fracture.

The main area of interest was the fixation plate and its bending behaviour under load because this has previously been identified as a cause of fixation failure[20, 42, 102]. The bone strain in the region of the stem was also investigated to determine the effects of load transfer through this region. Finally, the construct stiffness was used to evaluate the overall behaviour of the specimens under realistic loading conditions.

The aim of the section was to assess the ability of the computational model to replicate the behaviour of the experimental tests, in order to provide some validation and identify where the model predictions could be used in future studies as a predictive tool.

5.2 Intact Femur- Experimental vs. Computational Comparison

This section describes the comparison between the computational modelling of the intact Femur case and the experimental data collected from the corresponding experimental intact Femur specimens. The experimental methods related to this computational study are described in Chapter 3 while the computational methods used in this study are described in Chapter 4. The accurate modelling of the intact Femur construct would be the baseline model from which the more complex instrumentation cases would be developed. Only the results at the 0° loading condition are presented. The strain gauge calibration and measurement methods were still being developed while the intact Femur specimens were tested and the strain data collected at the 10° and 20° loading conditions were incomplete.

5.2.1 Intact Femur stiffness

The overall stiffness for the experimental and computational intact Femur case is shown in Figure 88. The computational models overestimated the construct stiffness of the experimental results by 48%. The difference between the experimental and computational intact Femur stiffness was much greater than the standard deviation of the experimental results.
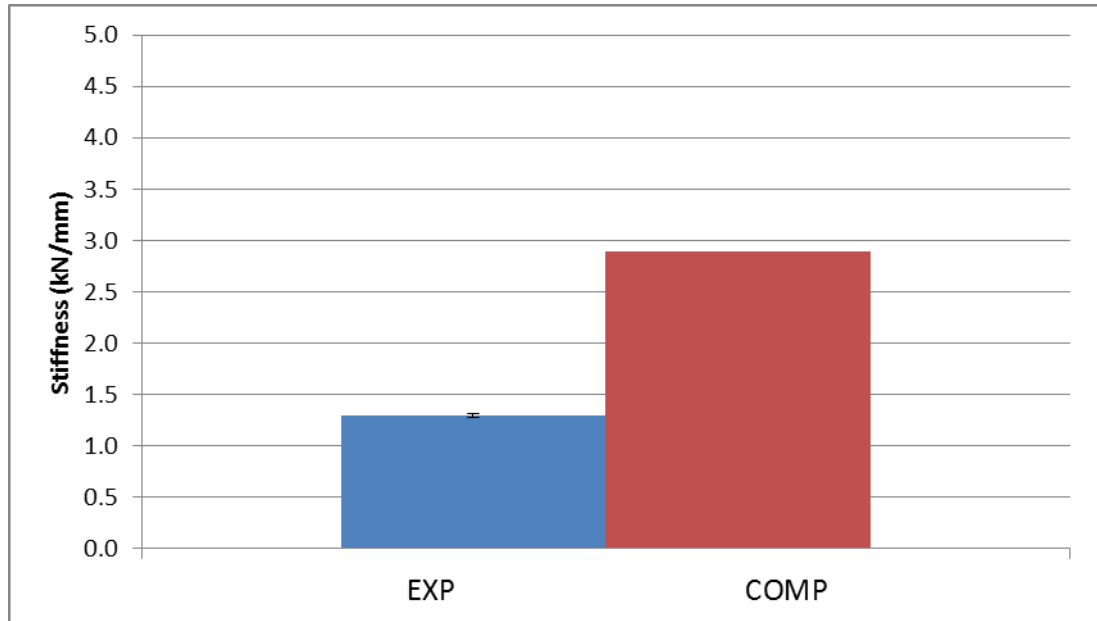
Figure 88 The experimental and computational intact Femur stiffness, for the 0° loading angle. The error bars represent the standard deviation between the six loading repeats.

5.2.2 Intact Femur bone strain comparison

The strain along the medial length of the Femur, for the intact Femur case, at the zero degree loading angle is shown in Figure 89. The overall bone strain distribution pattern compared fairly well between the experimental and computational model. There was a better match in the medial gauge locations than the very proximal and distal gauges. The difference between the experimental and computational strains was lowest at the strain gauge 2 location, while the largest difference in strain was observed is at the distally located gauge 4. The computational strains are consistently lower in magnitude than the corresponding experimental strains.
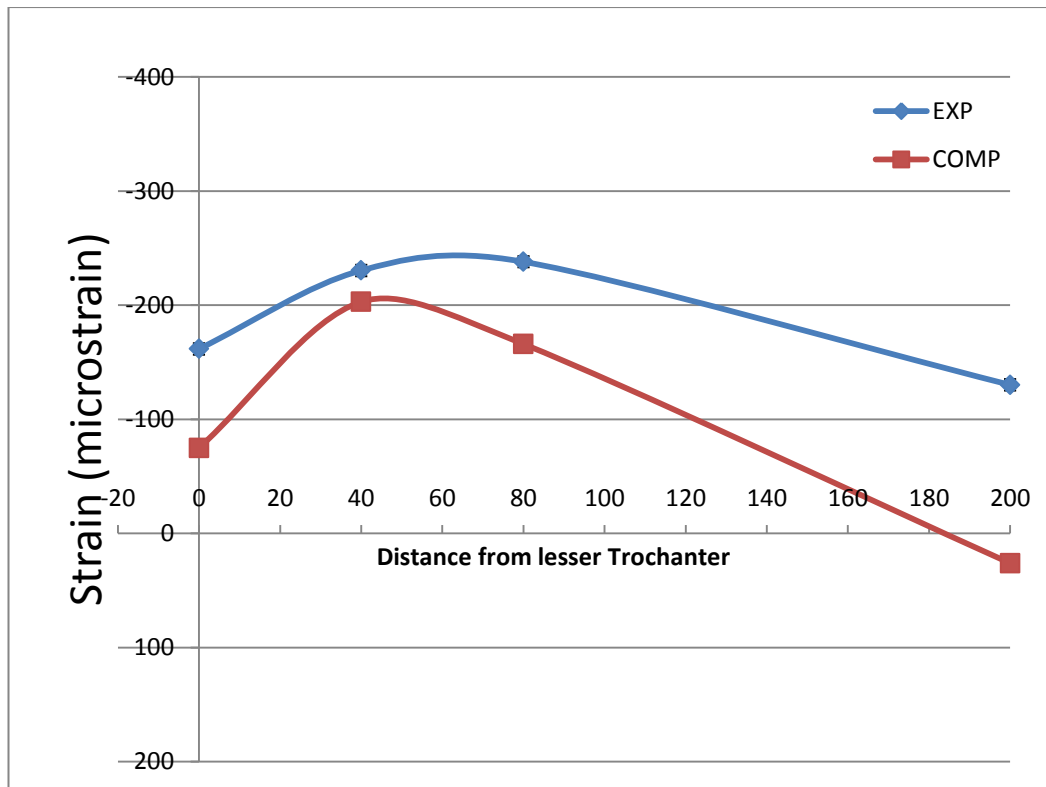
Figure 89 The strain along the medial length of the Femur, for the intact Femur case at the zero degree loading angle.

5.2.3 Intact Femur case summary

The experimental and computational results for the intact Femur case at the 0° loading angle was presented in this section.

Whilst overall strain pattern was similar, the computational model appeared to be stiffer than the experimental, leading to an underestimation in strain and overestimation in the overall stiffness. This could be due to the difficultly representing the head on flat plate boundary condition, with the difference in overall stiffness between the rigid plate and point load methods of applying the load to the Femur at 55%, section 4.2.2.1.

It was possible that the specimen material properties could be incorrect, with the stiffness overestimation due to the assigned modulus of the Sawbone being too high. However, since the modulus and strain are inversely proportional, this alone is unlikely to be the reason for such a large disparity between the results.

5.3 Total Hip Replacement- Experimental vs. Computational Comparison

This section describes the comparison between the computational modelling of the total hip replacement case and the experimental data collected from the corresponding experimental specimens. The total hip replacement models included the addition of the prosthesis stem and cement mantle compared to intact Femur model described in the previous section. The accurate modelling of the total hip replacement case was an important step towards the development of the plated periprosthetic fracture fixation models, because the inclusion of the fracture and plate fixation in addition to the prosthesis stem and cement mantle would have introduced too many variables to the model in one step, and could have made understanding and quantifying of the influence of the different components much more difficult.

5.3.1 THR Overall construct stiffness

The overall stiffness values for the experimental and computational total hip arthroplasty case over the three different loading angles are shown in Figure 90. As with the intact Femur case from the previously described section, section 5.2, the computational models consistently overestimated the construct stiffness of the corresponding experimental tests. The mean overall stiffness difference between the experimental and computational results over the investigated loading angles was 55%. The differences between the results were much greater than the standard deviation over the loading repeats of the experimental samples.

The difference between the experimental and computational stiffness was lowest at the anatomic 10° loading case while the greatest was at the 20° loading case. Comparing the overall stiffness patterns with respect to the loading angles, the same pattern was seen for both the experimental and computational results, with the highest stiffness seen at the 10° loading case while the lowest was seen at the 20° loading case.
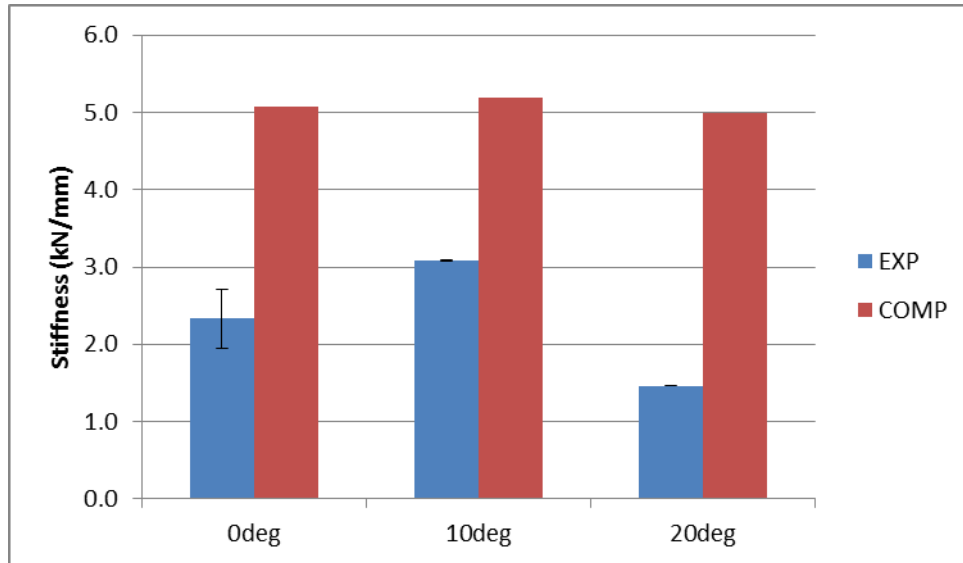
Figure 90 The experimental and computational THR overall construct stiffness, for the 0° 10° and 20° loading angles. The experimental error bars represent the standard deviation between the six loading repeats.

5.3.2 Bone Strain comparison strain along the medial length of the Femur for the range of investigated loading angles for the THR case

0°- The strain along the medial length of the Femur, for the THR case, for the zero degree loading angle is shown in Figure 91. The bone strain patterns compared well at the medial gauges in the region of the prosthesis stem, while larger differences in strain were observed at the very proximal and distal gauges. The difference between the experimental and computational strains was lowest at the strain gauge 2 location, while the largest difference in strain was observed at the distally located gauge 4. The computational strains were consistently lower in magnitude than the corresponding experimental strains.

10°- The strain along the medial length of the Femur, for the THR case, for the ten degree loading angle is shown in Figure 91. Similar to the zero degree loading angle results, the larger differences in strain between the experimental and computational results were observed at the very proximal and distal gauges, while smaller differences in strain were seen at the medial gauges in the region of the prosthesis stem. Unlike the zero degree results, while most of the computational strains were lower than the corresponding experimental strains, the computational strain at gauge 2 was higher than the experimental strain. The differences between the

experimental strains in the ten degree loading case were lower than the zero degree results.

20°- The strain along the medial length of the Femur, for the THR case, for the twenty degree loading angle is shown in Figure 91. Unlike the previous loading angle results for the THR case, most of the computational strains were higher in magnitude than the corresponding experimental strains, however, the computational strain at gauge 1 remained lower than the experimental strain. Unlike the strain patterns observed at the previous loading angles, the experimental and computational strain patterns along the medial length of the Femur between experimental and computational results were similar from the gauge 2 location to the distal gauge.
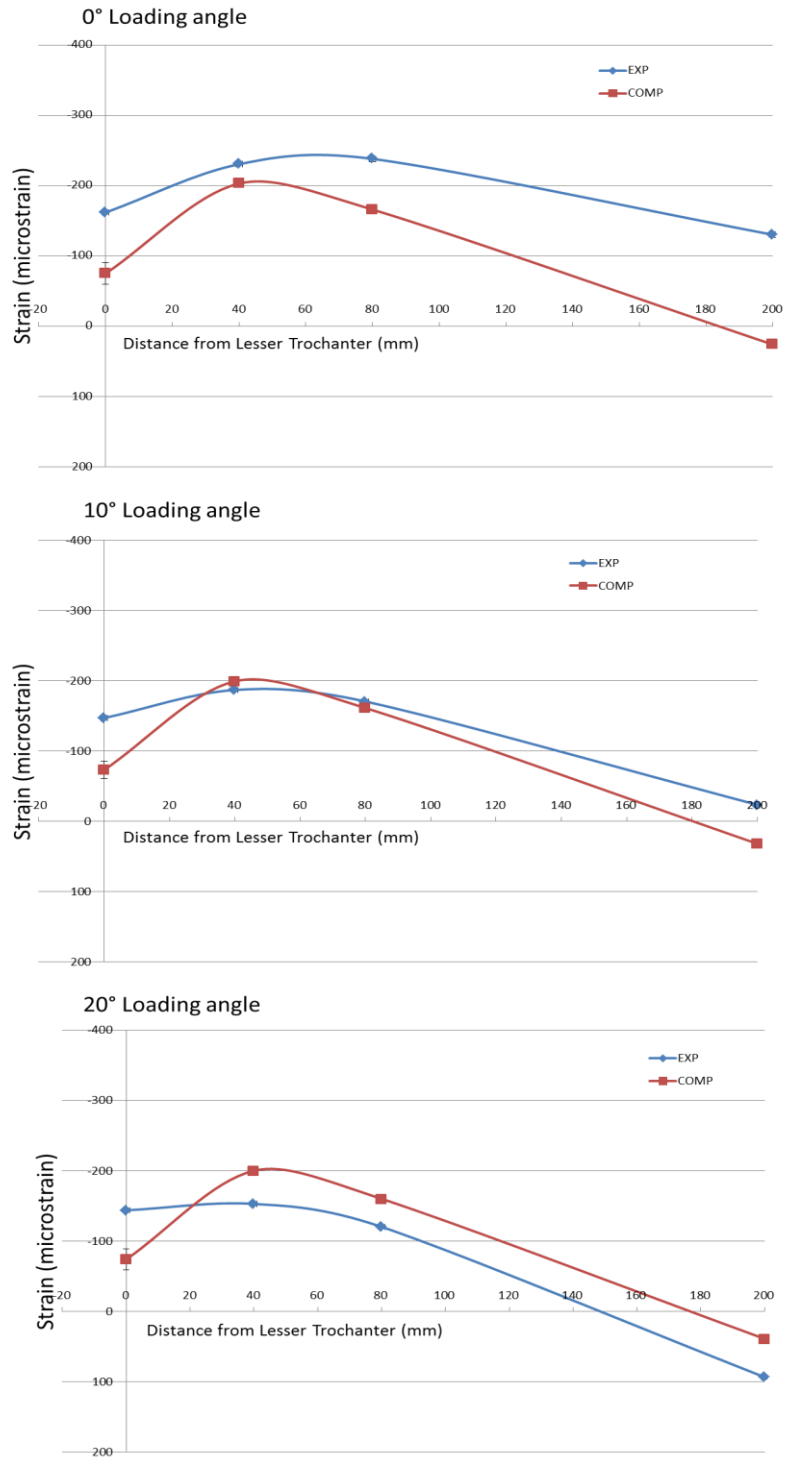
Figure 91 The strain along the medial length of the Femur, for the THR case, over all of the investigated loading angles.

5.3.3 Bone Strain comparison strain at the distal end of the Femur for the range of investigated loading angles for the THR case

0°- The strain at the distal end of the Femur, on both the medial and lateral sides, for the 0° loading case, is shown in Figure 92. The experimental distal strain pattern observed is opposite to that seen in the computational results. The strain at gauge 4, located on the medial side, was in compression in the experimental results and in tension in the computational results, while the strain at gauge 5, located on the lateral side, was in tension in the experimental results and in compression in the computational results. There were large differences in strain magnitude for both gauge locations between the experimental and computational results.

10°- The strain at the distal end of the Femur, on both the medial and lateral sides, for the 10° loading case, is shown in Figure 92. The experimental distal strain pattern observed was different to that seen in the computational results. The strain at gauge 4, located on the medial side, was in compression in the experimental results and in tension in the computational results, while for both the experimental and computational results, the strain at gauge 5, located on the lateral side was in compression.

20°- The strain at the distal end of the Femur, on both the medial and lateral sides, at the 20° loading case is shown in Figure 92. The same strain patterns were seen for both the experimental and computational results. Both strains on the medial side, gauge 4, were in tension, while both strains on the lateral side, gauge 5, were in compression.
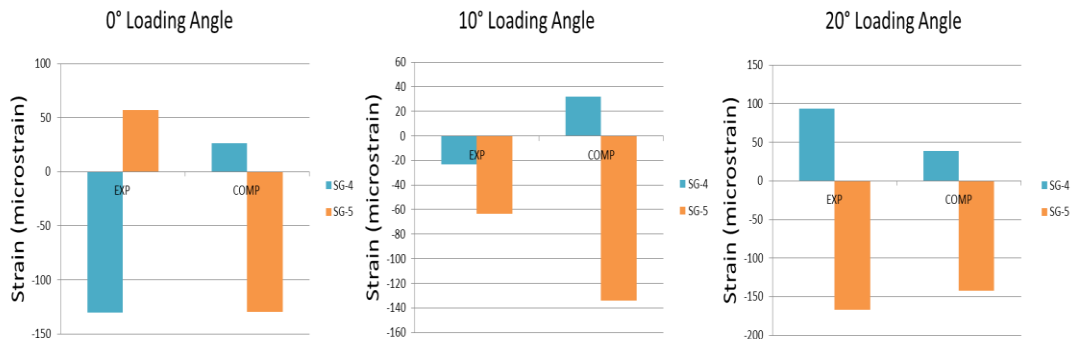
Figure 92 The strain at the distal end of the Femur, for the THR case, over all of the investigated loading angles.

5.3.4 Agreement between EXP and COMP Strain Plots

X-Y graphs plotting experimental strain against computational strain, for the THR case, over all of the investigated loading cases are shown in Figure 93. The Bland-Altman strain plots, for the THR case, over all of the investigated loading cases are shown in Figure 93.

The loading angle with the best agreement between the experimental and computational strain results was the 20° loading case, with an R² value of 0.74, while the worst agreement was seen at the 0° loading case.

For the 0° loading angle, there is very poor agreement between the experimental and computational results. The data points with the worst correlation are for the gauges located distally on the Femur.

For both the 10° and 20° loading angles, there is better correlation between the experimental and computational data sets. There are no specific points where there are excellent matches, however, the general correlation is much better than for the 0° loading angle.
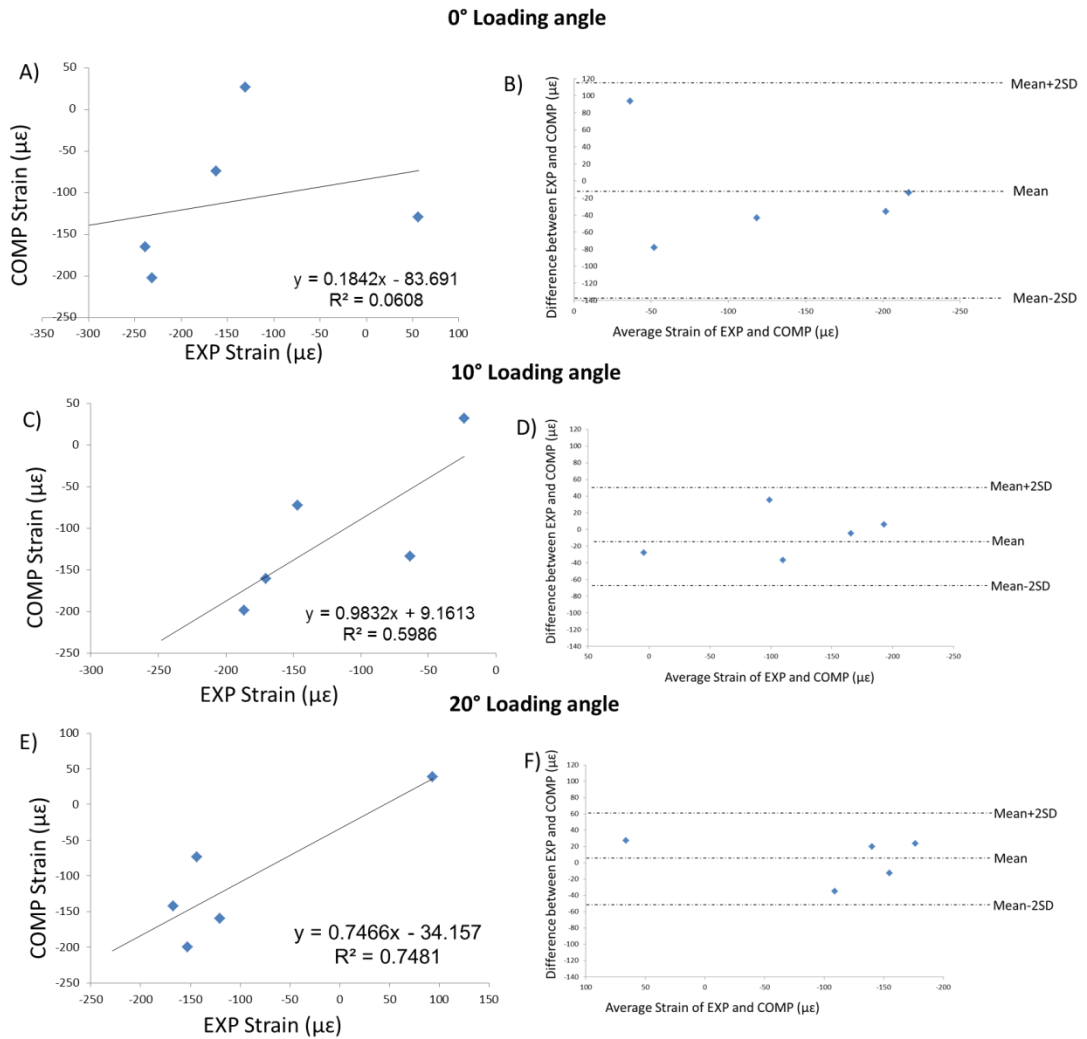
Figure 93 X-Y strain- EXP vs. COMP graphs, and Bland-Altman strain plots for all investigated loading angles

5.4.5 THR Summary

There was a reasonable level of agreement between the experimental and computational strains. Following the stiffness behaviour identified in the intact Femur models, there was an overestimation of overall construct stiffness at all investigated loading angles.

The closest match between computational and experimental strains and overall construct stiffness occurred at the anatomically realistic 10° loading angle. For all loading angles, best match at strain gauges positioned proximally on the Femur, in the region of the prosthesis stem.

The computational model does not match well at the distal gauge locations. The changes in strain pattern along the medial length of the Femur observed experimentally at the different loading angles were replicated reasonably in the models. The pattern of construct stiffness with respect to loading angle matches well with experimental results.

Interactions

The interaction between the cement and the cancellous bone is complicated *in vivo*, with interdigitation of the cement into the bone providing the stability and the bond between cement and bone surface at a minimum[103]. Neither the artificial bone nor its computational representation fully replicated this behaviour. Further experimental testing of this interface in isolation would be required to gain enough information to make a more sophisticated computational representation of the interface viable. The assumption of a simple geometry and perfect bond limit the computational representation of both artificial and real bone.

Distal bone strain and boundary conditions

The differences between computational and experimental distal strain (at Gauges 4 and 5) for all investigated cases are likely due to the differences in boundary conditions at the distal end of the Femur. The distal cement, grub screws and module were included in the model with the aim of making these conditions as realistic as possible[97, 100], but the interfaces remain idealised and cannot represent the inevitable micro-movement that occurs experimentally. As the loading angle was altered, the greatest changes in strain were seen in the distal gauges, with less effect at the gauges in the region of the stem. This would indicate the strain in the region of the stem tip, where the fracture and fixation construct are positioned, is less sensitive to any boundary condition effects than the distal end of the Femur. Therefore care should be taken in both experimental and computational cases in interpreting strain information near to this boundary. Equally, key aspects of the construct, should not be placed close to the distal boundary conditions.

5.4 PPF- Experimental vs. Computational Comparison

This section describes the comparison between the computational modelling of periprosthetic fracture fixation case and the experimental data collected from the corresponding experimental specimens. Developed from the total hip arthroplasty models detailed in the previous section, these models have the addition of a transverse fracture around the prosthesis tip, stabilised using a fixation plate and screws.

5.4.1 PPF overall construct stiffness

The construct stiffness values for the experimental and computational plated periprosthetic fracture fixation case over the three different loading angles are shown in Figure 94. The FE model outcomes showed the same trends in

behaviour as the experimental stiffness results, with the highest and lowest overall stiffness at the 10° and 20° loading angles respectively, however the computational models consistently overestimated the overall stiffness found experimentally. The lowest difference between the experimental and computational overall stiffness was seen at the 10° loading angle while the greatest difference was seen at the 20° loading angle.
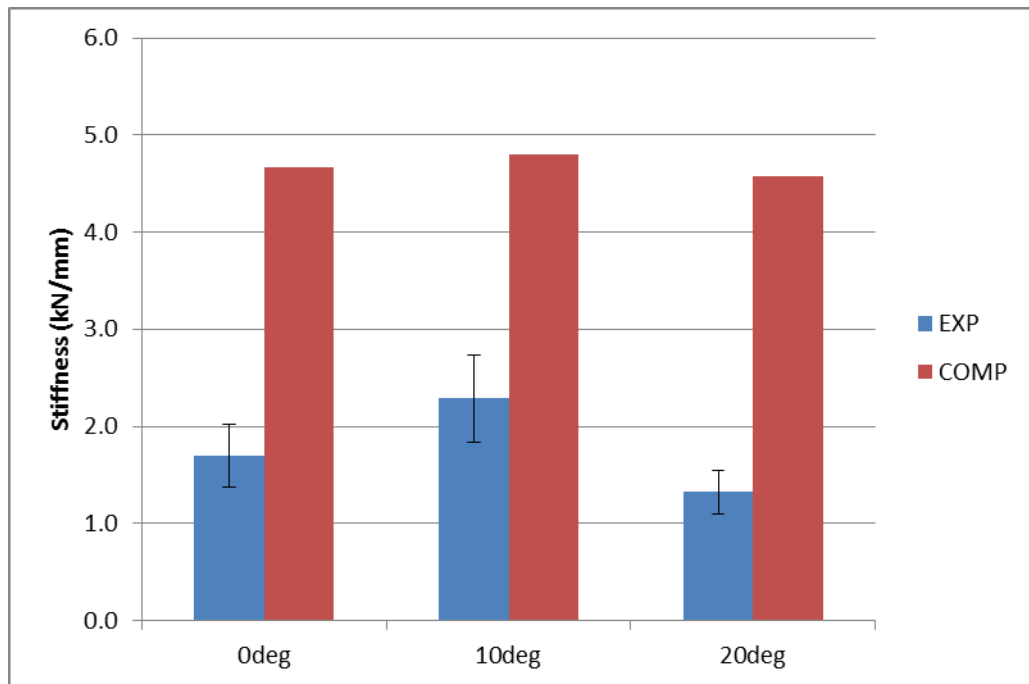
Figure 94 The experimental and computational intact Femur stiffness, for the 0° loading angle. The error bars represent the standard deviation between the six loading repeats

5.4.2 Bone Strain comparison strain along the medial length of the Femur for the range of investigated loading angles for the PPF case

0°- The strain along the medial length of the Femur, for the plate case, for the zero degree loading angle is shown in Figure 95. The experimental and computational bone strain patterns along the medial length of the Femur compared well for the proximal strain gauges, i.e. those located in the region of the stem. The strains at Gauges 1 and 2 were well matched. There was a mismatch at both gauge 3, located near the tip of the stem, and at gauge 4, located distally down the medial side, with the computational models not replicating the high strain recorded experimentally at these locations.

10°- The strain along the medial length of the Femur, for the Plate case, for the ten degree loading angle is shown in Figure 95. Similar to the zero degree loading angle results, the computational bone strain patterns in the proximal region of the prosthesis stem, gauges 1 and 2, compared well with the experimental results. There was still a mismatch in the bone strain at gauge location 3, located near the tip of the stem, where the high strains recorded experimentally were not seen in the computational models. However, unlike the zero degree loading case, the strain at the distally located gauge 4 matched well between the experimental and computational results.

20°- The strain along the medial length of the Femur, for the Plate case, for the twenty degree loading angle is shown in Figure 95. The magnitudes and pattern of the strain for the strain gauges located in the region of the stem correlated well between the experimental and computational bone strain results. For these gauges, the experimental strains were slightly higher for gauges 1 and 3, compared to the computational results, with the experimental strain recorded at gauge 2 being slightly lower than the computational model. The strain mismatch at the gauge 3 location around the stem tip seen in both previous loading angle tests was greatly reduced. While both the experimental and computational strain at the gauge 4 location were both in compression, there was a mismatch in strain magnitude, with the experimental strain in much greater compression than the corresponding computational results.
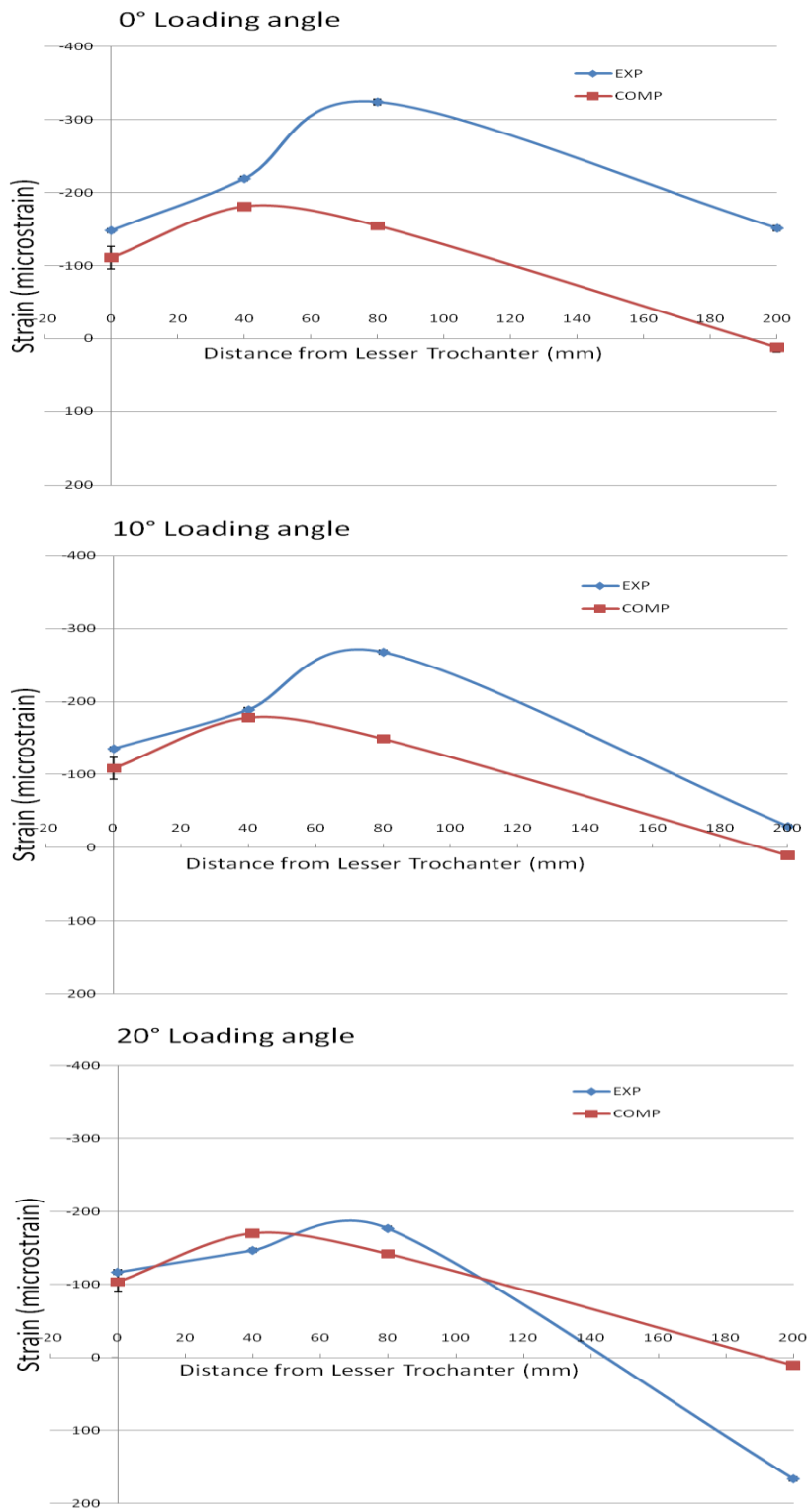
Figure 95 The strain along the medial length of the Femur, for the PPF case, over all of the investigated loading angles.

5.4.3 Bone Strain comparison strain at the distal end of the Femur for the range of investigated loading angles for the PPF case

0°- The strain at the distal end of the Femur, on both the medial and lateral sides, is shown in Figure 96. The strains for the gauges located at the distal end of the Femur did not compare as well between the experimental and computational results. The computational models were not able to replicate the same strain magnitudes or patterns as the experimental results for these gauges. The strain at gauge 4, located on the medial side, was in compression in the experimental results and in tension in the computational results. The strain at gauge 5, located on the lateral side, was in tension in the experimental results and in compression in the computational results. There were large differences in strain magnitude for both gauge locations between the experimental and computational results.

10°- The strain at the distal end of the Femur, on both the medial and lateral sides, at the ten degree loading case is shown in Figure 96. The experimental strain pattern observed at the distal femoral end was different to that seen in the computational results. In the experimental results, both gauges were in compression, while the computational results predicted the medially located gauge 4 in slight tension, with the laterally located gauge 5 in compression.

20°- The strain at the distal end of the Femur, on both the medial and lateral sides, at the twenty degree loading case is shown in Figure 96. The same strain patterns were seen for both the experimental and computational results. Both strains on the medial side, gauge 4, were in tension, while both strains on the lateral side, gauge 5, were in compression. However, the experimental strain magnitudes are greater than those in the computational model.
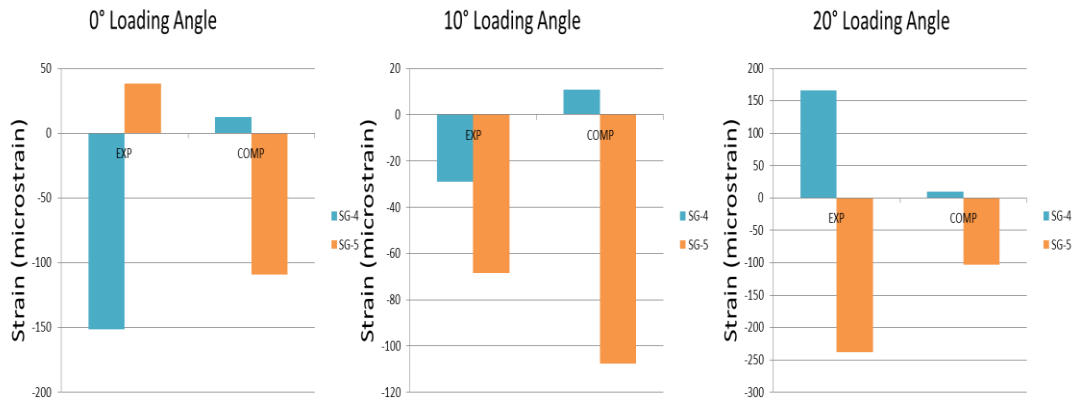
Figure 96 The strain at the distal end of the Femur, for the PPF case, over all of the investigated loading angles.

5.4.4 Plate Strain comparison strain for the range of investigated loading angles for the THR case

0°- The experimental and computational strains on the locking plate, at the zero degree loading angle, are presented in Figure 97. The values of the experimental and computational strain were of the same magnitude and there was a reasonable level of agreement between the respective strain patterns. The plate strain matched better at the most proximal and distal gauges, 6 and 8, positioned around the empty screw holes bridging the fracture gap, than for Gauge 7, located between the empty screw holes.

10°- The experimental and computational strains on the locking plate, at the ten degree loading angle, are presented in Figure 97. There were similar strain patterns between the experimental and computational strain, and while the magnitudes of the strains were similar, the computational models consistently underestimated the experimentally measured strains. The best correlation was at the most proximal gauge location, gauge 6, with the worst correlation occurring at gauge 7.

20°- The experimental and computational strains on the locking plate, at the twenty degree loading angle, are presented in Figure 97. There was a reasonable match in strain patterns between the experimental and computational strains. Similar to the previous loading angles, stain at gauges 6 and 7 were both in tension, while the strain at the most distally located gauges was in slight compression.
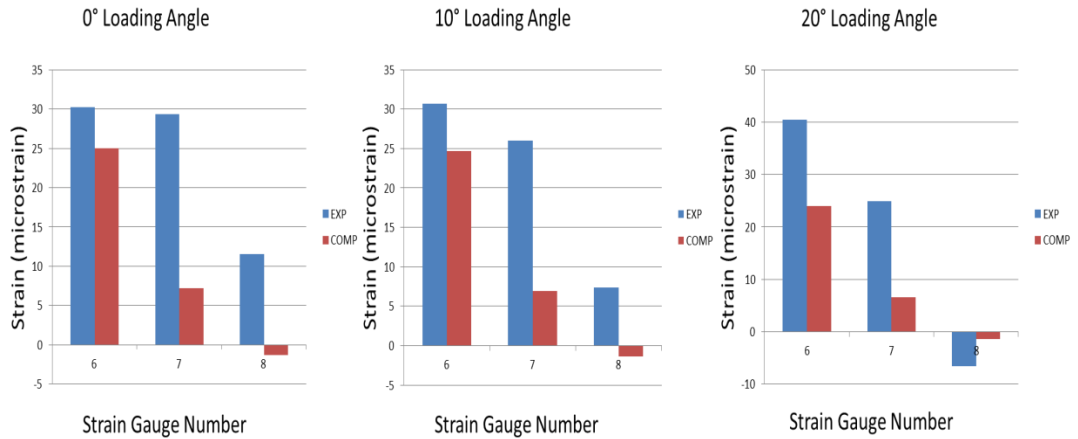
Figure 97 The strain on the locking plate, for the PPF case, over all of the investigated loading angles.

5.4.4.1 Detailed Computational Plate Strain

The computational strain along the central length of the plate upper surface, for 10° of adduction in the frontal plane, is plotted in Figure 98. Clusters of points on the graph correspond to sections of the plate between screw holes. This allows the trends in strain across the areas of the experimental strain gauges can be seen in detail.

It was found from the computational model that there were rapid changes in strain in the region of the plate bridging the fracture. This suggests that the experimental strain at Gauge 7 could be sensitive to factors such as gauge placement and gauge orientation. An underestimation of strain at the gauge located in the middle of the plate could be a result of rapid changes in strain magnitude in this region of the plate. There were also large changes in strain across the plate width, suggesting that the mismatch could have been due to

misalignment or uneven adhesion of a strain gauge.
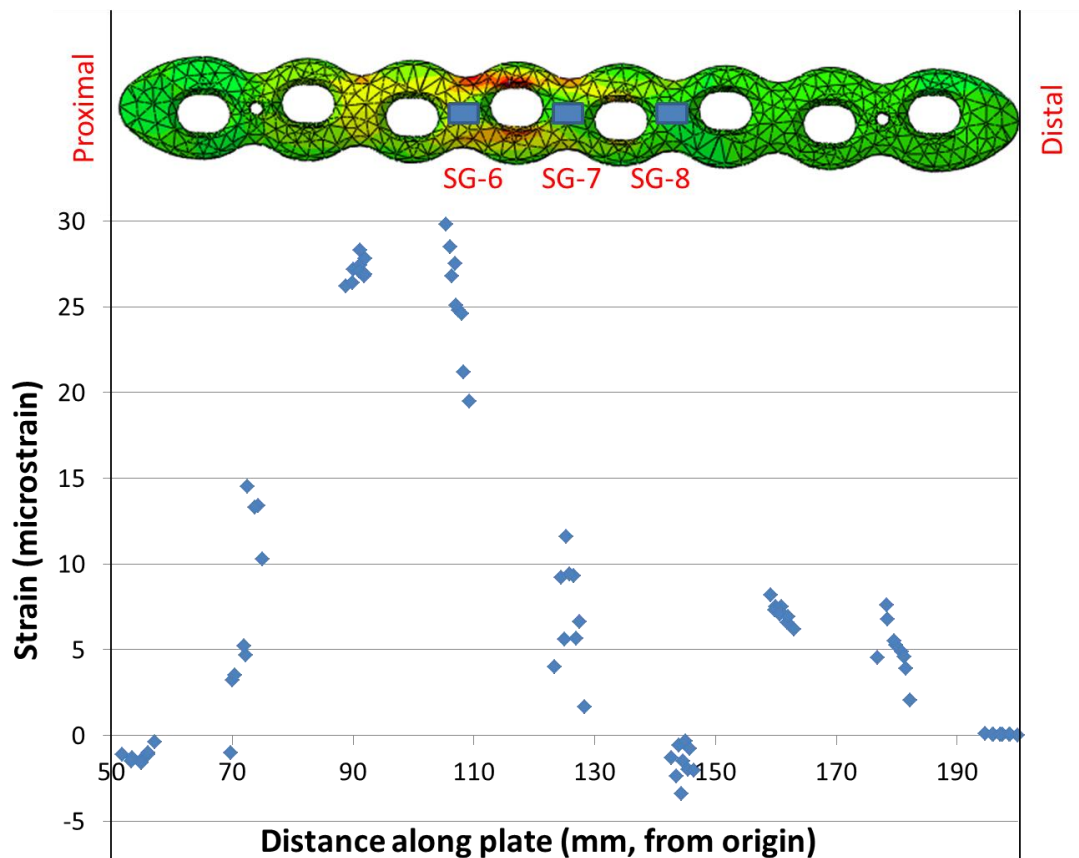
Figure 98 Computational strain along the central length of the plate upper surface for the 10° loading case. Clusters of points on the graph correspond to sections of the plate between screw holes.

5.4.5 Agreement between EXP and COMP Strain Plots

X-Y graphs plotting experimental strain against computational strain, for the PPF case, over all of the investigated loading cases are shown in Figure 99. The Bland-Altman strain plots, for the PPF case, over all of the investigated loading cases are shown in Figure 99.

The loading angle with the best agreement between the experimental and computational strain results was the 10° loading case, with an R² value of 0.82. There are no specific points where there are excellent matches, however, no points were poorly matched either.

The agreement for the 20° loading case was satisfactory with an R² value of 0.72. The three data points with the worst correlation were for the gauges located distally on the Femur, and the gauge located on the fixation plate bridging the fracture.

The worst agreement was seen at the 0° loading case where there was very poor agreement between the experimental and computational results. The three data points with the worst correlation are for the gauges located distally on the Femur, and the most distal gauge located in the region of the prosthesis, strain gauge 3.
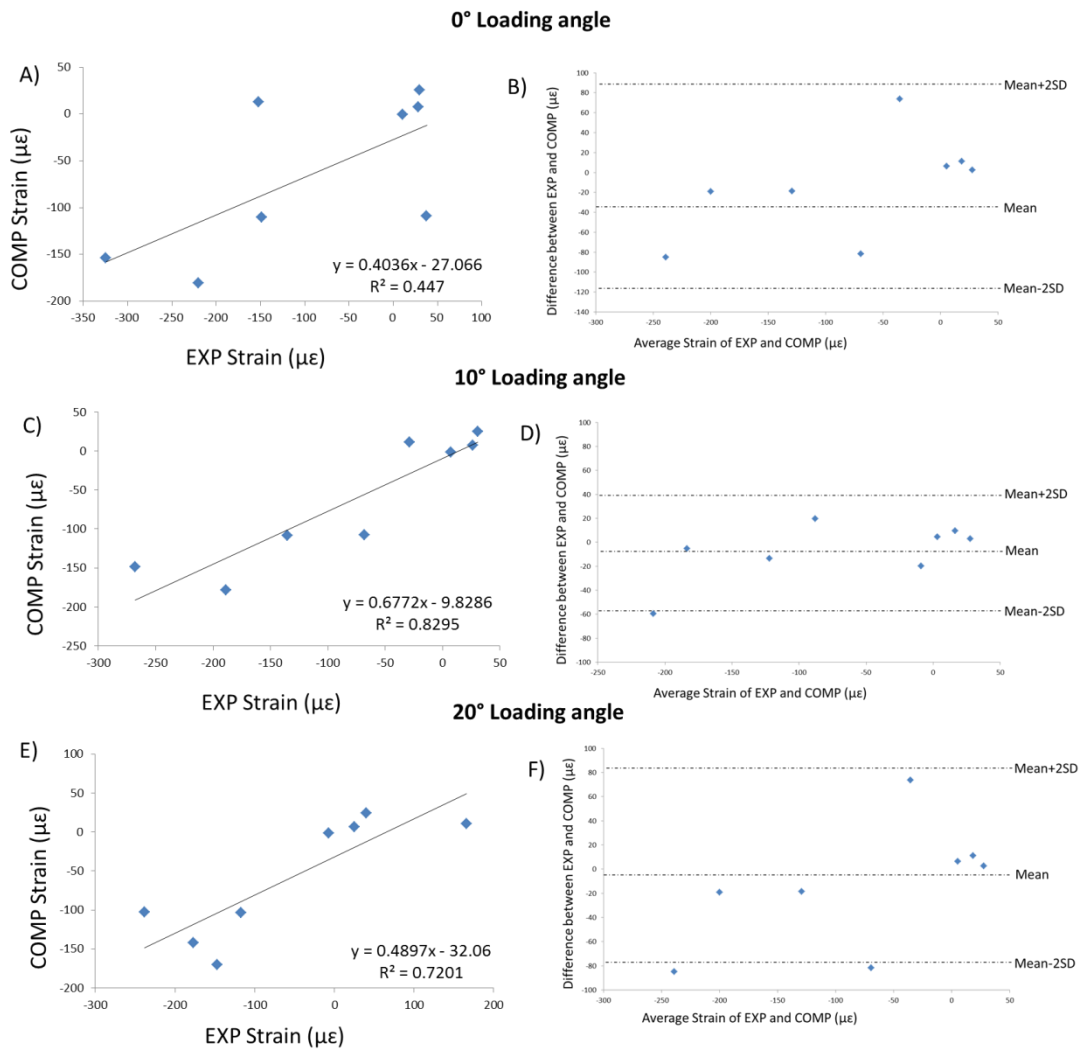
Figure 99 X-Y strain- EXP vs. COMP graphs, and Bland-Altman strain plots for all investigated loading angles

5.5.5 Plate Summary

The values of the experimental and computational strain were of the same magnitude and there was a reasonable level of agreement between them, although the computational values always slightly underestimated the experimental ones. The closest match between computational and experimental strains occurred at the anatomically realistic 10° loading angle. The changes in strain pattern on the plate observed experimentally at the different loading angles were also replicated in the models. The pattern of construct stiffness with changing loading angle was well match between experimental computational models.

Proximal bone strain and fracture representation

In the plate model, although the values of bone strain at the most proximal two gauge positions compared well between the computational and experimental results in both pattern and magnitude, the strain near to the fracture showed a mismatch. This difference in medial strain pattern is not observed in either the intact Femur or THR cases and is therefore likely that the bone strain in that area is dominated by the way in which the fracture is simulated. In the computational model, this was idealised as a contacting interface, whereas in the experiment, the fracture could never be perfectly reduced, and some areas were likely to be either initially not in contact or under some pre-strain. Future tests using this model would need to consider the effect of the modelling assumptions at the fracture site and perhaps simulate several interface conditions to cover a range of possible physical scenarios, resulting in different local stress/strain fields.

Plate strain prediction

Since this model development focuses on the reported locking plate failures, the most important mechanical behaviour for the model to replicate is that of the locking plate itself. The computational strains on the locking plate were found to correlate well with the experimental results, Figures 95, 99. An underestimation of strain at the gauge located in the middle of the plate could be a result of rapid changes in strain magnitude in this region of the plate, as illustrated in Figure 98. There were also large changes in strain across the plate width, suggesting that the mismatch could have been due to misalignment or uneven adhesion of the strain gauge. In general, the results indicate that the model is able to predict the magnitude of the strain in the plate and therefore the model could be used to compare the likelihood of plate failure between different fixation scenarios [66, 100].

Construct stiffness and over-constraint

The computational model consistently overestimated the construct stiffness and displayed smaller changes in strain with loading angle than were seen experimentally. The idealised distribution of homogenous material properties, the completely fixed boundary conditions and the tied contacts applied, all contribute to an overall increase in stiffness compared to the experimental specimen. This finding is not unique to the current study, and in a parallel study, this effect was examined and it was found that making the screws less constrained did affect the overall stiffness[104]. This stiffness overestimation was also observed during all the development stages of this model, indicating that the majority of the over constraint is independent of the fracture and plate fixation. During the development of this model, a series of sensitivity tests were undertaken but none succeeded in reducing the construct stiffness to the experimental level, Table 14 .

Interface assumptions and model scope

The computational model contained a large number of interfaces where assumptions and simplifications were made in order to represent the behaviour efficiently. The attachment of the screws to both the plate and the bone was represented by a simple geometry with relative movement prevented [66, 100]. The simplification of the bone screws by removing the screw threads and modelling the major diameter of the screws, significantly reduced computational costs but may have contributed to an overall stiffening of the construct[105]. Therefore, the model cannot be used to predict failure modes where micro-movement of the screws is a crucial aspect [24].

5.5 Summary of validation

The aim of this work was to assess the accuracy of a computational model of periprosthetic femoral fracture through comparison with experimental tests using artificial Femurs. The experimental and the computational models included necessary simplifications from the in vivo case, in terms of boundary conditions, interactions, loads and materials. However, the match between these aspects of the two models was kept as close as possible in order to strengthen the comparability of the two. The accuracy of the computational plate strain predictions provided assurance that the load sharing behaviour between the plate and the bone represented the experimental behaviour. The assessment of a range of loading angles during validation provided confidence that the model accuracy is not specific to a particular load distribution, although the 10° case did provide the closest match. It was found that the strain and stiffness behaviour of the experimental specimens varied greatly as the loading angle was changed.

The trends, but not the magnitudes of those changes, can be predicted using the computational model.

In conclusion, the periprosthetic fracture fixation model developed in this study could be used to investigate a range of clinical scenarios. The outcomes of this work indicate that the model could predict the magnitude of the strain in the plate and hence the likelihood of plate fracture, as well as assessing the relative stiffness of different fixation scenarios. Caution is needed however in measuring the local bone behaviour around the fracture and at the distal end of the Femur, since these outputs will be highly dependent of the way that the fracture and boundary conditions are represented. The model would be able to identify and predict changes in strain and stiffness between a set of comparative cases and be used to comment on their relative biomechanical performances. In the next chapter, the model will be used for to investigate periprosthetic fracture configurations and evaluate their effect on construct behaviour, Figure 100.
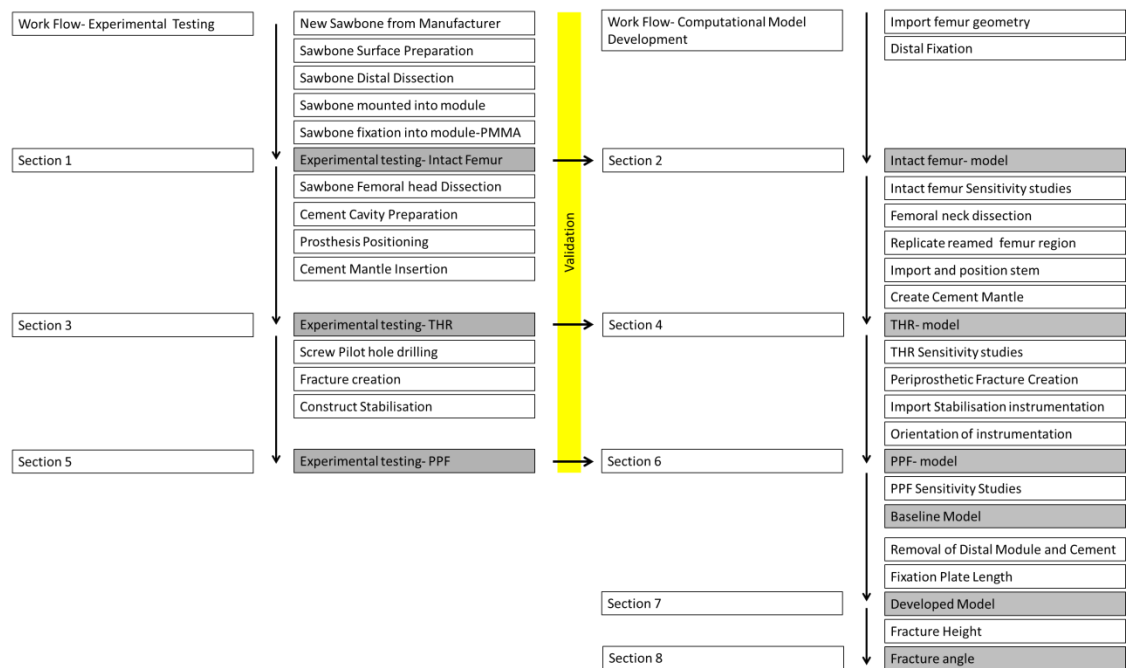
Figure 100 Full Work plan diagram

Chapter 6 **Computational studies**

6.1 Introduction

This chapter presents the results of the initial model development stages away from the baseline computational model. A computational model has been validated against experimental data and shown to be reasonably accurate in the region of the fracture. The intended application of the model was an investigation of the effects of fracture angle on stabilised construct behaviour. The eight hole plates (8HP) were available for stabilising the fractured specimens in the experiments, however, locking plates with 10 holes (10HP) are more clinically relevant. The increase in fixation plate length reduced the distance between the distal end of the plate and the distal boundary conditions. Previous sections of this study have identified that our model is not accurate in regions immediately adjacent to the boundary conditions, section 5.4.5. The effects of extending the model to increase this distance were investigated.

There were certain compromises made when selecting the loading set up and instrumentation configuration used to support and stabilise the periprosthetic fracture specimens. These compromises in validation methodology were made to optimise the comparison and validation process between the experimental tests and computational models. There were two main limiting factors involved in selecting the most suitable testing configuration in our study

The first factor was the distal fixation method used to support the specimens within the experimental setup. With the distal module and supporting potting cement included in the validation set up supporting the distal 80 mm of the femoral specimens, there was a 160 mm distance between the fracture site and the distal module. With a 170 mm length plate positioned bridging the fracture, there was approximately 75 mm between the distal end of the plate and the top of module. With the intention of investigating the effect of fracture height on construct biomechanics, the repositioning of the fracture distally down the Femur and the resulting position of the fixation plate might result in the distal end of the plate being too close to the module and being influenced by the distal boundary conditions. In order to avoid this possibility, this section will assess effect of removing the distal module and potting cement, and allow bending to occur in the previously supported 80 mm of distal Femur.

The second factor was the length of the locking fixation plate, and instrumentation combination used to stabilise the fracture. The

instrumentation combination used in the validation study used an 8 hole locking plate, with three unicortical screws used in the three most proximal plate holes, three bicortical screws used in the three most distal plate holes, and two empty plate holes bridging the fracture. This combination will be referenced as the baseline model. There was no standard combination previously used in literature for evaluation of periprosthetic fracture fixation constructs. The preferable combination for our fracture configuration used clinically would use a 10 hole locking plate, with four unicortical screws used in the four most proximal plate holes, four bicortical screws used in the four most distal plate holes, and two empty plate holes bridging the fracture. This section will assess the effect of replacing the 8 hole plate instrumentation combination used in the validation study with a 10 hole plate.

6.2 Method and test cases

Three test cases were investigated in this comparison: an 8-hole plate with the distal module (baseline), a 10-hole plate with the distal module, and a 10-hole without the distal module. Each of the investigated cases are shown in Figure 101.

The majority of the computational methods used in this study are described in Chapter 4, while the process of validating the baseline computational model from which these models were developed from is described in Chapter 5.

All of the cases included a transverse fracture and the 10-hole plates were placed with the same length of plate above and below the fracture, just as was done for the baseline 8-hole case. In these cases the 8 hole plate used in the baseline model was removed and replaced with a 10 hole plate. The placement of the plate was kept consistent, with the centre of the 10 hole plate bridging the transverse fracture. The three proximal unicortical screws and three distal bicortical screws used in the baseline model were retained, with an additional unicortical and bicortical screw added in the most proximal and most distal screw holes on the 10 hole plate.

Each case was loaded at 10° in the frontal plane. In test cases which include the distal module, this area was modelled as described in Section 4.1.8. Where the module was removed there was a maximum translation of the distal edge of the locking plate of 70 mm, equivalent to two femoral diameters, this left a distance of 80 mm from the distal end of the locking plate and the end of the distal Femur. The flat base of the Femur was fully fixed in all axes (encastre boundary condition).
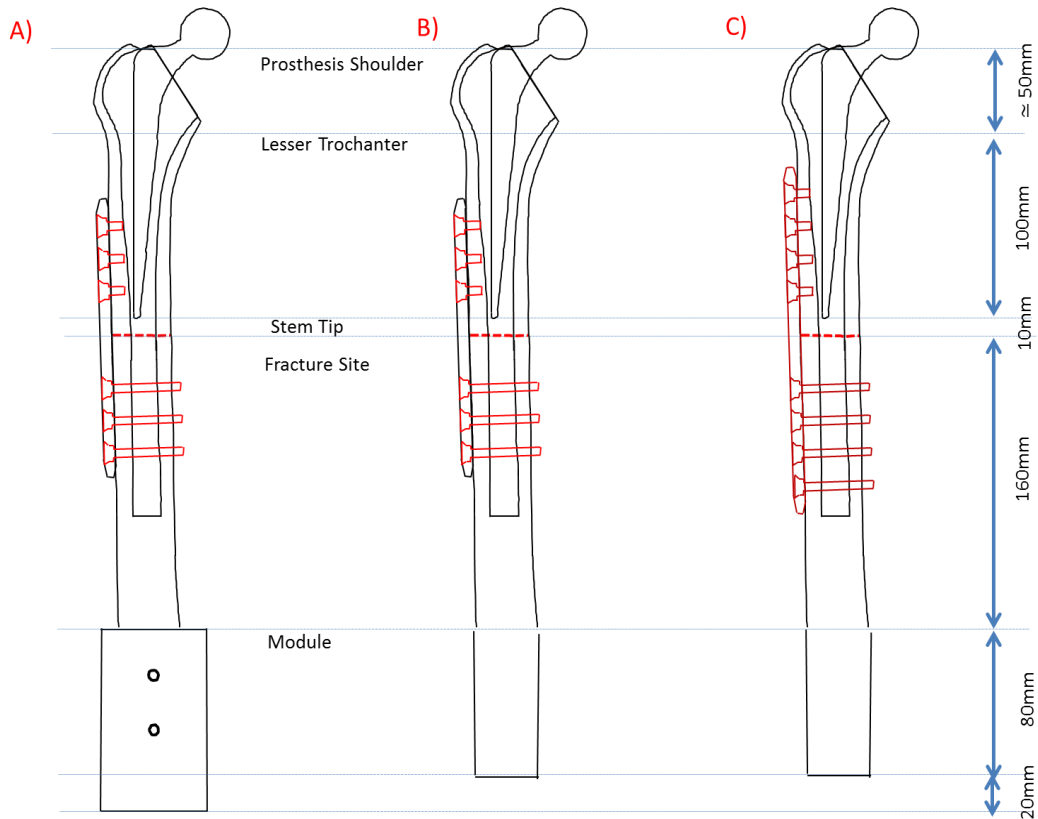
Figure 101 The investigated cases A) an 8-hole plate with the distal module (baseline), B) an 8-hole plate without the distal module, C) a 10-hole without the distal module.

6.3 Comparisons

In this section we are moving away from the validation baseline case of an 8 hole plate with distal module, and evaluating development cases which will aid in the future application of the model to specific problems. The investigated comparison cases are detailed as follows:

- The effect of distal module constraint on the 8-hole plate case- An 8 hole plate with distal module compared against an 8 hole plate without distal module. Cases A + B
- The effect of plate length on model without distal module- An 8 hole plate compared against 10 hole plate both with distal module removed. Cases B + C
- A comparison between the validated baseline case and developed model. A 8 hole plate with distal module compared against a 10 hole plate without distal module. Cases A + C

6.3.1 Effect of distal module constraint on the 8-hole plate case

This section describes the comparison between the baseline computational model, with the distal 80 mm of the Femur supported by a cemented distal module, and the same model with the distal module and potting cement removed.

6.3.1.1 Overall construct stiffness

The 8 hole plate model without distal module had a lower overall construct stiffness than the baseline model, Figure 102. The removal of the distal module and potting cement resulted in a 9% reduction in stiffness.
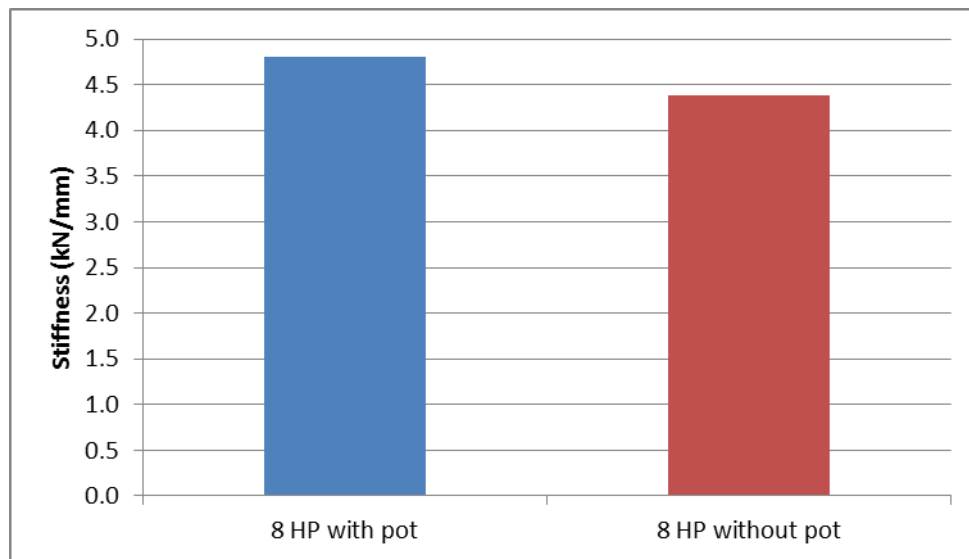
Figure 102 Computational stiffness for the 8 hole plate with distal module model and the 8 hole plate model without distal module cases, for the 10° loading angle.

6.3.1.2 Bone Strain comparison

Removal of the module for the 8-hole plates case caused some changes in medial bone strain, Figure 103. The medial surface strains for the model without a distal module were consistently higher in magnitude than those from the baseline model. The difference in strain increased as the distance from the lesser Trochanter increased, with the largest strain difference occurring at the most distally located gauge location. While there were differences in strain magnitude, the overall bone strain distribution pattern along the Femur did not change greatly between the two cases.
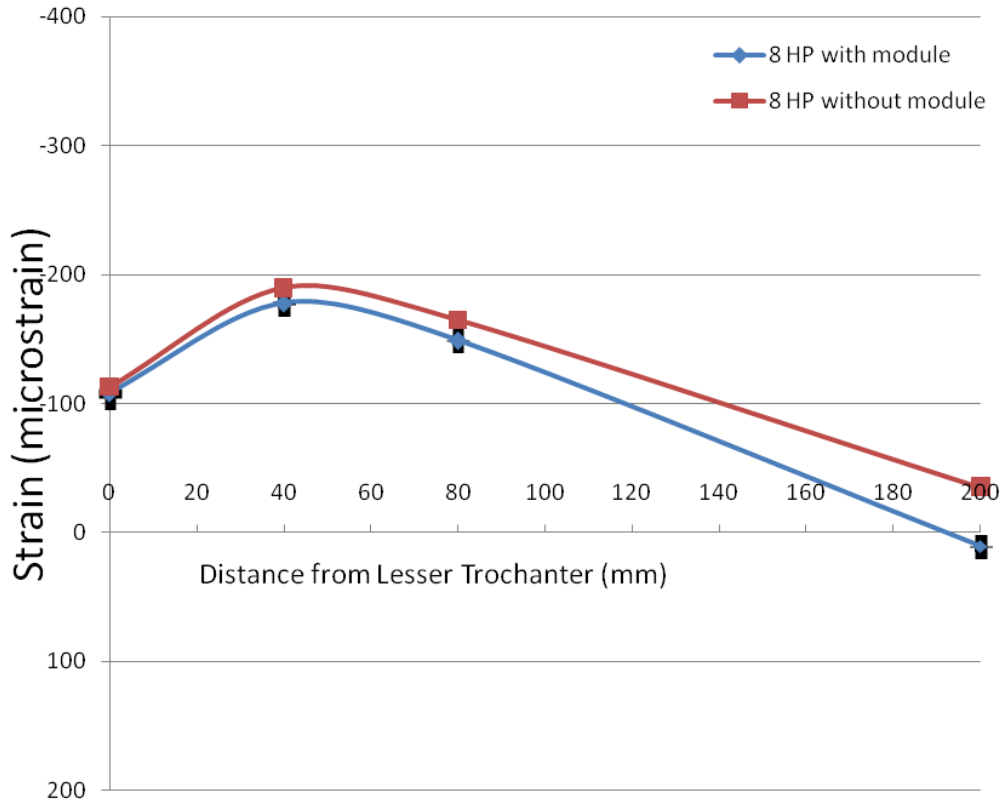
Figure 103 The strain along the medial length of the Femur, for the 8 hole plate with distal module model and the 8 hole plate model without distal module cases, for the 10° loading angle.

Removal of the module also created a different strain pattern at gauges 4 and 5, Figure 104. The strain on the medial side, gauge 4, is in tension for the base line model and in compression for the model with the module removed. While the strain on the lateral side, gauge 5 is in compression for both cases, there is a large decrease in strain magnitude for the model without a module compared to the baseline model.
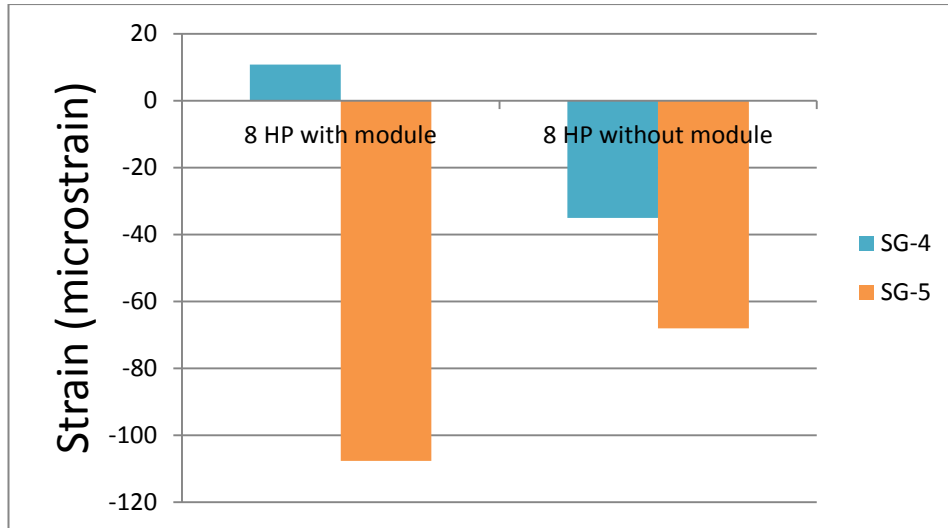
Figure 104 The strain at the distal end of the Femur, for the 8 hole plate with distal module model and the 8 hole plate model without distal module cases.

There is a slight increase in surface strain on the plate with the removal of the distal module, Figure 105. However, the overall strain pattern around the empty screw holes of the locking plate bridging the fracture remains the same. There is a slight increase in plate strain at all plate strain gauge locations for the model without a distal module compared to the baseline model.
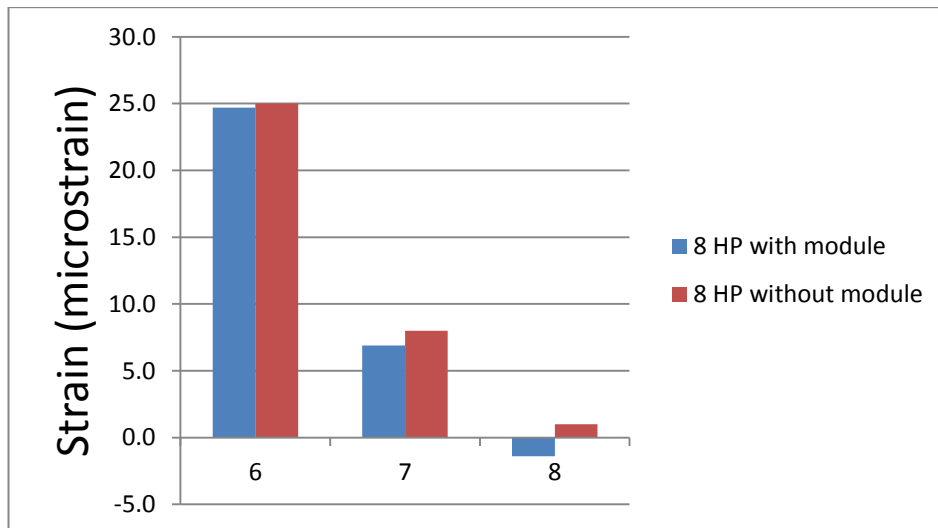
Figure 105 The strain on the locking plate, for the 8 hole plate with distal module model and the 8 hole plate model without distal module cases.

6.3.3 Summary

The removal of distal module resulted in a reduction in overall construct stiffness. The medial strain pattern along Femur and the strain on plate remained very similar. There was only a slight decrease in medial bone strain and slight increase in plate strain. While the strain pattern changes indicate that the removal of the module does have an effect, the magnitude of the strain differences between the models show that the effect is small and indicates that the region where the changes are occurring are elsewhere in the model.

The largest strain pattern variation occurred in the distal bone with large changes in distal strain pattern and distal strain magnitude. This could be due to the head of Femur remaining well constrained, but the changes in distal boundary conditions allowing more bending in the distal bone region.

The removal of the module and potting cement has the effect of lengthening the Femur and increasing the amount of bone included in the model below the fracture. This increases the distance of the boundary conditions from the distal strain gauges, gauges 4 and 5, reducing the influence of the boundary conditions on these gauges. The increase in bone length within a relatively weak region of the model, compared to the region of the fracture with the plated fixation construct or the proximal bone with the prosthesis stem and cement mantle, could mean that more bending is occurring in the distal bone region with the removal of the module. In addition, the presence of the module itself may also have an effect, as the removal of the stiff metal module would allow more bending in the distal bone region.

6.3.2 Comparison between 8 hole plate model and 10 hole plate model without the distal module

This section describes the comparison between the 8 hole plate model and 10 hole plate model, both with the distal module removed.

6.3.2.1 Overall construct stiffness

The 10 hole plate model had a higher overall construct stiffness than the 8 hole plate, Figure 106. There was a 3% increase in overall construct stiffness when increasing the plate length.
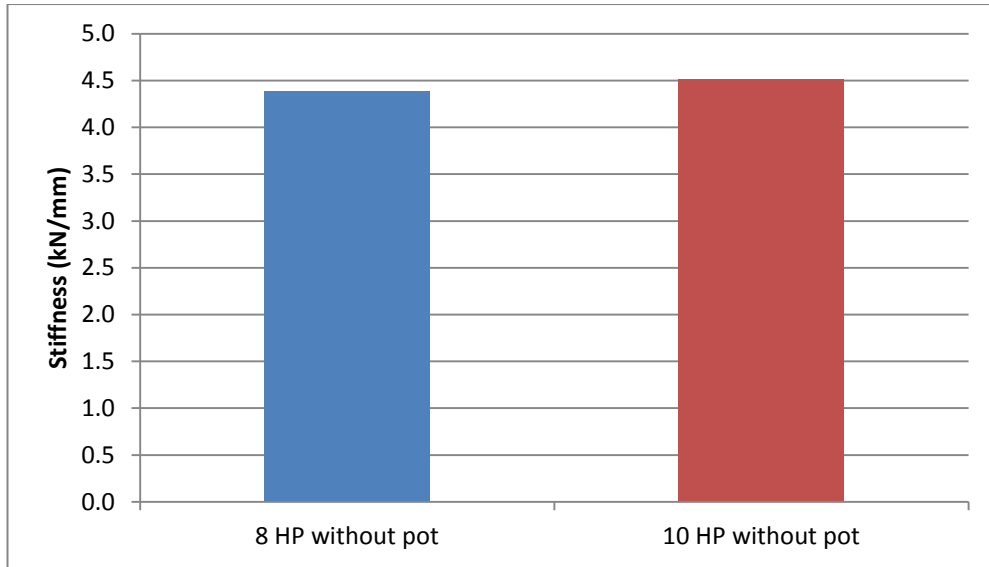
Figure 106 Computational stiffness for the 8 hole plate and the 10 hole plate models, both without a distal module, for the 10° loading angle

6.3.2.2 Bone Strain comparison

The overall strain pattern in medial bone strain was very similar between the 8-hole and 10-hole cases , with the exception of the strain at gauge 2, located near the middle of the prosthesis stem Figure 107. At this strain gauge site, the strain was higher for the 8 hole plate model.
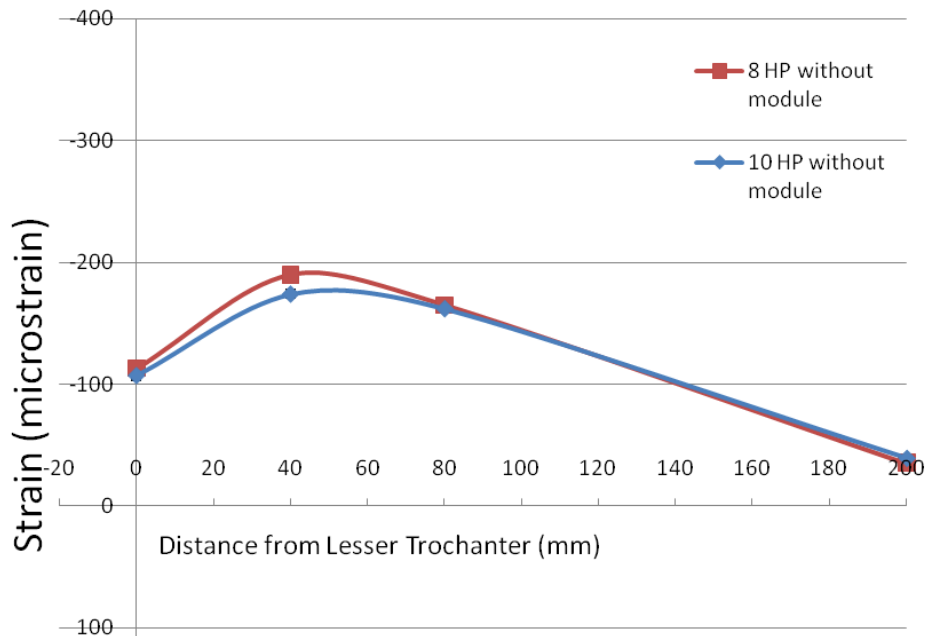
Figure 107 The strain along the medial length of the Femur for the 8 hole plate and the 10 hole plate models, both without a distal module, for the 10° loading angle.

There are very similar distal strain patterns between the 8-hole and 10-hole plate models, Figure 108 . For both cases, the strain on the medial (gauge 4) and lateral (gauge 5) sides are in compression. There was a slight increase in strain at gauge 4 and a slight decrease at gauge 5, for the 10 hole plate model.
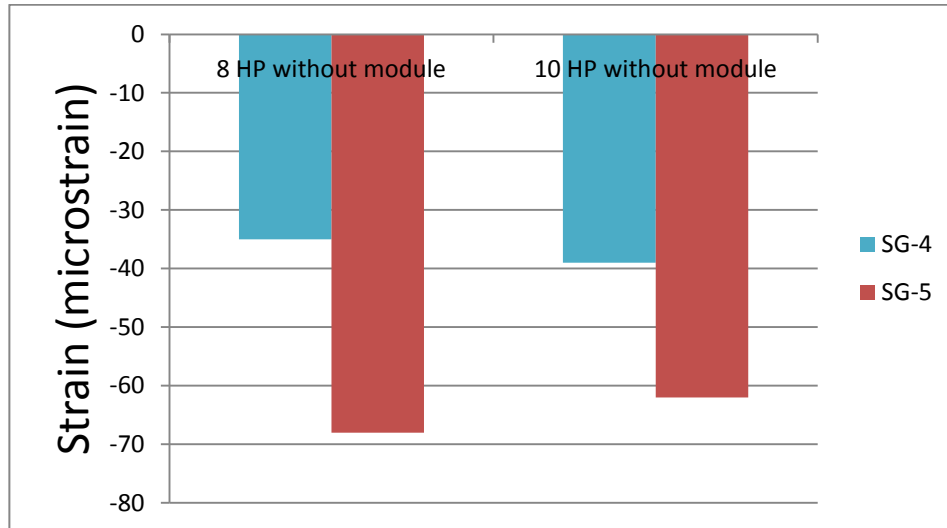
Figure 108 The strain at the distal end of the Femur for the 8 hole plate and the 10 hole plate models, both without a distal module.

Replacing the 8-hole plate with a 10-hole plate caused an increase in surface strain at the centre of the plate, Figure 109. However, the overall strain pattern on the locking plate, between the cases, remains similar.
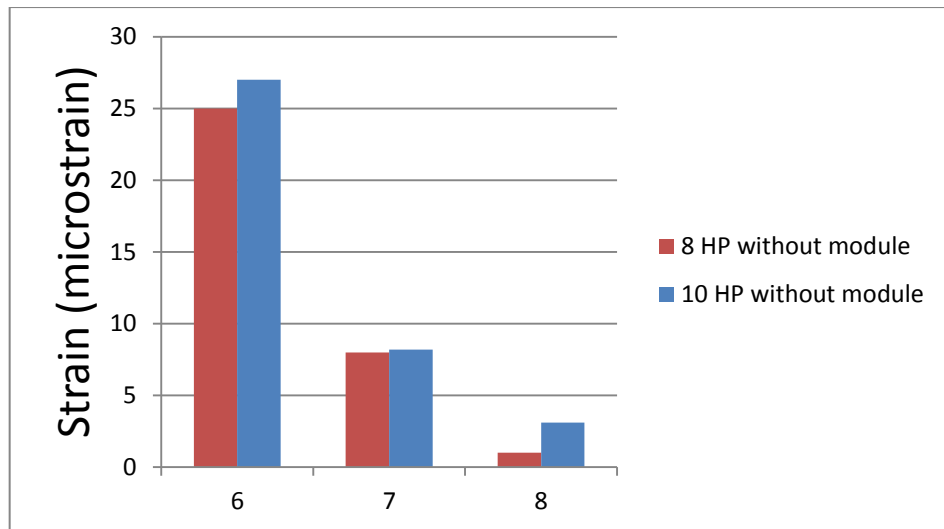
Figure 109 The strain on the locking plate, for the 8 hole plate and the 10 hole plate models, both without a distal module.

6.53 Summary

The increase in plate length and addition of two extra bone screws resulted in an increase in overall construct stiffness. The medial strain pattern along Femur was almost identical, with a slight increase in strain at the gauge 2 location the only major difference between the models. This strain difference is likely due to the addition of the extra proximal unicortical screw which is located opposite to strain gauge 2, on the lateral side. The influence of this proximally positioned screw, the increased amount of metal fixation plate and the increase in overlap between the prosthesis stem and fixation plate could result in an increase in stiffness in this region of the bone. In the distal bone region, the strain pattern was the same for both models with slight changes in strain magnitude. The increase in plate length did have an effect in this region, however, the small magnitude of the strain changes indicate that the effect is limited

6.3.3 Comparison between validated baseline case and developed model

This section describes the comparison between the validated baseline model, 8 hole plate model, with the distal 80mm of the Femur supported by a cemented distal module, and the developed model, a 10 hole plate model with the distal module and potting cement removed.

6.3.3.1 Overall construct stiffness

The removal of the distal module and the increase in length of the fixation plate had the effect of decreasing the overall construct stiffness of the specimens, Figure 110. There was a 6% decrease in overall construct stiffness from the 8 hole plate with module case, to the 10 hole plate without module case.
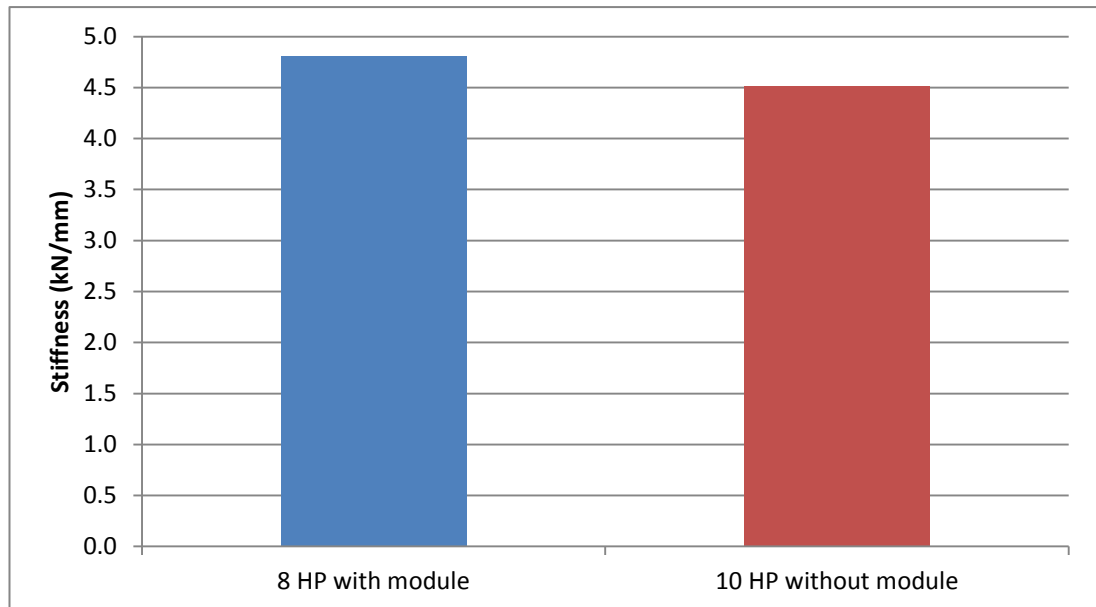

Figure 110 Computational stiffness for the 8 hole plate with distal module model and the 10 hole plate model without distal module cases, for the 10° loading angle.

6.3.3.2 Bone Strain comparison

The medial surface strains in the proximal region of the prosthesis remained the same for both cases, Figure 111. There were differences in strain magnitudes at gauge 3, located slightly proximal to the fracture site, with higher strain for the 10 hole plate without module case. The largest strain difference was seen at the distally located gauge 4, with lower strain for the 8 hole plate without module compared to the 10 hole plate with module case.
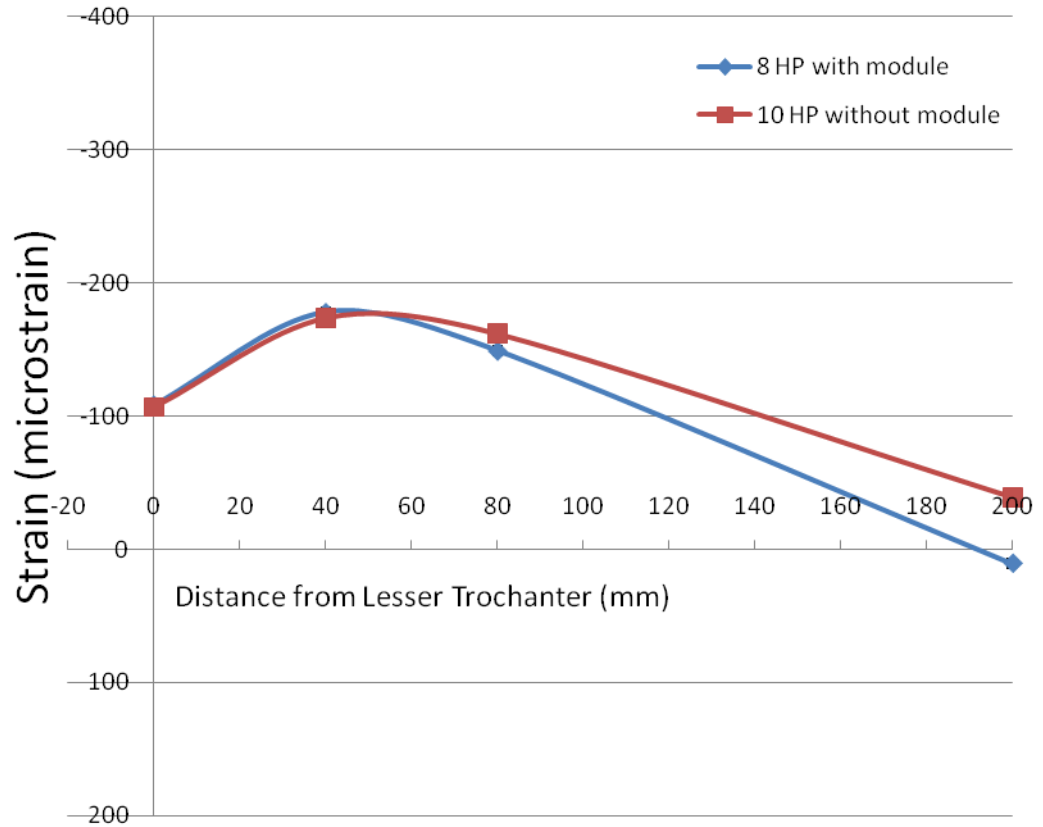
Figure 111 The strain along the medial length of the Femur, for the 8 hole plate with distal module model and the 10 hole plate model without distal module cases, for the 10° loading angle.

However, there are large changes in strain pattern between the cases. Figure 112. For the 8 hole plate with module case, gauge 4, located on the medial side, is in slight tension, while the laterally located gauge 5 is in compression. For the 10 hole plate without module case, both distal gauges are in compression.
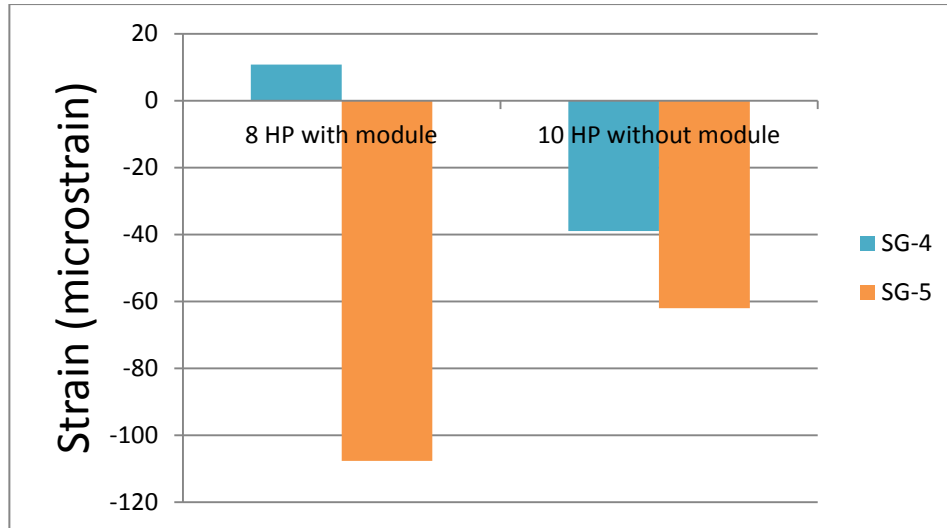
Figure 112 The strain at the distal end of the Femur, for the 10 hole plate with distal module model and the 10 hole plate model without distal module cases.

The computational strain on the locking plate, for the 8 hole plate with distal module model and the 10 hole plate model without distal module cases, are presented in Figure 113. There are slight increases in surface strain for both gauges locations 6 and 7, with the removal of the distal module, while there is a reduction in strain ate gauge 8. The overall strain pattern between the cases on the locking plate, around the empty screw holes bridging the fracture, remains the same.
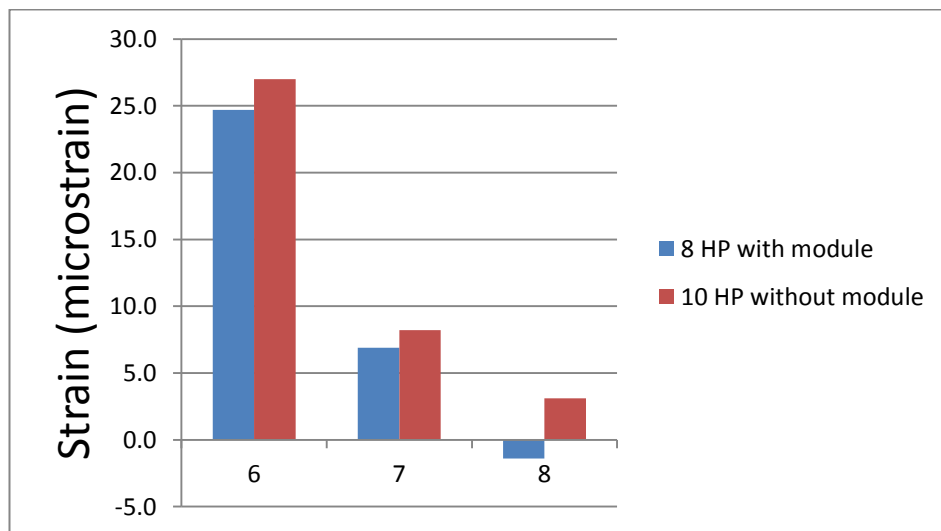

Figure 113 The strain on the locking plate, for the 10 hole plate with distal module model and the 10 hole plate model without distal module cases.

6.3.3.3 Summary

A summary of the tests results and their absolute error from the baseline model is presented in Table 16. The absolute error calculations for strain gauge 8 should be treated with a degree of scepticism as the numerical differences in strain magnitude were only 1-2 µε, but as the magnitude of the strain was small, the absolute error is very large.

The removal of distal module and the increase in plate length resulted in an increase in overall construct stiffness. While the strain in the proximal region of the prosthesis stem remained very similar, there were changes in strain around the fracture site and at the distal gauge locations. There were slight increases in plate strain magnitude, however, the plate strain pattern remained the similar.

The removal of the module and potting cement had the effect of lengthening the Femur and increasing the amount of bone included in the model below the fracture, increasing the possibility of bending in the distal bone region. However, an increase in fixation plate length, with the introduction of an extra unicortical proximally and bicortical screw distally, would have the effect of increasing the overall construct stiffness.

This comparison showed that the distal boundary conditions had a larger influence on construct behaviour than an increase in plate length by 2 screw holes.

Table 16 A summary of the computational study tests results and their absolute error from the baseline model

	8-hole, with module (baseline)	8-hole, no module	% difference from 8HwP	10-hole, no module	% difference from 8HwP
Stiffness (kN/mm)	4.80	4.38	9	4.51	6
Gauge 1 (με)	-108	-113	4	-107	1
Gauge 2 (με)	-178	-190	6	-174	2
Gauge 3 (με)	-149	-165	10	-162	8
Gauge 4 (με)	11	-35	131	-39	128
Gauge 5 (με)	-108	-68	58	-62	74
Gauge 6 (με)	24.7	25	1	27	9
Gauge 7 (με)	6.9	8	14	8.2	16
Gauge 8 (με)	-1.4	1	240	3.1	145

6.4 Discussion- Computational studies

The aim of this section was to investigate the effect of removing the distal module and the lengthening of the fixation plate to a more clinically relevant configuration.

The removal of the distal module and potting cement primarily affected the distal bone strain, while the bone strain in the proximal bone region and strain on the locking plate remained largely unaffected. The bone strain recorded at gauges 4 and 5, in the region of the distal Femur was the main region affected by the removal of the distal module and potting cement. Removing the distal module reduces influence of boundary conditions on distal strain gauges as the gauges remain at a fixed height from the fracture height, while the point at which the Femur is supported is moved away from the gauges. If the distal gauges were moved such that they were positioned with the same distance from the fixed end of the Femur once the distal module was removed, a similar pattern might be observed between the cases.

The change from the 8 hole to 10 hole plate instrumentation configuration did not have a large effect on the overall biomechanics of the fracture fixation construct. The bone strain difference in the region of the prosthesis stem was opposite to the additional unicortical screws introduced with the increased plate length. The anticipated overall construct stiffness increase, as a result of the longer locking plate and the increase in number of bone to screw fixation points, was observed between the two cases.

The main region of interest in these models when evaluating the performance of the fracture fixation constructs was the strain on the fixation plate and bending behaviour under load. As this study showed that the removal of the distal module affected mainly the distal bone region and not the fixation plate or proximal bone region, the removal of the module to facilitate the better modelling of different fracture heights could be recommended. The change from the baseline 8 hole plate to the 10 hole plate did not greatly change the overall mechanical performance of the specimens. The 10 hole plate models could be used in future studies with the knowledge that models including the lengthened plate would have a slight increase in stiffness and slight changes in strain pattern, from the validated baseline models.

Chapter 7 **Periprosthetic fracture configuration studies**

7.1 Introduction

This section presents the results of taking the developed computational model and introducing variations to the type of fracture investigated in the model. The effect of both changing the angle, and position of a periprosthetic fracture are investigated. The objective of this section was to investigate the effect of fracture angle on the potential for locking plate failure, in periprosthetic fracture cases where a stable hip prosthesis will remain in situ and the bone stock is good.

This work used the flexibility of the developed computational model, considering its strengths and limitations, to investigate different fracture variables and corresponding instrumentation constructs, and determine their effects on bulk biomechanics of the stabilised fractures. There were two main factors which were selected to be investigated in this study.

The first variable was the position of the fracture relative to the tip of the prosthesis stem. Both the experimental and computational model development stages described previously in Chapters 5 and 6, were performed with the fracture located 10 mm distal to the tip of the prosthesis stem. The fracture height was calculated from the distal tip of the stem to the midpoint of the fracture.

The second variable was the angle of the periprosthetic fracture. The effect of fracture angle on stabilised periprosthetic fracture biomechanics is unknown. There is a need to determine if fractures occurring in the Medial-to-Lateral (ML) direction have the same effect on biomechanics as fractures occurring in the Lateral-to-Medial (LM) directions, and also how these compare to the behaviour of transverse fractures. In addition there is a need to determine the effect of fracture angle on stabilised biomechanics.

7.2 Fracture height: distance between stem tip and fracture

7.2.1 Introduction

This section presents the results of the developed computational model, section 6.0, for two different fracture heights. The fracture height was measured as the distance from the tip of the stem to the midpoint of the fracture. In addition to the baseline fracture height, 10 mm between the prosthesis tip and fracture, the fracture was moved distally down the Femur such that the distance between the stem tip and the fracture was equivalent

to two femoral diameters, 70 mm. With the position of the fracture 70 mm distal to the stem tip, a more appropriate instrumentation combination used to stabilise the construct needed to be introduced.

Moving the existing 10 hole plate distally down the lateral side of the Femur so it was bridging the lowered fracture, would have resulted in only having a small overlap between the plate and prosthesis stem. Such an overlap, less than 40 mm or 2 plate holes in length, would have introduced a stress riser in this region of the bone and is avoided clinically[8]. To ensure the instrumentation combination used in the model was a clinically relevant stabilisation construct, the length of the plate was increased to a 12 hole plate, keeping the proximal end of the plate in the same position, and introducing two bicortical screws proximally above the fracture. These cases are shown in Figure 114. The computational methods used in this study are described in chapter 4.
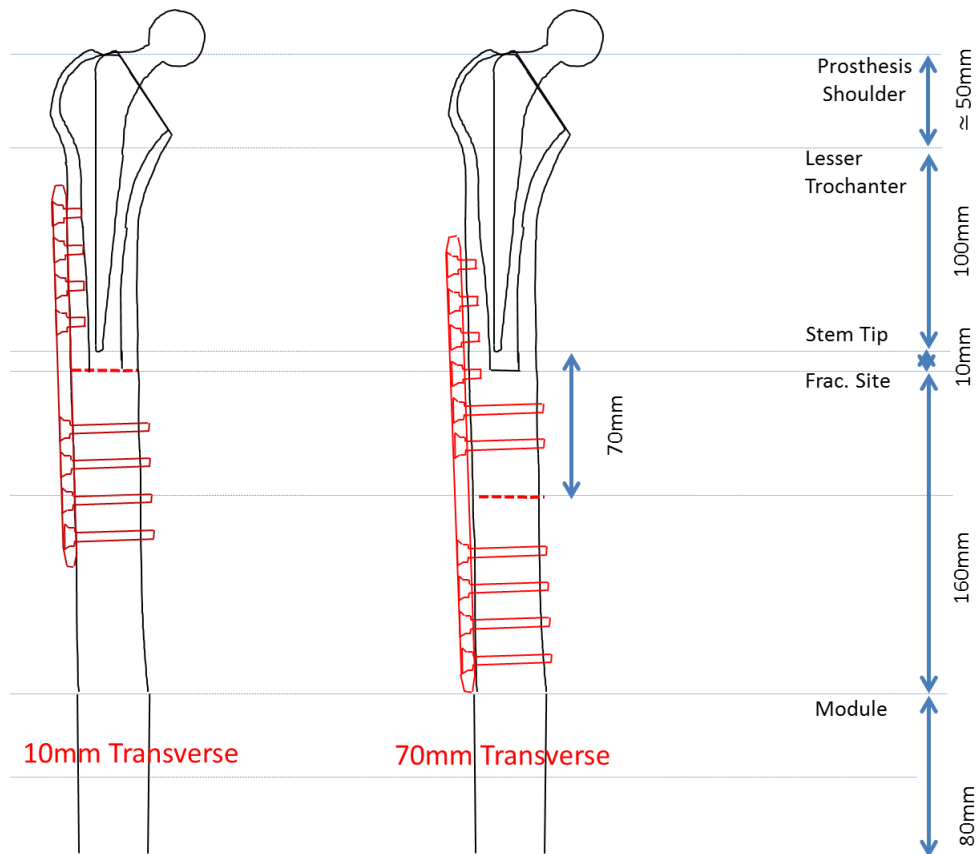
Figure 114 The investigated fracture angle cases positioned 10mm and 70mm distal to the stem tip.

7.3.2 Overall construct stiffness

The overall stiffness for the 10 mm and 70 mm fracture height cases is shown in Figure 115. The 10 mm fracture height model had a lower overall construct stiffness than the 70mm model. The fracture position two femoral diameters from the stem tip, with the addition of the relevant stabilisation instrumentation resulted in a 6% increase in stiffness.
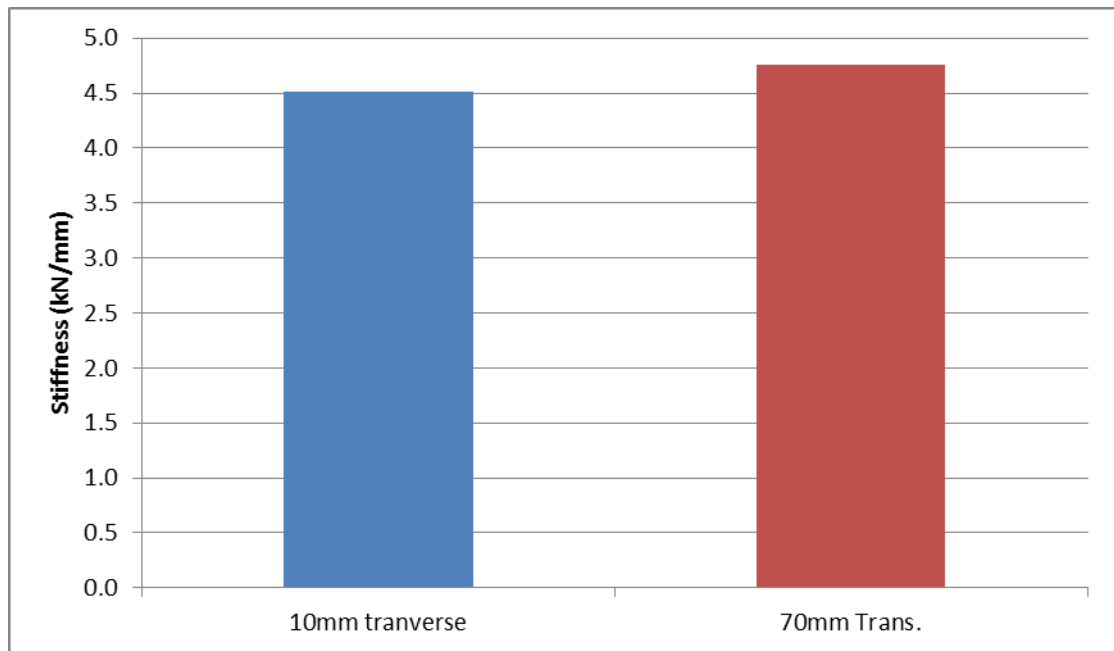
Figure 115 Overall construct stiffness for the developed model for both 10 mm and 70 mm distance of the fracture from the prosthesis tip cases.

7.3.3 Bone Strain comparison

The strain along the medial length of the Femur for both the 10 mm and 70 mm fracture height models, is shown in Figure 116. Due to the positioning of the 12 hole plate on the lateral side and presence of the bicortical screw tips on the medial side of the Femur, the surface bone strain at the distal strain gauges could not be collected. The strain in the region of the stem was largely unaffected by the change in fracture height, with only slight variations in medial bone strain between the two cases. The strains at gauge 1 and 2 were very similar between the two cases, while there was a strain decrease at the strain gauge 3 location for the 70 mm fracture height case.
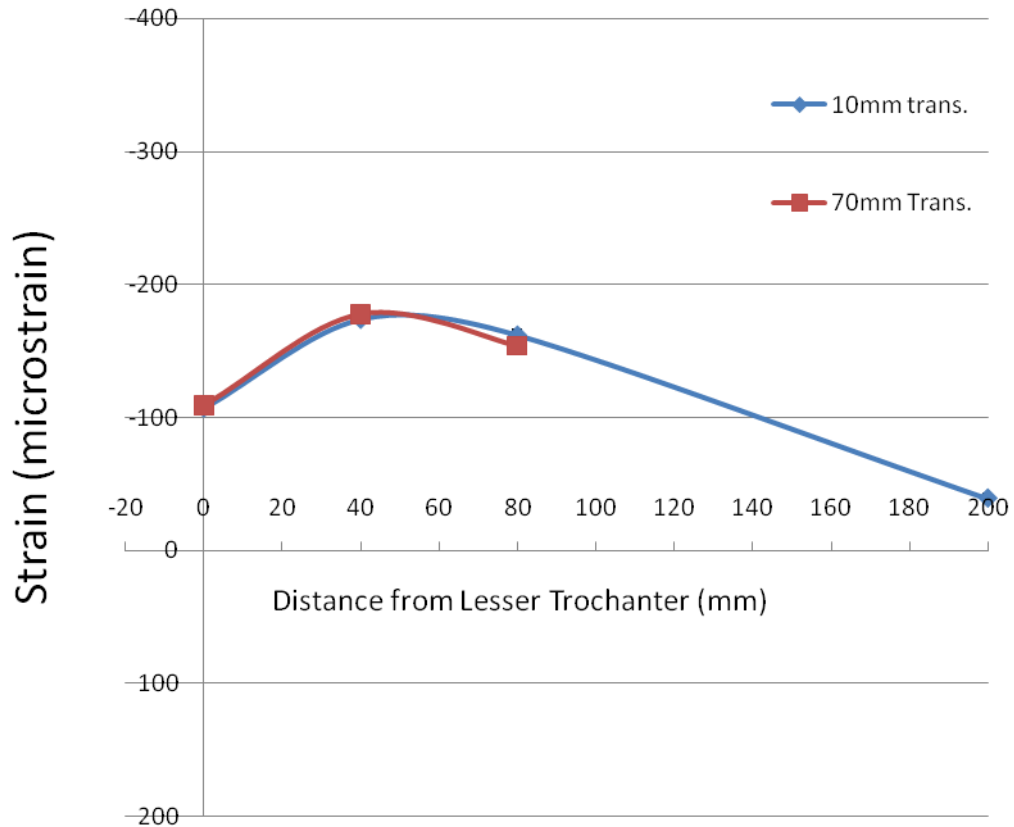
Figure 116 The strain along the medial length of the Femur, for both the 10 mm and 70 mm fracture height model cases, for the 10° loading angle.

The computational strain on the locking plate for both the 10 mm and 70 mm fracture height cases, are presented in Figure 117. For both cases, the plate strain was measured around the empty screw holes bridging the fracture.

There was a significant change in plate strain pattern between the 10mm and 70 mm fracture height cases. The most extreme change in plate strain occurred at gauge location 6, sited above the proximal screw hole bridging the fracture, with the plate in a large amount of tension in the 10 mm case, and in a large amount of compression in the 70 mm case. The same change in strain pattern was observed at gauge 8, located below the distal empty screw hole bridging the fracture, but with much smaller changes in strain magnitude. The strain at gauge 7, between the empty screw holes, remained in slight tension for both cases, with a small reduction in strain for the 70 mm fracture height case.
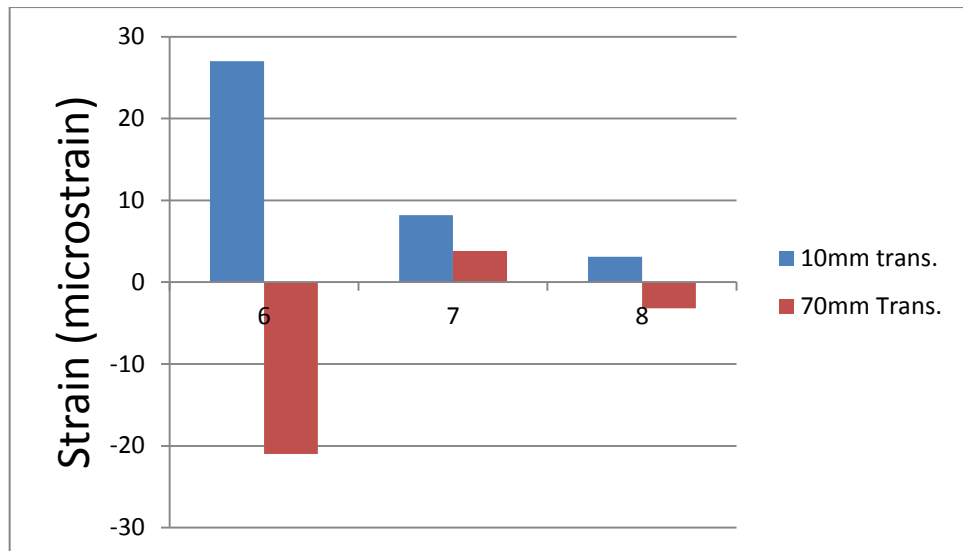
Figure 117 The strain on the locking plate, for both the 10mm and 70mm fracture height cases

7.3.4 Summary

Moving the height of the fractures 70 mm distal to the prosthesis stem tip had an effect on overall behaviour of the constructs. Only small changes in the proximal bone strain in the region of the prosthesis stem were observed. Large changes in strain were seen in the section of the plate bridging the fracture, along with an increase in overall construct stiffness.

The use of a longer locking plate to stabilise the fracture and the addition of two extra bicortical screws, will have had the effect of adding to the construct stability. The increase in plate length for the 70 mm case means that the distance between the most proximal and distal screws in contact along the length of the Femur is increased in addition to adding four extra cortices of contact between the instrumentation construct and bone.

When further developing the 70 mm fracture height models to investigate a range of different fracture angles and directions, the strain and stiffness relationships of moving the fracture distally and the changes in instrumentation construct, will need to be considered.

7.3 Fracture angles 10 mm distal to prosthesis stem tip

7.3.1 Introduction

This section presents the results of the developed computational model, section 6.0, over a range of fracture angles positioned 10mm distal to the stem tip.

The transverse bone fracture used until this point in this study was chosen as it was the most simple fracture case, which aided accuracy and repeatability of creating multiple experimental specimen constructs against which the computational models could be validated. There is currently no agreed upon standard fracture angle in the literature, with many previous studies using a simple transverse fracture[75, 76, 79]. Clinically, a wide range of fractures are encountered, however the angle of the bone fracture is not currently involved in the Vancouver classification of a periprosthetic fracture.

The investigated cases included a transverse fracture, angles of 20° and 45° in both sloping downwards from the medial to the lateral side (ML), and sloping downwards from the lateral to the medial side (LM). Fracture height was calculated from the midpoint of the fracture, where the fracture intercepted the centre line of the Femur. The fractures were checked to ensure that there was no overlap between the positioned fracture and the bone screws. These cases are shown in Figure 118.
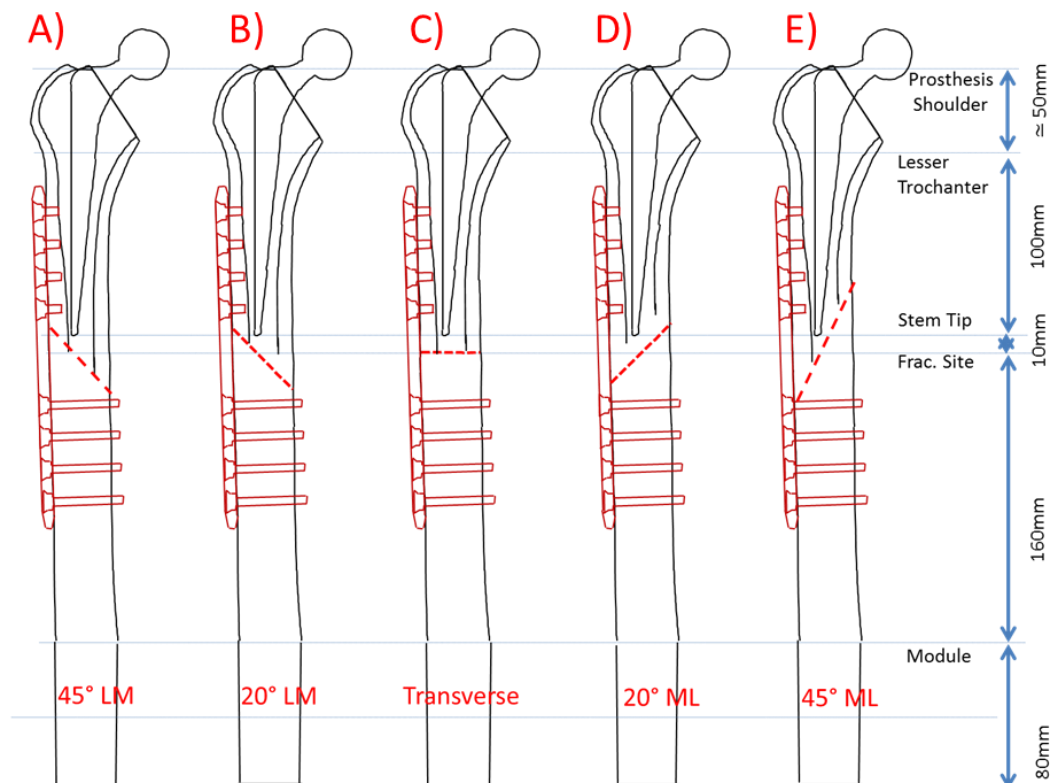
Figure 118 The investigated fracture angle cases positioned 10mm distal to the stem tip. A) 45° in the LM direction. B) 20° in the LM direction. C) A transverse fracture D) 20° in the medial- lateral direction. E) 45° in the medial- lateral direction

7.3.2 Overall construct stiffness

The overall stiffness for the five fracture angle cases positioned 10mm distal to the stem tip is shown in Figure 119. The transverse fracture had the highest overall construct stiffness of the investigated fracture angles. As the fracture angles were increased, the overall construct stiffness reduced. The cases with fractures in the ML direction had much lower overall stiffness compared to the cases with fractures in the LM direction. The case with the lowest overall stiffness was the 45° case in the ML direction.
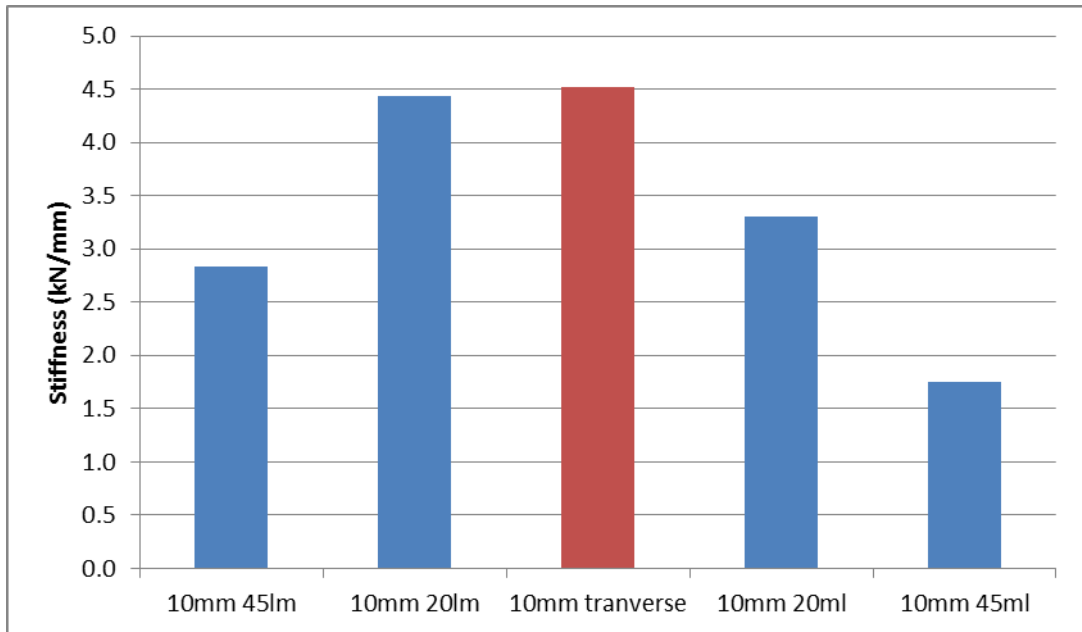
Figure 119 Overall construct stiffness for the five fracture angle cases positioned 10 mm distal to the stem tip. A) 45° in the LM direction. B) 20° in the LM direction. C) A transverse fracture D) 20° in the medial- lateral direction. E) 45° in the medial- lateral direction

7.3.3 Bone Strain comparison

The strain along the medial length of the Femur for the five fracture angle cases positioned 10 mm distal to the stem tip, is shown in Figure 120. There were large changes in medial surface strain as the fracture angles were varied. For both the 20° fracture angles, slight strain variations were observed at the gauges located in the region of the prosthesis stem when compared to the transverse case. The 45° ML fracture case had a reduction in strain at gauges 1 and 2, a slight strain increase at gauge 3, and a large increase in strain at the gauges 4 location. The largest strain variation was seen at the 45° lateral- medial fracture case. With a very large increase in strain at gauge location 3, located in the region of the prosthesis stem tip, with reductions in strain at all other gauge locations.
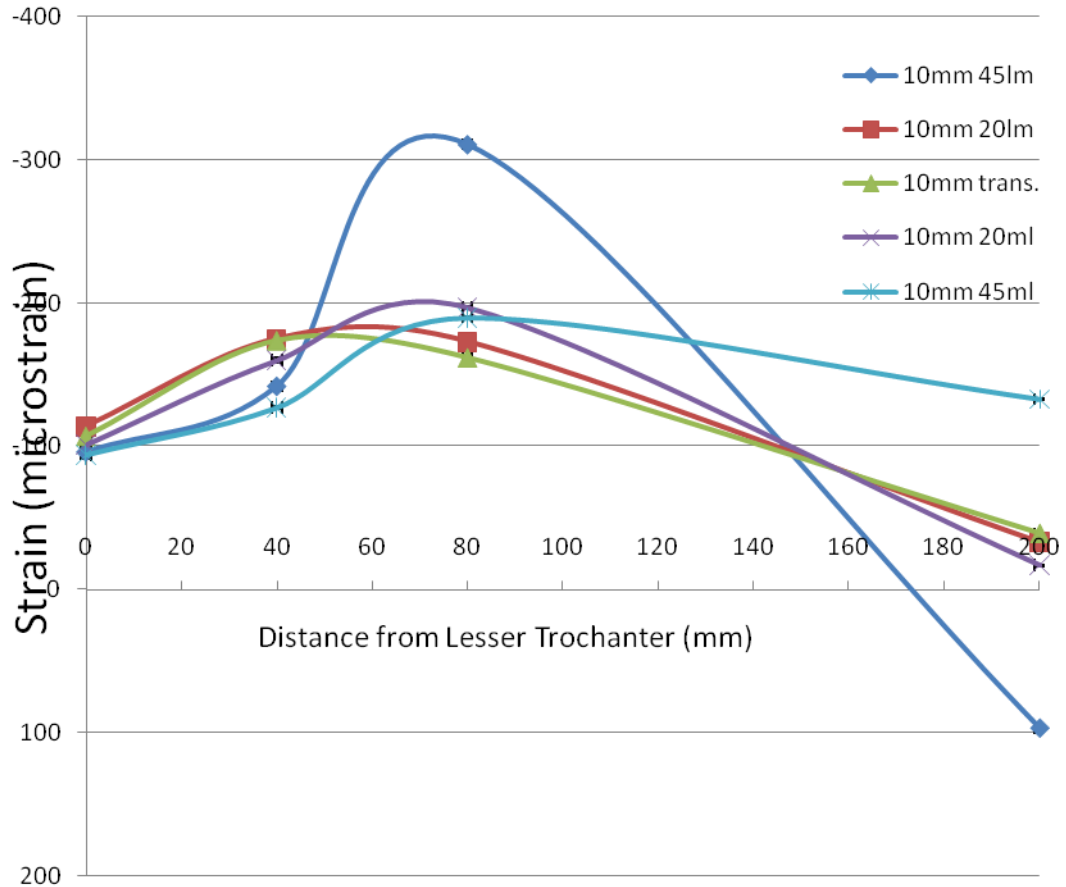
Figure 120 The strain along the medial length of the Femur, the five fracture angle cases positioned 10 mm distal to the stem tip, for the 10° loading angle.

The strain at the distal end of the Femur, the five fracture angle cases positioned 10 mm distal to the stem tip, is shown in Figure 121. The relationship between the distal gauges remains the same for most of the fracture angle cases, with both gauges in compression, however, for the 45° LM case, the strain at gauge 4 on the medial side is in tension, while the strain at gauge 5, on the lateral side, remains in compression. The magnitude of the strains at the lateral gauge five position increases as the fracture angles increase. The strain magnitude at the medial gauge four position is at its lowest for the 20° ML case with the largest at the 45° ML case.
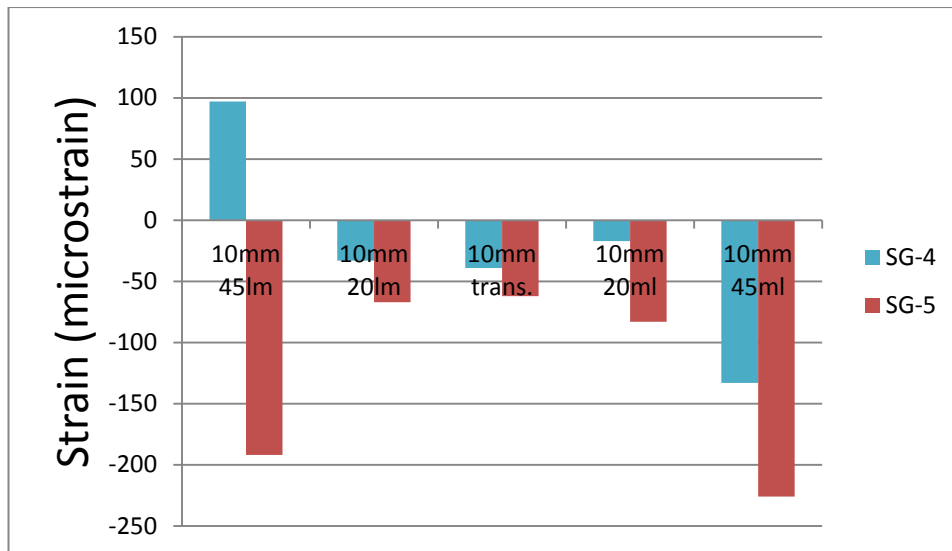
Figure 121 The strain at the distal end of the Femur, for the five fracture angle cases positioned 10 mm distal to the stem tip.

The computational strain on the locking plate, for the five fracture angle cases positioned 10 mm distal to the stem tip, are presented in Figure 122. Fractures in the ML direction resulted in larger changes in plate strain compared to the fractures in the LM direction. The case were the largest strain magnitude were observed was the 45° ML case with a strain peak of over 50με. There is a strain increase at the proximally positioned gauge 6 and a strain decrease at the distally positioned gauge 8 for both fracture angles in the ML direction, compared to the transverse case. The opposite pattern is observed for the fracture angles in the LM direction with strain decreases seen at gauge 6 and increases at gauge 8.
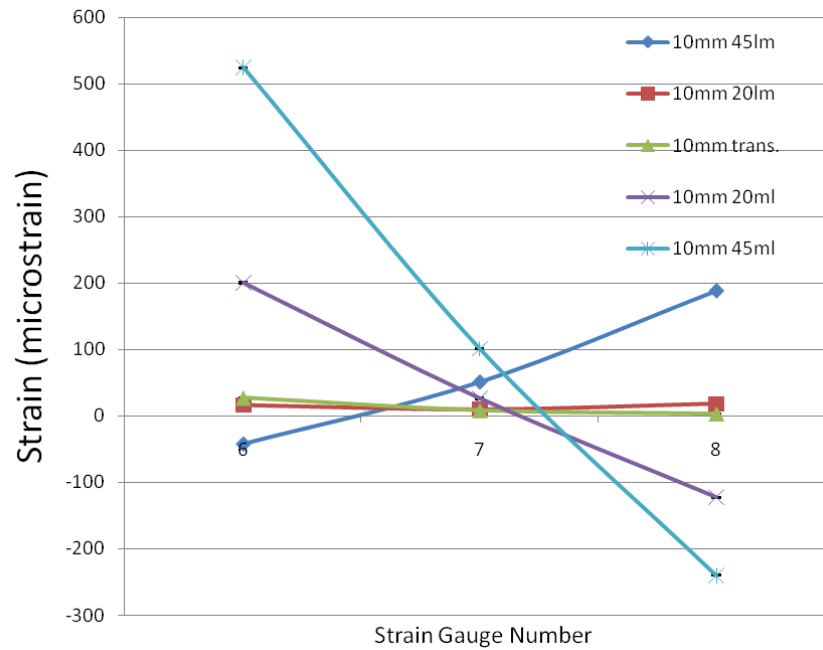
Figure 122 The strain on the locking plate, for the five fracture angle cases positioned 10mm distal to the stem tip.

7.4.4 Plate Stress comparison

The maximum Von Mises stress on the locking plate, for the five fracture angle cases positioned 10 mm distal to the stem tip, are presented in Figure 123. Lower maximum stresses were seen for fractures in the LM direction compared to fractures in the ML direction. The highest stress was at the 45 degree ML fracture with a maximum Von Mises stress of 222 MPa. This was much lower than both the Yield stress 792 MPa or the fatigue limit 310-448 MPa (at 10^7 cycles) of the locking plate.

The Von Mises stress across the whole plate, for the five fracture angle cases positioned 10 mm distal to the stem tip, are presented in Figure 124. For the fractures in the LM direction, the regions of high stress are located around the screw hole supporting the most distal unicortical screw, screw hole 4. For the Transverse and 20°ML fracture, this high stress region has moved distally down the plate, with the highest stress found around the most proximal empty screw hole bridging the fracture, screw hole 5. For the 45°ML fracture case, the region of high stress is located between the distal empty screw hole bridging the fracture and the screw hole supporting the most proximal bicortical screw, screw holes 6 and 7.
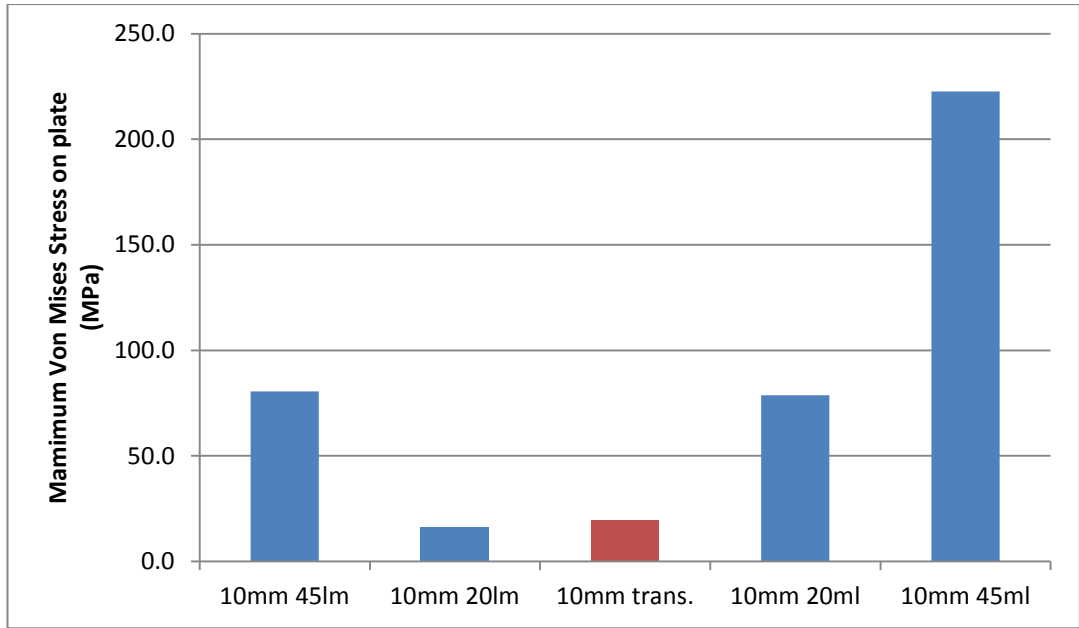
Figure 123 The maximum Von Mises stress on the plate, for the five fracture angle cases positioned 10mm distal to the stem tip
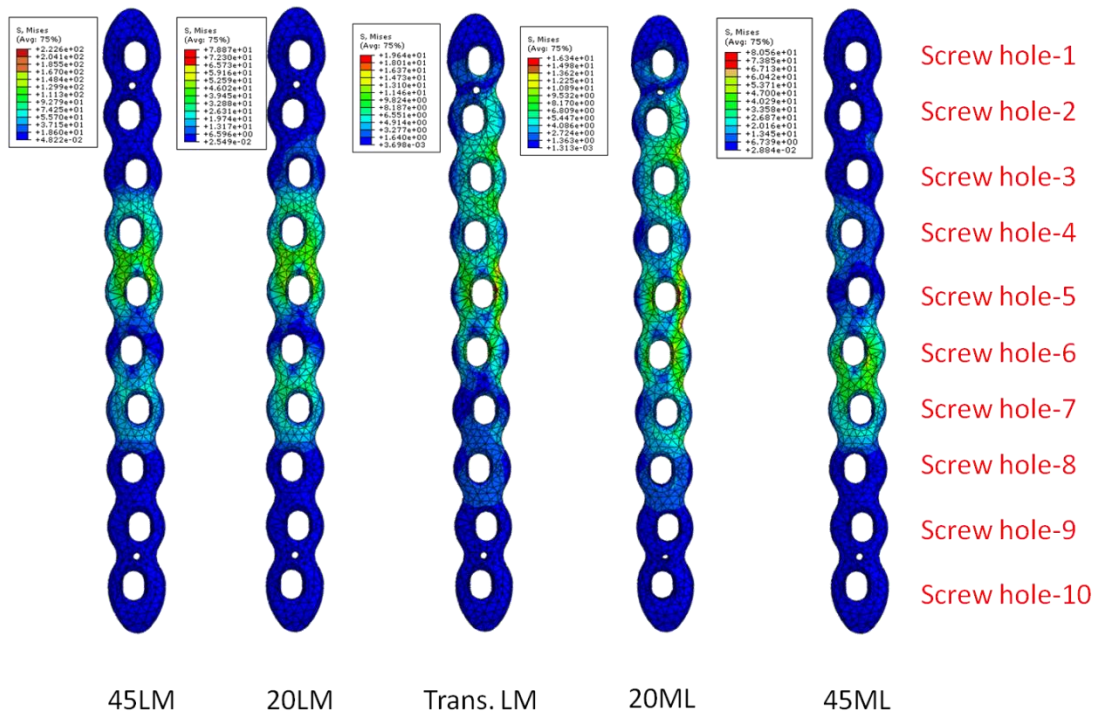
Figure 124 Von Mises Stress plot, for the five fracture angle cases positioned 10 mm distal to the stem tip

7.3.4 Summary

Varying the angle of the fracture from the transverse fracture used in the development of the baseline computational models had a large effect on overall behaviour of the constructs.

Different fracture directions affected the mechanics of the construct in very different ways. The bone strain patterns along the medial length of the Femur were very similar between the transverse case and both the 20° LM and 20° ML fracture angle cases. The 45° fracture angles had a much larger effect on bone strain with increased strains located directly proximal to the fracture site, with strain doubling to over 300 µε in the 45°LM case. There were large changes in plate strain between the transverse case and the 45° fracture angles. The largest strains were observed in the 45° ML case where there was a strain peak of over 500 µε. The plate strain pattern correlated with the pattern of maximum stress across the range of fractures.

While the computational model did not predict plate failure for any of the fractures tested at the 10 mm fracture height, the high strains seen at the 45° ML case indicate that the instrumentation combination used in this study could be optimised.

The magnitude of the changes in overall stiffness and strain on both the bone and locking plate are far greater than in any variable tested using the computational models previously. This indicates that the computational models are sensitive to the angle of the fracture.

7.4 Fracture angles 70mm distal to prosthesis stem tip

7.4.1 Introduction

This section presents the results of the developed computational model, section 6.0, over a range of fracture angles positioned 70 mm distal to the stem tip. The investigated cases included a transverse fracture, angles of 20° and 45° sloping downward in both the medial-lateral (ML) and downwards in the lateral-medial (LM) directions.

These cases are shown in Figure 125. The computational methods used in this study are described in chapter 4.
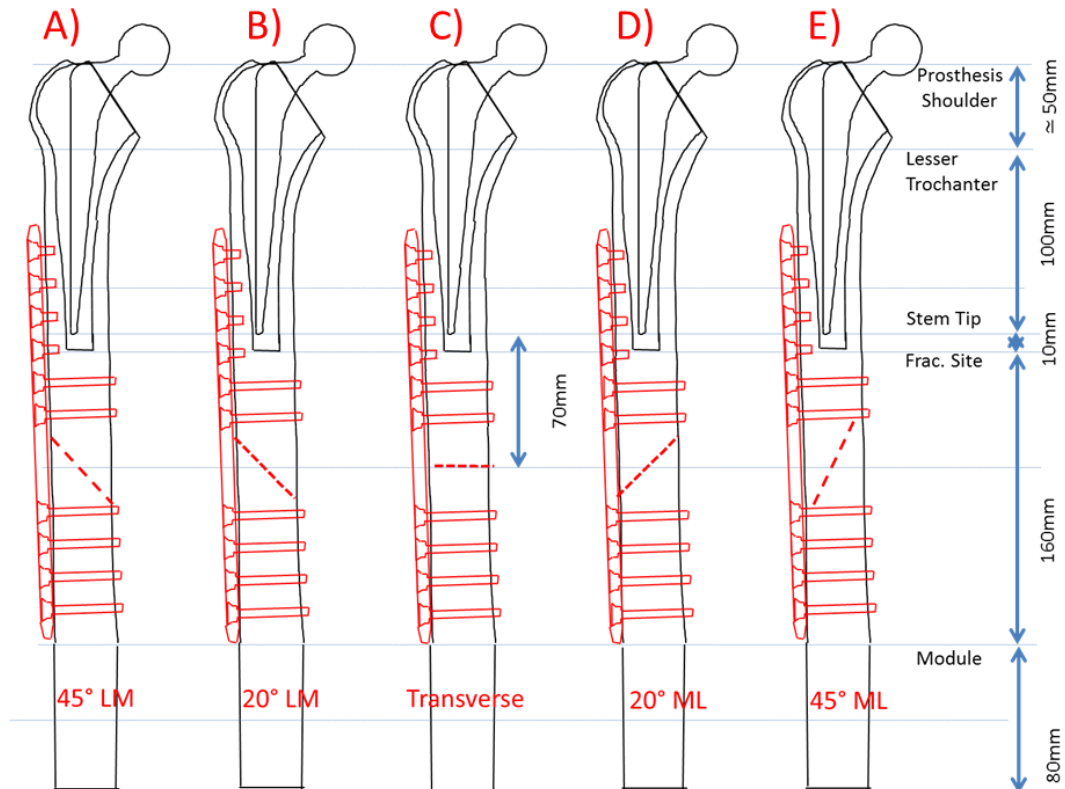
**Figure 125 The investigated fracture angle cases positioned 70mm distal to the stem tip. A) 45° downwards in the LM direction. B) 20° downwards in the LM direction. C) A transverse fracture D) 20° downwards in the medial- lateral direction. E) 45° downwards in the medial- lateral direction**

7.4.2 Overall construct stiffness

The overall stiffness for the five fracture angle cases positioned 70 mm distal to the stem tip is shown in Figure 126. The case with the highest overall stiffness was the transverse fracture case while the lowest was found at the 45° ML fracture case. As the fracture angles were increased, the overall construct stiffness reduced. The cases with fractures in the ML direction had much lower overall stiffness compared to the cases with fractures in the LM direction. The case with the lowest overall stiffness was the 45° case in the ML direction.
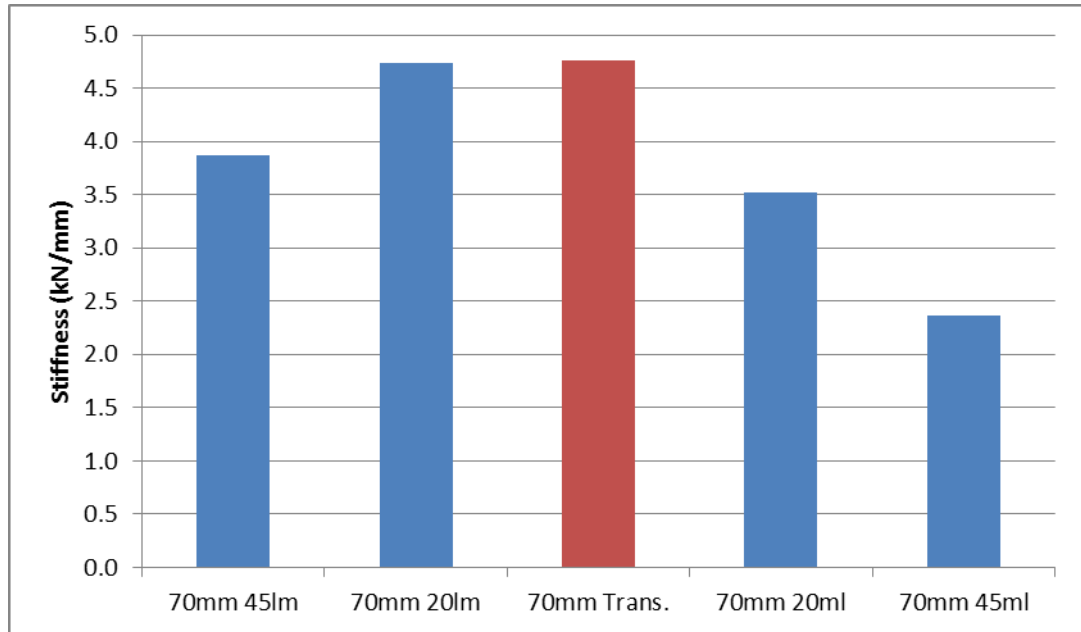
Figure 126 Computational overall stiffness for the five fracture angle cases positioned 70 mm distal to the stem tip. A) 45° downwards in the LM direction. B) 20° downwards in the LM direction. C) A transverse fracture D) 20° downwards in the medial- lateral direction. E) 45° downwards in the medial- lateral direction

7.4.3 Bone Strain comparison

The strain along the medial length of the Femur for the five fracture angle cases positioned 70 mm distal to the stem tip, is shown in Figure 127. Due to the positioning of the 12 hole plate on the lateral side and presence of the bicortical screw tips on the medial side of the Femur, the surface bone strain at the distal strain gauges could not be collected. The bone strain was only presented for the proximal gauges in the region of the prosthesis stem. The highest strains were found at the transverse case, with a reduction in strain at all the gauge locations as the fracture angle was increased. The fracture angles in the ML direction resulted in larger strain reductions compared to the fractures in the LM direction.
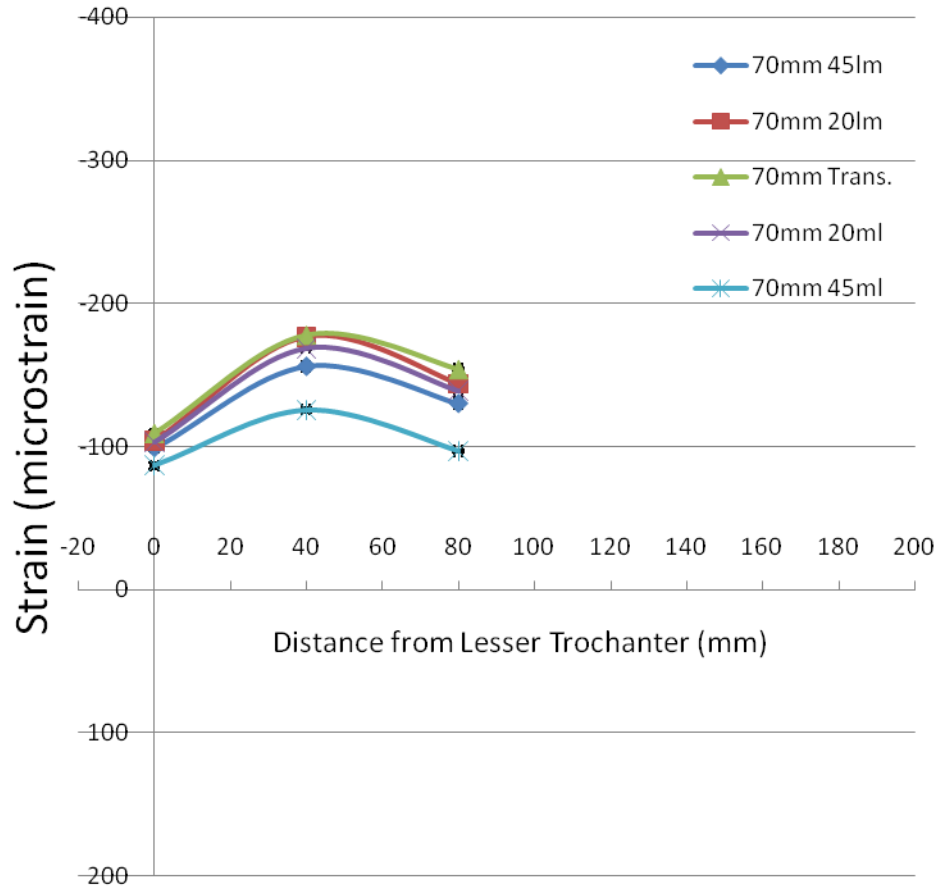
Figure 127 The strain along the medial length of the Femur, the five fracture angle cases positioned 70 mm distal to the stem tip, for the 10° loading angle.

The computational strain on the locking plate, for the five fracture angle cases positioned 70 mm distal to the stem tip, are presented in Figure 128.

Fractures sloping downwards in the ML direction resulted in far larger increases in plate strain magnitude compared to the fractures in the LM direction. For the ML fracture angles, the strain increased in tension, at all gauge locations compared to the transverse case. Between the 20° and 45° the ML fracture angle cases, the highest strains were seen at the proximally located gauge location 6, with a peak of over 360 µε.
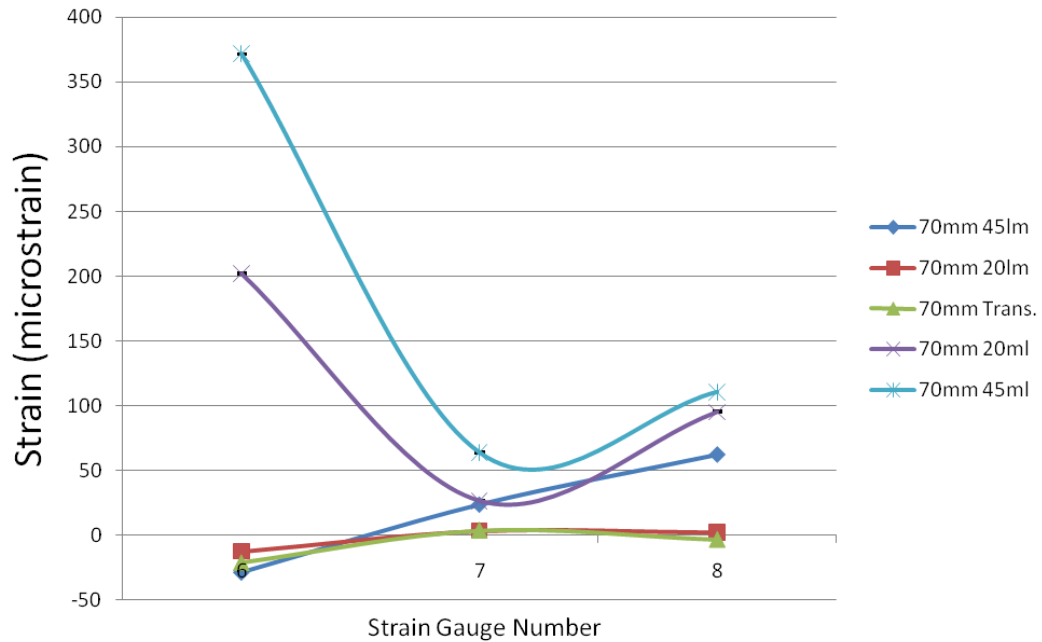
Figure 128 The strain on the locking plate, for the five fracture angle cases positioned 70mm distal to the stem tip.

7.5.4 Plate Stress comparison

The maximum Von Mises stress on the locking plate, for the five fracture angle cases positioned 70 mm distal to the stem tip, are presented in Figure 129. Lower maximum stresses were seen for fractures in the LM direction compared to fractures in the ML direction. The highest stress was at the 45 degree ML fracture with a maximum Von Mises stress of 553 MPa. Although the Yield stress (792 MPa) of the locking plate was not reached in any of the fracture cases, the fatigue limit 310-448 MPa (at 10^7 cycles) of the locking plate is exceeded in the 45 degree ML case, while the stress at the 45 degree LM case is very close.

The Von Mises stress across the whole plate, for the five fracture angle cases positioned 70 mm distal to the stem tip, are presented in Figure 130. For the 45LM fracture, the region of high stress was located between the distal empty screw hole bridging the fracture and the screw hole supporting the most proximal bicortical screw, screw holes 7 and 8. For the 20 LM and transverse fractures, the high stress region is located proximally around screw holes 2 and 3.

For the ML fractures, this high stress region has moved distally down the plate, with the highest stress found around the bicortical screw located proximal to the fracture, and the most proximal empty screw hole bridging the fracture, screw holes 6 and 7. For both fracture cases, there was also a region of high stress around screw hole 9, the most proximal bicortical screw located distal to the fracture.
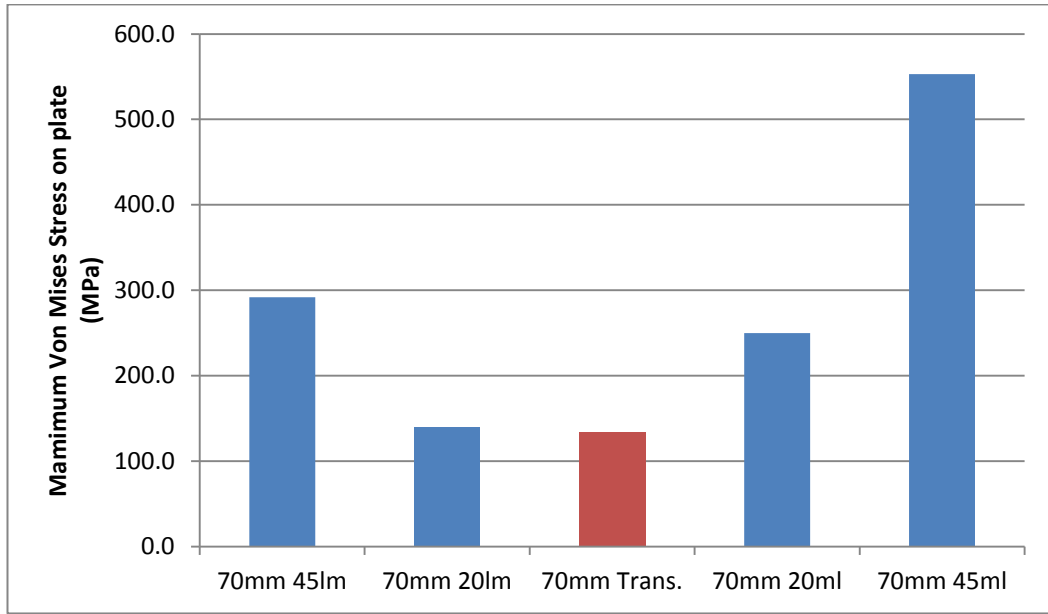
Figure 129 The maximum Von Mises stress on the plate, for the five fracture angle cases positioned 70mm distal to the stem tip
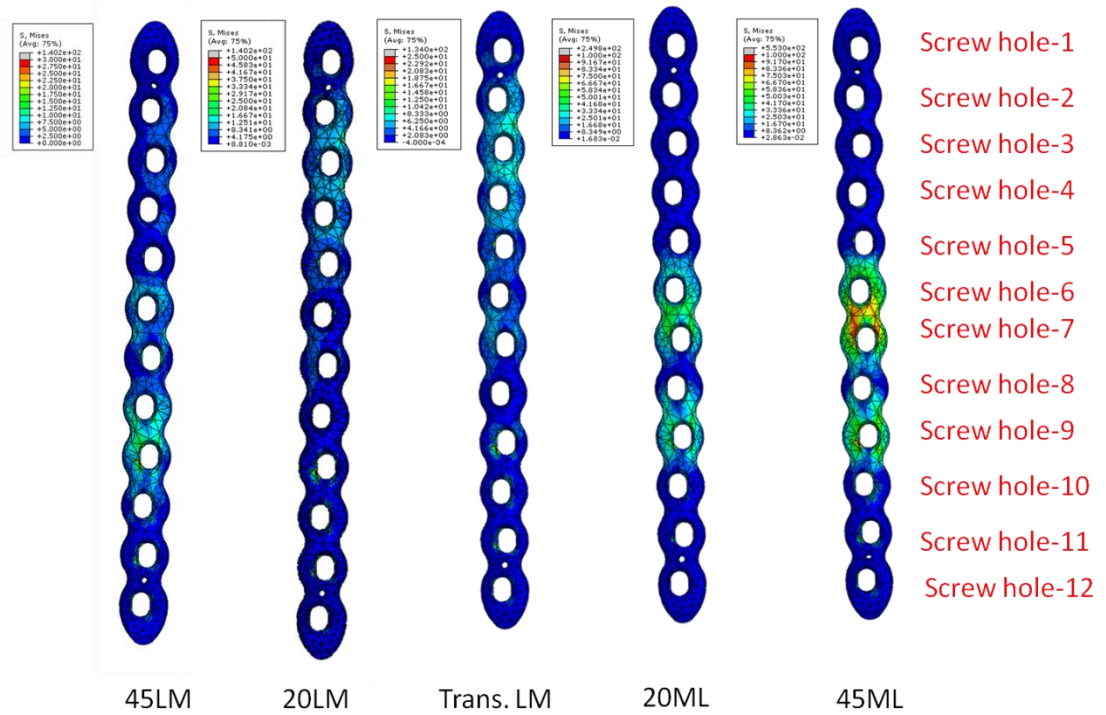
**Figure 130 Von Mises Stress plot, for the five fracture angle cases positioned 70 mm distal to the stem tip**

7.4.4 Summary

Moving the height of the fractures 70 mm distal to the prosthesis stem tip and varying the angle of the fracture had a large effect on overall behaviour of the constructs. Similar to the 10mm fracture height results, the stability of the constructs decreased as the fracture angles were increased, with different results seen in each fracture direction. Fractures in the ML direction had lower stiffness and higher plate strains than fractures in the LM direction. For both fracture directions, the 45° angles were less stable when compared to the 20° fracture angles. For both the transverse and the fracture angle cases in the LM direction, the plate strain remained low with only small changes in overall stiffness. However for the fracture angles in the ML direction, very high plate strains were recorded, with a corresponding drop in overall construct stiffness. Strain peaks on the plate of over 200 µε and 300 µε were seen for the 20° and 45° cases respectively. The plate strain pattern correlated with the pattern of maximum stress across the range of fractures.

The computational model predicts cyclic plate failure for the 45° ML case, with the 45° LM case also showing very high plate stress. This shows that the instrumentation combination used in this study is not suitable for these fracture configurations.

7.5 Discussion

The aim of this section was compare the validated fracture fixation case with a range of alternative clinical scenarios. The alternative scenarios involved adjusting the simple transverse fracture used in the development of the baseline computational models, to investigate the effect of fracture height and fracture angle on construct performance. In order to achieve this, a range of fractures were modelled at two distinct fracture heights. The displacement of the construct under load was used to compare the overall construct stiffness between the investigated cases. Surface bone and plate strain was used to identify any changes to the load sharing relationship of the construct. The peak stress within the plate for each fracture scenario was compared to the yield stress and fatigue life (cycling loading), as an indicator of plate failure risk.

7.5.1 Fracture Angle

The Vancouver classification system for periprosthetic fractures does not account for the angle of the fracture. Previous studies investigating the biomechanical performance of PFF fixation have focused on construct type and fixation methods, while the fracture has been simplified to an assumed worst case scenario, such as a transverse fracture [75, 76, 79]. Fracture

angle was found to have large effect on both strain and stress on the locking plate.

For the range of investigated fractures stabilised with the same instrumentation construct, fractures in the ML direction were found to be less stable than the comparable fractures in the LM direction. This difference in stabilised construct behaviour with fracture angle could be due to the orientation of the fracture in relation to the direction of the applied load. This could explain the differences between the ML and LM fracture instability.

For the fractures in the ML direction, the fracture is sloping towards the plate. When a load is applied at the 10° angle, the load component tangential to the fracture decreases, while the component normal to the fracture increases. This will reduce the amount of sliding at the fracture site and increase fracture site compression. This fracture movement would result in C- shape bending of the plate, with the lateral length of the plate in more tension overall. The strain at both gauge locations 6 and 8 are in tension. The bending of the plate can be seen in Figure 131.

Using the illustrated fracture in the diagram as reference, For the fractures in the LM direction, the fracture is sloping downwards away from the plate. When a load is applied at the 10° angle, the load component tangential to the fracture increases, while the component normal to the fracture reduces. This would cause a reduction in compression at the fracture site and increase sliding. This fracture movement would result in S- shape bending of the plate. The strain at gauge location 8 is in compression while gauge 6 is in tension. The bending of the plate can be seen in Figure 131. The residual tension in the plate is transferred down the lateral cortex.
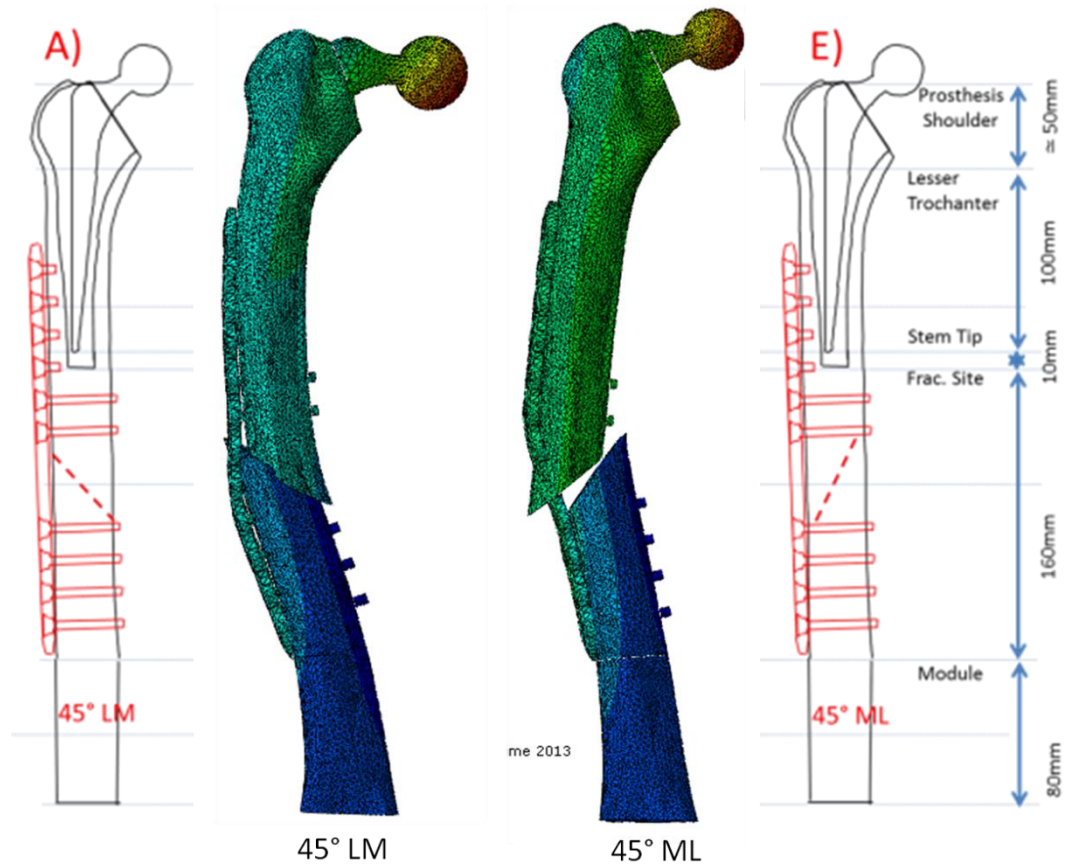
Figure 131 Exaggerated bending of both the 45°LM and 45ML cases, using a deformation scale factor of 100 and 50 respectively.

The overall stiffness results over the range of investigated fracture angles clearly show that severity of this effect is greater as the angle of the fracture is increased. The variation in plate strain with respect to loading angle indicate that changes in the strain distribution pattern changes correspond to the changes in fracture angle. Fractures in the LM direction were found to have a larger effect on bone strain while fractures in the ML direction had larger effect on plate strain. These results demonstrate that, in addition to the Vancouver classification, the orientation of the fracture should be also taken into account by surgeons when deciding on B1 PPF management.

7.5.2 Fracture height

Distinctly different loading patterns were seen between each of the investigated fracture heights. For the 10 mm fractures, the highest plate strains were found at both the 45° fracture cases, whereas for the 70 mm fractures, the highest plate strains were found for both of the fracture angles in the ML direction. With the translation of the fracture 60 mm distally down the Femur, the distance between the distal tip of the prosthesis and the fracture site has been increased, introducing a large volume of cortical bone

sited between the proximally positioned rigid prosthesis surrounded by the cement mantle, and the distal stabilised fracture. This introduced a significant volume of comparatively weak bone in a region of the construct where a large proportion of bending was expected to occur. The instrumentation combination used to stabilise the fracture changes as the fracture height is varied to remain appropriate to the fractures. In the 10 mm case, where there is a unicortical screw sited proximally to the fracture, there is fixation between the plate and the lateral bone cortex. The bicortical screw used proximally to the fracture in the 70 mm case, there is extra fixation afforded by the additional cortex as well as the increased stiffness of the longer screw, would result in this area of the bone becoming stiffer and would result in more load transfer to the plate. More bone bending would be expected in the 10 mm case, whereas with this region of the bone being stiffened in the 70 mm case, this would result in more plate bending in the proximal bridging region of the locking plate. The significant changes in plate strain pattern between the two fracture heights indicate that between the change in fracture location and the corresponding changes to the appropriate instrumentation combination to stabilise the fracture, is changing how the plate is loaded.

7.5.3 Plate stress

For the 70 mm fracture height, the plate stress at the 45° ML case exceeded the fatigue limit, while the peak plate stress at three of the other investigated fracture angles was also close to the fatigue limit. As discussed previously, section 5.6, the computational model developed in this study has a tendency to overestimate the construct stiffness and underestimate strain and stress. Some of the assumptions made in the model, such as homogenised bone representation, completely fixed boundary conditions, and perfect screw to bone interaction, all contribute to the stiffness overestimation. Therefore, the peak plate stress from the computational model results should be interpreted as the lowest predicted peak stress expected on the plate. The geometry used in the computational model represents a generalised periprosthetic fracture. Stress risers found in a patient specific Femur resulting from local variations in bone geometry and quantity would also influence construct mechanics. If these constraints were modelled in detail, it would be expected that the peak plate stress magnitude would be greater. For the cases where the peak plate stress was already close to the fatigue limit, this could have implications on their risk of failure.

The applied axial load of 500N corresponded to the recommended partial weight bearing after following stable plate fixation. This represents a patient performing a toe-tap load from a supported position. As the fracture heals, the load the patient will apply though the construct will increase through to a maximum of 2300N, representative of full weight bearing in an anatomical

one-legged stance. While it would be possible to increase the load in the computational model, the current model cannot accurate represent the bone remodelling that would take place across the fracture site. The rate of fracture healing is highly patient specific and a difficult scenario to simulate. The interaction between the proximal and distal femoral fragments is currently represented in this model by the friction co-efficient across the fracture site. With a case exceeding the fatigue limit of the plate and with three other fracture cases close to the limit, as the stabilised construct loading progresses beyond partial weight bearing and towards full weight bearing, there is a significant risk of failure of the fixation plate.

7.6 Conclusion

The developed periprosthetic fracture fixation model developed throughout this study was used to investigate a range of fracture configuration scenarios.

The angle of the fracture was shown to have a significant effect on stabilised construct mechanics and specifically, the direction of the fracture has a very large effect on fracture stabilisation. It is recommended that the orientation of the fracture should be taken into account by surgeons when deciding on B1 PPF management.

The position of the fracture from the tip of the stem changed the stiffness of the construct and the load transfer through the fixation plate. Clinicians must be aware that changing the method of proximal plate fixation immediately proximal to the bridging length of the plate may affect the load transfer through the plate.

Under partial weight bearing, the computational model predicted that instrumentation combination used in stabilise the PPF would fail under fatigue loading, while the risk of potential plate failure was identified in three other fracture cases. With the characteristics of the developed computational model and the potential for increases in postoperative load, augmentation of the current instrumentation or changing to an alternative combination is recommended.

The magnitude of the changes in overall stiffness and strain on both the bone and locking plate are far greater than in any variable tested using the computational models previously. This indicates that the computational model is sensitive to the angle of the fracture.

Chapter 8 **Discussion**

8.1 Introduction

The aim of this project was to evaluate fixation methods for periprosthetic fractures of the Femur, where the prosthesis stem was well fixed and did not require revision. This project focused on fracture stabilisation using locking trauma plates secured using screws. Comparisons conducted using finite element models were comprehensively validated against on-site experimental studies. A range of fracture configurations were tested and the performance of the fixation method evaluated in each case. This section discusses the limitations and future recommendations for the study and the overall conclusions of the study are presented.

8.2 General discussion

8.2.1 Experimental Work

One of the objectives of this study was to develop a loading rig and methodology to be able to apply load to the Sawbone specimens. The methods used to stabilise the fractured specimens performed well and ensured that the specimens remained fully supported throughout the loading cycles. There was a 3.5% experimental variability between rig assembly repeats with full disassembly of the rig between tests. The overall stiffness variability over the range of Sawbone specimens was 10%. There was good agreement in overall specimen stiffness between the results from the intact Femur case and similar work conducted by Heiner et al. with a 6% difference, based on results using a slightly different rig setup. There was a reasonable strain pattern agreement in bone strain between the results from the intact Femur case and similar work conducted by Pal et al. with large differences in loading setup. Clear changes in both overall construct stiffness and bone strain were observed between the experimentally investigated specimen cases, and there was also large changes in behaviour with loading angle.

The additional torsional loading rig configuration was unable to change the loading mode of the specimens, with no significant difference in behaviour identifies between either the THA or PPF specimens which were loaded with

and without additional torsion. It is likely that the 8° loading change was not large enough to result in a significant change in behaviour, and that by increasing this angle, differences in behaviour could be identified.

Experimental loading data was collected for the Intact Femur, THR and PPF cases. The range of loading angles was wide enough to result in large difference in behaviour between the 0°, anatomic 10° and the 20° loading cases. Identifying well-defined changes in behaviour for each case with respect to loading angle, and also between the tested cases, established clear patterns which the computational models could be evaluated against. The standard deviation for the overall construct stiffness loading repeats was much higher for the instrumented specimens than was seen for the same specimens at the intact Femur case. With the accuracy of the specimen preparation for stem implantation, manual positioning of the prosthesis and stabilisation instrumentation, dependent on the quality delivered by the surgeon performing the techniques. This human error factor could contribute to the observed stiffness variability.

The creation of a large fracture gap between the two bone fragments had a very large effect on construct stiffness. With the load being transmitted solely through the fixation plate, very large strain magnitude were observed on the fixation plate, while the strain pattern measured along the medial length of the bone was changed completely with respect to the perfectly reduced fracture results and also the THR and Intact Femur results.

8.2.2 Computational Work

The aim of the computational modelling was to produce a baseline model which could be used to investigate the effect of fracture configuration on stabilised construct behaviour. The models were developed in stages, with each stage validated against experimental results, in order to isolate and reduce possible sources of error. At each stage calibration of the model to the experimental results was avoided, meaning that the model inputs were not varied to purely match the computational with the experimentally outputs. An approach was taken where the sensitivity of the model to a specific variable was investigated, the relationship of the variable on overall behaviour was evaluated, before choosing the most appropriate value, not necessarily the best matching, to be used in later development stages.

The computational models consistently overestimated the stiffness of the experimental specimens, with the differences between the experimental and computational results consistently greater than the error over the range of specimens. While the models consistently replicated the correct proximal bone strain patterns and the overall construct stiffness patterns, however there was a significant magnitude mismatch between the computational model and the experimental results,, especially at the distal Femur. The intact Femur, THA and PPF cases had absolute errors of 48%, 55% and 62% respectively. As the complexity of the computational models increased, with the addition of additional interactions and stabilisation instrumentation, the error between the computational models and the experiments increased. The accuracy of the computational plate strain predictions provided assurance that the load sharing behaviour between the plate and the bone represented the experimental behaviour.

It was found that the model was very sensitive to the method of applying load to the model and the contact surface interactions. From the results of the sensitivity studies, in agreement with previous work in the literature, it has also shown that axial compression tests of long bone models can be very sensitive to the choice of interaction properties at the interfaces[106-108] and to the applied boundary conditions[109]. The assessment of a range of loading angles during validation provided confidence that the model accuracy is not specific to a particular load distribution, although the 10 degree case did provide the closest match. Our models were reasonably sensitive to the element type, the fracture site coefficient of friction, and the cortical bone material properties. While there were differences in overall construct stiffness magnitude, it was reassuring that both the experimental and computational model captured the relationship between overall stiffness and the loading angle of the specimens.

When comparing the computational model developed in this study against the previous studies in this area, using computational modelling to investigate periprosthetic fracture fixation, there are some clear differences in model behaviour. Compared to the study conducted by Shah et al[80], the correlation between computational and experimental strains are similar for the 10 degree loading case. However, the strains at the additional 0 and 20 degree loading angles investigated in this study do not correlate as well. While no other studies have investigated more than one loading angle, both the experimental and computational results from this study strongly indicate

that this would be observed with other fracture instrumentation combinations. This effect would likely be greatest in studies investigating fixations combinations which use cerclage cables only for proximal fixation. The computational stabilised specimen stiffness reported by Shah et al[80], 768-1102 N/mm are significantly lower than both the experimental and computational specimen stiffness reported in this study, 4580-4800 N/mm. This difference in stiffness is likely due to the 5mm fracture gap used in the Shah study, effectively resulting in an unstable fracture. As part of the overall work within the group, Mehran Moazen adapted the model developed in this study to include a 10mm fracture gap[104], resulting in a specimen stiffness of 1560N/mm, and a very close bone strain correlation. This indicates that the interaction at the fracture site adds significant complexity to a periprosthetic fracture model. It is interesting that a number of previous studies in the literature have specifically chosen not to report the experimental stiffness of their specimens when they would likely have had the data available[80, 88].

In order to investigate a stabilisation instrumentation combination which was more clinically relevant that the instrumentation used in the validation sections, the effect of lengthening of the fixation plate and adding additional screws was investigated. This increase in plate length necessitated the investigation of the effect of removing the distal module and the potting cement. The removal of the distal module and potting cement mainly primarily affected the distal bone strain, while the bone strain in the proximal bone region and strain on the locking plate remained largely unaffected. Removing the distal module reduces influence of boundary conditions on distal strain gauges as the gauges remain at a fixed height from the fracture height, while the point at which the Femur is supported is moved away from the gauges.

The change from the 8 hole to 10 hole plate instrumentation configuration did not have a large effect on the overall biomechanics of the fracture fixation construct. The change in anticipated overall construct stiffness, as a result of the longer locking plate and the increase in number of bone to screw fixation points, was an increase 6%. The removal of the distal module affected mainly the distal bone region and not the fixation plate or proximal bone region. As this study showed that the removal of the distal module affected mainly the distal bone region and not the fixation plate or proximal bone region, the removal of the module to facilitate the better modelling of

different fracture heights could be recommended. The change from the baseline 8 hole plate to the developed 10 hole plate did not greatly change the overall mechanical performance of the specimens.

8.2.3 Periprosthetic fracture configuration studies

The Vancouver classification system for periprosthetic fractures states that a type B fracture occurs around the stem or just below it[3, 28]. A type C fracture is described as occurring well below the prosthesis[3, 28]. This only provides an ambiguous guideline for fractures occurring distal to the prosthesis tip. With the possibility of different treatment methods used for different fracture classifications, there is a need for a clear definition of where a fracture ceases to be classified and treated as a type B fracture and starts to be treated as a type C fracture. No standard instrumentation configuration has been used in to investigate periprosthetic fractures in previous studies[96], with significant variations in fracture position seen between studies.

The magnitude of the changes in overall stiffness and strain on both the bone and locking plate are far greater than in any variable tested using the computational models previously. This indicates that the computational model is sensitive to the angle of the fracture.

Under partial weight bearing, the computational model predicted that instrumentation combination used in stabilise the PPF would fail under fatigue loading, while the risk of potential plate failure was identified in three other fracture cases. With the characteristics of the developed computational model and the potential for increases in postoperative load, augmentation of the current instrumentation or changing to an alternative combination is recommended.

The position of the fracture from the tip of the stem changed the stiffness of the construct and the load transfer through the fixation plate. Clinicians must be aware that changing the method of proximal plate fixation immediately proximal to the bridging length of the plate may affect the load transfer through the plate.

The angle of the fracture was shown to have a significant effect on stabilised construct mechanics and specifically, the direction of the fracture has a very large effect on fracture stabilisation. The current Vancouver classification system and the related treatment algorithms do not currently account for the angle of the fracture.

8.3 Limitations

8.3.1 Introduction

This section discusses some of the limitations of the experimental and computational methods used in this study.

At the beginning of the study, the focus of the project once the baseline validation had been completed was planned to be the investigation of the effect of screw fixation on overall behaviour. However, once the validation stage was completed, initial model investigations combined with the clinical need for guidance regarding the effect of fracture configuration on stabilised PPF performance changed the end focus point of the study.

8.3.2 Experimental Limitations

The most important limitation of the experimental section of the study was the use of synthetic Sawbones as a substitute for human Femurs. Previous work done in the literature comparing the performance between cadaveric Femurs and synthetic Sawbone Femurs have shown that the mechanical behaviour when under axial compression is very similar[86]. These studies relate to the Sawbones tested in an intact Femur test case. While the overall behaviour might be the same as the natural bone, the response to factors such as cement interaction were not completely representative. While interdigitation would occur as cement is introduced to the cancellous bone in the proximal Femur region, the homogeneous properties of the representative cancellous region of the Sawbone Femurs did not allow for optimal bonding between the cement and bone. This may have contributed to the overall construct stiffness mismatch between the experimental and computational results.

While every step was taken to ensure perfect fracture reduction, stabilising both femoral fragments with the fracture site completely in contact, the complex shape of the Femurs made securing the two bone fragments during plate fixation very difficult. The created fracture site was not consistently result in a fracture site with both fracture surfaces perfectly parallel when reduced. As a result, the resultant plate stabilised fracture reduction was not always perfect. As the clinical, plate fixation process was followed as faithfully as possible, during screw hole preparation, the drill guides and

surgical drill bits were used to create pilot holes in the synthetic Sawbone. The combination of very tight tolerances, high speed drill and the large surface area between the drill bit and guide resulted in high temperatures in the region of the bone surface and medial plate surface. This caused some of the loose material produced by the drilling to melt and clog up the pilot holes and also the threads on locking inserts. While the majority was removed, this did impede screw insertion. This may have contributed to the variations in performance between the experimental specimens and may have reduced the stability of the PPF specimens, reducing the overall construct stiffness, and thus may have contributed to the mismatch between the experimental and computational results.

The loading scenario chosen to apply loads to the test specimens was simplified compared to the range of anatomical loads experienced in a full gait cycle. The fact that the tested loading scenario was selected to replicate a toe touch load only, in combination with the lack of bone remodelling means that the findings of this study relate to the initial post-operating patient recovery period only. Consequently, the results of this study are comparable to previous periprosthetic fixation studies which have also concentrated low force, isometric loading, i.e. axial compression, lateral bending and torsional loading regimes[33, 34, 72-74, 76, 77, 80, 110]. In order to investigate fixation performance further into patient recovery, a physiological loading regime would need to be introduced, potentially including cyclic loading and larger forces [75, 79, 85].

8.3.3 Computational Limitations

A major limitation of the computational models was the representation of the screw threads within the cortical bone. The computational resources needed to accurately simulate the screw threads at every bone-to-screw interface in the model, were not available for this study. As a result, the screw threads were simplified and a simple tied contact condition was applied between the relevant screw and bone surfaces. Another member of the group developed a method to better represent the interface by using a combination of frictionless surfaces and springs to introduce compliance to the bone-to-screw interfaces in the model[24, 105]. While this method was a step towards full screw thread representation, accurate modelling of the thread interaction and local bone failure could not be achieved.

The computational model consistently overestimated the construct stiffness and displayed smaller changes in strain with loading angle than were seen experimentally. The idealised distribution of homogenous material properties, the completely fixed boundary conditions and the tied contacts applied, all contribute to an overall increase in stiffness compared to the experimental specimen. This finding is not unique to the current study[105]. A similar stiffness overestimation was also observed during the development stages of this model, where both an intact Femur and a THA case were investigated, indicating that the majority of the over constraint is independent of the fracture and plate fixation. The intact Femur, THA and PPF cases had absolute errors of 48%, 55% and 62% respectively. During the development of this model, a series of sensitivity tests were undertaken but none succeeded in reducing the construct stiffness to the experimental level.

The mismatch in distal femoral strain are likely due to the differences in boundary conditions at the distal end of the Femur. The distal cement, grub screws and pot were included in the model with the aim of making these conditions as realistic as possible ([97, 100]), but the interfaces remain idealised and cannot represent the inevitable micro-movement that occurs experimentally. As the loading angle was altered, the greatest changes in strain were seen in the distal gauges, with less effect at the gauges in the region of the stem. This would indicate the strain in the region of the stem tip, where the fracture and fixation construct are positioned, is less sensitive to any boundary condition effects than the distal end of the Femur. Therefore care should be taken in both experimental and computational cases in interpreting strain information near to this boundary. Equally, key aspects of the construct, such as the plate fixation to the bone using screws, should not be placed close to the distal boundary conditions.

Chapter 9 **Conclusions**

9.1.1 Computational and Experimental conclusions

The key conclusions which can be derived from this study are presented below:

- The loading behaviour between the experimental and computational results, for the Intact Femur, THR and PPF cases.

- This is the first study which has investigated the effect of loading angle on periprosthetic fixation performance. It was found that the strain and stiffness behaviour of the experimental specimens varied greatly as the loading angle was changed. The trends but not the magnitudes of those changes can be predicted using the computational model developed in this study.

- The assessment of a range of loading angles during model validation proved that the model accuracy is not specific to a particular loading angle. The 10º loading case was found to provide the closest experimental to computational match.

- The model developed in this study could predict the magnitude of the strain in the plate and hence the likelihood of plate fracture, as well as assessing the relative stiffness of different fixation scenarios.

- This is the first study which has investigated the effect of fracture angle on periprosthetic fracture fixation. The fracture was found to have a significant influence on potential plate failure, and must be a key consideration when choosing the appropriate treatment.

- Caution is needed when investigating local bone behaviour around the fracture and at the distal end of the Femur, since these outputs will be highly dependent of the way that the fracture and boundary conditions are represented.

- The model was able to identify and predict changes in strain and stiffness between a set of comparative cases and be used to comment on their relative biomechanical performances.

9.1.2 Clinical conclusions

The key clinical conclusions which can be derived from this study are presented below:

- The angle of a periprosthetic fracture was shown to have a significant effect on stabilised construct mechanics and specifically. The direction of the fracture was found to have a large effect on fracture stabilisation.

- It is strongly recommended that the orientation of the fracture should be taken into account by surgeons when deciding on B1 PPF management.

- Stabilised transverse fractures were found to have the lowest plate strains and were identified as the least likely to fail.

- Fractures in the ML direction were found to less stable than fractures in the LM direction.

- The 45 degree Medial to Lateral fracture case was the least stabile and the instrumentation configuration used in this study is clearly not optimal for this fracture case.

- Clinicians must be aware that changing the method of proximal plate fixation immediately proximal to the bridging length of the plate will affect the load transfer through the plate.

9.2 Future Work

The developed computational model could be used to investigate a number of future work packages.

As part of an MSc project within the group, experimental testing of the specimens used in this study, re-stabilised with both cerclage cables and bone screws, and cerclage cables only have been conducted. It would be interesting to developing the computational model to include proximal cable fixation, and to assess the difference between screw and cable PPF stabilisation fixation.

Developing the computational model to better represent the screw to bone interface would be interesting. Either by increasing the level of detail employed at the interface, or even using multi scale modelling could be used to investigate the influence of the screw threads on overall behaviour.

The range of fracture heights could be expanded to fully explore the effect of fracture height from the currently modelled fractures adjacent to the stem tip, to fractures which occur very distal around the knee.

The influence of the angle of the fracture was investigated in this study. The next step towards developing a treatment algorithm incorporating fracture angle into the Vancouver classification system would require the optimum fixation instrumentation combination to be identified for each fracture angle. For the existing fracture angle models, a range of plate lengths, screw lengths and screw placements could be investigated to expand the work of this study.

Chapter 10 **Appendix**

10.1 List of References

1.   Fink, B., M. Fuerst, and J. Singer, *Periprosthetic fractures of the femur associated with hip arthroplasty.* Archives of Orthopaedic and Trauma Surgery, 2005. 125(7): p. 433-442.
2.   Kavanagh, B.F., *FEMORAL FRACTURES ASSOCIATED WITH TOTAL HIP-ARTHROPLASTY.* Orthopedic Clinics of North America, 1992. 23(2): p. 249-257.
3.   Masri, B.A., R.M.D. Meek, and C.P. Duncan, *Periprosthetic fractures evaluation and treatment.* Clinical Orthopaedics and Related Research, 2004(420): p. 80-95.
4.   Emsley, D., et al., *National Joint Registry 6th Annual Report.* 2009.
5.   Porter, M., et al., *National Joint Registry 9th Annual Report.* 2012.
6.   Marieb, E.N. *Human Anatomy and Physiology.* 2004.
7.   Martini, F.H., ed. *Fundamentals of Anatomy and Physiology.* 5th ed. 2001, Prentice Hall.
8.   Learmonth, I.D., C. Young, and C. Rorabeck, *The operation of the century: total hip replacement.* Lancet, 2007. 370: p. 1508-1519.
9.   Allami, M.K., et al., *Outcome of Charnley total hip replacement across a single health region in England - The results at ten years from a regional arthroplasty register.* Journal of Bone and Joint Surgery-British Volume, 2006. 88B(10): p. 1293-1298.
10.   Berry, D.J., et al., *Twenty-five-year survivorship of two thousand consecutive primary Charnley total hip replacements - Factors affecting survivorship of acetabular and femoral components.* Journal of Bone and Joint Surgery-American Volume, 2002. 84A(2): p. 171-177.
11.   Fender, D., W.M. Harper, and P.J. Gregg, *Outcome of Charnley total hip replacement across a single health region in England - The results at five years from a regional hip register.* Journal of Bone and Joint Surgery-British Volume, 1999. 81B(4): p. 577-581.
12.   Crowninshield, R.D., et al., *ANALYSIS OF FEMORAL COMPONENT STEM DESIGN IN TOTAL HIP-ARTHROPLASTY.* Journal of Bone and Joint Surgery-American Volume, 1980. 62(1): p. 68-78.
13.   Ratner, B.D., et al., eds. *Biomaterials Science An Introduction to Materials in Medicine.* 2nd Edition ed. 2004, Elsever Academic Press.
14.   Virolainen, P., et al., *UP TO 10 YEARS FOLLOW UP OF THE USE OF 71 CORTICAL ALLOGRAFTS (STRUT-GRAFTS) FOR THE TREATMENT OF PERIPROSTHETIC FRACTURES.* Scandinavian Journal of Surgery, 2010. 99(4): p. 240-243.
15.   Erhardt, J.B., et al., *Periprosthetic fractures around polished collarless cemented stems: the effect of stem design on fracture pattern.* Hip International, 2013. 23(5): p. 459-464.

16.   Beals, R.K. and S.S. Tower, *Periprosthetic fractures of the femur - An analysis of 93 fractures.* Clinical Orthopaedics and Related Research, 1996(327): p. 238-246.

17.   Lindahl, H., et al., *Risk factors for failure after treatment of a periprosthetic fracture of the femur.* Journal of Bone and Joint Surgery-British Volume, 2006. 88B(1): p. 26-30.

18.   Wu, C.C., et al., *Risk factors for postoperative femoral fracture in cementless hip arthroplasty.* Journal of the Formosan Medical Association, 1999. 98(3): p. 190-194.

19.   Franklin, J. and H. Malchau, *Risk factors for periprosthetic femoral fracture.* Injury-International Journal of the Care of the Injured, 2007. 38(6): p. 655-660.

20.   Tsiridis, E., F.S. Haddad, and G.A. Gie, *The management of periprosthetic femoral fractures around hip replacements.* Injury-International Journal of the Care of the Injured, 2003. 34(2): p. 95-105.

21.   Tsiridis, E., et al., *Periprosthetic femoral fractures around hip arthroplasty: Current concepts in their management.* Hip International, 2009. 19(2): p. 75-86.

22.   Duncan, C.P. and B.A. Masri, *Fractures of the femur after hip replacement.* Instr Course Lect, 1995. 44: p. 293-304.

23.   Brady, O.H., et al., *The reliability and validity of the Vancouver classification of femoral fractures after hip replacement.* Journal of Arthroplasty, 2000. 15(1): p. 59-62.

24.   Leonidou, A., et al., *Evaluation of fracture topography and bone quality in periprosthetic femoral fractures: A preliminary radiographic study of consecutive clinical data.* Injury-International Journal of the Care of the Injured, 2013. 44(12): p. 1799-1804.

25.   Claes, L.E., et al., *Effects of mechanical factors on the fracture healing process.* Clinical Orthopaedics and Related Research, 1998(355): p. S132-S147.

26.   Perren, S.M., *THE BIOMECHANICS AND BIOLOGY OF INTERNAL-FIXATION USING PLATES AND NAILS.* Orthopedics, 1989. 12(1): p. 21-34.

27.   Zhou, S., et al., *Age-related intrinsic changes in human bone-marrow-derived mesenchymal stem cells and their differentiation to osteoblasts.* Aging Cell, 2008. 7(3): p. 335-343.

28.   Parvizi, J., et al., *Treatment protocol for proximal femoral periprosthetic fractures.* Journal of Bone and Joint Surgery-American Volume, 2004. 86A: p. 8-16.

29.   Springer, B.D., D.J. Berry, and D.G. Lewallen, *Treatment of periprosthetic femoral fractures following total hip arthroplasty with femoral component revision.* Journal of Bone and Joint Surgery-American Volume, 2003. 85A(11): p. 2156-2162.

30.   Tsiridis, E., F.S. Haddad, and G.A. Gie, *Dall-Miles plates for periprosthetic femoral fractures - A critical review of 16 cases.* Injury-International Journal of the Care of the Injured, 2003. 34(2): p. 107-110.

31.   Tsiridis, E., et al., *Dynamic compression plates for Vancouver type B periprosthetic femoral fractures - A 3-year follow-up of 18 cases.* Acta Orthopaedica, 2005. 76(4): p. 531-537.

32.	Baker, D., S. Kadambande, and P. Alderman, *Carbon fibre plates in the treatment of*

femoral periprosthetic fractures. Injury, Int. J. Care Injured, 2004. 35: p. 596-598.
33.	Dennis, M.G., et al., *Fixation of periprosthetic femoral shaft fractures occurring at the tip of the stem - A biomechanical study of 5 techniques.* Journal of Arthroplasty, 2000. 15(4): p. 523-528.
34.	Peters, C.L., K.N. Bachus, and J.S. Davitt, *Fixation of periprosthetic femur fractures: A biomechanical analysis comparing cortical strut allograft plates and conventional metal plates.* Orthopedics, 2003. 26(7): p. 695-699.
35.	Hedequist, D., J. Bishop, and T. Hresko, *Locking plate fixation for pediatric femur fractures.* Journal of Pediatric Orthopaedics, 2008. 28(1): p. 6-9.
36.	Haidukewych, G.J., *Innovations in locking plate technology.* Journal of the American Academy of Orthopaedic Surgeons, 2004. 12(4): p. 205-212.
37.	Bryant, G., et al., *Isolated locked compression plating for Vancouver Type B1 periprosthetic*

femoral fractures. Injury, 2009. In Press.
38.	Stoffel, K., et al., *Biomechanical testing of the LCP - how can stability in locked internal fixators be controlled?* Injury-International Journal of the Care of the Injured, 2003. 34: p. 11-19.
39.	Nassiri, M., B. MacDonald, and J. O'Byrne, *Locking compression plate breakage and fracture non-union: a Wnite element study of three patient-specific cases.* Eur J Orthop Surg Traumatol, 2012. 22: p. 275-281.
40.	Ahmad, M., et al., *Biomechanical testing of the locking compression plate: When does the distance between bone and implant significantly reduce construct stability?* Injury, 2007. 38: p. 358-364.
41.	Giannoudis, P.V., N.K. Kanakaris, and E. Tsiridis, *Principles of internal fixation and selection of implants for periprosthetic femoral fractures.* Injury-International Journal of the Care of the Injured, 2007. 38(6): p. 669-687.
42.	Buttaro, M.A., et al., *Locking compression plate fixation of Vancouver type-b1 periprosthetic femoral fractures.* Journal of Bone and Joint Surgery-American Volume, 2007. 89A(9): p. 1964-1969.
43.	Mennen, U., *A NEW METHOD OF INTERNAL-FIXATION BY A PARA-SKELETAL CLAMP ON PLATE.* Journal of Bone and Joint Surgery-British Volume, 1982. 64(1): p. 145-146.
44.	Noorda, R.J.P. and P. Wuisman, *Mennen plate fixation for the treatment of periprosthetic femoral fractures - A multicenter study of thirty-six fractures.* Journal of Bone and Joint Surgery-American Volume, 2002. 84A(12): p. 2211-2215.
45.	Kamineni, S. and H.E. Ware, *The Mennen plate: unsuitable for elderly femoral peri-prosthetic fractures.* Injury-International Journal of the Care of the Injured, 1999. 30(4): p. 257-260.
46.	Liu, A.M., M. Flores, and P. Nadarajan, *FAILURE OF MENNEN FEMORAL PLATE.* Injury-International Journal of the Care of the Injured, 1995. 26(3): p. 202-203.

47. Lenz, M., et al., *Mechanical behavior of fixation components for periprosthetic fracture surgery.* Clinical Biomechanics, 2013. 28(9-10): p. 988-993.

48. Perren, S.M., et al., *Cerclage, Evolution and Potential of a Cinderella Technology. An Overview with Reference to Periprosthetic Fractures.* Acta Chirurgiae Orthopaedicae Et Traumatologiae Cechoslovaca, 2011. 78(3): p. 190-199.

49. Zenni, E.J., D.L. Pomeroy, and R.J. Caudle, *OGDEN PLATE AND OTHER FIXATIONS FOR FRACTURES COMPLICATING FEMORAL ENDOPROSTHESES.* Clinical Orthopaedics and Related Research, 1988(231): p. 83-90.

50. Barden, B., et al., *Periprosthetic fractures with extensive bone loss treated*

with onlay strut allografts. International Orthopaedics 2003. 27: p. 164-167.

51. Evans, M., et al., *Design and Testing of External Fixator Bone Screws.* Journal of Biomedical Engineering, 1990. 12(6): p. 457-462.

52. Kaab, M.J., et al., *Locked internal fixator - Sensitivity of screw/plate stability to the correct insertion angle of the screw.* Journal of Orthopaedic Trauma, 2004. 18(8): p. 483-487.

53. Ansell, R.H. and J.T. Scales, *A study of some factors which affect the strength of screws and their insertion and holding power in bone.* Journal of Biomechanics, 1968. 1(4): p. 279-282, IN9-IN10, 283-300, IN11, 301-302.

54. Yerby, S., et al., *Effect of Cutting Flute Design on Cortical Bone Screw Insertion Torque and Pullout Strength.* Journal of Orthopaedic Trauma, 2001. 15(3): p. 216-221.

55. Strømsøe, K., et al., *Holding power of the 4.5 mm AO/ASIF cortex screw in cortical bone in relation to bone mineral.* Injury, 1993. 24(10): p. 656-659.

56. Benterud, J.G., et al., *Implant Holding Power of the Femoral-Head - a Cadaver Study of Fracture Screws.* Acta Orthopaedica Scandinavica, 1992. 63(1): p. 47-49.

57. Nunamaker, D.M. and S.M. Perren, *Force Measurements in Screw Fixation.* Journal of Biomechanics, 1976. 9(11): p. 669-675.

58. Chaudhary, N., et al., *Experimental and numerical modeling of screws used for rigid internal fixation of mandibular fractures.* Model. Simul. Eng., 2008. 2008: p. 1-11.

59. Daum, W.J., et al., *Pull-Out Strengths of Bone Screws at Various Sites About the Pelvis-A Preliminary Study.* Journal of Orthopaedic Trauma, 1988. 2(3): p. 229-233.

60. Zdero, R., et al., *Cortical screw pullout strength and effective shear stress in synthetic third generation composite femurs.* Journal of Biomechanical Engineering-Transactions of the Asme, 2007. 129(2): p. 289-293.

61. Chapman, J.R., et al., *Factors affecting the pullout strength of cancellous bone screws.* Journal of Biomechanical Engineering-Transactions of the Asme, 1996. 118(3): p. 391-398.

62. Tsai, W.-C., et al., *Comparison and prediction of pullout strength of conical and cylindrical pedicle screws within synthetic bone.* Bmc Musculoskeletal Disorders, 2009. 10(1): p. 44.

63.   Hsu, C.C., et al., *Increase of pullout strength of spinal pedicle screws with conical core: biomechanical tests and finite element analyses.* Journal of Orthopaedic Research, 2005. 23(4): p. 788-794.

64.   Zhang, Q.H., S.H. Tan, and S.M. Chou, *Investigation of fixation screw pull-out strength on human spine.* Journal of Biomechanics, 2004. 37(4): p. 479-485.

65.   Zhang, Q.H., S.H. Tan, and S.M. Chou, *Effects of bone materials on the screw pull-out strength in human spine.* Medical Engineering & Physics, 2006. 28(8): p. 795-801.

66.   Chen, S.I., R.M. Lin, and C.H. Chang, *Biomechanical investigation of pedicle screw-vertebrae complex: a finite element approach using bonded and contact interface conditions.* Medical Engineering & Physics, 2003. 25(4): p. 275-282.

67.   Chatzistergos, P.E., E.A. Magnissalis, and S.K. Kourkoulis, *A parametric study of cylindrical pedicle screw design implications on the pullout performance using an experimentally validated finite-element model.* Medical Engineering & Physics. 32(2): p. 145-154.

68.   Callister, W.D., ed. *Material Science and Engineering: An Introduction.* 6th ed. 2003, John Wiley and sons inc.

69.   Benham, *Mechanics of Engineering Materials.* 2nd ed. 1996: Prentice Hall

70.   National-Instruments *Measuring strain with strain gauges.* 2010.

71.   National-Instruments *NI 9237 Operating instructions and specifications.* 2009.

72.   Dennis, M.G., et al., *Fixation of periprosthetic femoral shaft fractures: A biomechanical comparison of two techniques.* Journal of Orthopaedic Trauma, 2001. 15(3): p. 177-180.

73.   Fulkerson, E., et al., *Fixation of periprosthetic femoral shaft fractures associated with cemented femoral stems - A biomechanical comparison of locked plating and conventional cable plates.* Journal of Orthopaedic Trauma, 2006. 20(2): p. 89-93.

74.   Kuptniratsaikul, S., et al., *Plate-screw-wiring technique for the treatment of periprosthetic fracture around the hip: A biomechanical study.* Journal of the Medical Association of Thailand, 2001. 84(Suppl. 1): p. S415-S422.

75.   Schmotzer, H., G.H. Tchejeyan, and D.M. Dall, *Surgical management of intra- and postoperative fractures of the femur about the tip of the stem in total hip arthroplasty.* Journal of Arthroplasty, 1996. 11(6): p. 709-717.

76.   Talbot, M., R. Zdero, and E.H. Schemitsch, *Cyclic loading of periprosthetic fracture fixation constructs.* Journal of Trauma-Injury Infection and Critical Care, 2008. 64(5): p. 1308-1312.

77.   Zdero, R., et al., *Biomechanical evaluation of periprosthetic femoral fracture fixation.* Journal of Bone and Joint Surgery-American Volume, 2008. 90A(5): p. 1068-1077.

78.   Moazen, M., et al., *Periprosthetic fracture fixation of the femur following total hip arthroplasty: A review of biomechanical testing.* Clinical Biomechanics, 2011. 26(1): p. 13-22.

79. Wilson, D., et al., *A biomechanical study comparing cortical onlay allograft struts and plates in the treatment of periprosthetic femoral fractures.* Clinical Biomechanics, 2005. 20(1): p. 70-76.

80. Shah, S., et al., *The biomechanics of plate fixation of periprosthetic femoral fractures near the tip of a total hip implant: cables, screws, or both?* Proceedings of the Institution of Mechanical Engineers Part H-Journal of Engineering in Medicine, 2011. 225(H9): p. 845-856.

81. Mihalko, W.M., et al., *FINITE-ELEMENT MODELING OF FEMORAL-SHAFT FRACTURE FIXATION TECHNIQUES POST TOTAL HIP-ARTHROPLASTY.* Journal of Biomechanics, 1992. 25(5): p. 469-476.

82. DeCoster, T.A., et al., *Optimizing Bone Screw Pullout Force.* Journal of Orthopaedic Trauma, 1990. 4(2): p. 169-174.

83. FINLAY, J.B., et al., *Analysis of the Pull-out Strength of Screws and Pegs Used to Secure Tibial Components Following Total Knee Arthroplasty.* Clinical Orthopaedics and Related Research, 1989. 247: p. 220-231.

84. Pfeiffer, F.M. and D.L. Abernathie, *A comparison of pullout strength for pedicle screws of different designs - A study using tapped and untapped pilot holes.* Spine, 2006. 31(23): p. E867-E870.

85. Barker, R., et al., *Reconstruction of femoral defects in revision hip surgery.* Journal of Bone and Joint Surgery-British Volume, 2006. 88B(6): p. 832-836.

86. Heiner, A. and T. Brown, *Structural properties of a new design of composite replicate femurs and tibias.* Journal of Biomechanics, 2001. 34(6): p. 773–781.

87. Pal, B., et al., *Strain and micromotion in intact and resurfaced composite femurs: Experimental and numerical investigations* Journal of Biomechanics 2010. 43: p. 1923-1930.

88. Pal, B., et al., *Strain and micromotion in intact and resurfaced composite femurs: Experimental and numerical investigations.* Journal of Biomechanics, 2010. 43(10): p. 1923-1930.

89. Tarsuslugil, S., *Computational Modelling of Spinal Burst Fractures for the Development of Calcium Phosphate Cement.* 2011, University of Leeds.

90. Heiner, A.D., *Structural properties of fourth-generation composite femurs and tibias.* Journal of Biomechanics, 2008. 41(15): p. 3282-3284.

91. Saha, S. and S. Pal, *MECHANICAL-PROPERTIES OF BONE-CEMENT - A REVIEW.* Journal of Biomedical Materials Research, 1984. 18(4): p. 435-462.

92. Wheeler, J.P.G., A. Miles, and S.E. Clift, *The influence of the stem–cement interface in total hip replacement—a comparison of experimental and finite element approaches.* Proc Instn Mech Engrs Vol, 1997. 211.

93. Verdonschot, N. and R. Huiskes, *Cement Debonding Process of Total Hip Arthroplasty Stems.* CLINICAL ORTHOPAEDICS AND RELATED RESEARCH, 1997. 336: p. 297-307.

94. P´erez, M., et al., *A comparative FEA of the debonding process in different concepts of cemented hip implants.* Medical Engineering & Physics, 2006. 28: p. 525-533.

95. Shockey, J., J. Von Fraunhofer, and D. Seligson, *A Measurement of the Coefficient of Static Friction of Human Long Bones.* Surface Technology, 1985. 25: p. 167-173.

96. Moazen, M., et al., *Periprosthetic fracture fixation of the femur following total hip arthroplasty: a review of biomechanical testing.* 2011. 26(1): p. 13-22.

97. Ebrahimi, H., et al., *Biomechanical properties of an intact, injured, repaired, and healed femur: An experimental and computational study journal of the mechanical behavior of biomedical materials,* 2012. 16: p. 121-135.

98. Mihalko, W., et al., *Finite-Element Modelling of the Femoral Shart Fracture Fixation Techniques Post Total Hip Arthroplasty.* Journal of Biomechanics, 1992. 25(5): p. 469-476.

99. Moazen, M., et al., *Rigid versus flexible plate fixation for periprosthetic femoral fracture—Computer modelling of a clinical case.* Medical engineering & physics, 2012. 34(8).

100. Shah, S., et al., *The biomechanics of plate fixation of periprosthetic femoral fractures near the tip of a total hip implant:cables, screws, or both? Proceedings of the Institution of Mechanical Engineers, Part H: Journal of Engineering in Medicine*, 2011. 225.

101. Vinceconti, M., *Extracting clinically relevant data from finite element simulations.* clinbiomec, 2005. 20: p. 451-454.

102. Erhardt, J., et al., *Treatment of Periprosthetic femur fractures with the non-contact bridging plate: a new angular stable implant.* Arch Orthop Trauma Surg, 2008. 128(4): p. 409-416.

103. Zhao, Y., et al., *Trabecular level analysis of bone cement augmentation: a comparative experimental and finite element study.* Ann Biomed Eng, 2012. 40(10): p. 2168-76.

104. Moazen, M., et al., *The Effect of Fracture Stability on the Performance of Locking Plate Fixation in Periprosthetic Femoral Fractures.* Journal of Arthroplasty, 2013. 28(9): p. 1589-1595.

105. Moazen, M., et al., *Evaluation of a new approach for modelling the screw-bone interface in a locking plate fixation: a corroboration study.* Proc Inst Mech Eng H, 2013. 227(7): p. 746-56.

106. Hayes, W. and S. Perren, *Plate-bone friction in the compression fixation of fractures.* Clin Orthop 1972. 89: p. 236-640.

107. Mann, K., D. Bartel, and T. Wright, *Coulomb frictional interfaces in modeling cemented total hip replacements: a more realistic model.* journal of Biomechanics, 1995. 28: p. 1067-1078.

108. Nuno, N., R. Groppetti, and N. Senin, *Static coefficient of friction between stainless steel and PMMA used in cemented hip and knee implants.* Clin Biomech 2006. 21: p. 956-962.

109. MacLeod, A., P. Pankaj, and R. Simpson, *Axial Compression Tests of Plated Bone: A Numerical Study to investigate the effect of Loading Conditions on the Mechanical Response*, in *Poster presented at the 19th Congress of the European Society of Biomechanics.* 2013.

110. Panjabi, M.M., et al., *EFFECT OF FEMORAL STEM LENGTH ON STRESS RAISERS ASSOCIATED WITH REVISION HIP-ARTHROPLASTY.* Journal of Orthopaedic Research, 1985. 3(4): p. 447-455.

10.2 Conference Presentations

Conference oral presentation:

19th Congress of the European Society of Biomechanics

Conference poster presentations:

SET for Britain (2009)

British Orthopaedic Research Society (BORS 2011)

Orthopaedic Research Society (ORS 2012)

10.3 Publications to date

- Moazen M; Mak JH; Etchels LW; Jin Z; Wilcox RK; Jones AC; Tsiridis E *Periprosthetic femoral fracture - a biomechanical comparison between vancouver type B1 and B2 fixation methods*. **Journal of Arthroplasty**, vol. 29, pp.495-500. 2014.
- Moazen M; Mak JH; Jones AC; Jin Z; Wilcox RK; Tsiridis E *Evaluation of a new approach for modelling the screw-bone interface in a locking plate fixation: a corroboration study*. **Proceedings of the Institution of Mechanical Engineers - Part H: Journal of Engineering in Medicine**, vol. 227, pp.746-756. 2013.
- Moazen M; Mak JH; Etchels LW; Jin Z; Wilcox RK; Jones AC; Tsiridis E *Periprosthetic Femoral Fracture - A Biomechanical Comparison Between Vancouver Type B1 and B2 Fixation Methods*. **Journal of Arthroplasty**, 2013.
- Moazen M; Mak JH; Etchels LW; Jin Z; Wilcox RK; Jones AC; Tsiridis E *The effect of fracture stability on the performance of locking plate fixation in periprosthetic femoral fractures*. **Journal of Arthroplasty**, vol. 28, pp.1589-1595. 2013.

10.4 Periprosthetic Literature review comparison tables

Table 17 Axial loading results[33, 72, 73, 76, 77]

Implant Type	Proximal fixation	Distal Fixation	Zdero (08)		Dennis (00)	Dennis (02)	Fulkerson(06)	Talbot (08)
			No-Gap	Gap				
Compression plate	Unicortical screws	Bicortical screws			4900			
Compression plate	Cerclage cables	Bicortical screws			900	474	304	
Compression plate	Cerclage cables	Cerclage cables			1000			
Compression plate	Unicortical Screws & Cerclage cables	Bicortical screws	1671	1104	5000			
Locking plate	Unicortical Screws & Cerclage cables	Bicortical screws	1614	963				
Locking plate	Unicortical screws	Bicortical screws	1586	935			420	750
Allograft struts	Cerclage plain wire	Cerclage plain wire						
Allograft struts	Cerclage cables	Cerclage cables			3000	442		
Compression plate + Allograft struts	Cerclage cables	Bicortical screws						
Compression plate + Allograft struts	Unicortical Screws & Cerclage cables	Bicortical screws	1926	1486				
Compression plate + Allograft struts	Unicortical Screws & Cerclage cables	Bicortical screws & Cerclage cables						800
Locking plate + Allograft struts	Unicortical Screws & Cerclage cables	Bicortical screws & Cerclage cables						900

Table 18 Lateral bending results[33, 72-74, 76, 77]

Implant Type	Proximal fixation	Distal Fixation	Zdero (08)		Dennis (00)	Dennis (02)	Fulkerson (06)	Kuptniratsaikul (01)	Talbot (08)
			No-Gap	Gap					
Compression plate	Unicortical screws	Bicortical screws			400			394	
Compression plate	Cerclage cables	Bicortical screws			200	490	8.26		
Compression plate	Cerclage cables	Cerclage cables			90				
Compression plate	Unicortical Screws & Cerclage cables	Bicortical screws	481	184	360			401	
Locking plate	Unicortical Screws & Cerclage cables	Bicortical screws	241	71					
Locking plate	Unicortical screws	Bicortical screws	269	71			7.56		25
Allograft struts	Cerclage plain wire	Cerclage plain wire							
Allograft struts	Cerclage cables	Cerclage cables			150	361			
Compression plate + Allograft struts	Cerclage cables	Bicortical screws							
Compression plate + Allograft struts	Unicortical Screws & Cerclage cables	Bicortical screws	1374	920					
Compression plate + Allograft struts	Unicortical Screws & Cerclage cables	Bicortical screws & Cerclage cables							48
Locking plate + Allograft struts	Unicortical Screws & Cerclage cables	Bicortical screws & Cerclage cables							44

Table 19 Torsional loading results[33, 72-74, 76, 77]

Implant Type	Proximal fixation	Distal Fixation	Zdero (08)		Dennis (00)	Dennis (02)	Fulkerson (06)	Kuptniratsaikul (01)	Talbot (08)
			No-Gap	Gap					
Compression plate	Unicortical screws	Bicortical screws			20			1.73	
Compression plate	Cerclage cables	Bicortical screws			12.5	621	0.54		
Compression plate	Cerclage cables	Cerclage cables			7.5				
Compression plate	Unicortical Screws & Cerclage cables	Bicortical screws	1048	963	22			1.73	
Locking plate	Unicortical Screws & Cerclage cables	Bicortical screws	850	935					
Locking plate	Unicortical screws	Bicortical screws	949	935			0.44		200
Allograft struts	Cerclage plain wire	Cerclage plain wire							
Allograft struts	Cerclage cables	Cerclage cables			9	615			
Compression plate + Allograft struts	Cerclage cables	Bicortical screws							
Compression plate + Allograft struts	Unicortical Screws & Cerclage cables	Bicortical screws	1274	1274					
Compression plate + Allograft struts	Unicortical Screws & Cerclage cables	Bicortical screws & Cerclage cables							245
Locking plate + Allograft struts	Unicortical Screws & Cerclage cables	Bicortical screws & Cerclage cables							255

Table 20 Cyclic loading results[72, 73, 76]

Implant Type	Proximal fixation	Distal Fixation	Dennis (02)	Fulkerson (06)	Talbot (08)	Dennis (02)	Fulkerson (06)	Talbot (08)	Dennis (02)	Fulkerson (06)	Talbot (08)
			Axial			Lateral			Torsional		
Compression plate	Unicortical screws	Bicortical screws									
Compression plate	Cerclage cables	Bicortical screws	464	323		348	7.42		616	0.56	
Compression plate	Cerclage cables	Cerclage cables									
Compression plate	Unicortical Screws & Cerclage cables	Bicortical screws									
Locking plate	Unicortical Screws & Cerclage cables	Bicortical screws									
Locking plate	Unicortical screws	Bicortical screws		228	800		8.54	26		0.36	205
Allograft struts	Cerclage plain wire	Cerclage plain wire									
Allograft struts	Cerclage cables	Cerclage cables	390			289			579		
Compression plate + Allograft struts	Cerclage cables	Bicortical screws									
Compression plate + Allograft struts	Unicortical Screws & Cerclage cables	Bicortical screws									
Compression plate + Allograft struts	Unicortical Screws & Cerclage cables	Bicortical screws & Cerclage cables			750			50			255
Locking plate + Allograft struts	Unicortical Screws & Cerclage cables	Bicortical screws & Cerclage cables			850			44			220

Table 21 Failure testing results[72, 73, 75-77]

Implant Type	Proximal fixation	Distal Fixation	Zdero (08)	Dennis (02)	Fulkerson (06)	Schmotzer (96)	Talbot (08)
Compression plate	Unicortical screws	Bicortical screws				240	
Compression plate	Cerclage cables	Bicortical screws		1295	31.6	100	
Compression plate	Cerclage cables	Cerclage cables					
Compression plate	Unicortical Screws & Cerclage cables	Bicortical screws	6600				
Locking plate	Unicortical Screws & Cerclage cables	Bicortical screws	5600				
Locking plate	Unicortical screws	Bicortical screws	5500		29.4		3400
Allograft struts	Cerclage plain wire	Cerclage plain wire				250	
Allograft struts	Cerclage cables	Cerclage cables		950		190	
Compression plate + Allograft struts	Cerclage cables	Bicortical screws					
Compression plate + Allograft struts	Unicortical Screws & Cerclage cables	Bicortical screws	6300				
Compression plate + Allograft struts	Unicortical Screws & Cerclage cables	Bicortical screws & Cerclage cables					4000
Locking plate + Allograft struts	Unicortical Screws & Cerclage cables	Bicortical screws & Cerclage cables					4000

10.5 Standard Operating Procedure for the experimental loading

1. Check 10kN load cell is mounted on Instron
2. Attach flat plate on upper Instron top adapter and base plate on lower Instron base adapter. Ensure both are securely fastened.

3. Turn Instron on and wait for system checks to be completed.

4. Turn supporting computer on and log in (Instron,Instron123)
5. Open BlueHill program
6. Select console settings-1st icon on the left top row and enable the frame
7. Select "Test", open Jonathan Mak folder in my documents and open TESTMETHOD
8. Select load cell setup dialog-2nd icon from the right top row and set the maximum limit to 9950N and check enable.
9. Place loading rig on base adapter and raise crossbar using toggle switch on bottom right of Instron

10. Place potted Femur module in the loading rig
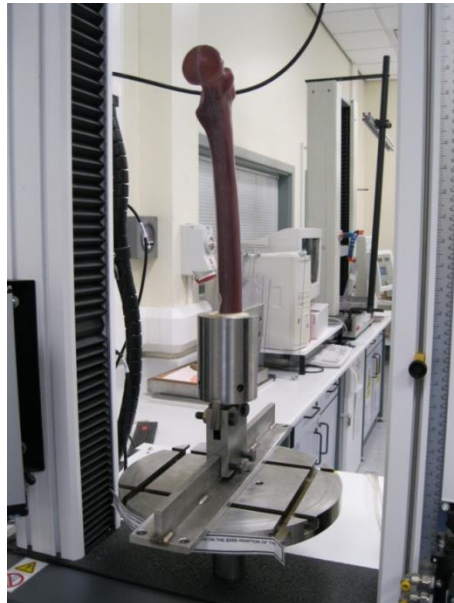
11. Position 10mm bolt through 0degree holes on loading rig and secure using a 10mm nut

12. Position rig such that Femur head is directly under the centre of the upper loading plate.

13. Secure loading rig to base plate using machining blocks with T nuts placed inside base plate groves. N.B for best attachment, bolts should be sited as close to rig end of machining blocks as possible. The back of the machining blocks need to be at the same level or higher than at the rig end.
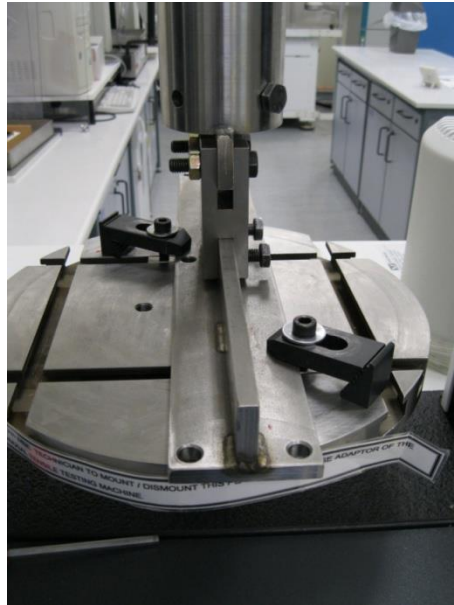
14. Adjust Manual limits stops

15. Attach safety screen (with cut out for mechanical stoppers on right hand side)

16. Move crosshead down to just above test sample
17. Select create new sample in folder – "Jonathan Mak". Create a new folder with the date (year month day), Sawbone number and a brief description of the test.
18. Balance load and reset gauge length
19. Start the Test

10.6 Supercomputer submission code

Example .sh file used to submit jobs to ARC1 supercomputer

```
#!/bin/sh
#$ -l h_rt=48:00:00
#$ -l h_vmem=8000M
#$ -m be
#$ -pe smp 10
#$ -cwd  -V
 ##only include the line below if memory requirement is above 12Gb.
#$ -l cputype=amd
module add abaqus
export LM_LICENSE_FILE=27004@menserv2.leeds.ac.uk
/apps/bin/memmon abaqus memory=75000mb cpus=$NSLOTS
input=B4E1.inp job=B4E1 mp_mode=threads scratch="/nobackup/mnjm" int
```